UNIVERSIDAD COMPLUTENSE DE MADRID
FACULTAD DE CIENCIAS GEOLÓGICAS

TESIS DOCTORAL

Remplazamiento de anhidrita por carbonato cálcico: un caso de estudio de procesos de carbonatación mineral

Replacement of anhydrite by calcium carbonate: a case study of mineral carbonation processes

MEMORIA PARA OPTAR AL GRADO DE DOCTORA

PRESENTADA POR

Iris Cuesta Mayorga

DIRECTORES

José Manuel Astilleros García-Monge
Lourdes Fernández Díaz

Madrid

UNIVERSIDAD COMPLUTENSE DE MADRID

FACULTAD DE CIENCIAS GEOLÓGICAS

DEPARTAMENTO DE MINERALOGÍA Y PETROLOGÍA

TESIS DOCTORAL

REMPLAZAMIENTO DE ANHIDRITA POR CARBONATO CÁLCICO: UN CASO DE ESTUDIO DE PROCESOS DE CARBONATACIÓN MINERAL

REPLACEMENT OF ANHYDRITE BY CALCIUM CARBONATE: A CASE STUDY OF MINERAL CARBONATION PROCESSES

MEMORIA PARA OPTAR AL GRADO DE DOCTOR PRESENTADA POR

IRIS CUESTA MAYORGA

DIRIGIDA POR

JOSÉ MANUEL ASTILLEROS GARCÍA-MONGE

LOURDES FERNÁNDEZ DÍAZ

MADRID, 2019

REMPLAZAMIENTO DE ANHIDRITA POR CARBONATO CÁLCICO: UN CASO DE ESTUDIO DE PROCESOS DE CARBONATACIÓN MINERAL

REEPLACEMENT OF AHNYDRITE BY CALCIUM CARBONATE: A CASE STUDY OF MINERAL CARBONATION PROCESSES

TESIS DOCTORAL FINANCIADA POR EL CONTRATO PREDOCTORAL PFI: BES-2014-070279

IRIS CUESTA MAYORGA

MEMORIA PARA OPTAR AL GRADO DE DOCTOR EN CIENCIAS GEOLÓGICAS (DOCTORADO EUROPEO)

MADRID, 2019

TESIS REALIZADA EN EL DEPARTAMENTO DE MINERALOGÍA Y PETROLOGÍA DE LA FACULTAD DE CIENCIAS GEOLÓGICAS DE LA UNIVERSIDAD COMPLUTENSE DE MADRID

LOS DIRECTORES:

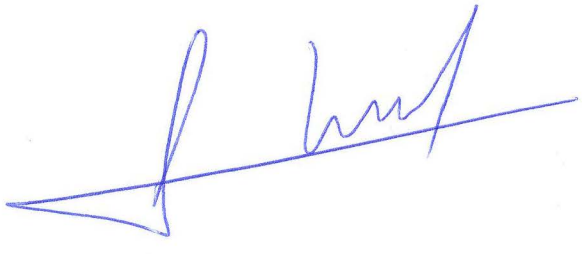

Dr. José Manuel Astilleros García-Monge

Dra. María Lourdes Fernández Díaz

UNIVERSIDAD COMPLUTENSE MADRID

DECLARACIÓN DE AUTORÍA Y ORIGINALIDAD DE LA TESIS PRESENTADA PARA OBTENER EL TÍTULO DE DOCTOR

D./Dña. IRIS CUESTA MAYORGA,
estudiante en el Programa de Doctorado DOCTORADO EN GEOLOGÍA E ING. GEOL.,
de la Facultad de Ciencias Geológicas de la Universidad Complutense de Madrid, como autor/a de la tesis presentada para la obtención del título de Doctor y titulada:

REEMPLAZAMIENTO DE ANHIDRITA POR CARBONATO CÁLCICO:
UN CASO DE ESTUDIO DE PROCESOS DE CARBONATACIÓN MINERAL

y dirigida por:
JOSÉ MANUEL ASTILLEROS GARCÍA-MONGE
MARÍA LOURDES FERNÁNDEZ DÍAZ

DECLARO QUE:

La tesis es una obra original que no infringe los derechos de propiedad intelectual ni los derechos de propiedad industrial u otros, de acuerdo con el ordenamiento jurídico vigente, en particular, la Ley de Propiedad Intelectual (R.D. legislativo 1/1996, de 12 de abril, por el que se aprueba el texto refundido de la Ley de Propiedad Intelectual, modificado por la Ley 2/2019, de 1 de marzo, regularizando, aclarando y armonizando las disposiciones legales vigentes sobre la materia), en particular, las disposiciones referidas al derecho de cita.

Del mismo modo, asumo frente a la Universidad cualquier responsabilidad que pudiera derivarse de la autoría o falta de originalidad del contenido de la tesis presentada de conformidad con el ordenamiento jurídico vigente.

En Madrid, a 17 de julio de 2019

Fdo.:

Esta DECLARACIÓN DE AUTORÍA Y ORIGINALIDAD debe ser insertada en la primera página de la tesis presentada para la obtención del título de Doctor.

AGRADECIMIENTOS

Esta tesis ha sido financiada mediante las ayudas del ministerio de economía y competitividad (MINECO):

- FPI: BES-2014-070279
- EEBB en 2016: EEBB-I-16-11452.
- EEBB en 2017: EEBB-I-17-12537.

Esta tesis doctoral se ha llevado a cabo bajo la dirección de:

- Mis directores de tesis: José Manuel Astilleros García-Monge y Lourdes Fernández Díaz.
- La persona responsable en las 3 estancias que he realizado: Liane G Benning.

Los experimentos y las técnicas de análisis y caracterización se realizaron en:

- Área de Cristalografía y Mineralogía del Departamento de Geología de la Universidad de Salamanca.
- Centro de Ayuda a la Investigación (CAI) de Difracción de Rayos X, de la UCM.
- Centro de Ayuda a la Investigación (CAI) de Técnicas Geológicas, en la UCM.
- Centro Nacional de Microscopía Electrónica (CNME).
- Geoforchungszentrum (GFZ).
- Instituto de Ciencias de Materiales de Madrid (ICMM, CSIC).
- Laboratorio Cohen.
- Laboratorio de Estudios Cristalográficos del Instituto Andaluz de Ciencias de la Tierra (IACT-CSIC-LEC).
- Museo Nacional de Ciencias Naturales (MNCN, CSIC).

ÍNDICE

European Cristallographic Association 2016

European Mineralogical Conference 2016

SEM 2017

GeoBremen 2017

SEM 2018

Epitactic overgrowth of calcite ($CaCO_3$) on anhydrite ($CaSO_4$) cleavage surfaces

Precipitation of $CaCO_3$ polymorphs from aqueous solutions: The role of pH and sulphate groups

ABSTRACT

The processes of mineral carbonation have played a very important role throughout the history of the Earth. For example, it is considered that large volumes of diagenetic limestones have been formed from carbonation processes of evaporite sulphate deposits, by interaction with carbonated waters. The minerals gypsum ($CaSO_4 \cdot 2H_2O$) and anhydrite ($CaSO_4$) are the main components of this type of deposits. When this doctoral thesis was started, there was vast information about the characteristics of gypsum carbonation, but the knowledge about different aspects of carbonation of anhydrite was more limited. This doctoral thesis has focused on expanding and deepening knowledge of these aspects.

The carbonation of anhydrite in contact with carbonated aqueous solutions is developed by coupled dissolution-crystallization reactions through the interface and leads to the formation of calcite pseudomorphs. This process has topotactic character, which significantly influences the development of the textural characteristics of the calcite pseudomorphs formed from anhydrite. On the other hand, the process of carbonation of anhydrite is accompanied by the generation of large volumes of porosity, which evolves over time. In addition, the characteristics of this process are affected by the concentration of the carbonated solution with which the anhydrite interacts, so that, when the carbonate concentration is low, the carbonation reaction is slower, involves the formation of larger volumes of porosity and develops through a more complex reaction pathway. This last aspect leads us to suggest that the SO_4^{2-}/CO_3^{2-} ratio in the aqueous phase exerts an influence similar to that of the Mg^{2+}/Ca^{2+}ratio on the $CaCO_3$ polymorphism.

The objectives of this thesis have been, therefore:

- Study the crystallographic relationships between calcite and anhydrite, and its effect on the kinetics and reaction pathways of the carbonation process of anhydrite.
- Characterize the porosity generated in this process and its spatio-temporal evolution.

- Study the influence of the initial carbonate concentration in the aqueous phase on the characteristics of the anhydrite carbonation process and the resulting pseudomorphs.
- Progress in the understanding of the role of SO_4^{2-}/CO_3^{2-} in the aqueous phase in the $CaCO_3$ polymorphism and the reaction pathways during the carbonation reaction.

This thesis is structured in 4 introductory chapters (Introduction, Objectives, Antecedents and Methodology) and in 5 chapters of results. Of these results, two correspond to works already published and the rest will be included in 3 works that are in the writing process.

Chapter 5 describes the epitaxy relationships between calcite and anhydrite. These relationships involve the planes $\{10\bar{1}4\}$ of the calcite and planes {100}, {010} and {001} of the anhydrite, with the directions $<\bar{4}41>$ of the calcite oriented parallel to the directions < 100>, <010> and <001> of the anhydrite.

Chapter 6 presents a study of the generation of porosity during the carbonation of anhydrite and its evolution. The generated porosity is mainly organized in interconnected channels, constituting a permeable network that allows communication between the carbonated solution and the calcite-anhydrite interface. The organization of the porosity is the result of a process of "Ostwald Ripening" that leads to the disappearance of smaller pores. The final result of this evolution are pseudomorphs containing a network of channels, mostly oriented along the direction [001] of the anhydrite, which points to a certain degree of structural control of the development of porosity.

Chapter 7 deals with the influence of the carbonate concentration in the aqueous solution on the characteristics of the carbonation. When the carbonate concentration in the solution is low, carbonation proceeds at a slower rate and occurs through a polymorph formation sequence of $CaCO_3$ much more complex than when the carbonate concentration is high. In addition, when the carbonate concentration is low, carbonation is associated with the generation of greater volumes of porosity for the same volume of primary carbonated phase and this

porosity is located mostly in a gap that develops between the primary and secondary phase(s). Moreover, the reproduction of the microtopography of the primary phase in the pseudomorphs is less perfect than when the carbonate concentration is high.

The high complexity of the pathway through which carbonation proceeds when the carbonate concentration in the solution is low, points to an important influence of the SO_4^{2-}/CO_3^{2-} ratio in the fluid phase on the $CaCO_3$ polymorphism. Chapter 8 focuses on the study of this influence. It presents the results of precipitation experiments and aging of $CaCO_3$ precipitates in aqueous solutions with different SO_4^{2-}/CO_3^{2-} ratios. It is observed that when precipitation and aging occur in the presence of low concentrations of SO_4^{2-} (or low SO_4^{2-}/CO_3^{2-}), vaterite and calcite are formed, with calcite being the only polymorph present in the system after long aging times. When the concentration of SO_4^{2-} is medium, precipitation of vaterite is observed, accompanied by a small amount of calcite. In this case, the aging of the precipitates leads to the appearance of aragonite at long times. In the case that the concentration of SO_4^{2-} is high, only the precipitation of vaterite is observed, which evolves into aragonite, also forming gypsum after long aging times. The results obtained indicate that increasing the amount of SO_4^{2-} in the aqueous phase inhibits the formation of calcite, at least in the initial moments of the process. On the other hand, the SO_4^{2-}/CO_3^{2-} ratio in the solution affects the morphology of the calcite crystals, which extend parallel to the c-axis as the reaction time increases. This elongation becomes more evident the higher the concentration of SO_4^{2-} is. Aragonite is formed as an alternative phase to calcite, probably due to a combined effect of inhibition of growth and increase of the solubility of calcite when SO_4^{2-} groups are incorporated into its structure. This incorporation of SO_4^{2-} is supported by the results of EDX analysis. The content of S in calcite decreases throughout aging.

Chapter 9 presents the differences found in reaction pathways during the interaction of gypsum or anhydrite fragments with aqueous solutions of Na_2CO_3 of different concentration (0.05M and 0.5M). This interaction using a low carbonate concentration (0.05M) leads to the formation of calcite as the only polymorph in the case of anhydrite, and vaterite and calcite in the case of gypsum. When increasing

the carbonate concentration to 0.5M, starting from anhydrite, the polymorphs formed are vaterite and calcite, with calcite being the only solid phase present in the system at long times. In the case of interaction with gypsum a large amount of vaterite and calcite is formed, in addition to small amounts of aragonite at long times. With regard to the composition of the solution, the concentration of Na remains constant throughout the process, while the concentration of S and that of Ca increases. The most obvious difference between the interaction with gypsum or with anhydrite is related to the kinetics of the process, which is much faster in the case of gypsum. In both cases, the greater the initial concentration of carbonate in the solution ($[CO_3^{2-}]_0$), the higher the concentration of S ([S]) and the lower the concentration of Ca ([Ca]) that is reached during the process. Also in both cases, the pH of the solution decreases more slowly when $[CO_3^{2-}]_0$ is higher.

RESUMEN

Los procesos de carbonatación mineral han jugado un papel muy relevante a lo largo de la historia de la Tierra. Por ejemplo, se considera que grandes volúmenes de calizas diagenéticas se han formado a partir de procesos de carbonatación de depósitos de sulfatos evaporíticos, por interacción con aguas carbonatadas. Los minerales yeso ($CaSO_4 \cdot 2H_2O$) y anhidrita ($CaSO_4$) son los componentes principales de este tipo de depósitos. Cuando se inicia esta tesis doctoral se contaba con amplia información sobre las características de la carbonatación del yeso, pero el conocimiento sobre distintos aspectos de la carbonatación de la anhidrita era más limitado. Esta tesis doctoral se ha centrado en ampliar y profundizar el conocimiento de esos aspectos.

La carbonatación de anhidrita en contacto con disoluciones acuosas carbonatadas se desarrolla a través de reacciones de disolución-cristalización acopladas a través de la interfase y conduce a la formación de pseudomorfos de calcita. Este proceso tiene carácter topotáctico, lo que influye significativamente en el desarrollo de las características texturales de los pseudomorfos formados a partir de anhidrita. Por otro lado, el proceso de carbonatación de la anhidrita va acompañado por la generación de grandes volúmenes de porosidad, la cual evoluciona a lo largo del tiempo. Además, las características de este proceso se ven afectadas por la concentración de la disolución carbonatada con la que interacciona la anhidrita, de modo que, cuando la concentración de carbonato es pequeña, la reacción de carbonatación es más lenta, involucra la formación de mayores volúmenes de porosidad y se desarrolla a través de un camino de reacción más complejo. Este último aspecto lleva a plantear que la relación SO_4^{2-}/CO_3^{2-} en la fase acuosa ejerza sobre el polimorfismo del $CaCO_3$ una influencia similar a la de la relación Mg^{2+}/Ca^{2+}.

Los objetivos de esta tesis han sido, por tanto:

- Estudiar las relaciones cristalográficas existentes entre la calcita y la anhidrita de partida, y su efecto en la cinética y los caminos de reacción del proceso de carbonatación de la anhidrita.

- Caracterizar la porosidad generada en este proceso y su evolución espacio-temporal.
- Estudiar la influencia de la concentración inicial de carbonato en la fase acuosa en las características del proceso de carbonatación de anhidrita y de los pseudomorfos resultantes.
- Avanzar en la comprensión del papel de la relación SO_4^{2-}/CO_3^{2-} en la fase acuosa en el polimorfismo del $CaCO_3$ y los caminos de reacción durante la reacción de carbonatación.

Esta tesis se estructura en 4 capítulos introductorios (Introducción, Objetivos, Antecedentes y Metodología) y en 5 capítulos de resultados. De estos resultados, dos corresponden a trabajos ya publicados y el resto se incluirán en 3 trabajos que se encuentran en su proceso de redacción.

El capítulo 5 describe las relaciones de epitaxia entre la calcita y la anhidrita. Estas relaciones involucran a los planos $\{10\bar{1}4\}$ de la calcita y los planos {100}, {010} y {001} de la anhidrita, con las direcciones $<\bar{4}41>$ de la calcita orientadas paralelamente a las direcciones <100>, <010> y <001> de la anhidrita.

El capítulo 6 presenta un estudio de la generación de porosidad durante la carbonatación de la anhidrita y su evolución. La porosidad generada se organiza, principalmente, en canales interconectados, constituyendo un entramado permeable que permite la comunicación entre la disolución carbonatada y la interfase calcita-anhidrita. La organización de la porosidad es el resultado de un proceso de "Ostwald Ripening" que conduce a la desaparición de poros más pequeños. El resultado final de esta evolución son pesudomorfos que contienen un entramado de canales, mayoritariamente orientados a lo largo de la dirección [001] de la anhidrita, lo que apunta a cierto grado de control estructural del desarrollo de la porosidad.

El capítulo 7 trata de la influencia de la concentración de carbonato en la disolución acuosa en las características de la carbonatación. Cuando la concentración de carbonato en la disolución es pequeña, la carbonatación avanza a menor velocidad y se produce a través de una secuencia de formación de polimorfos

del $CaCO_3$ mucho más compleja que cuando la concentración de carbonato es alta. Además, cuando la concentración de carbonato es baja, la carbonatación se asocia a la generación de mayores volúmenes de porosidad para un mismo volumen de fase primaria carbonatada y esta porosidad se localiza en su mayor parte en un hueco que se desarrolla entre las fases primaria y secundaria(s). También, la reproducción de la microtopografía de la fase primaria en pseudomorfo es menos perfecta que cuando la concentración de carbonato es alta.

La alta complejidad del camino de reacción a través del cual procede la carbonatación cuando la concentración de carbonato en la disolución es baja apunta a una importante influencia de la relación SO_4^{2-}/CO_3^{2-} en la fase fluida sobre el polimorfismo del $CaCO_3$. El capítulo 8 se centra en el estudio de esta influencia. En él se presentan los resultados de experimentos de precipitación y envejecimiento de los precipitados formados de $CaCO_3$ en disoluciones acuosas con distintas relaciones SO_4^{2-}/CO_3^{2-}. Se observa que cuando la precipitación y el envejecimiento se producen en presencia de concentraciones bajas de SO_4^{2-} (o bajas relaciones SO_4^{2-}/CO_3^{2-}) se forma vaterita y calcita, siendo la calcita el único polimorfo presente en el sistema tras tiempos de envejecimiento largos. Cuando concentración de SO_4^{2-} es media, se observa la precipitación de vaterita, acompañada por una cantidad pequeña de calcita. En este caso, el envejecimiento de los precipitados conduce a la aparición de aragonito a tiempos largos. En el caso de que la concentración de SO_4^{2-} sea alta, sólo se observa la precipitación de vaterita, la cual evoluciona a aragonito, formándose además yeso tras tiempos de envejecimiento largos. Los resultados obtenidos indican que al aumentar la cantidad de SO_4^{2-} en la fase acuosa inhibe la formación de calcita, al menos en los momentos iniciales del proceso. Por otro lado, la relación SO_4^{2-}/CO_3^{2-} en la disolución afecta a la morfología de los cristales de calcita, que se alargan paralelamente al eje *c* al aumentar el tiempo de reacción. Este alargamiento se hace más evidente cuanto mayor es la concentración de SO_4^{2-}. El aragonito se forma como fase alternativa a la calcita, probablemente debido a un efecto combinado de inhibición del crecimiento y de aumento de su solubilidad al incorporarse grupos SO_4^{2-} en su estructura. Esta incorporación de SO_4^{2-} es apoyada

por los resultados de análisis EDX. El contenido de S en la calcita disminuye a lo largo del envejecimiento.

El capítulo 9 presenta las diferencias encontradas en los caminos de reacción durante la interacción de fragmentos de yeso o de anhidrita con disoluciones acuosas de Na_2CO_3 de distinta concentración (0.05M y 0.5M). Esta interacción empleando una concentración baja de carbonato (0.05M) conduce a la formación de calcita como único polimorfo en el caso de la anhidrita, y vaterita y calcita en el caso del yeso. Al aumentar la concentración de carbonato a 0.5M, partiendo de anhidrita, los polimorfos formados son vaterita y calcita, siendo la calcita la única fase sólida presente en el sistema a tiempos largos. En el caso de la interacción con yeso se forma una gran cantidad de vaterita y calcita, además de pequeñas cantidades de aragonito a tiempos largos. En cuanto a la composición de la disolución, la concentración de Na se mantiene constante durante todo el proceso, mientras que la concentración de S y el de Ca aumenta. La diferencia más evidente entre que la interacción se produzca con yeso o con anhidrita se relaciona con la cinética del proceso, siendo ésta mucho más rápida en el caso del yeso. En ambos casos, cuanto mayor es la concentración inicial de carbonato en la disolución ($[CO_3^{2-}]_0$), mayor es también la concentración de S ([S]) y menor la de Ca ([Ca]) que se alcanza durante el proceso. También en ambos casos, el pH de la disolución desciende más lentamente cuanto mayor es $[CO_3^{2-}]_0$.

1. INTRODUCCIÓN

1. INTRODUCCIÓN

Los minerales formadores de roca yeso ($CaSO_4 \cdot 2H_2O$) y anhidrita ($CaSO_4$) son los sulfatos más comunes en la superficie terrestre. Ambos se forman en ambientes evaporíticos, el yeso por precipitación directa en un amplio rango de temperaturas, mientras que la formación de anhidrita se interpreta normalmente como secundaria, a partir de yeso, aunque distintos autores han atribuido un origen primario a la anhidrita cuando ésta se forma en condiciones de muy alta salinidad y en presencia de bacterias halofílicas (Anthony et al., 2003; Cody and Hull, 1980; Freyer and Voigt, 2003). La anhidrita también es un mineral relevante en campos hidrotermales submarinos, donde los procesos de disolución-cristalización y reemplazamiento mineral que afectan a esta fase contribuyen a incrementar la permeabilidad de las estructuras hidrotermales y hacen que juegue un papel fundamental en los ciclos geoquímicos del S y de distintos metales (Kuhn et al., 2003).

Distintos autores han destacado la relevancia de los procesos de reemplazamiento mineral que involucran a sulfatos formadores de roca en una variedad de problemas geológicos, desde la formación de depósitos explotables de algunos minerales a la regulación de los niveles de CO_2 en la atmósfera. Por ejemplo, los grandes depósitos de celestina ($SrSO_4$), la principal fuente de Sr y un mineral poco común en comparación con otros sulfatos de cationes divalentes, aparecen normalmente asociados a rocas sedimentarias y su formación ha sido atribuida por Hanor (2004) a la interacción de yeso y/o anhidrita con disoluciones acuosas que contienen Ba y Sr. Esta interacción conduciría a un progresivo enriquecimiento relativo de la disolución acuosa en Sr, mediado por la disolución de los sulfatos cálcicos y la subsecuente precipitación de barita, lo que eventualmente garantizaría que se alcanzaran las condiciones de concentración de Sr óptimas para la precipitación de celestina. De forma similar, se ha atribuido un origen diagenético a la formación de grandes volúmenes de carbonatos en cuencas sedimentarias, los cuales habrían resultado de la interacción de aguas carbonatadas con depósitos de sulfatos cálcicos evaporíticos a lo largo de etapas prolongadas (Alonso-Zarza et al., 2002; Azam, 2007; Dejonghe et al., 1998; Kendall, 2001; Pierre and Rouchy, 1988;

Rouchy et al., 1998; Sanz-Rubio et al., 2001; Stafford et al., 2008). Es evidente la importancia que este último proceso puede haber tenido a lo largo de la historia de la Tierra, al promover la fijación de CO_2 atmosférico y su almacenamiento en forma de rocas calizas. Como se explica extensamente en el capítulo 3 (Antecedentes), este proceso ha sido estudiado experimentalmente en detalle para el caso del yeso, evidenciándose la no existencia de relaciones topotácticas entre las fases sólidas implicadas en la carbonatación del yeso, que el avance del proceso va acompañado por la generación de grandes volúmenes de porosidad y que la concentración de carbonato en la disolución acuosa que interacciona con los cristales de yeso afecta a la secuencia de formación de fases del $CaCO_3$ a través de la cual se desarrolla su carbonatación. Este último aspecto de la carbonatación del yeso tiene una especial importancia porque se relaciona de forma directa con el polimorfismo del $CaCO_3$, uno de los problemas fundamentales de la mineralogía y sobre el cual se ha centrado a lo largo de las últimas dos décadas la atención de distintas disciplinas, desde la química a la nanociencia (Bots et al., 2012; Gebauer et al., 2010; Meldrum and Cölfen, 2008). Es bien sabido que las fases del $CaCO_3$ son ubicuas en la naturaleza, donde pueden tener un origen puramente inorgánico o biogénico, tanto si se forman a través de procesos mediados por la actividad metabólica de organismos vivos como si son el constituyente inorgánico de tejidos duros biológicos (Carlson, 1983; Radha and Navrotsky, 2013). Además, estas fases tienen numerosas aplicaciones tecnológicas y su formación indeseada en determinados contextos industriales representa un problema de dimensiones enormes en todo el planeta (Meldrum and Cölfen, 2008; Sheikholeslami and Ong, 2003).

En el momento de iniciarse esta tesis doctoral se conocían algunos aspectos sobre la carbonatación de la anhidrita que apuntaban a la existencia de diferencias significativas con respecto a las conocidas sobre la carbonatación del yeso. Una de estas diferencias se refiere al carácter topotáctico de la carbonatación de anhidrita, que se había constatado pero cuyas características concretas estaban pendientes de ser analizadas. También se conocía que el volumen de porosidad generado durante la carbonatación de anhidrita es mucho menor que en el caso del yeso y se organiza de forma diferente. El estudio de las características de esta organización y de su

evolución espacio-temporal no se había iniciado. Otra diferencia fundamental entre las características de la carbonatación de yeso y anhidrita se refiere a la secuencia de reacción a través de la cual procede esta última. La exploración de esta secuencia y su dependencia con respecto a la concentración de carbonato en la fase acuosa es un problema que también estaba pendiente de abordar. Por otro lado, la observación de que la carbonatación del yeso involucra la formación de distintas fases de $CaCO_3$ dependiendo de la concentración de carbonato en la disolución acuosa con la que interacciona apunta a un papel significativo del oxoanión sulfato (SO_4^{2-}) en el polimorfismo del $CaCO_3$. Este posible papel del sulfato ya había sido planteado por distintos autores (Arroyo-de Dompablo et al., 2015; Bots et al., 2011; Fernández-Díaz et al., 2010). Sin embargo, está lejos de ser comprendido totalmente y un estudio detallado de la carbonatación de la anhidrita puede aportar información que arroje luz sobre sus características.

`

2. OBJETIVOS

2. OBJETIVOS

Teniendo en cuenta las consideraciones expuestas en los párrafos anteriores, se han definido los siguientes objetivos para Tesis Doctoral:

1. Identificar y caracterizar las relaciones cristalográficas (epitaxia) que se establecen entre la fase primaria anhidrita ($CaSO_4$) y la fase secundaria calcita ($CaCO_3$) durante la carbonatación de la primera en contacto con una disolución acuosa, tomando en consideración las tres superficies principales de la anhidrita: (100), (010), (001).

2. Evaluar y discutir la influencia de la existencia de relaciones cristalográficas entre calcita y anhidrita en la cinética del proceso de carbonatación.

3. Caracterizar la porosidad generada durante el proceso de carbonatación de la anhidrita, su organización espacial y la evolución espacio-temporal de sus características durante el envejecimiento en contacto con la disolución acuosa.

4. Evaluar la posible existencia de una relación entre la organización de la porosidad generada en la carbonatación y las características estructurales de la anhidrita.

5. Estudiar la influencia de la concentración de carbonato en la disolución acuosa en el desarrollo de características texturales durante la carbonatación de anhidrita.

6. Estudiar la influencia de la concentración de carbonato en la disolución acuosa en el camino de reacción a través del cual se desarrolla la carbonatación de anhidrita.

7. Avanzar en la comprensión de la influencia del oxoanión sulfato en el polimorfismo del $CaCO_3$.

3. ANTECEDENTES

3. ANTECEDENTES

3.1. REACCIONES ACOPLADAS DE DISOLUCIÓN – CRISTALIZACIÓN MINERAL

Una gran parte de los procesos que afectan a minerales en ambientes superficiales y subsuperficiales se desarrollan a través de reacciones que implican la disolución de una fase inicial y dan lugar a la cristalización de una o más fases secundarias. Este tipo de reacciones están implicadas en la formación de algunos depósitos minerales, como por ejemplo los de origen hidrotermal, los volcano-sedimentarios o los supergénicos, en procesos metasomáticos, en la diagénesis y, en general, en cualquier tipo de proceso en el cual una disolución acuosa multicomponente interacciona con un mineral (Pohl, 2011; Tucker, 2001).

Durante el desarrollo de las reacciones de disolución-cristalización que tienen lugar cuando un fluido multicomponente entra en contacto con una fase mineral, las características fisicoquímicas concretas de la fase fluida (composición, pH, etc.) y las propiedades termodinámicas y cinéticas de la fase mineral original, como su solubilidad o la velocidad de disolución de sus diferentes caras cristalográficas, pueden favorecer un acoplamiento entre la velocidad a la que se disuelve la fase primaria y la velocidad a la que se forma la(s) fase(s) secundaria(s). Cuando se da este acoplamiento, se desarrollan fenómenos de remplazamiento mineral que tienen carácter pseudomórfico, es decir, transcurren con preservación de la forma externa de la fase primaria (Putnis, 2002). Con frecuencia, el grado de acoplamiento es tal que garantiza que, además de la forma externa, en la(s) fase(s) secundaria(s) queden preservados los detalles más delicados de las superficies de la fase primaria, a veces hasta su nanotopografía. Los estudios de distintos autores han demostrado que, en ocasiones, se pueden transferir a la(s) fase(s) secundaria(s) algunas características texturales y/o microestructurales de la fase primaria, como pueden ser planos de macla y otros defectos planares o el tamaño del cristalito (Casella et al., 2018; Xia et al., 2009a). Se ha definido como escala del pseudomorfismo (Fernández-Díaz et al., 2009; Pöml et al., 2007) el grado de perfección con el que las distintas características

de la fase primaria se transfieren a la(s) fase(s) secundaria(s). Se ha contrastado que la escala del pseudomorfismo viene determinada por el grado de ajuste entre las cinéticas de disolución de la fase primaria y precipitación de la(s) fase(s) secundaria(s) (Fernández-Díaz et al., 2009; Pöml et al., 2007; Xia et al., 2009a). El principal requerimiento para que este ajuste sea bueno es que el proceso limitante de la reacción sea la disolución de la fase primaria, mientras que la precipitación de la(s) fase(s) secundaria(s) se produce de forma instantánea, es decir, con un tiempo de inducción que tiende a cero (Putnis, 2002; Putnis, 2009; Putnis, 2015; Putnis and Putnis, 2007; Ruiz-Agudo et al., 2016; Ruiz-Agudo et al., 2014). Habitualmente, estas reacciones acopladas conducen a la formación de agregados cristalinos a partir de monocristales. Estos agregados están constituidos por numerosos cristales cuyo tamaño es tanto menor cuanto mejor es el acoplamiento entre el proceso de disolución de la fase primaria y el de cristalización de la(s) fase(s) secundaria (Fernández-Díaz et al., 2009). Un buen acoplamiento entre las cinéticas de ambos procesos también se refleja en una reproducción más exacta de los detalles de la topografía original de la fase primaria en el pseudomorfo, ya que la cristalización es inmediata en el momento en el que se produce la disolución, sin que se desmonte la superficie antes de que se produzca la nucleación. A esta buena reproducción también contribuye el que la superficie original quede recubierta por una alfombra de cristales muy pequeños.

3.2. PROGRESO DE LOS PROCESOS DE REEMPLAZAMIENTO MINERAL: GENERACIÓN DE POROSIDAD Y SU EVOLUCIÓN

Para que un proceso de reemplazamiento mineral que se desarrolla a través de una reacción acoplada de disolución-cristalización pueda progresar es necesario que exista una comunicación continua entre la fase fluida y la interfase que surge entre las fases minerales primaria y secundaria(s). En efecto, es en esta interfase donde tiene lugar la reacción acoplada. Esta comunicación entre interfase y volumen de la fase fluida garantizada cuando el proceso del reemplazamiento lleva asociada la generación de porosidad. Esta porosidad tiene un carácter transitorio, es decir, sus

características evolucionan a lo largo del tiempo y puede llegar a desaparecer como consecuencia de esta evolución (Putnis, 2002; Putnis, 2015). La formación de esta porosidad es una consecuencia directa del carácter pseudomórfico del reemplazamiento mineral cuando el cambio de volumen molar asociado a la reacción es negativo. A la componente de porosidad que resulta de esta pérdida de volumen molar puede sumarse otro componente más cuando la fase primaria es más soluble que la(s) fase(s) secundaria(s) (Pollok et al., 2011; Pöml et al., 2007; Putnis 2002; Putnis 2009; Ruiz-Agudo et al., 2014).

El volumen total de porosidad que se genera durante los procesos de reemplazamiento mineral se distribuye en el interior de la capa reemplazada por la(s) fase(s) secundaria(s). Sin embargo, en aquellos casos en los que la diferencia negativa de volumen molar entre las fases primaria y secundaria es muy elevada, la porosidad confinada en la capa reemplazada es insuficiente para dar cuenta de esta diferencia de volumen. Ello determina que, según va progresando la reacción de disolución-cristalización, se produzca una acumulación de porosidad en la interfase entre las fases, eventualmente dando lugar a la formación de un hueco que rodea al núcleo de la fase primaria que todavía no ha reaccionado. El tamaño de este hueco aumenta al avanzar el reemplazamiento y, cuando este proceso culmina, puede resultar en la formación de pseudomorfos que consisten en un agregado policristalino y poros de la(s) fase(s) secundaria(s) con un hueco central (Fernández-Díaz et al., 2009; Pöml et al., 2007; Xia et al., 2009a).

Aunque la generación de porosidad facilita los procesos de reemplazamiento mineral, un cambio de volumen molar negativo y una mayor solubilidad de la fase primaria pueden no garantizar el que la reacción de disolución-cristalización avance a una velocidad relevante. Este puede ser el caso cuando existen relaciones epitaxiales entre la fase primaria y la(s) fase(s) secundaria(s) y el crecimiento de la(s) última(s) sobre la primera forma un tapiz que la recubre por completo y la aísla de la fase fluida, impidiendo de forma efectiva que interaccionen. Este aspecto se discute en detalle más adelante en la sección 3.3.

De lo discutido hasta el momento se podría concluir que la existencia de un cambio de volumen molar negativo es un prerrequisito imprescindible para que una reacción de reemplazamiento mineral proceda a través de una reacción acoplada de disolución-cristalización. Sin embargo, existen numerosos ejemplos en la naturaleza que demuestran que este fenómeno puede tener lugar incluso cuando el cambio de volumen molar implicado es positivo y tiene un valor significativo. Este es el caso, por ejemplo, de las reacciones que tiene lugar durante la serpentinización de forsterita (Kelemen and Hirth, 2012; Plümper et al., 2012) o las transformaciones pseudomórficas de aragonito en calcita (Perdikouri et al., 2013), de calcopirita en bornita (Zhao et al., 2014), de hematites en calcopirita (Zhao et al., 2014), de magnetita en pirita (Qian et al., 2010) o de magnetita en marcasita (Qian et al., 2010). Los estudios experimentales realizados en estos sistemas muestran que, a pesar de que durante el desarrollo de los procesos de reemplazamiento mineral no se genera una porosidad significativa, estos procesos pueden avanzar gracias a la formación de fracturas en la fase primaria. Estas fracturas se interpretan como consecuencia de la presión de cristalización que la(s) fase(s) secundaria(s) ejerce(n) sobre la primaria. La fase fluida puede percolar a través de estas fracturas, las cuales proveen, además, nuevas superficies de la fase primaria que quedan expuestas a la interacción con la fase fluida. Aunque la velocidad de la reacción puede verse afectada negativamente cuando el cambio de volumen molar implicado es positivo y el reemplazamiento puede afectar sólo a un pequeño volumen de la fase primaria, una secuencia de eventos de cristalización de la(s) fase(s) secundaria(s) y fracturación de la fase primaria puede concluir con el total reemplazamiento de esta última (Altree-Williams et al., 2015; Putnis, 2009). En estos casos, la preservación de la forma externa de la fase primaria suele ser pobre. De hecho, es habitual que se formen sobrecrecimentos de la(s) fase(s) secundaria(s) en la superficie de la fase primaria. Estos sobrecrecimientos suelen ser muy porosos, acumulándose la porosidad en el contacto entre la capa reemplazada y el sobrecrecimiento (Altree-Williams et al., 2015; Putnis, 2002; Putnis, 2009; Putnis, 2015; Putnis and Putnis, 2007; Ruiz-Agudo et al., 2014; Ruiz-Agudo et al., 2016).

3.3. RELACIONES EPITAXIALES Y CINÉTICA DE LA REACCIÓN ACOPLADA DE DISOLUCIÓN-CRISTALIZACIÓN

El punto inicial de un proceso de reemplazamiento mineral implica la nucleación de cristales de la(s) fase(s) secundaria(s) sobre la superficie externa de la fase primaria. Puede ocurrir que las fases implicadas en el reemplazamiento compartan elementos estructurales y/o cristaloquímicos (Qian et al., 2011; Xia et al., 2009a; Xia et al., 2009b). En estos casos, con frecuencia los núcleos de la(s) fase(s) secundaria(s) guardan relaciones epitaxiales con el substrato primario y pueden pasivar parcial o totalmente a este substrato, al aislarlo del contacto con la fase fluida. Como resultado se produce un retardo significativo de la cinética del reemplazamiento. Esta situación se puede esperar cuando el cambio de volumen molar asociado al reemplazamiento es muy pequeño y, en consecuencia, la superficie de la fase primaria queda rápidamente recubierta por una delgada capa compacta de cristales de la(s) fase(s) secundaria(s). Este efecto es especialmente marcado cuando las fases primaria y secundaria son isoestructurales, ya que la capa epitaxial que recubre el substrato primario en estos casos suele tener un espesor de tan solo unos pocos nanómetros y mostrar una perfecta continuidad (Pérez-Garrido et al., 2007; Prieto et al., 2003). Efectivamente, son numerosos los ejemplos de sistemas en los que la formación de una capa nanométrica de cristales de una fase secundaria isoestructural con la fase que constituye el sustrato primario ha resultado en una inhibición completa de la interacción de este con la fase fluida. Esto ha sido demostrado experimentalmente durante la interacción de superficies de calcita ($CaCO_3$) con disoluciones acuosas que contiene cationes como Cd^{2+} o Mn^{2+}, cuyos carbonatos, otavita ($CdCO_3$) y rodocrosita ($MnCO_3$) son isoestructurales con la calcita y existen soluciones sólidas más o menos extensas entre estos miembros finales (Pérez-Garrido et al., 2007; Pérez-Garrido et al., 2009). Una situación similar se ha observado en el caso de la interacción de barita ($BaSO_4$) con disoluciones que contienen Cr(VI). La hashemita ($BaCrO_4$) es isoestructural con la barita, con la que forma una solución sólida completa (Becker et al., 2006). La interacción con la fase fluida resulta, en este caso, en la formación de una capa epitaxial nanométrica que rápidamente pasiva la superficie de los cristales de barita (Shtukenberg et al., 2005).

Aunque se ha evidenciado en muchos sistemas que la existencia de relaciones epitaxiales entre las fases primaria y secundaria(s) se correlaciona con cinéticas muy lentas de la reacción de reemplazamiento mineral, es importante matizar que este impacto negativo se restringe a aquellos casos en los que existe un ajuste casi perfecto entre las estructuras de las fases implicadas en la epitaxia, que permite la formación de núcleos bidimensionales que crecen según los mecanismos de Frank-van der Merwe o Stranski-Krastanov (Chernov, 1984). En aquellos casos en los que la bondad del ajuste entre las estructuras es menor, el crecimiento epitaxial tiene lugar a través del mecanismo de Volmer-Weber, que implica el crecimiento sobre la superficie de la fase primaria de numerosas islas tridimensionales de la fase secundaria. Estas islas se forman con distintas orientaciones relacionadas a través de aquellos operadores de simetría que están presenten en la fase primaria y que se disponen perpendiculares a la interfase (Cuesta Mayorga et al., 2018; Morales et al., 2013). La coalescencia de estas islas con distintas orientaciones da lugar a la formación de maclas inducidas por la simetría del sustrato y, en última instancia, resulta en la formación de una capa que contiene una porosidad intracristalina. Esta porosidad tiene un carácter intrínseco y se asocia al mecanismo de crecimiento epitaxial de Volmer-Weber. Aunque sí se puede esperar una ralentización de la reacción de disolución-cristalización por la formación de una capa epitaxial con estas características, la presencia de esta porosidad intrínseca previene el sellado perfecto del substrato primario y garantiza la comunicación entre la interfase y el volumen de la disolución acuosa, permitiendo, por tanto, que la reacción de disolución-cristalización pueda progresar. Existen distintos ejemplos de fenómenos de reemplazamiento mineral en los que una reacción de disolución-cristalización acoplada se desarrolla a través de la formación de una capa epitaxial constituida por cristales tridimensionales con distintas orientaciones relacionadas por operados de simetría presentes en la fase primaria. Entre estos ejemplos se pueden destacar los casos la formación de farmacolita ($CaHAsO_4 \cdot 2H_2O$) sobre yeso en contacto con una disolución acuosa que contiene As(V) o de anglesita ($PbSO_4$) sobre anhidrita en contacto con una disolución con Pb^{2+} (Morales et al., 2013; Morales et al., 2014; Prieto et al., 2003; Prieto et al., 2013; Rodríguez et al., 2008; Rodríguez-Blanco et al., 2007).

3.4. FENÓMENOS DE CARBONATACIÓN MINERAL

Uno de los procesos de disolución-cristalización que tiene implicaciones más relevantes en el contexto actual de cambio climático promovido por un progresivo y continuo aumento de la presión de CO_2 en la atmosfera terrestre es aquel que conduce al reemplazamiento de minerales de composición variada, desde silicatos a sulfatos, por fases carbonatadas (Oelkers et al., 2008). A lo largo de la historia de la Tierra la precipitación de carbonatos ha ejercido como un proceso tampón que ha impedido un aumento desmesurado de la concentración de CO_2, incluso en aquellas etapas en las que grandes volúmenes de este gas se liberaban a la atmosfera a través de la actividad volcánica. En efecto, uno de los mecanismos más eficientes y seguros para eliminar CO_2 de la atmosfera es la precipitación de carbonatos. Los fenómenos de carbonatación mineral se pueden desarrollar en una gran variedad de contextos geológicos. Por ejemplo, la formación de carbonatos de Mg y/o Ca (magnesita, dolomita y calcita) es un fenómeno frecuentemente asociado a los procesos de serpentinización de peridotitas (Rudge et al., 2010) que ha inspirado los esfuerzos de distintos investigadores para desarrollar metodologías que permitan reducir las emisiones de gases invernadero a la atmósfera a través de su eliminación mediante la precipitación de fases minerales de baja solubilidad (Gislason and Oelkers, 2014; Kelemen et al., 2008; Matter et al., 2009; Peuble et al., 2018; Power et al. 2013; Ulven et al., 2017; Zhu et al., 2016).

3.4.1. Carbonatación mineral en cuencas sedimentarias

3.4.1.1. Formación secundaria de estroncianita ($SrCO_3$) y witherita ($BaCO_3$)

Aunque los fenómenos de carbonatación afectan a todo tipo de minerales, son especialmente comunes en cuencas sedimentarias. El pH de las aguas meteóricas equilibradas con CO_2 y oxígeno atmosférico se sitúa habitualmente en valores cercanos a 5.6. Al atravesar rocas calizas y dolomías, estas aguas se cargan de iones carbonato y se vuelven alcalinas. Su interacción con las fases minerales no carbonatadas presentes en rocas sedimentarias puede dar lugar a reacciones disolución-cristalización y a la formación de pseudomorfos. Con frecuencia, estos procesos de carbonatación afectan a sulfatos sedimentarios. La formación de

estroncianita y witherita en estos ambientes se interpreta como un ejemplo de carbonatación mineral. La estroncianita y la witherita son los miembros finales de la solución sólida $(Ba,Sr)CO_3$. Esta solución sólida tiene estructura aragonito y, desde el punto de vista de sus propiedades termodinámicas, se puede describir como ideal. En consecuencia, las composiciones intermedias entre sus miembros finales son estables (Brice and Chang, 1973; Chang, 1971). Por ello, resulta sorprendente que estos términos intermedios apenas estén representados en la naturaleza (Speer, 1983), y que prácticamente todas las witheritas contengan porcentajes de Sr inferiores a 11 mol % $SrCO_3$ y en la mayor parte de las estroncianitas los contenidos de Ba sean incluso más bajos (Baldasari and Speer, 1979). La escasez en la naturaleza de términos intermedios de esta solución sólida resulta todavía más sorprendente si se considera que estas composiciones se sintetizan fácilmente en el laboratorio, donde los experimentos de precipitación por mezcla de soluciones o de crecimiento en geles indefectiblemente conducen a la formación de cristales de $(Ba,Sr)CO_3$ cuya relación Ba/Sr es muy similar a la de la fase líquida a partir de la cual crecen (Böttcher et al., 1997; Fernández-González, 1996; Prieto et al., 1997). Estos resultados experimentales son consistentes con los valores de los productos de solubilidad de estas fases ($Ksp_{Str}=10^{-9.27}$ (Busenberg and Plummer, 1984); $Ksp_{Wth}=10^{-8.56}$ (Busenberg and Plummer, 1986)), que, al ser muy similares, determinan que las curvas de solidus y solutus se proyecten muy próximas entre sí en el diagrama de Lippmann de esta solución sólida y, por tanto, las relaciones Ba/Sr en el sólido y el líquido en equilibrio sean muy similares. Estas circunstancias han llevado a distintos investigadores a concluir que la mayoría de los cristales de $(Ba,Sr)CO_3$ que se encuentran en la naturaleza no tienen origen primario, sino que se han formado a través de procesos de carbonatación de sulfatos minerales correspondientes a la solución sólida barita-celestina $(Ba,Sr)SO_4$ (Speer, 1983; Chang et al., 1998). Esta solución sólida posee una marcada bimodalidad composicional debido a la gran diferencia en los productos de solubilidad de sus miembros finales (a 25º C, $Ksp_{Brt} = 10^{-9.98}$ (Blount et al., 1977) y $Ksp_{Cls}=10^{-6.63}$ (Reardon and Amstrong, 1987)), por lo que sólo un rango muy estrecho relaciones Ba/Sr en la fase líquida pueden dar lugar a sólidos de composiciones intermedias.

La carbonatación de celestina ($SrSO_4$) ha sido estudiada experimentalmente por Suarez-Orduña et al. (Suarez-Orduña et al., 2004) utilizando condiciones hidrotermales y disoluciones acuosas alcalinas en el rango de temperaturas entre 150 y 250º C. Estos autores establecieron que en estas condiciones la transformación de celestina en estroncianita tiene carácter topotáctico, produce pseudomorfos y se desarrolla a través de reacciones de disolución-cristalización acopladas. Se ha evidenciado mediante observaciones a nanoescala usando microscopia de fuerza atómica que el carácter topotáctico de la transformación se inicia con la nucleación epitaxial de islas bidimensionales de estroncianita sobre la superficie de los cristales de celestina (Sánchez-Pastor, 2007; Sánchez-Pastor et al., 2007a; Sánchez-Pastor et al., 2007b). Los pseudomorfos de estroncianita a partir de celestina son agregados de cristales que muestran una textura específica, la cual encierra un importante volumen de porosidad organizada en canales (Suárez-Orduña et al., 2007). Esta porosidad se origina durante la transformación, compensando el cambio de volumen molar negativo asociado a la misma, y facilita la comunicación entre la fase acuosa y la interfase entre celestina y estroncianita.

La transformación de barita ($BaSO_4$) en witherita ($BaCO_3$) ha sido estudiada por Rendón-Ángeles et al. (Rendón-Ángeles et al., 2008). Estos autores han establecido que las características de esta transformación en el rango de temperaturas entre 150 y 250º C en presencia disoluciones acuosa cargadas de carbonato son similares a las que muestra la transformación de celestina en estroncianita. Es decir, también tiene carácter topotáctico y da lugar a pseudomorfos, los cuales encierran una porosidad organizada en canales que conecta el volumen de la fase acuosa con la interfase barita-celestina (Rendón-Ángeles et al., 2008; Sánchez-Pastor 2007; Sánchez-Pastor et al., 2007a; Sánchez-Pastor et al., 2007b; Speer and Hensley-Dunn, 1976).

3.4.1.2. Formación de carbonatos cálcicos diagenéticos por reemplazamiento de sulfatos cálcicos evaporíticos

Uno de los procesos de carbonatación mineral más relevantes es el que afecta a los sulfatos cálcicos evaporíticos anhidrita y yeso. El yeso es el sulfato más

abundante en la corteza terrestre, seguido por la anhidrita. La carbonatación de yeso y anhidrita es un fenómeno que se ha estado desarrollando desde el Precámbrico y que, con carácter exclusivamente inorgánico o con participación bacteriana, ha estado involucrado en la formación de grandes volúmenes de carbonatos diagenéticos a lo largo de la historia de la Tierra (Alonso-Zarza et al., 2002; Anadón et al., 1992; Cañaveras et al., 1996; Cañaveras et al., 1998; Kendall, 2001; Rouchy et al., 1998; Rouchy et al., 1994; Sanz-Rubio et al., 2001). Estos procesos de carbonatación que se desarrollan en cuencas sedimentarias han contribuido de forma relevante a la evolución de las trampas sedimentarias de fluidos naturales como aguas y petróleo, ya que han facilitado el desarrollo de porosidad interconectada, incrementando la permeabilidad de las rocas sedimentarias. Un mecanismo que involucra la disolución de sulfatos cálcicos primarios y la precipitación de carbonatos en la formación de calizas ha sido apoyado por análisis isotópicos (Sanz-Rubio et al., 2001).

Distintos autores han abordado experimentalmente el estudio del reemplazamiento de cristales yeso en contacto con disoluciones acuosas ricas en carbonato (Fernández-Díaz et al., 2009; Flörke, 1961). Este proceso de reemplazamiento muestra las características típicas de las reacciones de disolución-cristalización acopladas: En primer lugar, la transformación se inicia en la superficie de los cristales de yeso y progresa hacia su interior. Además, tiene lugar con preservación de la forma externa de los cristales de yeso y está acompañado por la generación de porosidad. Como consecuencia, la capa reemplazada por carbonato cálcico es porosa. Finalmente, el contacto entre esta capa y el núcleo remanente de yeso aparece agudo y marcado durante el avance de la reacción. Este proceso de reemplazamiento mineral muestra también algunas peculiaridades que se relacionan con el gran cambio negativo de volumen molar implicado en la transformación (volumen molar del yeso = 74.5 cm^3/mol; volumen molar de la calcita = 36.40 cm^3/mol), lo que determina que el volumen de porosidad que debe generarse durante la transformación para garantizar su carácter pseudomórfico sea elevadísimo. A ello hay que sumar, además la porosidad que se deriva de la gran diferencia entre las solubilidades de yeso y calcita ($Ksp_{Gp}=10^{-4.58}$ (Parkhurst and

Appelo, 2010); $Ksp_{Cal}=10^{-8.48}$, (Plummer and Busenberg, 1982)). El enorme volumen de porosidad que se genera durante el reemplazamiento de yeso por carbonato cálcico garantiza el contacto continuo entre el volumen de la disolución carbonatada y la interfase entre las fases primaria y secundaria y, por tanto, el avance de la reacción. Por otro lado, este gran volumen de porosidad no puede quedar completamente contenido en la capa reemplazada. Ello da lugar a la generación de un hueco en la interfase. La anchura de este hueco aumenta al progresar la reacción y, junto con la gran cantidad de porosidad contenida en la capa reemplazada, determina que los pesudomorfos de carbonato cálcico formados a partir de yeso sean tremendamente frágiles (Fernández-Díaz et al., 2009).

Un aspecto especialmente interesante del reemplazamiento pseudomórfico de yeso por carbonato cálcico en contacto con disoluciones carbonatadas es que progresa a través de caminos de reacción distintos dependiendo de la concentración de la disolución. Cuando esta concentración es muy elevada (0.5M Na_2CO_3) el proceso se inicia con la formación de una capa relativamente gruesa y continua de nanopartículas de carbonato cálcico amorfo (ACC). Esta capa, que tapiza completamente la superficie del cristal de yeso, se transforma rápidamente en una mezcla de vaterita y calcita. Posteriormente, la vaterita se transforma en calcita. Esta secuencia de transformaciones se desarrolla simultáneamente al avance del frente de reemplazamiento, hasta que todo el pseudomorfo queda constituido exclusivamente por calcita. Cuando el reemplazamiento se produce en contacto con disoluciones con concentraciones intermedias de carbonato (0.25M Na_2CO_3), la capa de ACC es más fina y menos continua y la presencia de vaterita como fase constituyente del pseudomorfo se prolonga durante un tiempo más largo, aunque en última instancia, la calcita es la única fase de $CaCO_3$ tras tiempos de interacción largos. Cuando el remplazamiento tiene lugar en presencia de concentraciones de carbonato más bajas (0.1M o 0.05M), sólo se observan la formación de pequeños parches discontinuos de ACC que desaparecen rápidamente. Además, en este caso se observa también la formación de aragonito, que permanece como constituyente del pseudomorfo coexistiendo con la calcita incluso después de que no quede ningún rastro de la presencia de vaterita. En cualquier caso, independientemente de la concentración

inicial de carbonato en la fase fluida, tras periodos prolongados de interacción el único polimorfo presente en los pesudomorfos de carbonato cálcico formados a partir de yeso es la calcita, independientemente de la concentración inicial de carbonato en la disolución acuosa. Esta calcita se organiza en columnas de cristales orientados con su eje *c* perpendicular a la dirección del plano de exfoliación del yeso (010). Esta orientación preferente no es consecuencia de la existencia de relaciones epitaxiales entre las estructuras de yeso y calcita, sino de un fenómeno de crecimiento competitivo. En etapas tempranas del proceso de reemplazamiento los cristales de calcita aparecen orientados al azar. Sin embargo, debido a que su crecimiento se produce a mayor velocidad a lo largo del eje *c*, sólo aquellos en los cuales este eje está orientado perpendicularmente a la superficie del yeso pueden desarrollarse sin restricciones. El resultado final es el desarrollo de texturas en empalizada (Fernández-Díaz et al., 2009).

Hay que destacar también que la concentración de carbonato en la disolución afecta a características texturales como la escala del pseudomorfismo. Las características microtopográficas de los cristales de yeso son reproducidas de forma más fidedigna en aquellos pseudomorfos que se generan en contacto con disoluciones con altas concentraciones de carbonato.

Los estudios experimentales del remplazamiento de monocristales de anhidrita por carbonato cálcico han evidenciado que este proceso tiene diferencias significativas con respecto al reemplazamiento de monocristales de yeso (Altree-Williams et al., 2017; Roncal-Herrero et al., 2017). Estas diferencias se relacionan tanto con aspectos texturales de los pesudomorfos como con los caminos de reacción a través de los cuales avanza el reemplazamiento. Durante el reemplazamiento de los cristales de anhidrita en contacto con disoluciones 0.5M Na_2CO_3 no se observa la formación de ACC sobre ninguna de las superficies principales de exfoliación (100), (010) y (001). Además de la calcita, sólo se observa la formación de una cantidad mínima de vaterita, que desaparece rápidamente, sobre la superficie (001). Esta superficie es la que se disuelve a mayor velocidad y, por tanto, sobre la que la nucleación de carbonato cálcico tiene lugar a mayor sobresaturación. Los pseudomorfos están constituidos exclusivamente por calcita

desde los momentos iniciales del proceso de reemplazamiento. Esta diferencia en los caminos de reacción se ha relacionado con el hecho de que los cristales de calcita crecen orientados sobre las tres superficies de exfoliación de la anhidrita (Roncal-Herrero et al., 2017). La existencia de relaciones epitaxiales entre calcita y anhidrita rebaja la barrera energética para la nucleación de este polimorfo del $CaCO_3$, contrarrestando los efectos cinéticos que promueven la formación de otras fases menos estables durante las etapas tempranas del reemplazamiento de los cristales de yeso, especialmente cuando estos interaccionan con disoluciones con altas concentraciones de carbonato y, en consecuencia, la nucleación tiene lugar en condiciones de muy alta sobresaturación (Fernández-Díaz et al., 2009).

En cuanto a las diferencias texturales que se observan entre los pseudomorfos que se forman por reemplazamiento de yeso y anhidrita es de destacar el volumen de porosidad mucho menor que contienen los últimos, así como el hecho de que estos carezcan de un hueco significativo entre la capa reemplazada y el cristal primario remanente. Ambos aspectos contribuyen a que los pseudomorfos formados a partir de anhidrita sean más compactos y menos frágiles. Ello es consistente con el cambio de volumen molar que se asocia a la transformación de anhidrita en calcita (~20%, (Smyth and McCormick., 1995)), que es significativamente más pequeño, en comparación con el caso de yeso (>50%) (Altree-Williams et al., 2017; Fernández-Díaz et al., 2009; Roncal-Herrero et al., 2017). Otra diferencia textural significativa entre los pesudomorfos formados a partir de yeso y los formados a partir de anhidrita es la ausencia de texturas en empalizada en estos últimos. Esta ausencia se puede explicar como consecuencia de la nucleación orientada de calcita sobre las superficies de exfoliación de la anhidrita, que elimina la posibilidad de que se desarrollen procesos de crecimiento competitivo entre cristales con distinta orientación.

En esta tesis doctoral se continúa avanzando en la comprensión de los factores que influyen en las características de los procesos de carbonatación focalizando el estudio en el caso de la anhidrita y considerando sus tres planos de exfoliación principales y distintas composiciones de la disolución acuosa y abordando el análisis

en profundidad de la generación y evolución de porosidad durante la carbonatación de esta fase.

3.5. INFLUENCIA DEL OXOANIÓN SULFATO (SO_4^{2-}) EN EL POLIMORFISMO DEL $CaCO_3$

La observación de distintas secuencias de transformación vía solvente durante la carbonatación de monocristales de yeso dependiendo de la concentración inicial de carbonato presente en la disolución acuosa con la que estos interaccionan apunta a que la presencia de sulfato en el medio de cristalización pudiera jugar un papel relevante en la selección polimórfica del carbonato cálcico, contribuyendo a estabilizar fases metaestables. Si se atiende a las diferencias que se pueden esperar en la fisicoquímica de la disolución acuosa en contacto con yeso una vez un cristal de esta fase empieza a disolverse, estas se reducen al valor de la sobresaturación con respecto a las fases de $CaCO_3$, que será más alta cuanto mayor sea la concentración inicial de la disolución carbonatada, y a la relación SO_4^{2-}/CO_3^{2-}, que será más alta cuanto más baja sea dicha concentración inicial.

Fernández-Díaz y colaboradores (2010) abordaron el estudio experimental del efecto del oxoanión sulfato (SO_4^{2-}) en la precipitación del $CaCO_3$ a partir de la mezcla de disoluciones bajo condiciones de muy alta sobresaturación y altos pHs. Estos autores también estudiaron la evolución de la mineralogía de dichos precipitados durante su envejecimiento en contacto con la disolución madre durante periodos de tiempo que variaron entre cinco minutos y 14 días. Los resultados obtenidos por estos autores indicaron que bajo las condiciones exploradas, la presencia de sulfato en el medio de cristalización promueve la formación de vaterita y estabiliza a esta fase, inhibiendo su transformación en calcita durante tiempos que son tanto más largos cuanto mayor es la relación inicial de SO_4^{2-}/CO_3^{2-} en la fase fluida. Estos autores interpretaron el comportamiento observado como la consecuencia de una combinación de factores cinéticos y termodinámicos. Las altas condiciones de sobresaturación favorecen la formación de fases metaestables como la vaterita, que se observa a tiempos de envejecimiento cortos incluso en ausencia

del oxoanión sulfato. Sin embargo, el efecto inhibidor de la transformación de la fase vaterita en la fase, en principio, más estable calcita no se explica fácilmente tomando en consideración solamente factores cinéticos. Fernández-Díaz y colaboradores (2010) plantearon la posibilidad de que la incorporación de oxoaniones sulfato sustituyendo a grupos carbonato tuviera efectos energéticos distintos sobre la estructura de los distintos polimorfos del carbonato y que estas diferencias se tradujeran en cruces de estabilidad entre polimorfos o, al menos, en la aproximación de sus energías. Para contrastar esta hipótesis, estos autores llevaron a cabo modelizaciones computacionales que evidenciaron que la incorporación de una pequeña cantidad de grupos sulfato en la estructura de la vaterita apenas introduce distorsiones en la misma y, por tanto, tiene muy poco impacto en los parámetros energéticos de este polimorfo del $CaCO_3$. Sin embargo, la misma incorporación de iones sulfato en la estructura de la calcita la distorsiona significativamente y, por tanto, incrementa su energía y reduce la estabilidad de esta fase. Un efecto todavía más marcado se produciría si la sustitución de grupos carbonato por grupos sulfato se produjera en el polimorfo aragonito, ya que la distorsión que se introduce en la estructura de este polimorfo es dramática. Los resultados de la modelización llevada a cabo por Fernández-Díaz y colaboradores (2010) son consistentes con los datos reportados por Busenberg y colaboradores (1985) quienes determinaron que la solubilidad del aragonito puro es menor que la de calcita que contiene un 3% molar de $CaSO_4$, y con los contenidos de sulfato determinados en calcita y aragonitos naturales de origen inorgánico, que son entre 1.8 y 4.2 veces más elevados en el caso de la primera. Las conclusiones derivadas de las modelizaciones llevadas a cabo por Fernández-Díaz y colaboradores (2010) han sido posteriormente validadas por los resultados de la modelización realizada por Balan y colaboradores (2014) aplicando la aproximación de primeros principios, y por los del estudio de los efectos energéticos de la incorporación de distintos oxoaniones, incluido el sulfato, en la estructura de los polimorfos del $CaCO_3$, que más recientemente llevó a cabo Arroyo-de Dompablo y colaboradores (2015) aplicando la Teoría de Densidad Funcional. Aunque ninguno de estos trabajos apoya la existencia de cruces de estabilidad entre polimorfos del $CaCO_3$ asociados a efectos energéticos inducidos por la sustitución isomórfica en su estructura de grupos carbonato por grupos sulfato, los resultados

de todos apuntan a que sí se produce una reducción de la diferencia entre las energías de calcita y vaterita que incorporan cantidades idénticas de sulfato. Esto resulta en una reducción efectiva de la fuerza conductora para la transformación de vaterita en calcita y puede explicar, al menos parcialmente, la estabilización de esta fase durante tiempos prolongados (Arroyo-de Dompablo et al., 2015).

A pesar del interés que despierta el efecto del sulfato en el polimorfismo del carbonato cálcico y del esfuerzo que diversos autores han invertido en comprenderlo, este tema está lejos de estar resulto. De hecho, las diversas investigaciones realizadas han contribuido a evidenciar que este efecto es extremadamente complejo y para interpretarlo es necesario combinar distintas aproximaciones. Por ejemplo, resultan de especial interés algunos trabajos experimentales que han puesto de manifiesto que, en determinadas circunstancias, la presencia de sulfato en el medio de cristalización puede promover la formación de aragonito (Bots et al., 2011; Dydo et al., 2003; Tang et al., 2012; Wagterveld et al., 2014). Estos resultados parecen indicar que el papel de este oxoanión podría ser similar al que tradicionalmente se ha atribuido al Mg^{2+}, al facilitar la formación del polimorfo en el que su incorporación es menos favorable (Morse et al., 2007; Radha and Navrotsky, 2013). En esta tesis doctoral se realizan experimentos que buscan completar el dibujo de este interesante y relevante problema y aportar elementos nuevos para su discusión.

3.6. ESTRUCTURA DE LA ANHIDRITA

La anhidrita cristaliza en el sistema cristalino ortorrómbico, con grupo espacial *Amma*. Sus parámetros de red son a=6.993Å, b=6.995 Å, c=6.245 Å. En esta estructura se distinguen cadenas que discurren paralelas a [001] y que están constituidas por la alternancia de tetraedros SO_4 y dodecaedros CaO_8. Estas cadenas se conectan lateralmente entre sí a lo largo de la dirección [100] al compartirse aristas entre los dodecaedros CaO_8 y vértices entre los tetraedros SO_4. Además, están cadenas se unen a lo largo de [010] al compartirse vértices tanto de los tetraedros SO_4 como de los dodecaedros CaO_8 (De Leeuw and Parker, 1997;

Hawthorne et al., 2000; Hawthorne and Ferguson, 1975; Redfern and Parker, 1998). Estas características de la estructura de la anhidrita determinan que tenga una exfoliación paralela a los tres planos principales (010), (100) y (001), los cuales se corresponden con caras de tipo F, de acuerdo con el modelo de Hartman-Perdok (Hartman and Perdok, 1955a; Hartman and Perdok, 1955b; Redfern and Parker, 1998). Estas caras son, además, las que se encuentran con mayor frecuencia en los cristales naturales de anhidrita (Kostov and Kostov, 1999). En ellas, y en las diferencias de comportamiento que exhiben durante la carbonatación se centran las observaciones presentadas en esta tesis sobre las características de la carbonatación de anhidrita.

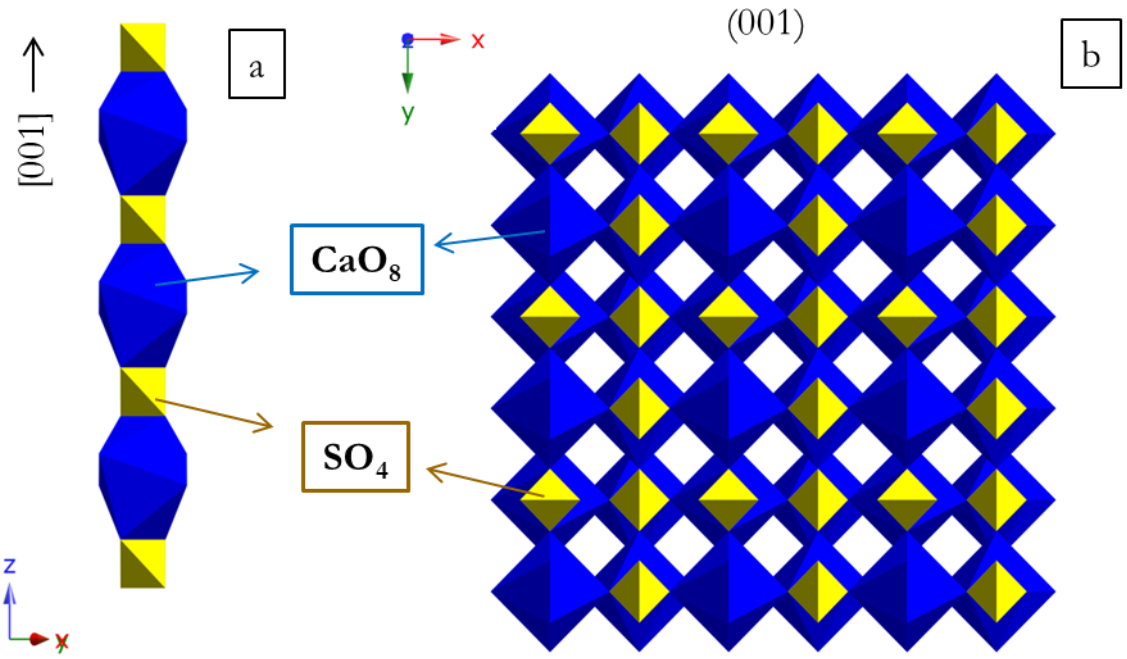

Figura 3.1. Estructura de la anhidrita. a: Columna de dodecaedros y tetraedros unidos mediante aristas. Los dodecaedros corresponden a la fórmula CaO_8 y los tetraedros a la fórmula SO_4, respectivamente, donde los oxígenos se sitúan en los vértices el poliedro, y el Ca y S en el interior del mismo; y b: Proyección del plano (001) en el que se observa que la unión de dodecaedros y tetraedros de distintas columnas se da mediante vértices.

3.7. ESTRUCTURA DE LA CALCITA

La calcita cristaliza en el sistema hexagonal (grupo espacial $R\bar{3}c$). Sus parámetros de red son $a=b=4.990$Å, $c=17.061$Å (Deer et al., 1992). Su estructura se puede describir como constituida por planos de Ca^{2+} y grupos triangulares planos CO_3^{2-} que se disponen alternantes y paralelos entre sí a lo largo del eje c, con respecto al cual son perpendiculares. Todos los grupos carbonato presentan la misma orientación dentro de un mismo plano, pero aparecen girados 180º en planos alternos. Los átomos de Ca^{2+} ocupan huecos octaédricos rodeados de 6 oxígenos, cada uno de los cuales corresponde a un grupo carbonato distinto, de modo que los octaedros CaO_6 se encuentran aislados entre sí. El hábito más común de la calcita está definido por el romboedro $\{10\bar{1}4\}$.

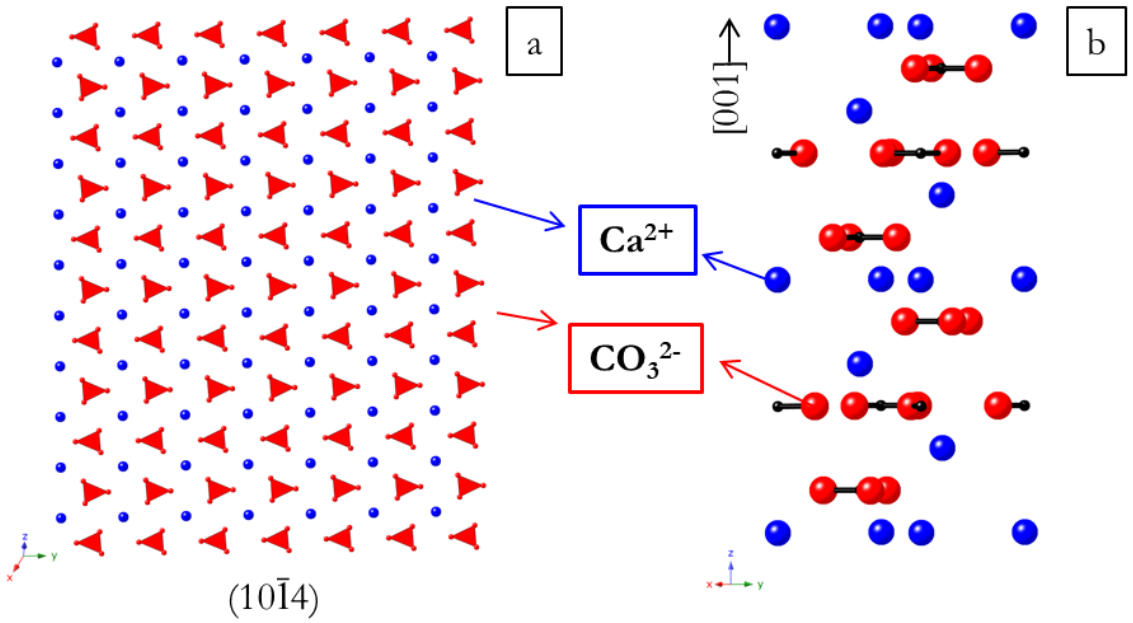

Figura 3.2. Estructura de la calcita. Proyección del plano $(10\bar{1}4)$ correspondiente a las caras del romboedro. Aunque dichos planos no sean paralelos a los planos de los carbonatos, se aprecia como los carbonatos alternan su orientación en los distintos planos. A la derecha observamos los planos alternos de calcio y carbonatos a lo largo de la dirección [001]. El triángulo que forman los carbonatos es paralelo al plano (001). Los triángulos corresponden a la fórmula CO_3.

En esta tesis se analizan y discuten las relaciones epitaxiales existentes entre las estructuras de calcita y anhidrita y que influyen de forma determinante en las características de la carbonatación de los monocristales de anhidrita.

4. METODOLOGÍA

4. METODOLOGÍA

4.1. EXPERIMENTOS DE INTERACCIÓN DE DISOLUCIONES ACUOSAS CARBONATADAS CON MONOCRISTALES DE ANHIDRITA

Se diseñaron y ejecutaron tres tipos de experimentos de interacción de disoluciones acuosas carbonatadas con monocristales de anhidrita. El objetivo de estos experimentos fue:

(a) Experimentos tipo 1: Obtener muestras que permitieran estudiar las relaciones epitaxiales entre anhidrita y calcita, considerando de forma independiente los tres planos de exfoliación principales de la anhidrita (100), (010) y (001),

(b) Experimentos tipo 2: Obtener muestras para caracterizar la porosidad generada durante la carbonatación de anhidrita y la evolución espacio-temporal de esta porosidad durante el envejecimiento, así como estudiar la influencia de la composición de la fase fluida en las características texturales, y

(c) Experimentos tipo 3: Estudiar los caminos de reacción que sigue la carbonatación de anhidrita dependiendo de la superficie de ésta sobre la que se desarrolla la interacción con la disolución carbonatada y la concentración de esta disolución.

En todos estos experimentos se emplearon fragmentos de anhidrita recién exfoliados a partir de monocristales procedentes de la mina de Naica, Chihuahua (México), que se exfoliaron paralelamente a los planos (100), (010) y (001). El tamaño de estos fragmentos fue de aproximadamente 3x3x1mm en el caso de los experimentos de tipo 1, 2x2x2mm en los de tipo 2, y $1.6 \leq x \leq 2.0$mm en los de tipo 3. En los experimentos 1 y 2 los fragmentos se sumergieron en disoluciones de Na_2CO_3 (Fluka) preparadas con agua MilliQ (resistitvidad$\leq$18.2 MΩ·cm a 25º C), situadas en reactores cerrados de polipropileno. En los experimentos tipo 3, se utilizaron erlenmeyeres de pirex. La concentración de la disolución fue 0.5M en los experimentos de tipo 1 y 2, y de 0.5M y 0.05M en los de tipo 3. El volumen de disolución fue 5mL en los experimentos de tipo 1, 1mL en los de tipo 2 y 25mL en

los experimentos tipo 3. Los experimentos tipo 1 y 2 transcurrieron sin agitación, los experimentos tipo 3, con agitación, todos a una temperatura controlada de 25±0.5° C y a presión atmosférica. En todos los casos se realizaron experimentos independientes para cada tiempo de reacción considerado. En los experimentos de tipo 1, los tiempos de reacción variaron entre 15 minutos y 4 días. En los experimentos de tipo 2, el tiempo de reacción varió entre 1 día y 14 días. Finalmente, en los experimentos de tipo 3, el tiempo de reacción varió entre 1 día y 2 meses. Las condiciones utilizadas en cada tipo de experimento se resumen en la tabla 4.1.

Una vez transcurridos los tiempos de reacción correspondientes, los cristales se extrajeron de la disolución acuosa (bien con ayuda de unas pinzas en los experimentos de tipo 1 y 2, o filtrándolos con un embudo Büchner y un matraz kitasato en el caso de los experimentos tipo 3), se lavaron cuidadosamente con agua ultrapura (MilliQ), se depositaron sobre papel absorbente y se dejaron secar a temperatura ambiente durante al menos 24 horas. Estas muestras se reservaron para su posterior caracterización, siguiendo los protocolos descritos en la sección 4.3.

4.2. EXPERIMENTOS DE PRECIPITACIÓN POR MEZCLA DE DISOLUCIONES Y ENVEJECIMIENTO DE LOS PRECIPITADOS

Se llevó a cabo una serie de experimentos dirigidos a obtener precipitados de $CaCO_3$ formados a partir de disoluciones acuosas con distintas relaciones SO_4^{2-}/CO_3^{2-}, y a seguir la evolución de las características del sistema a lo largo del tiempo. Para ello se mezclaron 50mL de una disolución de $CaCl_2$ (Fluka, 1M) (disolución 1) con 50mL de otra disolución de $NaHCO_3$ (99.7%, Panreac) y Na_2SO_4 (>99%, Sigma-Aldrich) (disolución 2). En la preparación de ambas disoluciones se utilizó agua ultrapura MilliQ (resistitvidad≤18.2 MΩ·cm a 25º C). La mezcla de las disoluciones se llevó a cabo vertiendo rápidamente la disolución 2 sobre la disolución 1, que se mantuvo agitada a 250 rpm mediante un agitador magnético en todo momento. El envejecimiento de la disolución resultante se desarrolló a temperatura ambiente (25º ± 0.5º C) y también con agitación magnética. Las

Tabla 4.1. Condiciones utilizadas en cada tipo de experimento. Aparecen la cantidad de anhidrita utilizada y el tamaño de la misma, la concentración y el volumen de disolución de carbonato, el tiempo de reacción considerado para cada serie de experimentos, y el objetivo del estudio de los mismos.

Experimento	Cantidad de Anh	Tamaño de Anh (mm)	$[CO_3^{2-}]$ (M)	Volumen CO_3^{2-} (mL)	Tiempo de Reacción	Estudio
Tipo 1	1 cristal	3x3x1	0.5	5	15 minutos-4 días	Epitaxia
Tipo 2	1 cristal	2x2x1	0.5, 0.05	1	1 día-14 días	Porosidad Influencia de la concentración
Tipo 3	0.50-0.51 g	1.6-2.0	0.5, 0.05	25	1 día-60 días	Batch

concentraciones de los reactivos en las disoluciones 1 y 2 se ajustaron de modo que la disolución resultante de la mezcla tuviera aproximadamente los mismos valores de índices de saturación (SI) con respecto a los distintos polimorfos de $CaCO_3$ en todos los experimentos, independientemente de la relación SO_4^{2-}/CO_3^{2-} empleada. La tabla 4.2. resume las concentraciones y el pH de las disoluciones empleadas en estos experimentos. Los precipitados formados como consecuencia de la mezcla de las disoluciones 1 y 2 se dejaron envejecer durante tiempos comprendidos entre 5 minutos y 14 días, realizándose experimentos independientes para cada relación inicial de SO_4^{2-}/CO_3^{2-} en la disolución resultante de la mezcla y cada tiempo de reacción. Una vez concluido cada experimento, se procedió a filtrar a vacío la disolución, usando una membrana de acetato de celulosa de 0.45-µm (Sartorius stedim; Albet). El precipitado recogido se lavó, primero con agua ultrapura MilliQ y, a continuación, con etanol absoluto con el fin de eliminar toda traza posible de agua y parar su evolución, se dejó secar a 30º C durante 48 horas y se reservó para su posterior caracterización. La disolución filtrada se analizó por ICP-OES.

Tabla 4.2. Composición inicial de la disolución para los experimentos 4.2. Aparecen las concentraciones de cada reactivo empleado en molaridad (M) y el pH de la misma calculado con el software PHREEQC

Experimento	Composición de la disolución			
	$[CaCl_2]$ (M)	$[NaHCO_3]$ (M)	$[Na_2SO_4]$ (M)	pH
A0	0.050	0.05		7.62
A3	0.040	0.050	0.003	7.66
A5	0.040	0.050	0.005	7.67
A7	0.040	0.050	0.007	7.67
A15	0.050	0.050	0.015	7.64
A20	0.050	0.050	0.020	7.65
A22	0.050	0.050	0.022	7.65
A25	0.050	0.050	0.025	7.65

4.3. CARACTERIZACIÓN DE LAS FASES SÓLIDAS

4.3.1. Microscopia óptica de luz polarizada transmitida

La orientación, paralela a los planos (100) (010) o (001), de los fragmentos de anhidrita, utilizados en los experimentos de tipo 1 y de tipo 3 descritos en el apartado 4.1 se determinó mediante la observación de la figura de interferencia. Para esta observación se utilizó un microscopio Nikon (modelo 104) ubicado en el departamento de Mineralogía y Petrología de la Facultad de Ciencias Geológicas de la UCM. Los cristales de anhidrita son biáxicos, con signo óptico positivo. La relación entre sus direcciones ópticas y cristalográficas es $\alpha = y$, $\beta = x$, $\gamma = z$ (Deer et al., 1992). Por tanto, las secciones de los cristales anhidrita que son paralelas a (100) muestran una figura de interferencia de tipo "flash", a las que son paralelas a (010) les corresponde una figura de interferencia de bisectriz obtusa y, finalmente, las que son paralelas a (001) se caracterizan por mostrar figuras de interferencia de bisectriz aguda.

4.3.2. Difracción de rayos X (XRD)

Se utilizó difracción de rayos X (XRD) para identificar las fases minerales cristalinas presentes en las muestras obtenidas en los distintos experimentos descritos en las secciones 4.1 y 4.2. En todos los casos, los difractogramas se obtuvieron utilizando radiación $K\alpha_1$ de Cu (1.540598Å) y el voltaje y la intensidad aplicados en la generación del haz de rayos X fueron de 45kV y 40mA respectivamente. Los detalles de la metodología de análisis aplicada variaron dependiendo del tipo de muestra, y se describe a continuación.

Las muestras obtenidas en los experimentos tipo 1 descritos en la sección 4.1 se estudiaron mediante difracción de rayos X de incidencia rasante GIXRD para comprobar la presencia de calcita creciendo epitaxialmente sobre la superficie de las tres caras de exfoliación principales de la anhidrita, (100), (010) y (001). En este estudio se empleó un difractómetro Philips X'Pert PRO MRD. Los difractogramas se recogieron con un ángulo de incidencia de los rayos X sobre la muestra de 0.1º y un tiempo de paso de 0.8º/min. Para la identificación de las fases se compararon los

picos de reflexión presentes en los diagramas con los patrones 010-072-0503 (anhidrita), 01-071-3699 (calcita), 00-001-0628 (aragonito), y 00-024-0030 (vaterita) de la base de datos ICDD-PDF2.

Los precipitados obtenidos en los experimentos descritos en la sección 4.2 se analizaron utilizando un difractómetro PANalytical X'Pert PRO MRD, mientras que las muestras obtenidas en los experimentos de tipo 3 descritos en la sección 4.1 se analizaron con un difractómetro PANanlytical Empyrean de 2kW. En ambos casos se utilizó el método del polvo cristalino, lo que requirió moler las muestras obtenidas en los experimentos tipo 3 en un mortero de ágata. Los diagramas de difracción se recogieron en rango de 2θ entre 20º y 60º, con un tamaño de paso de 0.04º y un tiempo de paso de 1s. En algunos casos, el barrido se amplió al intervalo de 2θ de 10º a 60º. La asignación de reflexiones presentes en los difractogramas a fases minerales se realizó por comparación con los patrones de 00-005-0586 (calcita), 01-080-2790 (aragonito), 04-017-8634 (vaterita) y 04-016-3025 (yeso) de la base de datos ICDD-PDF2. Todos los difractómetros están ubicados en el Centro de Ayuda a la Investigación (CAI) de Difracción de Rayos X de la UCM.

4.3.3. Espectroscopia infrarroja por transformada de Fourier (FTIR)

Se han utilizado los análisis de espectroscopia infrarroja para confirmar la identificación de fases minerales realizada mediante XRD en las muestras obtenidas en los experimentos de precipitación y envejecimiento descritos en la sección 4.2. En estas muestras se midió la energía absorbida en el rango de número de onda entre 250cm^{-1} y 4000cm^{-1}. Se utilizó un espectrómetro modelo BRUKER IFS 66v/S, equipado con un detector TGS que una precisión de 0.2cm^{-1}, ubicados ambos en el Instituto de Ciencias de Materiales de Madrid (ICMM, CSIC). Previamente a la recogida de espectros, las muestras se diluyeron con KBr (sustancia transparente a la radiación IR).

4.3.4. Espectroscopia Raman (RAMAN)

La identificación de fases mediante espectroscopia Raman, se realizó con las muestras de los experimentos de interacción de disoluciones acuosas carbonatadas

con monocristales de anhidrita (4.1) tipo 3. Se midieron los modos vibracionales de número de onda comprendido entre 100cm^{-1} y 4500cm^{-1}. La energía de excitación fue de 488nm (azul). El espectrómetro utilizado fue HORIBA Jobin Yvon LabRAM HR800 UV-VIS, el microscopio Olympus BX41, y el detector CCD (1024 x 256 pixel), todos ellos localizados en el Geoforchungszentrum (GFZ), en Potsdam. No fue necesario triturar las muestras.

4.3.5. Microscopia electrónica de barrido (SEM)

Se utilizó la microscopia electrónica de barrido para caracterizar las muestras obtenidas en todos los experimentos descritos en las secciones 4.1 y 4.2. Las muestras se montaron sobre soportes cilíndricos de una aleación metálica y se recubrieron con una fina película de carbono y/u oro (con el evaporador QUORUM modelo Q150TE, y el metalizador QUORUM Q150RS respectivamente), dependiendo de sus características concretas. El doble recubrimiento, depositando una capa de 8nm de espesor de carbono primero, seguida por otra de oro, se utilizó en aquellas muestras que mostraban una mayor tendencia a cargarse. Se tomaron imágenes utilizando dos microscopios: Un JEOL JSM 6400 ubicado en el Centro Nacional de Microscopía Electrónica (CNME), en la UCM; y un FEI Quanta 3D FEG Dual Beam localizado en el GFZ de Potsdam. Se operó a 20KV, una distancia de trabajo de 15mm, una intensidad de 80mA y filamento de W. El software empleado fue el programa INCA. Estas imágenes correspondieron a los cristales y agregados cristalinos presentes en los precipitados obtenidos en los experimentos que se describen en la sección 4.2 y a las superficies de las muestras obtenidas en los experimentos que se describen en la sección 4.1 y permitieron estudiar los distintos hábitos cristalinos. Todas estas imágenes se recogieron utilizando los electrones secundarios. En el caso de las muestras obtenidas en los experimentos tipos 2 y 3 de los descritos en la sección 4.1, también se recogieron imágenes sobre la superficie de secciones cortadas perpendicularmente a las caras principales de los cristales originales de anhidrita. En la obtención de estas imágenes se emplearon tanto electrones secundarios como electrones retrodirspersados. Las diferencias de contraste en las imágenes obtenidas

usando estos últimos permitieron distinguir las zonas de la muestra transformadas y sin transformar, aportando información sobre la cinética de la reacción.

4.3.6. Espectroscopía de rayos X de energía dispersiva (EDS)

El microscopio electrónico de barrido JEOL JSM 6400 utilizado en la caracterización de las algunas de las muestras obtenidas en los experimentos cuenta como accesorio con un sistema de energía dispersiva de rayos X (Oxford). Este sistema permite realizar análisis elementales cuantitativos y semicuantitativos puntuales y de áreas de la muestra estudiada. La información de estos análisis se deriva de la energía de los rayos X que emite al ser iluminada por el haz de electrones. Esta energía es característica para cada elemento químico, ya que los rayos X son emitidos al caer electrones de capas externas para rellenar los huecos dejados en capas internas por electrones que las han abandonado tras la transferencia de parte de la energía del haz de electrones incidente. Al igual que el microscopio JEOL JSM 6400, el accesorio de energía dispersiva Link System está ubicado en el Centro Nacional de Microscopía Electrónica (CNME), en la UCM.

4.4. CARACTERIZACIÓN DE LA EPITAXIA DE CALCITA SOBRE ANHIDRITA

4.4.1. Difracción de electrones retrodispersados (EBSD)

Se realizaron análisis de EBSD con el fin de obtener información sobre las relaciones cristalográficas entre fases secundarias (calcita) y primaria (anhidrita) en las muestras obtenidas en los experimentos tipo 1 de los descritos en la sección 4.1. La técnica EBSD permite medir las orientaciones de los cristales formados sobre un substrato determinado mediante la indexación automática de los patrones Kikuchi resultantes de la difracción de electrones retrodispersados sobre la superficie de la muestra. Esta información suele representarse en un diagrama o figura de polos, donde se proyectan estereográficamente las distintas orientaciones que presentan los cristales de la fase secundaria, en nuestro caso la calcita, sobre un substrato, en nuestro caso las distintas caras de la anhidrita. Una orientación preferente de estos

cristales sobre el substrato se reflejaría en la aparición en la figura de polos, de áreas de menor o mayor tamaño y de distinto color que indicarían del grado de coorientación entre el precipitado y el substrato. Las mediciones de EBSD se realizaron mediante un equipo EVO 15 MA (ZEISS) SEM equipado con un detector HKL Nordlys (Oxford), utilizando un voltaje de aceleración de 17 kV del haz primario y una distancia de trabajo de ~ 14 mm. Los datos de EBSD se procesaron posteriormente utilizando el software Aztec (Oxford Instruments) y CHANNEL 5. El equipo utilizado se localiza en el Laboratorio de Estudios Cristalográficos del Instituto Andaluz de Ciencias de la Tierra (IACT-CSIC-LEC). La geometría del haz-muestra-detector se fijó a una inclinación de ~70° respecto a la horizontal. En todas las mediciones, las superficies de anhidrita se orientaron antes de colocarlas en el soporte de la muestra.

4.4.2. Software cristalográfico

4.4.2.1 *CrystalMaker* ®

El software de construcción y proyección de estructuras cristalográficas CrystalMaker® (Palmer 2005), y su librería, se han utilizado para proyectar las estructuras de la anhidrita sobre sus planos (100), (010) y (001) y de la calcita sobre su plano $\{10\bar{1}4\}$. Además, este software se ha utilizado para medir periodos de repetición a lo largo de direcciones concretas contenidas en dichas proyecciones, así como para medir ángulos entre esas direcciones. Esta información ha sido empleada para establecer las relaciones epitaxiales entre calcita y anhidrita, con la ayuda de la información obtenida de las observaciones realizadas mediante SEM y EBSD en las muestras de los experimentos de tipo 1 descritos en la sección 4.1.

4.4.2.2. *JCrystal* ®

El programa JCrystal® es un software que permite modelizar morfologías cristalinas utilizando información referente a la clase de simetría de la fase cristalina considerada, sus parámetros de red y la distancia de una determina forma cristalina al centro del cristal. La variación de este último parámetro, que se puede considerar proporcional a la velocidad de crecimiento normal de la forma, permite modelizar

las variaciones que puede sufrir el hábito de un cristal como consecuencia del cambio relativo de la velocidad de crecimiento normal de sus distintas caras a lo largo de su crecimiento. En esta tesis doctoral este programa se ha utilizado para construir el hábito de los cristales de calcita que crecen epitaxialmente sobre anhidrita, según se observa en las muestras obtenidas en los experimentos de tipo 1 descritos en la sección 4.1, y de los que forman parte de los precipitados obtenidos en los experimentos que se describen en la sección 4.2.

4.5. CARACTERIZACIÓN DE LA POROSIDAD GENERADA DURANTE EL REMPLAZAMIENTO MINERAL

4.5.1. Tomografía computerizada (CT-SCAN)

La tomografía es una técnica no destructiva que se basa en irradiar la muestra a estudiar con radiación X para obtener información detallada de sus características internas. La muestra es radiografiada en varias direcciones, al tiempo que se gira 360º. Mediante un algoritmo, se combina el conjunto de radiografías obtenidas (sinograma) obteniéndose un modelo 3D de la muestra. En este modelo, las diferencias entre zonas de la muestra con distintas características (en esta tesis, fase sólida y porosidad en su interior) se evidencian a través de cambios en una escala de grises, con la porosidad definida por el color negro.

Se ha llevado a cabo un análisis CT sobre las muestras obtenidas en los experimentos tipo 2 de los descritos en la sección 4.1. En este análisis se utilizado un tomógrafo CT-SCAN Nikon XT H-160, operando entre 30kV y 160kV. Para la construcción de los modelos 3D se ha utilizado el software *myVGL*®. Este software discrimina entre valores de la escala de grises y de este modo distingue entre fases diferentes, que en el caso presente son fase sólida y porosidad. Además, permite describir numéricamente estas fases a través de propiedades como su área o su volumen.

Es importante destacar que en el análisis de porosidad en el que se ha empleado este software se interpreta como un único poro todas las cavidades que

están conectadas entre sí y aisladas de las restantes. Para cada poro que se defina de acuerdo con los parámetros de borde que se impongan, este software permite caracterizar su volumen, superficie y número de voxeles que incluye, además de su geometría, su posición y su tamaño absoluto y relativo con respecto al de otros poros. Todos los análisis realizados con esta técnica, tanto la obtención de las imágenes como su reconstrucción, se han realizado en el Museo Nacional de Ciencias Naturales (MNCN, CSIC).

4.5.2. Análisis de área superficial BET

El análisis de superficie BET (Brunauer–Emmett–Teller) se emplea para cuantificar la superficie específica de un material. La técnica se basa en introducir un gas (N_2), condensarlo a baja temperatura (77K) sobre la superficie a estudiar, y cuantificar su cantidad midiendo la presión del mismo. El N_2 se adsorbe físicamente sobre la superficie de la muestra, de tal modo que, si se conoce la cantidad de N_2 adsorbida (midiendo la presión), se puede conocer la superficie del material a estudiar. Esta técnica se ha empleado en el estudio de la porosidad, muestras correspondientes al apartado 4.2 tipo 2. Las medidas fueron realizadas con un aparato Micrometrics ASAP2000, ubicado en el Área de Cristalografía y Mineralogía del Departamento de Geología de la Universidad de Salamanca.

4.6. CARACTERIZACIÓN DE FASES LÍQUIDAS

4.6.1. Espectroscopia de emisión atómica acoplada a plasma inductivo (ICP-OES)

Se ha analizado la composición de las muestras líquidas recuperadas de los experimentos que se describen en la sección 4.2 Estos análisis se han realizado mediante espectroscopia de emisión atómica acoplada a plasma inductivo (ICP-OES), que permite cuantificar los elementos presentes en una disolución. Esta técnica de análisis se basa en la aplicación de un campo magnético oscilante al gas (argón) que contiene la muestra. Debido a las altas temperaturas que se generan (8000º C), la muestra se separa en sus átomos y se ioniza, dando lugar a transiciones electrónicas, que son características de cada elemento. La intensidad de señal

correspondiente al espectro de cada elemento, definido por frecuencias concretas, es proporcional a la concentración de este elemento en la muestra. Se ha analizado la cantidad de S para los experimentos incluidos en el apartado 4.2., con un espectrómetro Varian 720ES ICP-OES, en el CAI de Técnicas Geológicas localizado en la Facultad de Ciencias Geológicas, y la cantidad de S, Na y Ca para los experimentos tipo 3 del apartado 4.1 con un espectrómetro Thermo Fisher Scientific, modelo Element 2XR, ubicado en el GFZ de Potsdam.

4.7. MODELIZACIÓN GEOQUÍMICA

4.7.1. PhreeqC Interactive (Version 2)

PHREEQC es un código geoquímico que permite determinar la especiación química de disoluciones y su estado de saturación con respecto a fases minerales (Parkhurst and Appelo, 2010). Este código se utilizó para ajustar las concentraciones de los reactivos en las disoluciones empleadas en los experimentos descritos en la sección 4.2., de modo que los valores iniciales de los índices de saturación (SI) del sistema con respecto a los distintos polimorfos de $CaCO_3$ fueran aproximadamente iguales en todos los experimentos. En estos cálculos, el código PHREEQC se combinó con la base de datos phreeqc.dat (Parkhurst and Appelo, 2010), la cual incluye los valores de los productos de solubilidad de calcita ($Ksp_{Cal}=10^{-8.48}$), aragonito ($Ksp_{Arg}=10^{-8.34}$), yeso ($Ksp_{Gp}=10^{-4.58}$), y anhidrita ($Ksp_{Anh}=10^{-4.36}$). Esta base de datos tuvo que ser completada, incorporándole manualmente los valores del producto de solubilidad de la vaterita ($Ksp_{Vtr}=10^{-7.91}$, Plummer and Busenber, 1982) y del carbonato de calcio amorfo (ACC) ($Ksp_{ACC}=10^{-6.0}$, Ogino et al., 1987).

El código PHREEQC se empleó también en los cálculos previos para estimar las concentraciones de las disoluciones que podrían garantizar la reacción completa de los cristales de anhidrita en los experimentos tipo 2 y 3 descritos en la sección 4.1., así como para modelizar la evolución del sistema durante la reacción.

4.8 OTROS SOFTWARES UTILIZADOS

4.8.1. OriginPro 8

Origin es un software de análisis y representación gráfica que se ha empleado en el tratamiento de datos y en la construcción de todas las gráficas que aparecen en este trabajo.

4.8.2. X'Pert HighScore 2.2a (2.2.1)

Este software se ha utilizado en la identificación de fases minerales presentes en las muestras obtenidas en los experimentos descritos en 4.1 y 4.2 comparando los difractogramas correspondientes a esas muestras con los de los patrones contenidos en la base de datos ICDD-PDF2.

5. EPITACTIC OVERGROWTHS OF CALCITE ($CaCO_3$) ON ANHYDRITE ($CaSO_4$) CLEAVAGE SURFACES

5. EPITACTIC OVERGROWTHS OF CALCITE ($CaCO_3$) ON ANHYDRITE ($CaSO_4$) CLEAVAGE SURFACES

The carbonation of anhydrite crystals in contact with carbonate aqueous solutions initiates with the nucleation and growth of calcite crystals on anhydrite surfaces. Roncal-Herrero et al. (2017) stated that this nucleation and growth has an epitatic character on the three main cleavage surfaces of anhydrite (100), (010) and (001). The faces are also the most common ones in the habit of natural anhydrite crystals Here, data on the epitatic growth of calcite on these three faces are presented with the aim of determining: a) the structural elements that enable the development of epitactic relationships between both phases and b) the connection between the degree of epitactic fit and those textural characteristics of the calcite overgrowth. A quantitative understanding of the structural factors that control the formation of calcite epitactic overgrowths can be useful to predictively assess the viability of using the carbonation of anhydrite as a mean to sequester and store carbon dioxide.

5.1. RESULTS

SEM micrographs of anhydrite (100), (010) and (001) surfaces after interaction with a carbonate-bearing aqueous solution evidence the formation of an overgrowth, which appears as a more or less continuous layer (Figure 5.1). The degree of coverage of the anhydrite surfaces by the overgrowth increases with time. However, for a given time the degree of coverage varies and depends on the crystallographic orientation of anhydrite surface. In all cases the (001) face always showed the highest degree of coverage. The overgrowths mostly consisted of evenly sized (3-5 μm), euhedral lozenge-shaped microcrystals (Figure 5.1). In some cases, a few sphere-like aggregates could also be distinguished in the overgrowths formed on anhydrite (010) and (001) surfaces at early stages of reaction (Figure 5.1c). GIXRD analyses showed calcite was the main overgrowth component on all anhydrite faces considered, while vaterite was a very minor constituent on the (001) faces. Moreover, although minor vaterite was also observed on the anhydrite (010) surface

after a few minutes interaction, this phase was much less abundant than on $(001)_{Anh}$ and was almost absent on $(100)_{Anh}$ regardless the time of interaction.

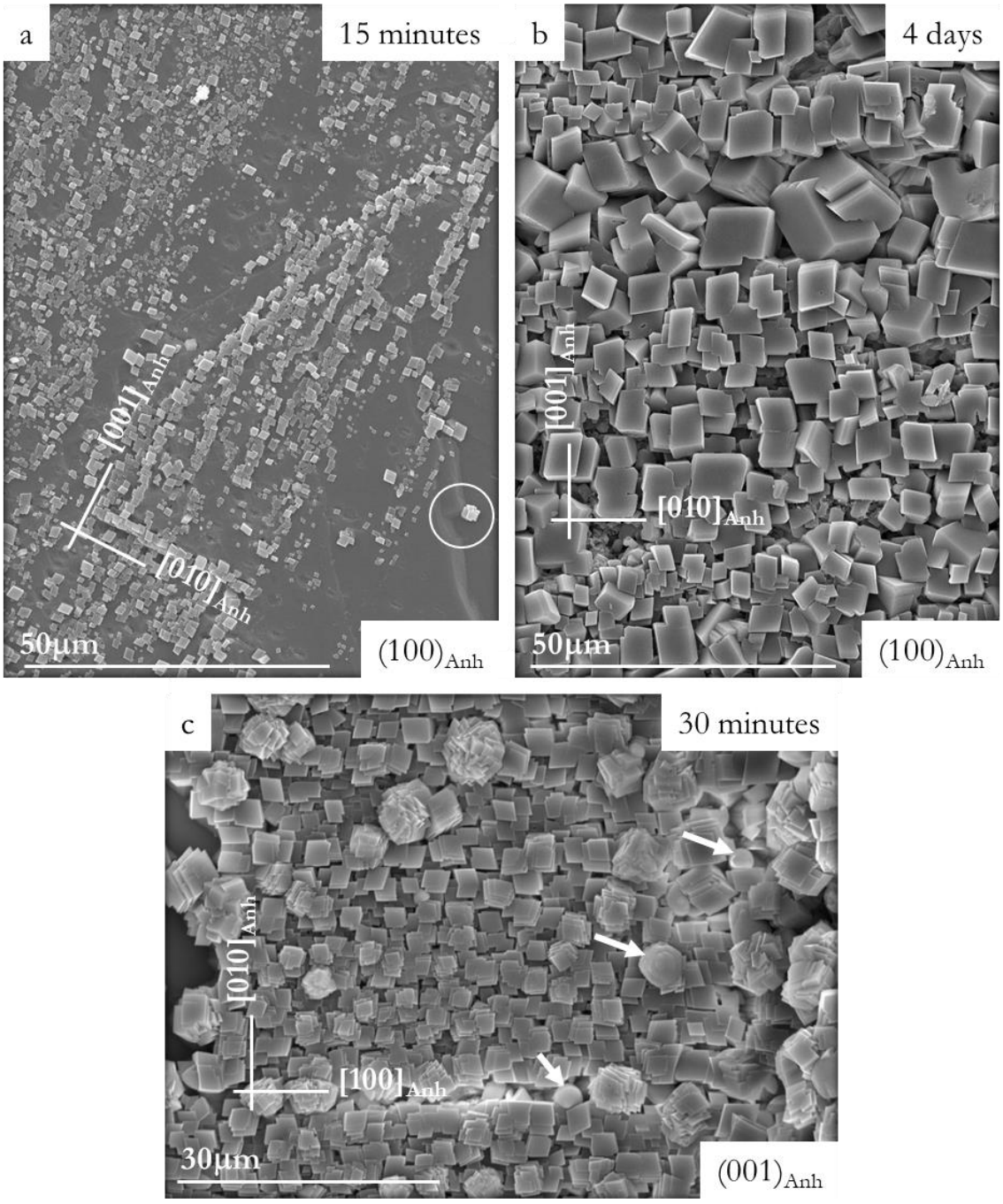

Figure 5.1. SEM images obtained after 15 minutes (a), 4 days (b) and 30 minutes (c) of exposure of anhydrite (100) and (001) surfaces to 0.5 M Na_2CO_3 solutions. The anhydrite surface is covered by a more or less discontinuous layer of small calcite crystals specifically oriented with respect to the substrate. (a) Etch pits orientation (encircled area) enables the identification of the main crystallographic directions on the anhydrite surfaces. (c) Some sphere-like aggregates of vaterite can be distinguished in the overgrowths formed on anhydrite (001) surface (see white arrows).

Thus we can safely assert that the lozenge-like morphologies correspond to calcite and the sphere-like morphologies correspond to vaterite (Roncal-Herrero et al., 2017). According to the angles between faces and edges measured on the SEM micrographs, the habit of calcite crystals is always dominated by the $\{10\bar{1}4\}$ rhombohedron. The calcite crystals grow oriented on the anhydrite substrate, defining an epitactic relationship regardless the orientation of the substrate. Nevertheless, marked differences in specific epitactic relationships between calcite and the anhydrite (100), (010) and (001) surfaces were observed.

5.1.1. Calcite overgrowth on anhydrite (100) and (010)

The microtopography of anhydrite (100) surfaces is characterized by large and very flat terraces, bounded by macrosteps that run parallel to the [010] and [001] directions (Figure 5.1a). Post reaction with the carbonate-rich aqueous solution, the anhydrite (100) surfaces developed clear signs of dissolution, in the form of etch pits along [001] (Figure 5.1a). The orientation and morphology of these etch pits helped us confirm the main crystallographic directions. In addition, the dissolution of the surface was accompanied by the growth of new calcite crystals, which formed preferentially on edges and surface defects of the anhydrite (Figure 5.1a). After 15 minutes of interaction, around a third of the (100) anhydrite substrate was covered (Figure 5.1a) by calcite crystals while after five hours the substrate was fully covered (Roncal-Herrero et al., 2017). Such a homogeneous calcite layer on the anhydrite (100) surface after 4 days of reaction (Figure 5.1b) consists of evenly sized calcite crystals (~5 μm or larger), whose habit is bounded by $\{10\bar{1}4\}$ faces. These calcite crystals appear oriented with respect to the anhydrite substrate in a way that one of the calcite rhombohedron faces is always in contact with the anhydrite (100) plane, defining the epitactic relationship $(100)_{Anh} \parallel \{10\bar{1}4\}_{Cal}$ (Figure 5.2a). Moreover, in the majority of these oriented calcite crystals (from here on denoted as Cal_1), one of their $<\bar{4}41>$ edges (either $[\bar{4}41]$ or its symmetry-equivalent $[48\bar{1}]$, both resulting from the intersection of the different faces of the $\{10\bar{1}4\}$ form) is oriented parallel to the [001] direction of the anhydrite substrate. A detailed inspection of the micrograph in Figure 5.2a reveals a second, much less numerous, population of

crystals (from here on Cal_2), which are oriented with one of their $<\bar{4}41>$ edges parallel to the $[010]_{Anh}$. Consequently, both calcite crystal populations (Cal_1 and Cal_2), are related to each other by a 11.9º rotation about the axis parallel to $[100]_{Anh}$.

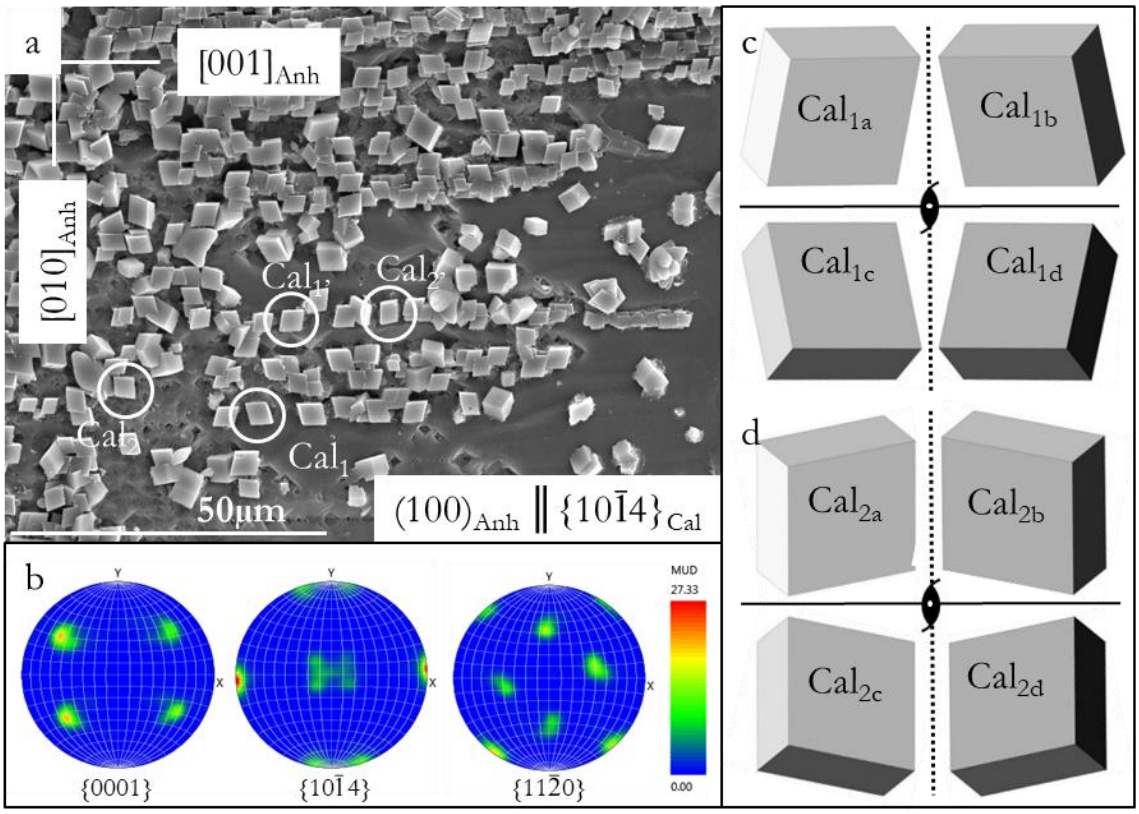

Figure 5.2. (a) SEM image of calcite crystals grown oriented on the (100) surface of an anhydrite cleaved crystal after 2 hours of interaction. The epitaxy involves a matching of the plane (100) of anhydrite with the plane (10$\bar{1}$4) of calcite. The encircled crystals show four different orientations of calcite on the anhydrite substrate which are symmetrically related two by two: Cal_1-Cal_1' and Cal_2-Cal_2' with some of the $<\bar{4}41>$ edges running parallel to the $[001]_{Anh}$ and $[010]_{Anh}$, respectively. (b) EBSD pole-orientation density distribution figures which show the crystallographic orientation relationships between the $(100)_{Anh}$ and the overgrown calcite crystals: $(100)_{Anh} \parallel (10\bar{1}4)_{Cal}$. The number of poles is four times higher than expected reflecting the four alternative orientations shown by the calcite crystals (c) Four alternative orientations: Cal_{1a}, Cal_{1b}, Cal_{1c} and Cal_{1d}, can be deduced from the pole figures. They reflect the symmetry operators inherent to the anhydrite structure that are normal to the $(100)_{Anh}$ substrate. (d) Four alternative orientations envisaged for the Cal_2 population of crystals.

The preferential orientations of these calcite crystal overgrowths in relation to the (100) anhydrite cleavage surface was clarified through EBSD analyses (Figure 5.2b). The pole-orientation density distribution figures (Figure 5.2a) obtained for the {0001}, $\{\bar{4}41\}$ and $\{11\bar{2}0\}$ are consistent with the orientation deduced from the SEM photomicrographs for the larger population of calcite crystals (Cal_1).

Moreover, EBSD analysis also showed a fourfold increase in the number of poles, indicating the existence of four symmetry related orientations in Cal_1: Cal_{1a}, Cal_{1b}, Cal_{1c} and Cal_{1d} (Figure 5.2c). This increase in the number of poles is the result of the existence of symmetric operators inherent to the anhydrite structure and normal to the (100) substrate plane. These are a twofold screw axis, mirror planes, glide planes as well as a centre of symmetry contained in this plane. Furthermore, the existence of a slight tilt of the pole positions with respect to the expected ones was also noticeable. This is most likely due to a small displacement of the anhydrite crystal in the sample holder during sample preparation for EBSD analyses.

The Cal_2 crystals were far rarer and thus their pole figures are not as clearly recognizable in the EBDS analysis (Figure 5.2b). However, the slight dispersion around the pole positions could reflect a slight misorientation of the Cal_1 crystals and/or the presence of this smaller population of Cal_2 crystals. This is particular because the Cal_2 crystals are only slightly rotated (~11.9º) with respect to the major Cal_1 population. Nevertheless, similarly to the Cal_1 crystals, we could define four symmetry related orientations for calcite crystals of the Cal_2 population: Cal_{2a}, Cal_{2b}, Cal_{2c} and Cal_{2d} (Figure 5.2d).

Comparing SEM micrographs of different anhydrite surfaces evidences that (010) surfaces showed similar features to (100) surfaces (Figure 5.3a). Both surfaces were dominated by large and very flat terraces, bounded by macrosteps that ran parallel to [100] and [001] directions. Moreover, calcite crystals formed on such surfaces were also bound by $\{10\bar{1}4\}$ faces and oriented with one of these faces parallel to the anhydrite (010) substrate ($(010)_{Anh} \parallel \{10\bar{1}4\}_{Cal}$). Furthermore, a majority of calcite crystals had a set of their $<\bar{4}41>$ edges oriented parallel to the [001] direction of the anhydrite substrate (Cal_3), while a smaller population had these set of $<\bar{4}41>$ edges parallel to the $[100]_{Anh}$ (Cal_4). Pole-orientation density distributions figures obtained by EBSD analyses along the $(010)_{Anh}$ - calcite phase boundary again revealed similar features to those obtained for the $(100)_{Anh}$ (Figure 5.3b). Indeed, the presence of twofold and twofold screw axes, mirror and glide planes as well as a symmetry centre in the anhydrite structure determined the

existence of four statistically equivalent orientations of calcite crystals with respect to the anhydrite (010) substrate for each one of the two alternative epitactic relationships defined above.

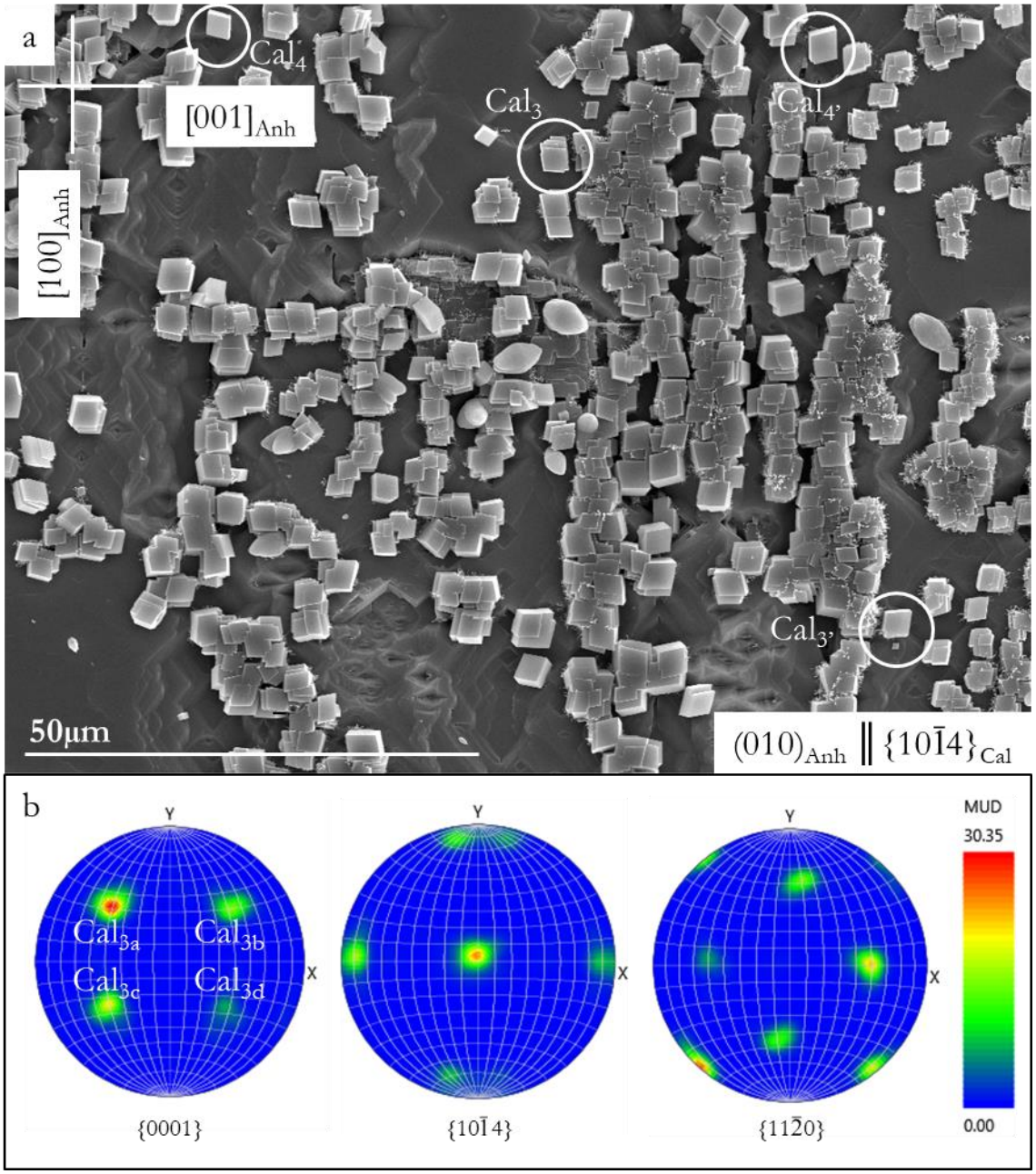

Figure 5.3. (a) SEM image of calcite crystals grown oriented on the anhydrite (010) surface after 2 hours of interaction with the carbonate-rich aqueous solution. The epitaxy is defined by $(100)_{Anh} \parallel (10\bar{1}4)_{Cal}$. The encircled crystals show the four different orientations of calcite crystals on the anhydrite substrate, which are symmetrically related two by two: Cal_3-Cal_3' and Cal_4-Cal_4'. (b) EBSD pole-orientation density distribution figures. The number of poles is four times higher than expected, reflecting the four alternative orientations shown by the calcite crystals which constitute the Cal_3 population: Cal_{3a}, Cal_{3b}, Cal_{3c} and Cal_{3d}.

5.1.2 Calcite overgrowth on anhydrite (001)

Anhydrite (001) surfaces were also characterized by flat terraces, bounded by macrosteps that run parallel to the [100] and [010] directions. Post reaction of these surfaces with the carbonate-rich solutions revealed significantly higher average densities of calcite crystals than on the anhydrite (100) and (010) substrates. The anhydrite (001) substrate was almost completely covered by calcite crystals after 1 hour of reaction with the solution (Roncal-Herrero et al., 2017). However, at very early stages we observed the development of deep, dissolution-related grooves on the anhydrite (001) substrate, which were oriented parallel to [100] (Figure 5.4a). This enabled us to define the main crystallographic directions on this surface (Shindo et al., 2001). Similarly to our observations on both the (100) and (010) surfaces, on the (001) surface calcite crystals with the typical rhombohedron-like habit, bounded by the six faces of the $\{10\bar{1}4\}$, are formed. The calcite crystals were oriented with one of their rhombohedron faces parallel to the anhydrite (001) substrate (defining the matching $(001)_{Anh} \parallel \{10\bar{1}4\}_{Cal}$). Some of these calcite crystals (Cal_5, Figure 5.4a) are oriented with a set of the $<\bar{4}41>$ edges parallel to [100] in the anhydrite substrate. This defines the epitactic relationships $[100]_{Anh} \parallel <\bar{4}41>_{Cal}$. However, a second population of calcite crystals (Cal_6) was slightly tilted (< 12º) with respect to those that constitute the Cal_5 population. This tilting occurs in such a way that the $<\bar{4}41>$ edges of the calcite run parallel to $[010]_{Anh}$, defining the relationship: $[010]_{Anh} \parallel <\bar{4}41>_{Cal}$. On this (001) anhydrite substrate, the population of Cal_5 crystals was significantly larger than that of Cal_6 crystals. EBSD analyses of the adjacent anhydrite and calcite boundaries also yielded similar crystallographic orientations as those described for the (100) and (010) anhydrite surfaces (Figure 5.4b).

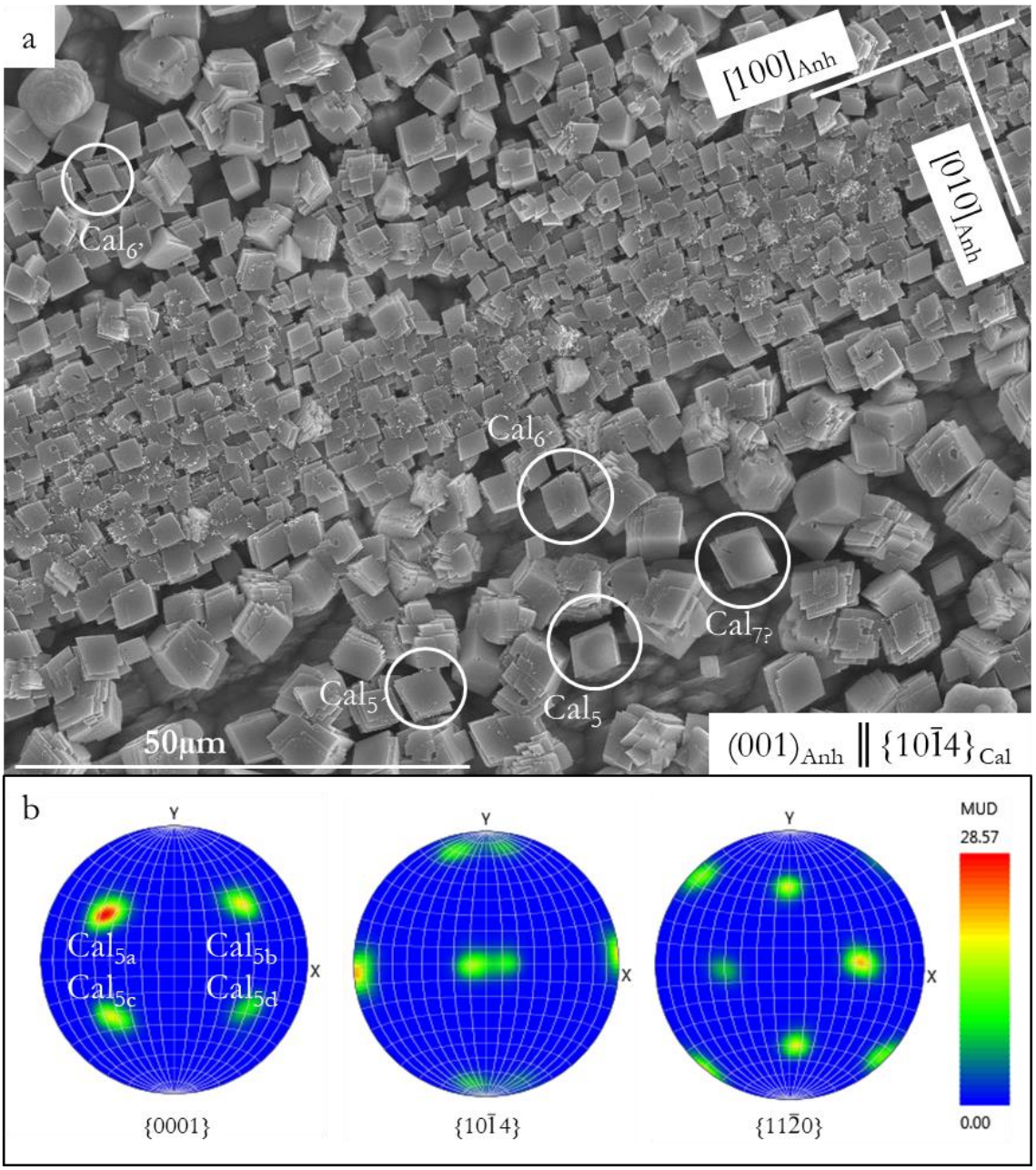

Figure 5.4. (a) SEM image of calcite crystals grown specifically oriented on the (001) surface of an anhydrite cleavage fragment. The epitaxy involves the matching of the plane (001) of anhydrite with the plane (10$\bar{1}$4) of calcite. The encircled crystals show alternative orientations of calcite on the anhydrite substrate. The density of the crystals is significantly higher than observed on $(100)_{Anh}$ and on $(010)_{Anh}$ for the same interaction time (2 hours). (b) Pole-orientation density distribution figures obtained using EBDS. The number of poles is four times higher than expected, reflecting the four alternative orientations for the Cal_5 population: Cal_{5a}, Cal_{5b}, Cal_{5c} and Cal_{5d}.

Finally, we also observed that the nucleation of calcite crystals on the anhydrite substrate with such different and symmetry related orientations often lead to the formation of substrate-induced twins as differently oriented calcite crystals grew and eventually coalesced (Figure 5.5).

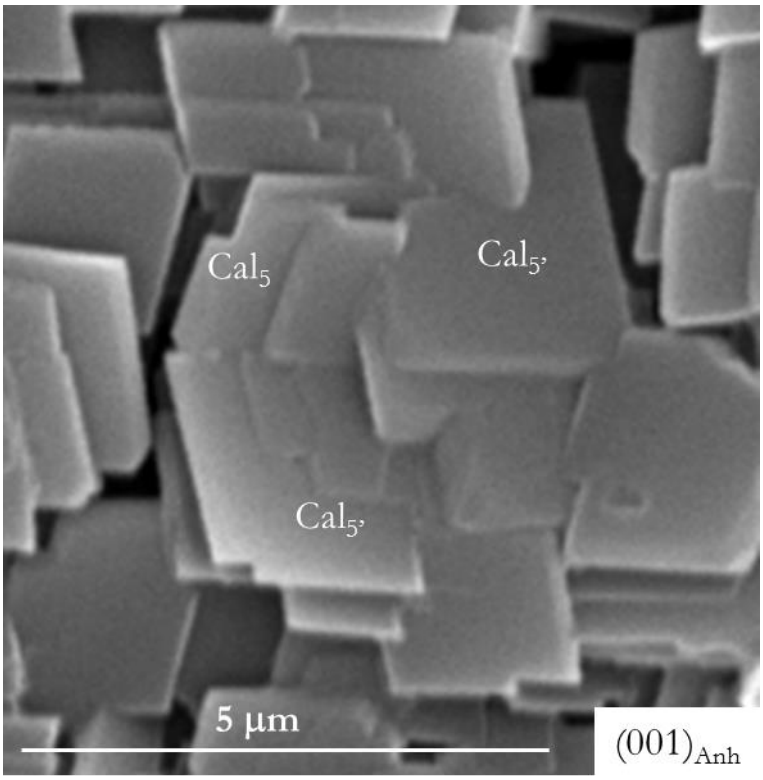

Figure 5.5. SEM image of substrate-induced calcite twins grown on an anhydrite (001) surface. This type of twins develops when two neighbour, differently oriented calcite crystals (Cal_5 and $Cal_{5'}$) belonging to the same epitactic population (Cal_5) grow to coalesce. The crystal individuals forming the twin are related one to other through a reflection operator belonging to the anhydrite substrate (see Figure 5.3c).

5.2. DISCUSSION

We demonstrated that the density of calcite crystals formed upon interaction between specific anhydrite surfaces with carbonate-rich aqueous solution was significantly higher at earlier stages of reaction on $(001)_{Anh}$ compared to on $(100)_{Anh}$ and $(010)_{Anh}$. This is a consequence of the significantly higher reactivity of the $(001)_{Anh}$ surfaces, which dissolves at a much faster rate than both $(100)_{Anh}$ and $(010)_{Anh}$ (Shindo et al., 2010). Consequently, the rate at which Ca^{2+} ions were released from an anhydrite (001) substrate was also faster, resulting in a more rapid increase of local supersaturation in the vicinity of the $(001)_{Anh}$-aqueous solution interface compared to the interface between the aqueous solution and the other two anhydrite cleavage surfaces, (100) and (010). The nucleation of $CaCO_3$ at higher supersaturation levels can, in turn, explain both, the formation of a higher number

of calcite nuclei as well as the formation of a small amount of metastable vaterite at the early stages of the reaction (Roncal-Herrero et al., 2017).

Unsurprisingly the habit of all calcite crystals that grew on the three anhydrite surfaces was bounded by the {10$\bar{1}$4} form, that is, the cleavage rhombohedron. This form is the most stable one among the calcite forms because the four different periodic bond chains (PBCs) contained in a $d_{\{10\bar{1}4\}}$ slide, provide it with a very strong F character (Aquilano et al., 2011; Hartman and Perdok, 1955a; Paquette and Reeder, 1995). These PBCs run parallel to [$\bar{4}$41], [48$\bar{1}$], [2$\bar{2}$1], and [010] directions in the calcite structure (Heijnen, 1985). The two first directions mentioned above are relatively straight chains of carbonate-calcium-carbonate bonds, whereas PBCs parallel to the [2$\bar{2}$1] and [010] directions consist in undulating bond chains, also composed by carbonate-calcium-carbonate bonds (Figure 5.6).

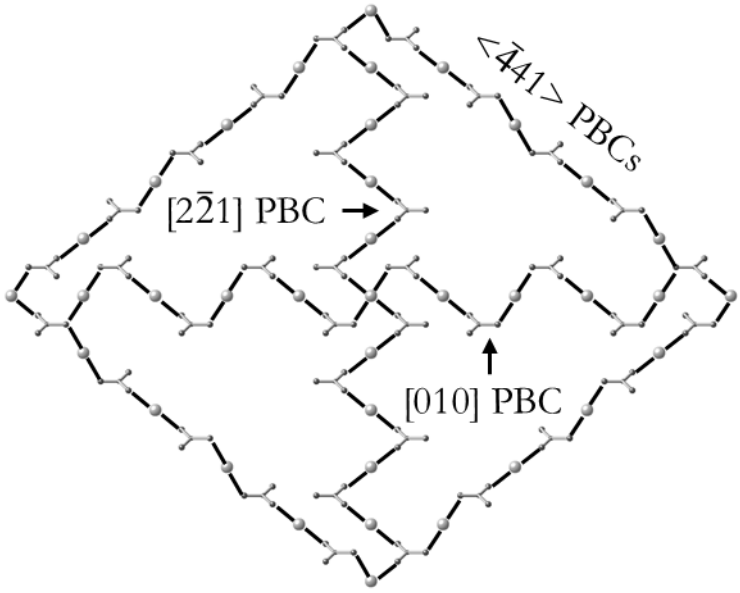

Figure 5.6. Schematic projection showing the three non-equivalent PBCs contained in the calcite {10$\bar{1}$4} surface. The [2$\bar{2}$1] direction runs parallel to the short diagonal of the rhombus defined by <$\bar{4}$41> directions. The [010] direction runs parallel the long diagonal. Ca^{2+} cations are depicted by spheres, whereas ball and sticks groups represent CO_3^{2-}.

Although the development of an epitaxy between an overgrowth and a substrate is not exclusively ruled by geometrical factors the existence of geometrical

similarities between the structures of the involved phases is a requirement for the epitaxy to be possible. These similarities are present in the structures of anhydrite and calcite, despite the fact that both phases crystallize in different crystal systems (anhydrite: space group *Amma*, a = 6.993 Å, b = 6.995 Å, and c = 6.245 Å; calcite: space group $R\bar{3}c$, a = 4.990 Å, and c = 17.061 Å (Effenberger et al., 1981; Hawthorne and Ferguson, 1975). The structures of the $\{100\}_{Anh}$, $\{010\}_{Anh}$, and $\{001\}_{Anh}$ surfaces and the $\{10\bar{1}4\}$ form of calcite are based on chains of alternating oxyanion polyhedra and [*n*]- coordinated Ca^{2+}. These chains link to each other, forming layers. In the anhydrite structure three sulphate-calcium-sulphate bond chains can be distinguished (Aquilano et al., 1992). These PBCs run parallel to the crystallographic axes. Consequently, they provide an F-character to the three main anhydrite surfaces since all of them contain two groups of coplanar PBCs. As a result of these crystallographic similarities, the formation of a $\{10\bar{1}4\}$ layer of calcite on any of the three anhydrite surfaces does not interrupt the SO_4 – Ca sequence and can ideally continue and match the structure of anhydrite. Indeed, structural continuity "represents the master condition which has to be respected when two crystalline individuals grow within the twinning or epitaxial relationships" (Massaro et al., 2008). Moreover, although the geometries of the sulphate (SO_4^{2-}, tetrahedron) and carbonate (CO_3^{2-}, triangle) oxyanions are different, both are identically charged and have a similar size, which contributes to make possible the development of epitatic relationships between both phases. As a matter of fact, it has been demonstrated that calcite can incorporate small amounts of sulphate substituting carbonate in its bulk structure (Arroyo-de Dompablo et al., 2015; Balan et al., 2017; Fernández-Díaz et al., 2010; Frisia et al., 2005; Perrin et al., 2017).

Beyond the structural similarities, the formation of the interface between layers of two different phases also requires a good matching of their lattice planes. The mismatch through the interface between the lattices of the two phases involved in the epitaxy can be described by the lattice misfit (*mf*), which is frequently expressed by means of the equation (Van der Merwe, 1978):

$$mf(\%) = \frac{t_{[uvw]_{Cal}} - t_{[uvw]_{Anh}}}{t_{[uvw]_{Anh}}} \cdot 100$$

where $t_{[uvw]}$ is the repeating period along the [*uvw*] direction of the substrate (anhydrite) and overgrowth (calcite). Negative misfit values mean that the unit cell of the overgrowth is contracted along [*uvw*] in comparison to the unit cell of the substrate ($t_{[uvw]_{Cal}} < t_{[uvw]_{Anh}}$), whereas a positive misfit value indicates an expansion of the overgrowth unit cell along the same direction. If the difference between the corresponding lattice constants *mf* is ≤ 10% to 12%, the lattice matching results in the formation of a coherent substrate–overgrowth interface. This is furthermore, accompanied by the generation of elastic strain and stress and the formation of an epitaxy (Chernov, 1984; Shtukenberg et al., 2005). Figures 5.7 a-d display the projections of the structure of anhydrite on the (100), (010) and (001) planes, and the structure of calcite on the $(10\bar{1}4)$ plane. The superimposed lozenges on the anhydrite structure projections depict a calcite rhombohedron, bounded by $<\bar{4}41>$ edges and with one of its $(10\bar{1}4)$ faces siting on the projected anhydrite plane. These lozenges are oriented with a pair of their $<\bar{4}41>$ edges parallel to a main direction in the anhydrite projection. This matches our observations from the SEM images and EBSD analyses results (Figures 5.2-5.4).

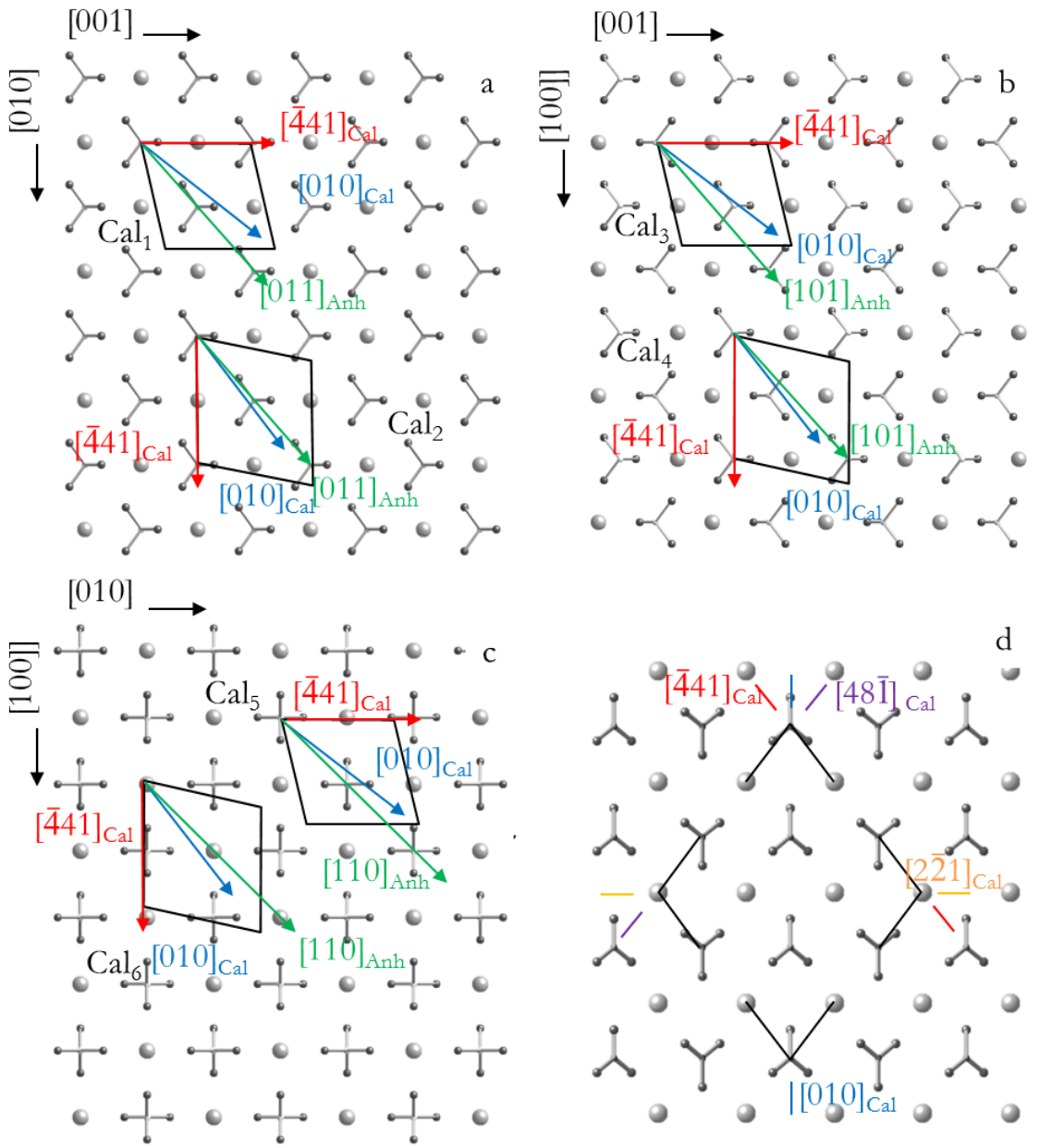

Figure 5.7. Projections of the crystal structures of a slice of (a) $(200)_{Anh}$, (b) $(020)_{Anh}$, and (c) $(002)_{Anh}$. The superimposed rhombus depicts the $(10\bar{1}4)$ face of the calcite rhombohedron projected in the same orientation as shown in the SEM images (d) Schematic of the $(10\bar{1}4)_{Cal}$ surface of calcite showing the main directions. Ca^{2+} cations are depicted by spheres, whereas ball and sticks groups represent SO_4^{2-} and CO_3^{2-}.

As explained above, in most of the calcite crystals (Cal_1 and Cal_3) the epitactic overgrowth of $\{10\bar{1}4\}_{Cal}$ on $(100)_{Anh}$ and $(010)_{Anh}$ was controlled by the parallelism between the $<\bar{4}41>_{Cal}$ and $[001]_{Anh}$. For anhydrite, the distance between successive SO_4 groups along [001] is 6.245 Å, i.e., it coincides with the anhydrite *c* cell parameter. In the calcite structure, the distance between successive equivalent CO_3 groups (repeating period) is 12.850 Å, which is about twice the distance between

successive SO_4 groups along $[001]_{Anh}$ (2 x 6.245 Å = 12.49 Å). Similar repeating periods guarantee a good matching between the two structures. Considering a 1:2 ratio between the repeating periods along $[001]_{Anh}$ and $<\bar{4}41>_{Cal}$, the misfit is 2.88% (Table 5.1), which clearly lies within the limits required for epitactic nucleation from solution (Chernov, 1984). Thus our data show that the excellent matching between both surfaces along these directions explains the development of an oriented overgrowth of calcite on both $(100)_{Anh}$ and $(010)_{Anh}$ surfaces. One additional pair of directions within these contact planes can also be defined in both anhydrite surfaces, $<011>_{Anh} \parallel [010]_{Cal}$ and $<101>_{Anh} \parallel [010]_{Cal}$. These pairs show relatively good matching with linear misfit close to 6.4% (see Table 5.1). However, an angular divergence between both directions of ~ 9.20º does not support the possibility that matching along these directions contribute to the development of the epitaxies.

Table 5.1 Epitactic relationships between anhydrite ($CaSO_4$) and calcite ($CaCO_3$).

Anhydrite ($CaSO_4$)		Calcite ($CaCO_3$)		Misfit (%)		
Contact Plane	Parameter (Å)	Contact Plane	Parameter (Å)	Calcite population	Linear	Angular
(100)	2 × [001] = 12.490	($10\bar{1}4$)	$<\bar{4}41>$ = 12.850	1	2.88	-
	<011> = 4.689		[010] = 4.990		6.42	~ 9.20°
	2 × [010] = 13.990		$<\bar{4}41>$ = 12.850	2	-8.14	-
	<011> = 4.689		[010] = 4.990		6.42	~ 2.70°
(010)	$<\bar{4}41>$ = 12.850	($10\bar{1}4$)	$<\bar{4}41>$ = 12.850	3	2.88	-
	2 × [010] = 9.980		2 × [010] = 9.980		6.44	~ 9.20°
	$<\bar{4}41>$ = 12.850		$<\bar{4}41>$ = 12.850	4	-8.12	-
	2 × [010] = 9.980		2 × [010] = 9.980		6.44	~ 2.70°

Anhydrite ($CaSO_4$)		Calcite ($CaCO_3$)		Misfit (%)		
Contact Plane	Parameter (Å)	Contact Plane	Parameter (Å)	Calcite population	Linear	Angular
(001)	2 × [100] = 13.986	($10\bar{1}4$)	$<\bar{4}41>$ = 12.850	5	-8.12	-
	<110> = 9.891		2 × [010] = 9.980		0.90	~ 5.50°
	2 × [010] = 13.990		$<\bar{4}41>$ = 12.850	6	-8.14	-
	<110> = 9.891		2 × [010] = 9.980		0.90	~ 5.50°
	<110> = 9.891		2 × [010] = 9.980	7	0.90	~ 5.50°
	2 × [100] = 13.986		$<\bar{4}41>$ = 12.850		-8.12	-
	2 × [010] = 13.990		$<\bar{4}41>$ = 12.850		-8.14	-

As we have shown in the SEM images (Figures 5.2a and 5.3a), there was a secondary, much less numerous population of calcite crystals, which included two crystal populations (Cal_2 and Cal_4), with one of their $<\bar{4}41>_{Cal}$ aligned parallel to the [010] and [100] directions of the $(100)_{Anh}$ and $(010)_{Anh}$ surfaces, respectively. Since the *a* and *b* axes in the anhydrite structure are almost identical in length ($b - a$ = 0.002 Å), the linear misfits between the calcite and anhydrite structures along both of these directions are also very similar with ~ 8% for both the $[010]_{Anh} \| <\bar{4}41>_{Cal}$ and the $[100]_{Anh} \| <\bar{4}41>_{Cal}$ alignments. It was also possible to define a second pair of alignments, with $<011>_{Anh} \| [010]_{Cal}$ (Cal_2) and $<101>_{Anh} \| [010]_{Cal}$ (Cal_4), which were identical to those described for Cal_1 and Cal_3, although with a lower angular divergence (~2.7º). Although the matches described for Cal_2 and Cal_4 were not as good as those calculated for the Cal_1 and Cal_3 populations, they nevertheless still guarantee the development of an epitactic overgrowth of so oriented calcite crystals on the $(100)_{Anh}$ and $(010)_{Anh}$ surfaces. The good match between the two pair of directions in this second orientation explains, therefore, the development of two non-symmetrically related populations of calcite crystals rotated by ~12° with respect to each other. On anhydrite {001} surfaces we have suggested a match between $[100]_{Anh} \| <\bar{4}41>_{Cal}$ and $<110>_{Anh} \| [010]_{Cal}$ for Cal_5, and $[010]_{Anh} \| <\bar{4}41>_{Cal}$ and $<110>_{Anh} \| [010]_{Cal}$ for Cal_6 with a slightly better misfits for Cal_5 than Cal_6 (see Table 1). This higher fitting goodness explains the much larger population of Cal_5 crystals.

It is possible to evaluate epitaxy relationship solely on the basis of structural similarities and misfit values. However, as stated by the PBC theory, a minimum interface energy is achieved when, apart from a matching of parallel planes of the substrate and the overgrowth, there is a coincidence between the close-packed atomic rows (defined by the PBCs) contained in these planes (Chernov, 1984). In all the epitactic relationships defined above, the better match involves crystallographic directions parallel to PBCs in both calcite and anhydrite. This factor further favours the development of the oriented overgrowth. Indeed, other alternative epitactic relationships with low misfits values can be envisaged. For instance, the $[110]_{Anh} \| <010>_{Cal}$ alignment on $(001)_{Anh}$ exhibits an excellent match with a linear

misfit of 0.90%. However, such an epitaxy is in principle energetically unfavorable with respect to the epitaxies defined above, since the $[110]_{Anh}$ is not parallel to any PBC in the anhydrite structure. Furthermore, although the $[010]_{Cal}$ direction corresponds to a PBC, this is a rough, high energy and thus less favourable PBC (Aquilano et al. 2011). In Figure 5.7c, some crystals could be oriented following this orientation (Cal_7), although this is not clearly supported by SEM observations and EBDS analyses (Table 5.1).

The existence of epitactic relationships between anhydrite surfaces and calcite overgrowths can influence the kinetics of the carbonation reaction. It has been shown that under certain conditions the development of epitactic overgrowths can lead to surface passivation (Prieto et al., 2013), and, as a result, to a slow down or even full inhibition of any further dissolution-precipitation after the formation of a thin overgrowth. Such overgrowths are often only nanometer-thin, as in the cases of the epitactic overgrowths of otavite ($CdCO_3$) and rhodochrosite ($MnCO_3$) on a calcite $\{10\bar{1}4\}$ substrate or of hashemite ($BaCrO_4$) on a barite ($BaSO_4$) (001) (Godelitsas et al., 2010; Pérez-Garrido et al., 2007; Pérez-Garrido et al., 2009; Riechers and Kerisit, 2018; Shtukenberg et al., 2005). Overgrowths can result from the development of two-dimensional, yet only a few nanometers high nuclei. These spread rapidly on a substrate and coalesce according to a Frank-van der Merwe or Stranski-Krastanov epitactic growth mechanisms (Pérez-Garrido et al., 2007; Prieto et al., 2013; Shtukenberg et al., 2005). Depending on the goodness of the lattice misfit this commonly involves isostructural phases, which belong to the same mineral group. The formation of this type of overgrowths leads to the almost perfect preservation of the nano-topography of the surface of a substrate (Astilleros et al., 2003a; Astilleros et al., 2006). A second type of epitactic overgrowth involves the formation on a dissolving substrate of three-dimensional crystals, according to a Volmer-Weber growth mechanism. Commonly, the formation of 3-D crystals takes place when the primary and the secondary phases are non-isostructural but share some structural features and the matching through certain interfaces is good. In this case, even if the overgrowth completely carpets the substrate (like in the case of our calcite crystals growing on the anhydrite surfaces), the armouring is usually

imperfect. The existence of hollows, left between differently oriented crystals in the overgrowth, allows a continuous communication between the aqueous solution and the substrate. This way, the progress of the dissolution-crystallization reaction is guaranteed, even if its kinetics is slowed down. Excellent examples of this type of epitaxy are the oriented growth of pharmacolite ($CaHAsO_4 \cdot 2H_2O$) on gypsum and of anglesite ($PbSO_4$) on anhydrite (Morales et al., 2013; Rodriguez-Blanco et al., 2007). In the latter case, it was demonstrated that the formation of the overgrowth did not prevent the dissolution-precipitation reaction progressing until the complete replacement of anhydrite by anglesite.

The anhydrite – calcite epitaxy described here clearly fits in this latter category. The coalescence of micrometer sized blocky calcite crystals that are differently oriented on the anhydrite substrates will necessarily lead to the formation of a porous overgrowth. This will nevertheless, fail to perfectly seal the substrate. The effect of this imperfect sealing is further enhanced by the fact that the replacement of anhydrite by calcite leads to a negative volume change, further contributing to an increase in the porosity of the overgrowth calcite layer and explaining that anhydrite crystals in contact with carbonate-bearing solutions can become completely replaced by aggregates of calcite crystals in relatively short times (~15 days under the experimental conditions used in this work)(Roncal-Herrero et al., 2017).

It is worth highlighting that the existence of two or more equiprobable orientations of the calcite crystals on the anhydrite substrates leads to the development of so called substrate-induced twinning (Pinto et al., 2009). The formation of such twins (Figure 5.5) is a consequence of the coalescence of individuals that are differently oriented with respect to the substrate, but whose orientations are related to each other by symmetry operators inherent to the substrate structure (Morales et al., 2014; Pinto et al., 2009). The twin law is, therefore, determined by the substrate symmetry. For instance, in the anhydrite – calcite epitaxy in this current study, individual crystal *a* can be related with individual crystal *d* through a centre of symmetry which acts as a twin centre (Figure 5.2c). The formation of substrate-induced twins is a general phenomenon, which has so far been reported to occur during pseudomorphic mineral replacement processes

through interface coupled dissolution-crystallization reactions (Morales et al., 2014; Pinto et al., 2009).

6. POROSITY GENERATION AND EVOLUTION DURING THE CARBOBANTION OF ANHYDRITE

6. POROSITY GENERATION AND EVOLUTION DURING THE CARBOBANTION OF ANHYDRITE

As has been stated, anhydrite carbonation involves the generation of a large volume of porosity. In order to study the generation and evolution of porosity as a result of the carbonation process, experiments of anhydrite single crystal replacement after interaction with carbonate aqueous solutions were conducted. The characterization of the resulting pseudomorphs using SEM and CT-scan analyses provides information that sheds light on the factors that control the porosity organization within calcium carbonate pseudomorphs after anhydrite at different stages of the replacement process. The conclusions derived can be extended to other systems where relevant rock-forming minerals undergo mineral replacement processes.

6.1. RESULTS

Interaction of anhydrite single crystals with carbonate bearing aqueous solutions (0.5M and 0.05M Na_2CO_3) leads to their pseudomorphic replacement by calcite together with minor amounts of vaterite and/or aragonite. In all the experiments conducted the external shape is preserved and the main original microscopic features of the surface of the primary anhydrite crystal are preserved after the mineral replacement reaction. All anhydrite surfaces show cleavage steps and marked striations which are apparent on (001) surfaces by SEM. These features are still distinguishable in the pseudomorphs formed after anhydrite transformation into calcite (Figure 6.1).

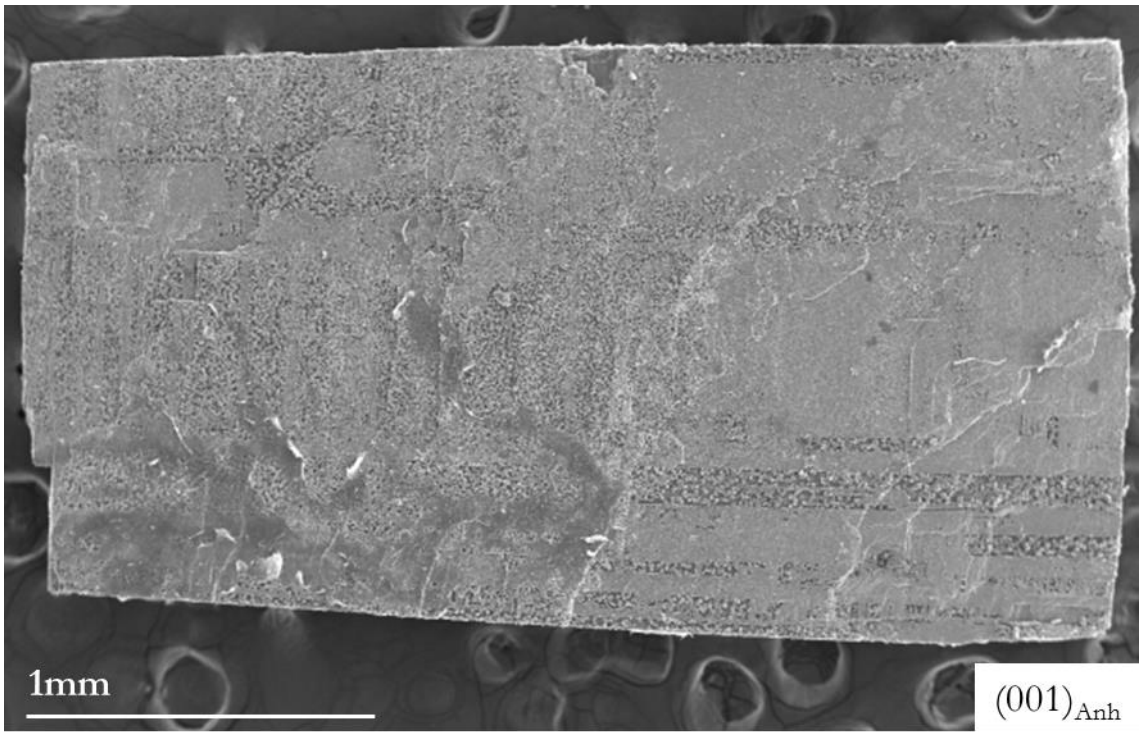

Figure 6.1. SEM image of the (001) surface of anhydrite. Cleavage steps can be seen on it.

CT scanning of anhydrite crystals prior to interaction with carbonate solutions reveals that they contain numerous fluid inclusions (Figure 6.2). These fluid inclusions are bounded by flat (100), (010) and (001) surfaces and appear strongly elongated. Most of them are arranged with their lengths running parallel to [001], defining pre-existent channels within the anhydrite crystal. Inclusions during the recrystallization of Barite with carbonate bearing solutions have also been observed (Weber et al., 2017; Weber et al., 2018).

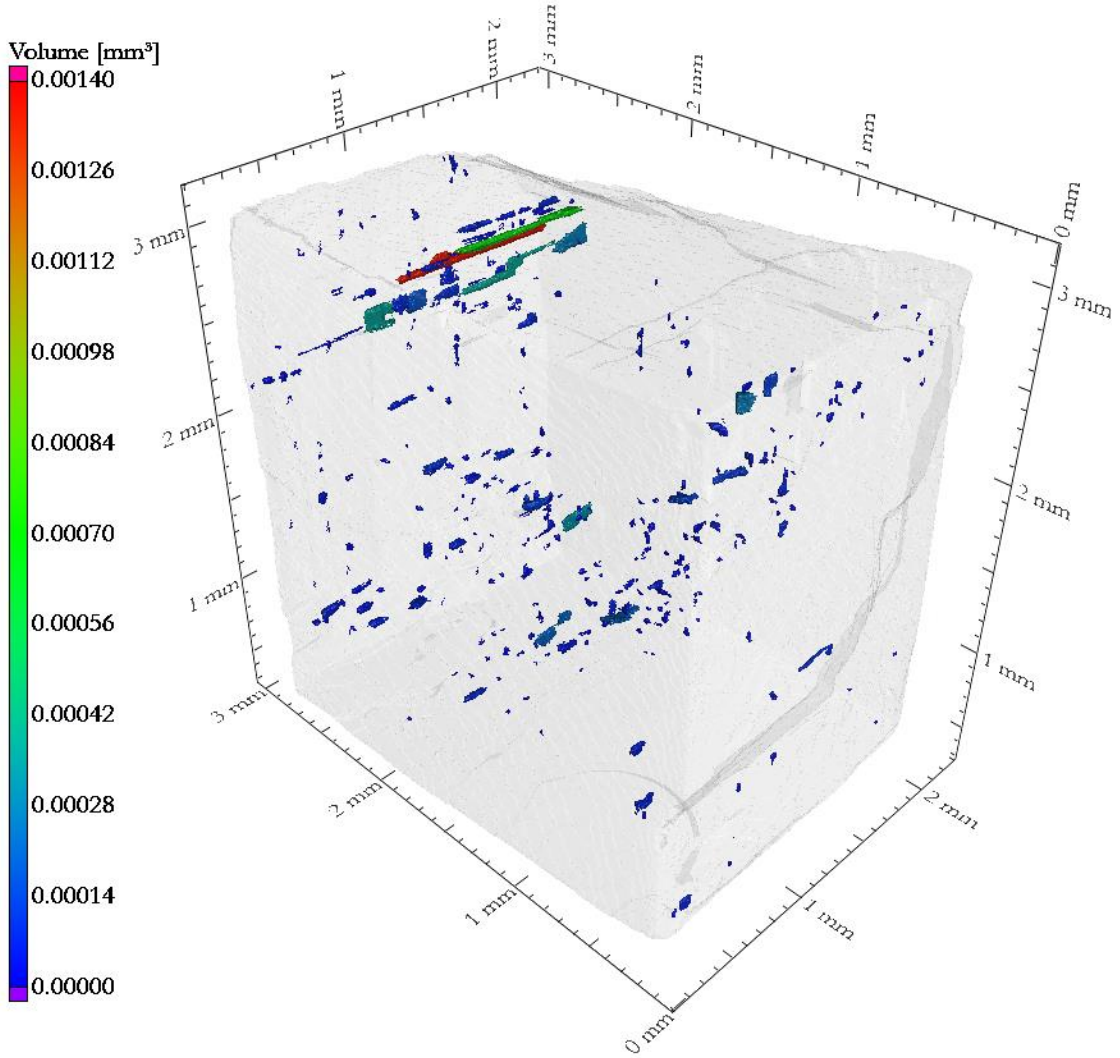

Figure 6.2. Reconstruction of the X-CT dataset of an anhydrite single crystal prior to the beginning of the reaction. Results of data segmentation on the whole volume. The inclusions in red are bigger than the ones in green, which are bigger that the ones in blue. These areas correspond to fluid inclusions. Most fluid inclusions are bounded by flat surfaces approximately parallel to {100}, {010} and {001}, strongly elongated along the [001] direction and, consequently, define an arrangement of parallel channels.

These inclusions are also preserved after the development of the Inducted Coupled Dissolution-Crystallization (ICDC) reaction that leads to the formation of pseudomorphs, as can be seen in Figure 6.3., where a SEM image of a partially replaced anhydrite crystal is shown. The large fluid inclusions present in this crystal serve as channels along which the carbonate fluid phase encounters enhanced access to the anhydrite crystal interior. The existence of these fluid inclusions facilitates the inwards advancement of the replacement reaction parallel to the inclusion walls, defining a complex reaction front.

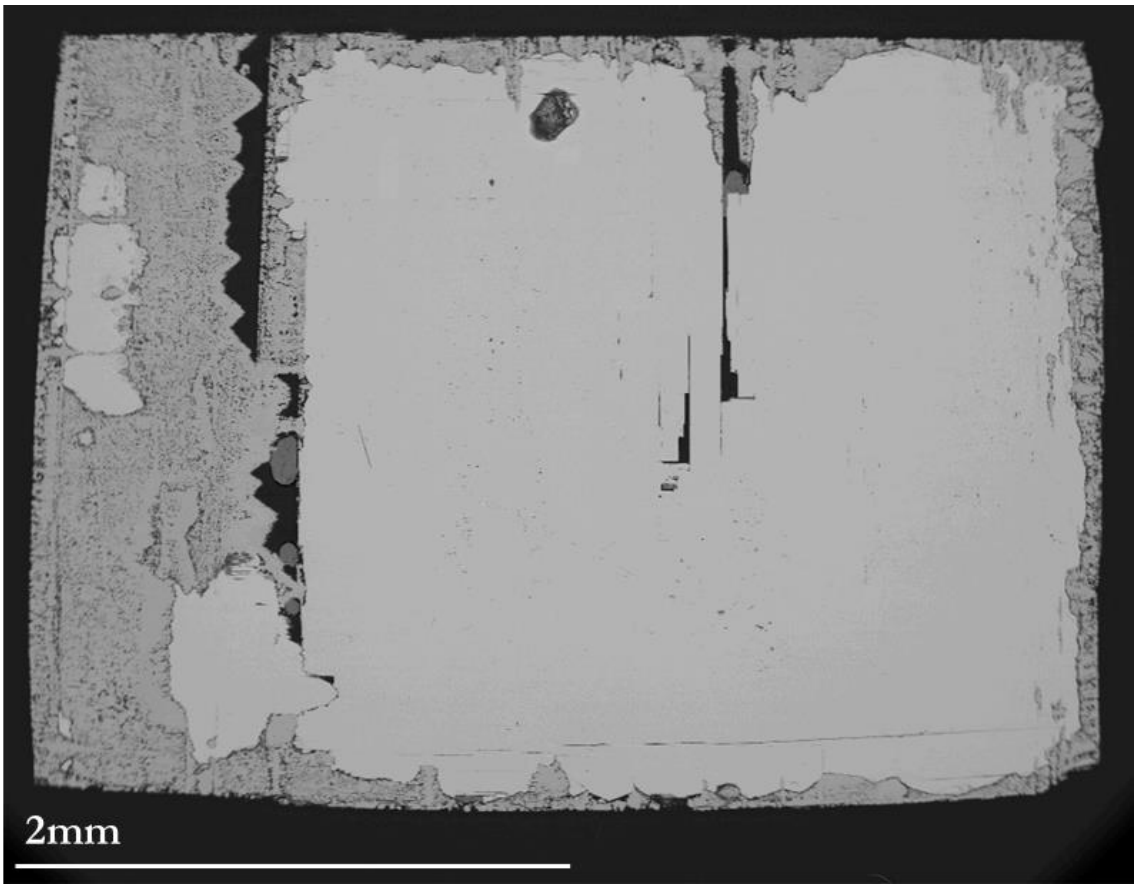

Figure 6.3. Section of a partially replaced anhydrite crystal after 24 hours interaction with a 0.5M Na_2CO_3 aqueous solution. The original anhydrite crystal contains large fluid inclusions whose shape is still visible in those regions that has already undergone transformation. Enhanced fluid penetration along these inclusions facilitates that the mineral replacement reaction takes place preferentially on inclusion walls, leading to the development of a complex-shaped reaction front.

Similar features are observed in the X-CT reconstruction shown in Figure 6.4., where a 3D-volume rendering of an anhydrite crystal after it has interacted during 24 hours with the carbonate solution can be seen. The complex organization of the reaction front, whose surface is defined by differently penetrating fingers approximately parallel to [001], is clearly depicted. It is worthwhile to note the much deeper penetration of the reaction front in those areas where the penetration of the fluid phase was facilitated by the presence of pre-existing fluid inclusions. These fluid inclusions act as channels for the fluid phase, allowing the interaction to take place over larger areas.

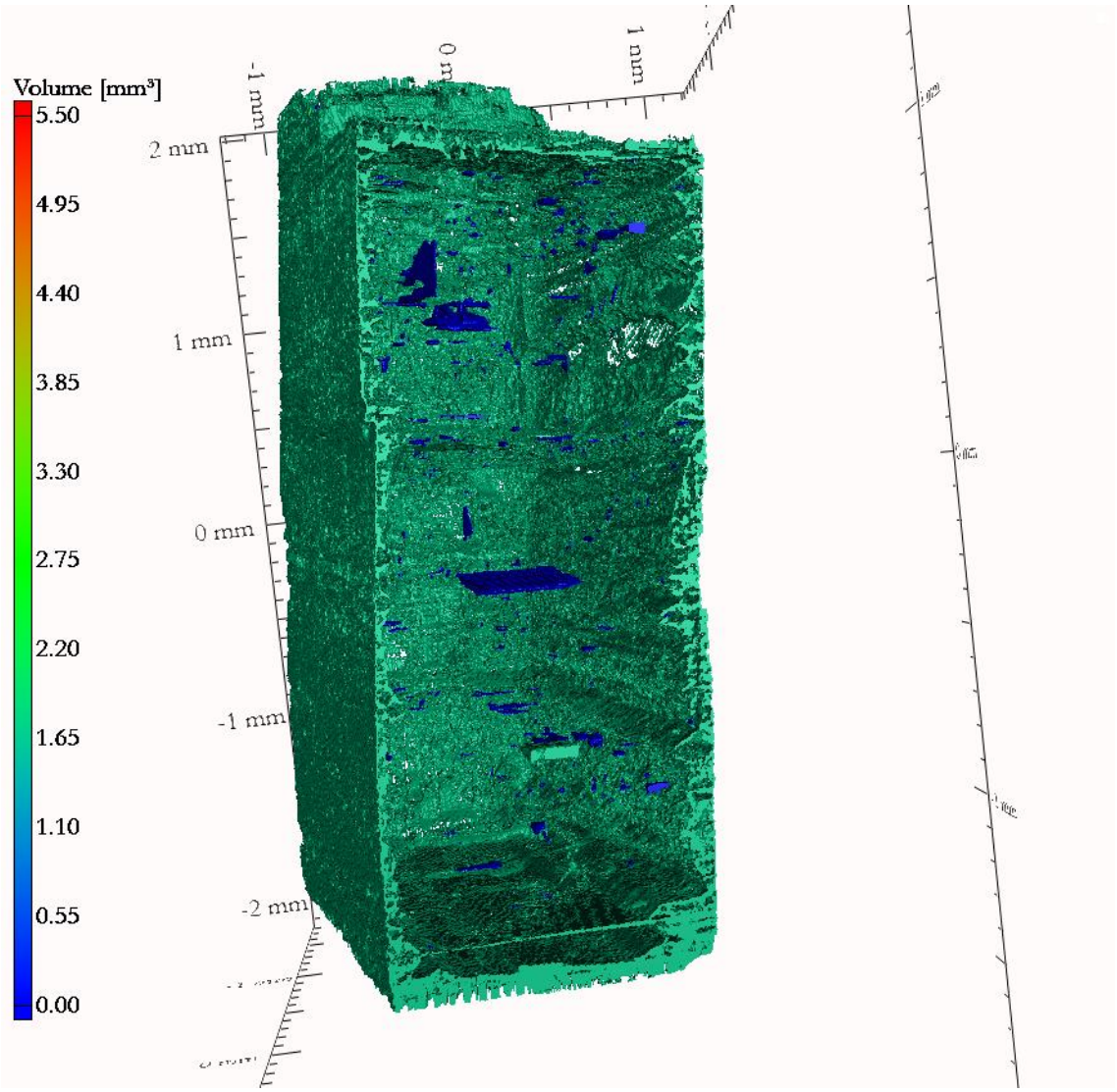

Figure 6.4. Reconstruction of the X-CT dataset of an anhydrite single crystal interacted during 24 hours with a 0.5M carbonate-bearing solution. Results of data segmentation on the whole volume. The colour code scale indicates how much volume is contained in the cavity expressed in mm^3. The reaction front shows a complex structure, characterized by the development of fingers that run parallel to anhydrite [001] direction. This fingering arises from the much deeper penetration reached by the reaction front where it meets pre-existent fluid inclusions.

After 3 days of interaction two regions can be clearly distinguished within the anhydrite crystal from the outside towards the inside, an outer carbonate layer, whose thickness progressively increases, and a retreating, unreacted anhydrite core. A sharp contact defines the transition between the carbonate layer and the unreacted core. The carbonate layer is porous and, according to porosity features and organization, it can be further subdivided into three subregions (Figure 6.5):

- Zone 1: An almost porosity free outer rim.

- Zone 2: An intermediate region where coarse porosity is arranged approximately perpendicular to the primary phase surface displaying porous channels that alternate with poorly porous calcite columns.
- Zone 3: An inner subregion where a fine porosity appears homogeneously distributed in between small calcite crystals.

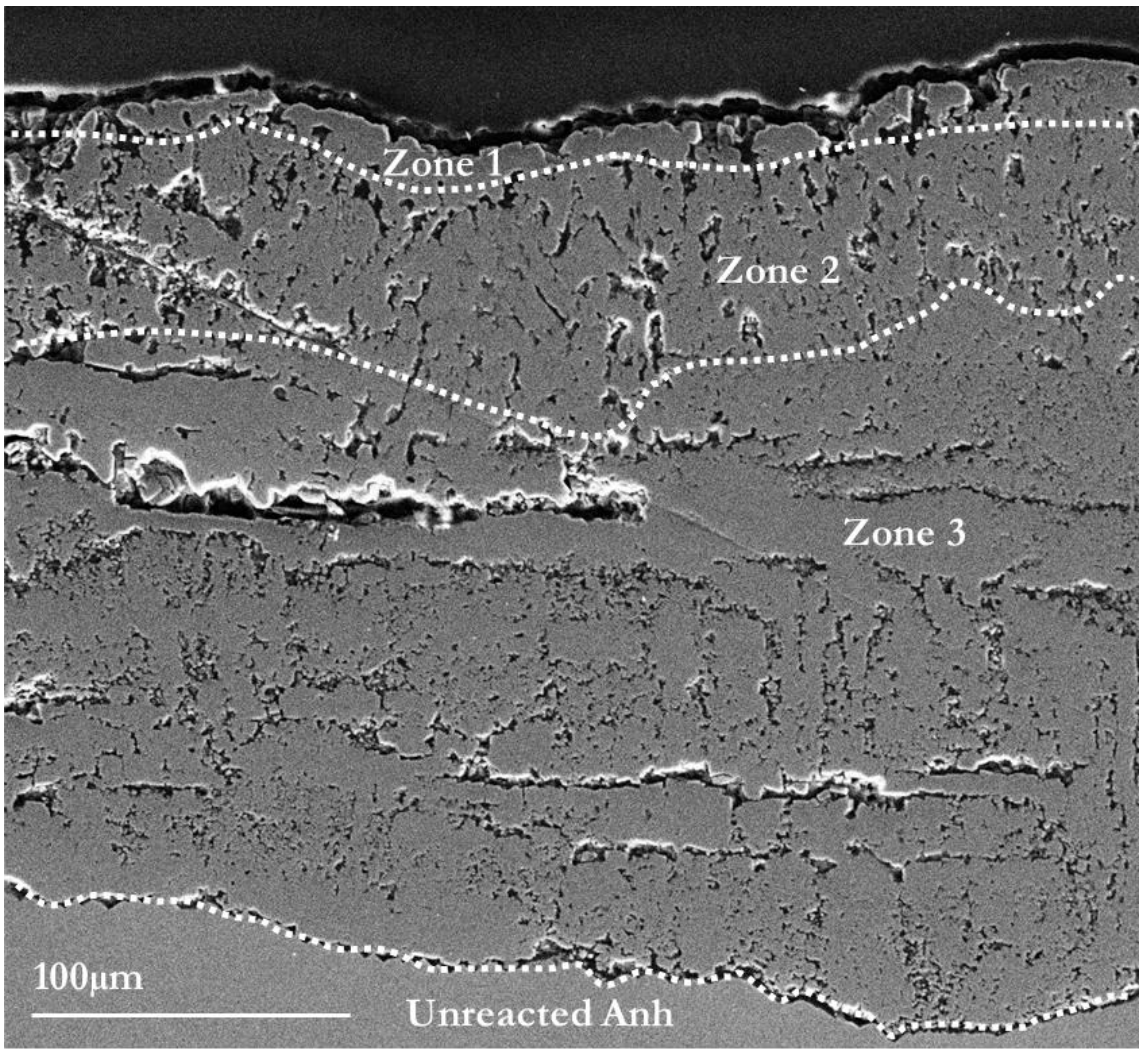

Figure 6.5. SEM micrograph of a section of an anhydrite crystal after interaction with a 0.5M Na_2CO_3 aqueous solution during 3 days. The sharp contact between the carbonate layer and the unreacted anhydrite is apparent. From rim to the core of anhydrite, three zones can be distinguished within the carbonate layer according to the texture that arises as a result of porosity organization and distribution: Zone 1 is located in the outer region of the carbonate layer and contains little porosity. Zone 2 occupies the intermediate region and contains porosity arranged in channels. Zone 3 is the region closer to the anhydrite core and contains a fine porosity that appears more homogeneously distributed.

The outer subregion (zone 1) is a continuous, very thin (few micrometers wide) rim that only contains submicrometric pores. This subregion appears as soon as the reaction starts and tends to rapidly disappear substituted by the intermediate subregion (zone 2) as the replacement advances (Figure 6.6a). A similar behavior is followed by the inner subregion of homogenously distributed porosity (zone 3). This subregion is located between the intermediate subregion and the unreacted anhydrite core. It starts to develop early during the ICDC reaction, dominating the carbonate layer shortly after the beginning of the interaction. Porosity in this subregion consists of interconnected pores that are several micrometers to submicrometric in size (Figure 6.6b).

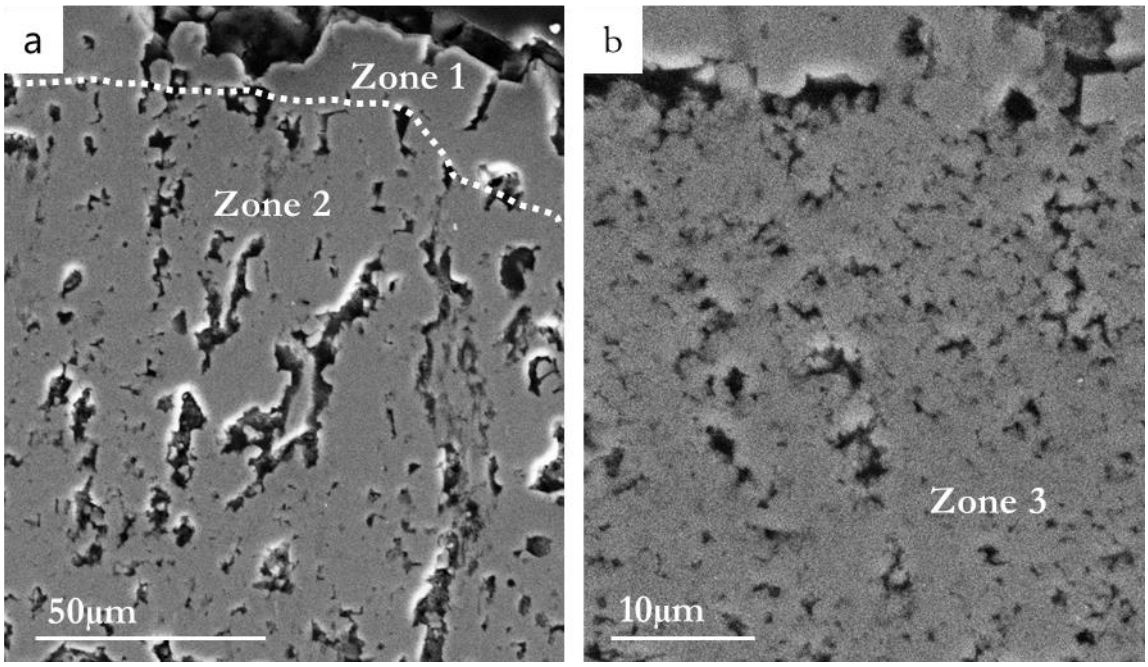

Figure 6.6. SEM micrographs of the different zones in the carbonate layer of an anhydrite crystal reacted with a 0.5M Na_2CO_3 aqueous solution during 3 days. (a) The different texture of zone 1 and zone 2 is apparent. Whilst zone 1 is nearly porosity free, zone 2 is characterized by a porosity which is distributed in channels arranged in an approximately perpendicular to the original crystal surface disposition. (b) Porosity in zone 3 consists of submicrometric pores more homogeneously distributed.

Although the inner subregion of homogeneously distributed porosity (zone 3) still occupies most of the replaced layer after 5 days of interaction with the carbonate aqueous solution (Figure 6.7), its relative thickness progressively

decreases until completely disappearing, substituted by the intermediate subregion (zone 2) 14 days after the beginning of the mineral replacement reaction.

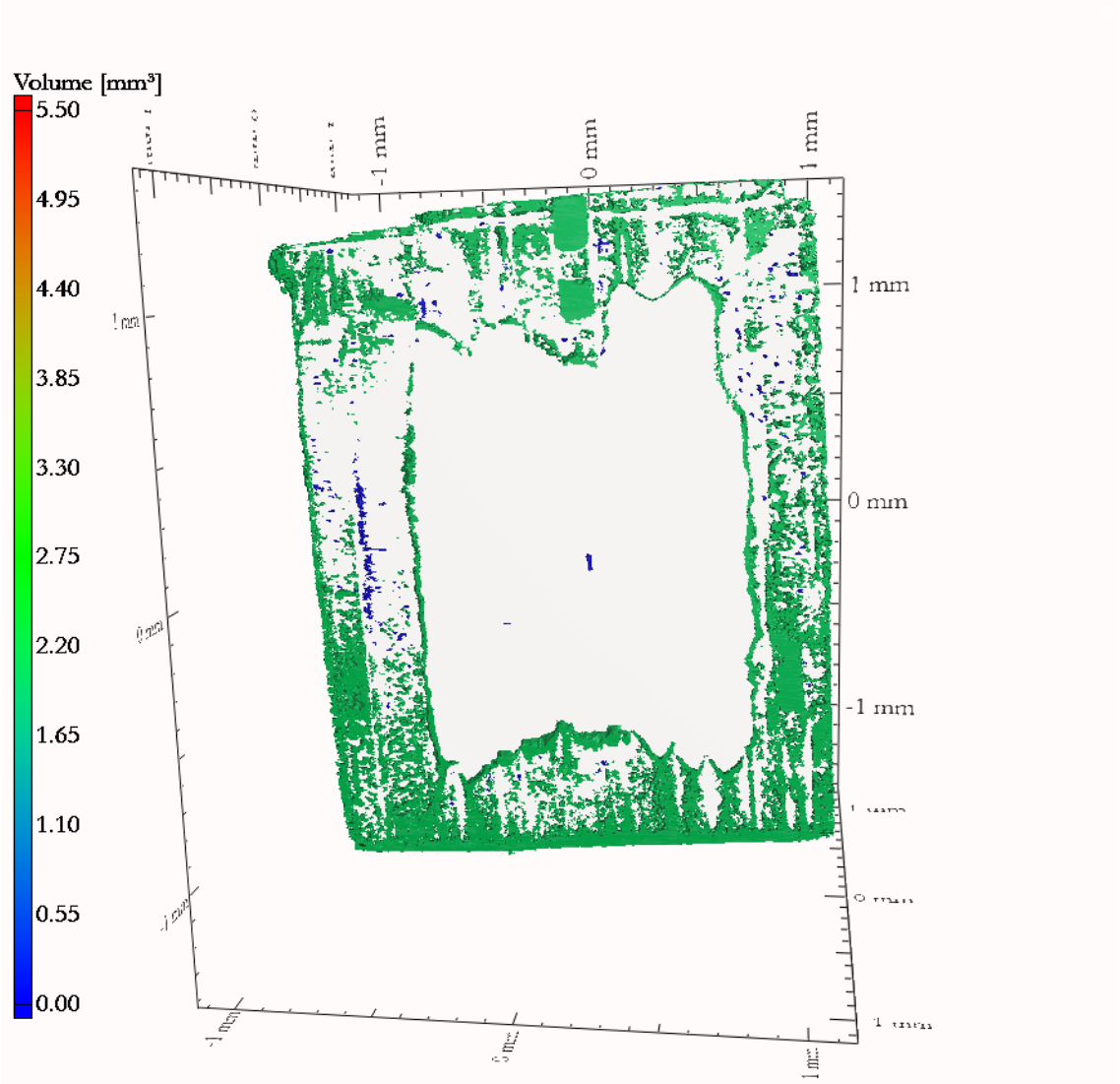

Figure 6.7. Reconstruction of the X-CT dataset of an anhydrite single crystal interacted during 5 days with the carbonate-bearing solution. Results of data segmentation on the whole volume. The colour code scale indicates how much volume is contained in the cavity expressed in mm^3. The reacted area appears in shades of greenish and blue. The complex architecture of the reaction front is apparent. Three sub-regions can be distinguished in the reacted layer: A thin low porosity external rim (upper area of the image), an intermediate region arranged in channels where porosity concentrates alternating with poorly porous columns, and a large sub-region of homogeneously distributed porosity located between the intermediate sub-region and the unreacted anhydrite core. The intermediate sub-region is quite developed. Well defined channels are restricted to external zone. These channels appear arranged mainly parallel to [001].

The intermediate subregion (zone 2) progressively develops and gains importance, growing at expenses of the other two ones. It dominates the carbonate secondary layer after 7 days of interaction and becomes the only relevant subregion

14 days after the beginning of the mineral replacement reaction, as evidenced in the X-CT scanning images shown in figure 6.8. In this subregion calcite columns only contain submicrometric pores and are separated by regions where porosity accumulates. The width of the calcite columns increases as the reaction progresses. This thickening of poorly porous calcite columns is accompanied by a progressive thinning of the alternating highly porous regions. This thinning takes places concomitantly to a porosity coarsening that leads to the arrangement of this porosity in wide channels. This evolution finally results after 14 days interaction in an alternating pattern of columns of porosity-free calcite and 20-50 micrometers wide channels (Figure 6.8). These channels appear mainly arranged parallel to [001]. Poorly defined channels that run along [100] and [010] are also distinguishable.

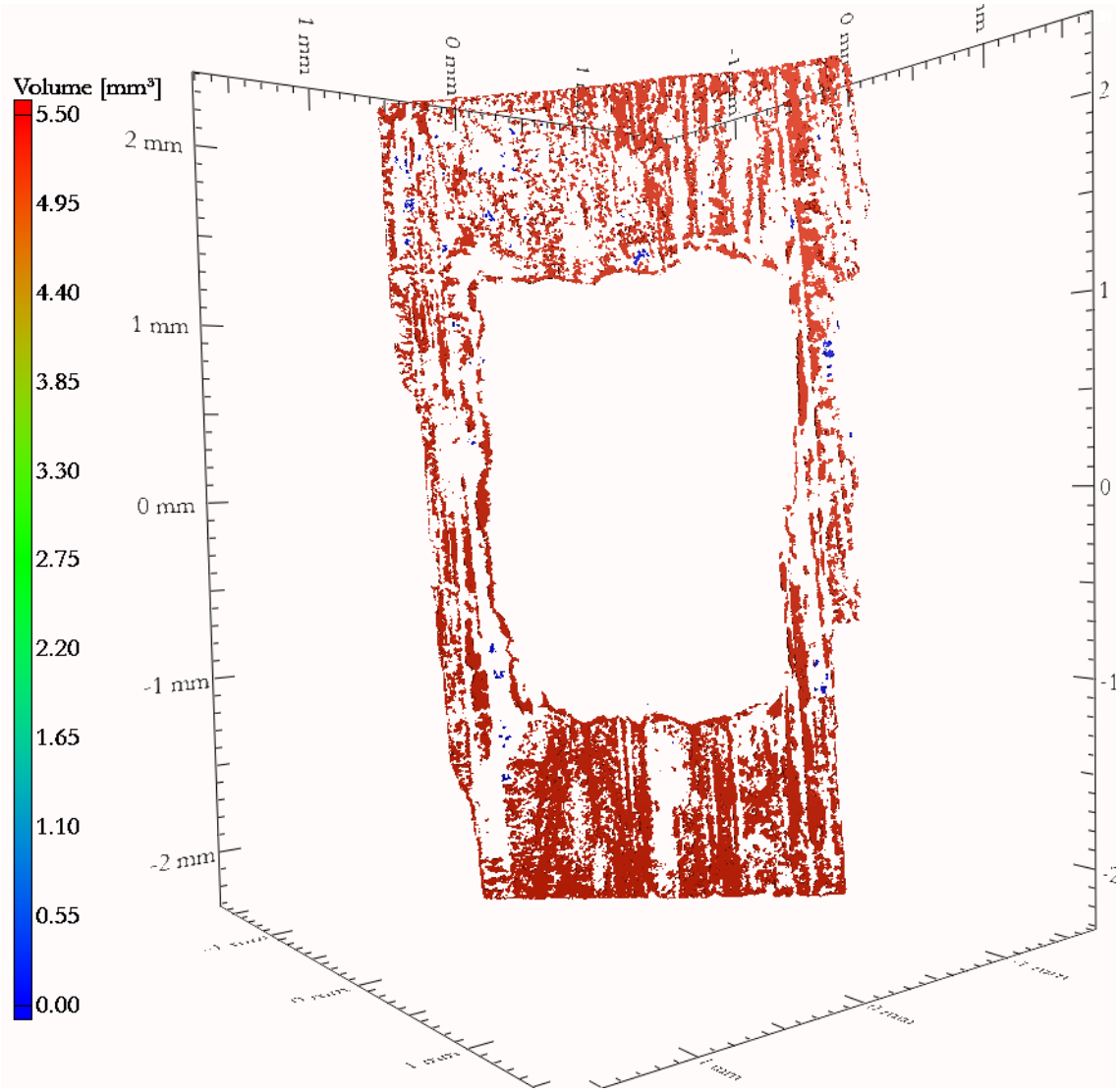

Figure 6.8. Reconstruction of the X-CT dataset of an anhydrite single crystal interacted during 14 days with the carbonate-bearing solution. Results of data segmentation on the whole volume. The colour code scale indicates how much volume is contained in the cavity expressed in mm^3. The reacted area appears in shades of redish and blue. The reacted region is fully occupied by the intermediate subregion. This subregion consists of channels, where porosity concentrates, alternating with poorly porous columns. Both channels and columns are well developed and run parallel to the vertical axis of the image.

The porosity increases with time. This increase regards both, the volume (Figure 6.9a) and the surface of porosity (Figure 6.9b), which is located at the replaced phase. The anomalous value of data corresponding to the sample interacted with the carbonate solution during 3 days results from the presence in its interior of a pre-existing extremely large inclusion.

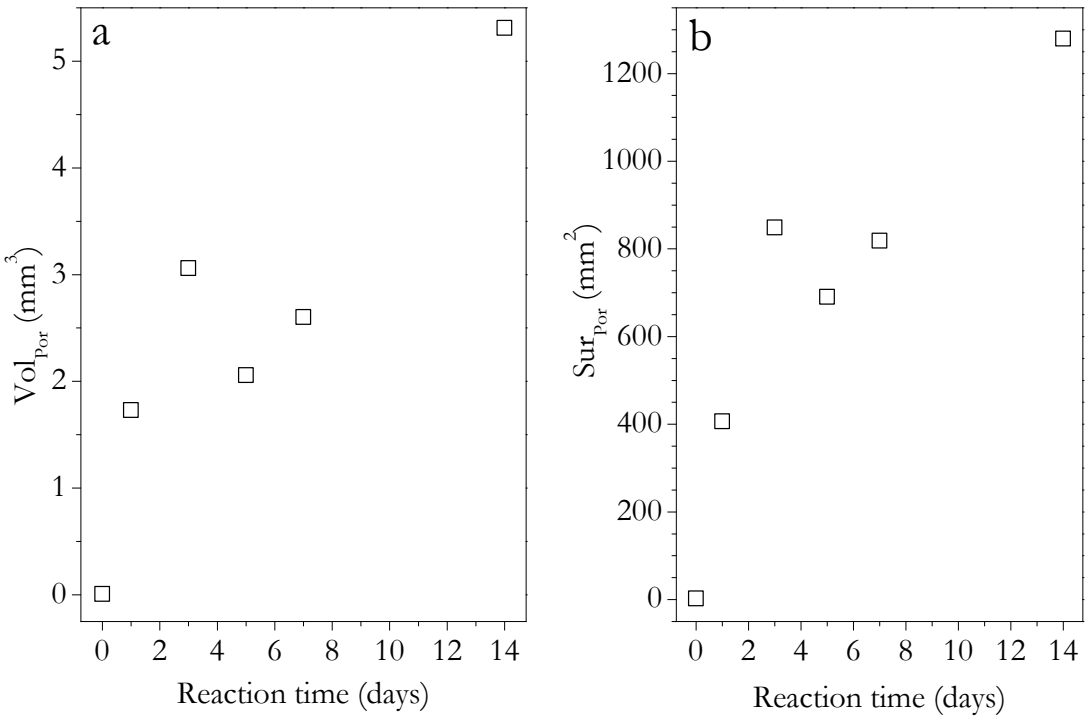

Figure 6.9. Volume (Vol_{Por}) (mm^3) and surface (Sur_{Por}) (mm^2) of porosity in function of reaction time (days). They both increase with reaction time.

Table 6.1 summarizes porosity values and pore sizes in the after 1 day, 3 days, 5 days, 7 days and 14 days interaction between the anhydrite single crystal and a 0.5M Na_2CO_3 aqueous solution. As can be seen, the percentage of porosity volume with respect to the volume of the original anhydrite single crystal follows an increasing during the first 7 days. Afterwards, this percentage decreases, approaching values similar to those corresponding of 3 days of interaction of the anhydrite single crystals with 0.5M Na_2CO_3 aqueous solution. The percentage of porosity volume with respect to the volume of the replaced layer shows a constant value of 32±4%, regardless the interaction time. In contrast, the ratio between the porosity surface and the volume of the replaced layer shows an increasing trend during the first 5 days of the interaction process, followed by a decreasing one afterwards.

Table 6.1. Porosity values of the samples after their interaction with 0.5M carbonate aqueous solution. First, second and third columns correspond to: Vol_{Por}/Vol_{Tot} (%): Porosity volume with respect to volume of the original anhydrite single crystal; $Vol_{Por}/Vol_{RepLayer}$ (%): Porosity volume with respect to the replaced layer volume (%); and Sur_{Por}/Vol_{Rep} (mm^{-1}): porosity surface with respect to the replaced phase volume (mm^{-1}).

Sample	Vol_{Por}/Vol_{Tot} (%)	$Vol_{Por}/Vol_{RepLayer}$ (%)	Sur_{Por}/Vol_{Rep} (mm^{-1})
A05-1d	11.09	33.21	77.87
A05-3d	16.21	28.53	78.98
A05-5d	21.47	30.79	102.18
A05-7d	31.55	36.12	99.22
A05-14d	24.41	33.05	79.27

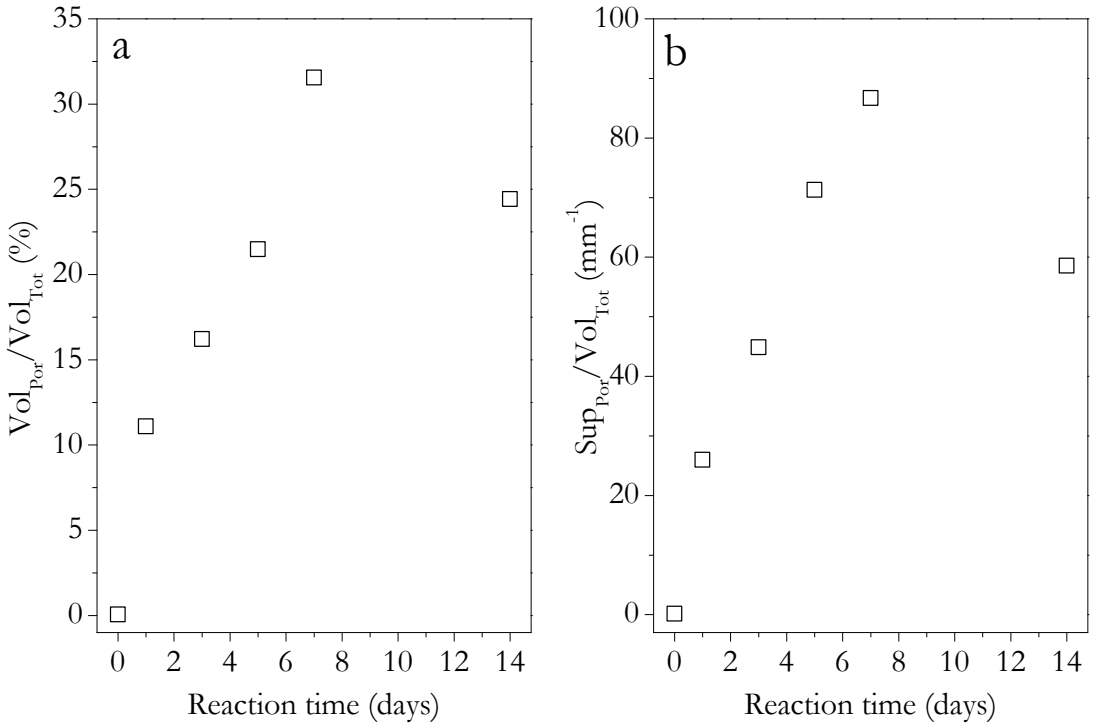

Figure 6.10. Volume of porosity with respect to the total volume (%) (Vol_{Por}/Vol_{Tot} (%)) (a) and porosity surface with respect to the total volume (mm^{-1}) (Vol_{Sur}/Vol_{Tot}) (b). They both increase up to 7 days and decrease until 14 days.

A similar evolution trend as shown by both, the percentage of porosity volume with respect to the volume of the original anhydrite single crystal and the ratio between the porosity surface and the volume of the replaced layer is observed in the

evolution of specific surface area values obtained in BET measurements. The results of the BET analysis of anhydrite interacted samples are summarized in Figure 6.11. As can be seen, the specific surface area increases during the first 10 days of interaction to decrease afterwards.

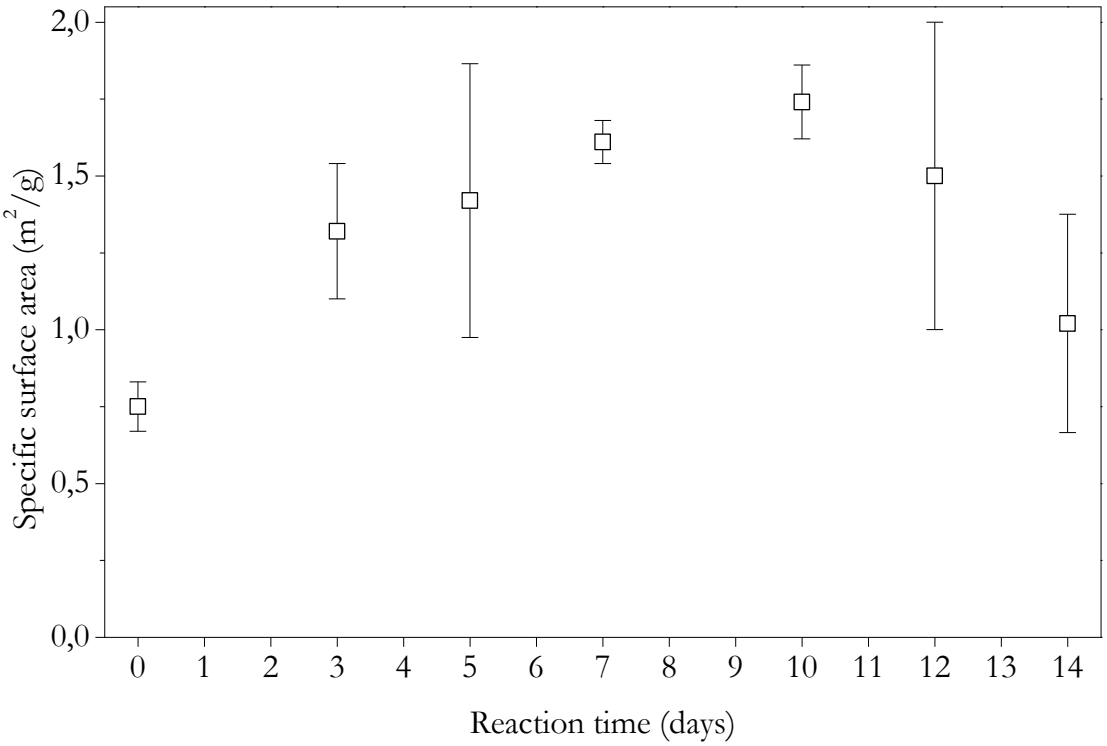

Figure 6.11. BET measurements of the anhydrite single crystals after their interactions with 0.5M carbonate bearing solutions during 0, 3, 5, 7, 10, 12, and 14 days. The specific surface area increases until 10 days, and decrease until 14 days since the beginning of the reaction.

Porosity evolution is characterized by a progressive increase of the volume corresponding to larger pores. This evolution is driven by a progressive widening and lengthening of porosity channels arranged perpendicular to the anhydrite crystal external surfaces, particularly those oriented along anhydrite [001] direction. The lengthening takes place at a much faster rate than the widening, which result in a progressive increase of the length to width ratio of these channels. Thus, the porosity channels evolve from ~7.2 times longer than their width when 24 hours had elapsed since the beginning of the reaction up to ~20 longer than their width

when the interaction with the 0.5M Na_2CO_3 aqueous solution had been taking place during 14 days.

Significant differences in both the advancement of the reaction front and the organization of the porosity generated during the mineral replacement reaction are observed depending on the concentration of the carbonate bearing solution. When less concentrated carbonate-bearing solutions (0.05M Na_2CO_3) are used, the reaction front advances at a much lower rate compared to its advancement rate when the mineral replacement reaction takes place in contact with a a 0.5M Na_2CO_3 aqueous solution. Thus, after 14 days since the beginning of the reaction with a 0.05M Na_2CO_3 aqueous solution, the thickness of the carbonate layer is between 20 and 80 micrometers, while its thickness is between 200 and 900 micrometers when the reaction takes place with a 0.5M Na_2CO_3 aqueous solution. Most importantly regarding the porosity generated during the mineral replacement process, it is not restricted to the carbonate layer but accumulates in a gap that occupies the interface between the carbonate layer and the retreating anhydrite core. The thickness of this gap increases as the reaction proceeds. After 14 days interaction with a 0.05M Na_2CO_3 aqueous solution, it varies between 20 and 70 micrometers, depending on the zone, (Figure 6.12). This gap is not noticeable when the reaction takes place with a 0.5M Na_2CO_3 aqueous solution.

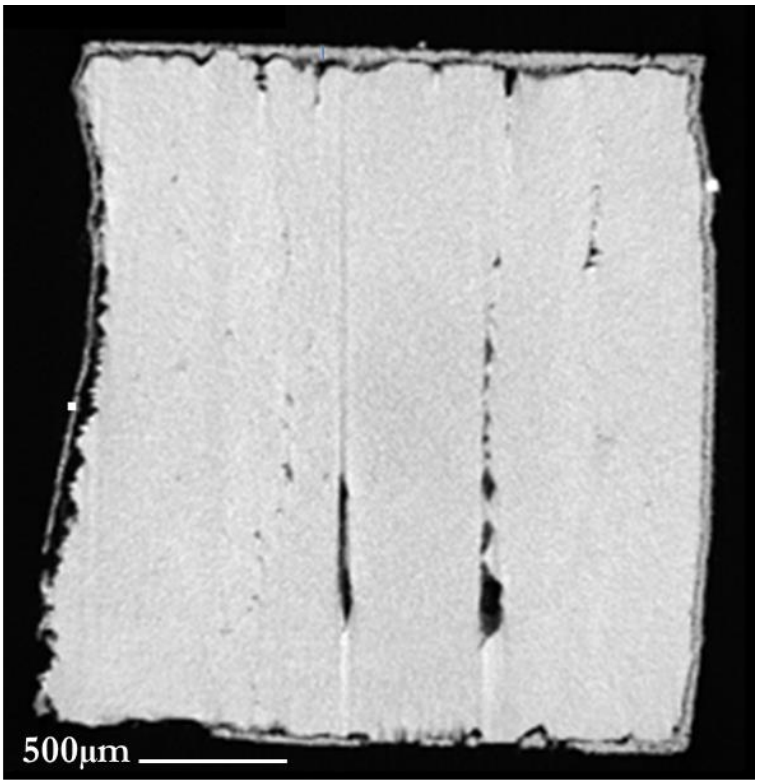

Figure 6.12. Section of an anhydrite crystal after interaction with a 0.05M Na_2CO_3 aqueous solution during 14 days. Note the thin carbonate layer and the wide gap between the former and the anhydrite unreacted core. It is worthwhile paying attention to deep wells that result where the gap meets pre-existent inclusions.

The morphology of the reaction fronts shares similar features. In both cases, they show a complex topography, characterized by numerous short fingers that are arranged perpendicular to the external surfaces of the original crystal (Figure 6.13). As occurs when higher carbonate concentrations are used, fingers perpendicular to {001} surfaces reach larger developments and appear better defined than those that run along [100] and [001] directions.

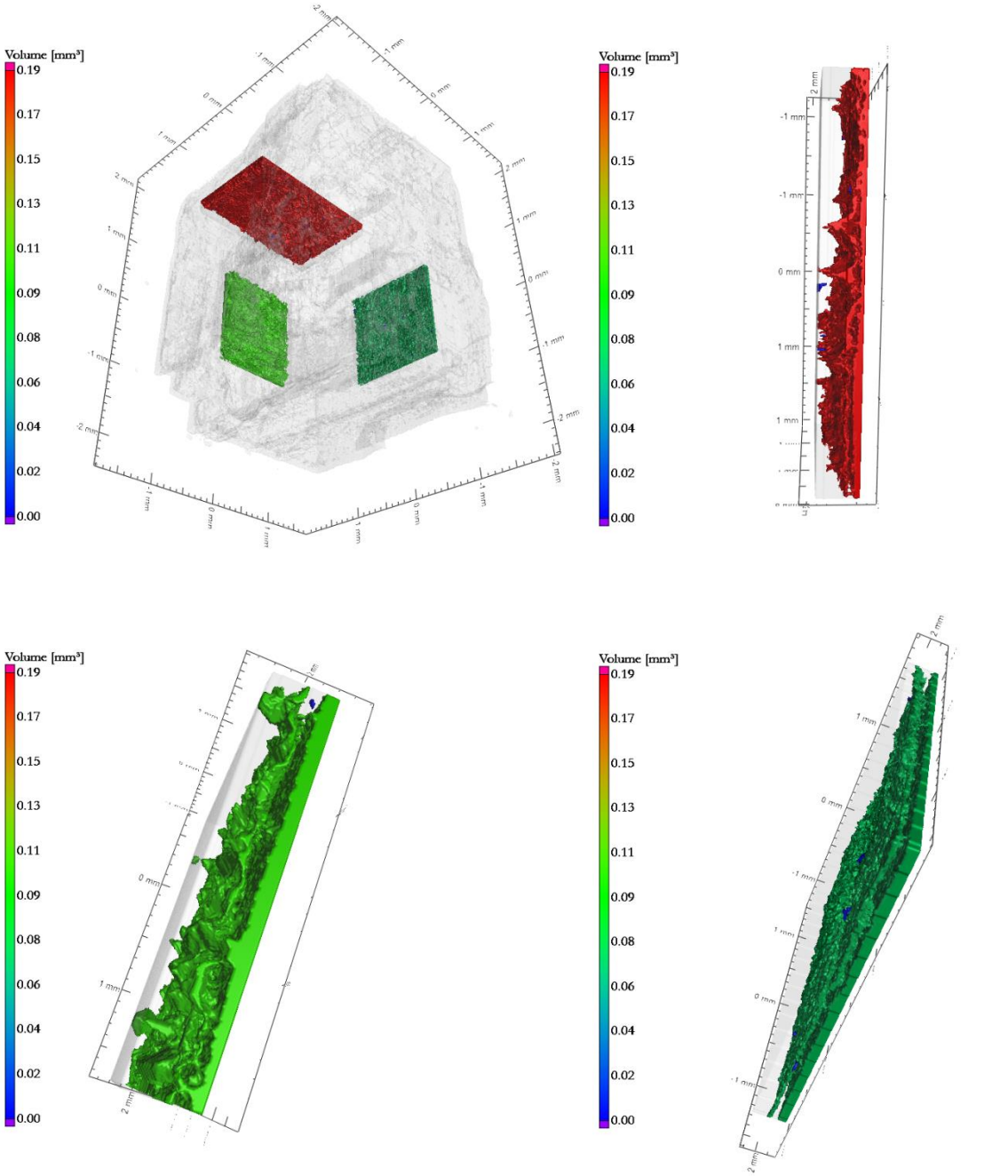

Figure 6.13. Reconstruction of the X-CT dataset of an anhydrite single crystal interacted during 14 days with a 0.05M carbonate-bearing solution. Results of data segmentation on the whole volume. The colour code scale indicates how much volume is contained in the cavity expressed in mm^3. Note the complex topography of the reaction front, characterized by a marked fingering. It is worthwhile to note that the smaller pores are located in a region of the carbonate layer close to the external surface of the original crystal.

6.2. DISCUSSION

As explained in the introduction, the replacement of anhydrite by calcite is an ICDC reaction that involves a negative molar volume change. Since this reaction has a pseudomorphic character, it involves the generation of a large volume of porosity that compensates the volume loss associated to the reaction (~20%), thereby guaranteeing the external shape preservation. The porosity evolution observed results from internal rearrangements that involve the concomitant growth of both, pores and calcite crystals. This porosity initially consists of fine pores that are homogeneously distributed in the reaction region. Initial inhomogeneities in porosity distribution arise from the pre-existence of fluid inclusions within the anhydrite crystal. Since these fluid inclusions are mainly arranged parallel to [001], fluid access to the reaction front is enhanced along this direction. This sums up to the fact that (001) is the fastest dissolving surface of the three main anhydrite cleavage surfaces (Shindo et al., 2010). Therefore, a higher amount of porosity accumulates at the reaction front advancing from this surface compared to the reaction fronts moving inwards from (100) and (010). Inhomogeneities in the distribution of pre-existing fluid inclusions in the anhydrite together with the shape of these inclusions constitute the starting point for the development of the fingering observed in the reaction front. This fingering is further developed because of the positive feedback that arises when small pores formed at the reaction front connect and form pipes. These pipes act as channels where the fluid flow takes place at a faster rate, determining a more efficient dissolution crystallization reaction at their tips (Beaudoin et al., 2018). This mechanism of fingering formation has been described for numerous dissolution related processes, including mineral replacement reactions, karst formation, crystallization in caves, etc. (Beaudoin et al. 2018; Ortoleva et al., 1987; Raufaste et al., 2010; Renard et al., 1998).

We distinguish three regions in the carbonate layer according to porosity distribution, whose development takes place at different stages during the replacement reaction. The almost porosity-free one (Figures 5 and 6; zone 1) is the first to form. It is formed by tiny crystals of calcite with little space between them. The small size of these crystals is the consequence of their formation under the very

high supersaturation conditions existing in the fluid at the interface when the replacement reaction starts. The existence of epitactic relationships between calcite crystals and all the three surfaces bounding the anhydrite crystal further contribute to explain the small size of the pores trapped within zone 1 in the carbonate layer (Cuesta et al., 2018). As soon as a nanometric layer of calcite crystals forms on the anhydrite surface, communication between the bulk carbonate solution and the interface is restricted and only takes place by diffusion through the porosity network in the carbonate layer. Therefore, the fluid phase at the interface does not re-equilibrate with the bulk solution rapidly enough. The epitactic nature of the carbonate layer further contributes to the hindering of the re-equilibration between the fluid at the interface and the bulk solution. As a result, the concentration of dissolved carbonate at the interface steadily drops, while the concentration of dissolved sulfate increases. This determines that the supersaturation at which calcite crystallization takes place also progressively drops as the transformation front moves forward. Moreover, saturation with respect to anhydrite is more easily reached the higher the concentration of sulfate in the fluid phase is (Fernández Díaz et al., 2010). The evolution in the composition of the fluid phase at the interface has two direct consequences: (1) The rate of advancement of the reaction front decreases and, (2) since calcite crystallizes under lower supersaturations, a smaller number of nuclei forms, determining that calcite crystals reach larger sizes than in zone 1, leaving pores between them which are approximately isometric. These larger calcite crystals build up zone 3 in the carbonate layer. As explained above, most pores in zone 3, although larger than those observed in zone 1, are still submicrometric.

As explained in the introduction, porosity has a transient character and it evolves since the very first moment of its formation. In some cases, porosity is only an hour-scale lived, as it occurs during the replacement of some soluble like KBr by KCl (Beaudoin et al., 2018; Putnis et al., 2005; Raufaste et al., 2010). Most often porosity is long-lived and last over millions of years, during which it continuously rearranges as long as its constituent pores are filled by an aqueous phase (Jonas et al., 2013; Jonas et al., 2014; Pedrosa et al., 2016a; Pedrosa et al., 2016b; Putnis 2009;

Putnis 2015). The most obvious driving force for porosity rearrangements is the reduction of pore surface area, which leads to a reduction of the total surface free energy. In the case of the carbonate layer formed during the replacement of anhydrite by calcite pore walls are defined by calcite crystal surfaces. The reduction in pore surface takes place concomitantly to, and as a result, of the reduction in the total surface area of the numerous calcite crystals that build up zone 3. This decrease in crystal surface area occurs through the growth of larger crystals at expenses of the smaller calcite crystals via a dissolution-crystallization process. This process leads to the coalescence of growing crystals and ends up with the disappearance of tiny calcite crystals. The presence of pre-existing-fluid-inclusion-related inhomogeneities in the carbonate layer provides a starting pattern of larger and smaller pores and crystals. The dissolution-crystallization process that leads to the coalescence of large calcite crystals reproduces and coarsens this pattern. As a result, coalescent calcite crystals joint to form porosity-free columns, while the dissolution of tiny crystals leads to the formation of almost crystal-free channels that run parallel to the calcite columns. Both, calcite columns and porosity channels arrange in an alternating pattern, defining zone 2. As explained above, this zone develops later than zone 3 and mainly grows at its expense. The formation of zone 2 overlaps the development of zone 3. A possible mechanism that facilitates the coarsening of porosity channels has been described by Beaudoin et al., (2018) who explains the coarsening of fingers during the replacement of KBr by KCl as linked to the elongation of these fingers. When fingers become too long reactant delivery to their tips become inefficient, which results in the chemical gradient at the wall of the fingers overcoming the chemical gradient at their tips.

Chemical factors may play a complementary role to the reduction of total surface free energy as the driving force for porosity distribution and organization rearrangements in the carbonate layer during anhydrite replacement by calcite. Indeed, EDX analyses of these carbonate layer show that it is chemically inhomogeneous and small differences can be observed regarding the concentration of minor elements between areas constituted by calcite small crystals (zone 3) and those corresponding to poorly porous calcite columns in zone 2. These differences

refer to their S, Sr, Na content, which tends to be slightly higher in crystals constituting zone 3. Since the incorporation of these elements into calcite would increase its solubility with respect to that of pure calcite, the dissolution-crystallization process that leads to the coalescence of calcite crystals and the coarsening of porosity is accompanied and, in part, driven by a chemical change that involves the reduction of the amount of impurities incorporated into calcite structure.

As explained in the results section, a main difference in the organization of porosity in calcite pseudomorphs after anhydrite formed as a result of reaction of single crystals of the latter phase with differently concentrated carbonate-bearing aqueous solutions is the existence or absence of a large gap a the interface between the replaced layer and the unreacted anhydrite core. The presence of this gap in pseudomorphs formed in contact with 0.05M Na_2CO_3 aqueous solution is the consequence of an inefficient re-equilibration between the fluid phase at the interface and the bulk solution, which leads to a progressive decrease of the concentration of carbonate ions in the former. As a result, the amount of anhydrite that must dissolve for the fluid at the interface to reach a supersaturation high enough to allow calcite crystallization to proceed becomes progressively larger. The direct consequence is an increase in the negative volume balance resulting from the dissolution-crystallization process. This extra negative volume change does not accumulate in the carbonate layer since it corresponds to anhydrite dissolution that is not concomitant to calcite precipitation, explaining the development of the gap. The influence of the concentration of carbonate in the aqueous phase in the porosity generation and evolution as well as in other characteristics of the pseudomorphs and the carbonation process are presented and further discussed in chapter 7.

7. INFLUENCE OF THE FLUID PHASE COMPOSITION ON REACTION PATHWAYS AND TEXTURAL FEATURES DURING THE PSEUDOMORPHIC CARBONATION OF ANHYDRITE

7. INFLUENCE OF THE FLUID PHASE COMPOSITION ON REACTION PATHWAYS AND TEXTURAL FEATURES DURING THE PSEUDOMORPHIC CARBONATION OF ANHYDRITE

The interaction between carbonate-bearing aqueous solutions and anhydrite single crystals leads to the development of dissolution-crystallization reactions that result in the formation of $CaCO_3$ pseudomorphs. Interaction experiments using aqueous solutions with different carbonate concentrations show that this parameter strongly influences the kinetics of the carbonation reaction, the pathway through which this reaction takes place and numerous textural aspects of the resulting $CaCO_3$ pseudomorphs.

7.1. RESULTS

7.1.1. Influence of the carbonate concentration of the aqueous solution in the kinetics of anhydrite carbonation

The replacement of anhydrite single crystals by calcium carbonate occurs at much faster rate the higher the concentration of carbonate in the aqueous solution is. Thus, when this concentration is 0.5M, the thickness of the carbonate layer that surrounds the unreacted anhydrite core is around 50-200 micrometers after 24 hours interaction between the original anhydrite crystal and the fluid phase. This thickness reaches 200-800 micrometers after 5 days and is 300-1600 micrometers after 14 days. In contrast, when the carbonate concentration in the solution is 0.05M, the carbonation reaction is restricted to a very thin rim that surrounds the unreacted anhydrite core. The thickness of this rim only reaches 10-70 micrometers after 3 days interaction between the crystal and the 0.05 M aqueous solution and is as thin as 20-80 micrometers after 14 days. SEM micrographs in Figure 7.1 illustrate the different thickness of the carbonate layer formed as a result of the interaction of anhydrite single crystals after interaction with a 0.5M (Figure 7.1a) and a 0.05M (Figure 7.1b) Na_2CO_3 aqueous solution during 3 days.

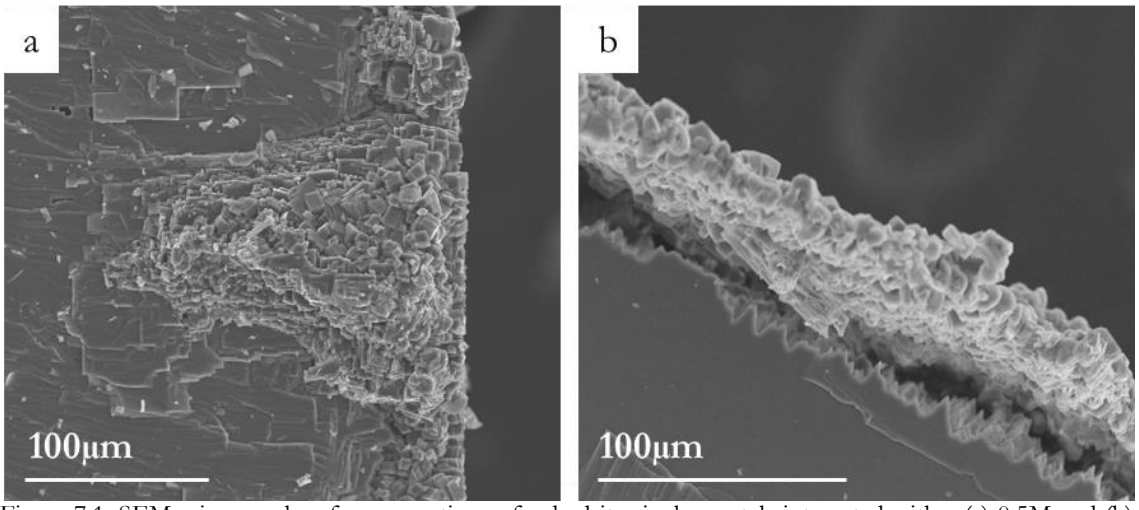

Figure 7.1. SEM micrographs of cross-sections of anhydrite single crystals interacted with a (a) 0.5M and (b) 0.05M Na_2CO_3 aqueous solution.

It is important to note that regardless the concentration of the carbonate concentration in the solution, differences in the kinetics of the carbonation reaction are observed between the different anhydrite cleavage surfaces {100}, {010} and {001}. While this reaction takes a place at a similar rate on {100} and {010}, its kinetics is much faster on {001}, as can be concluded from the much larger thickness of the carbonate layer that forms on this surface after given interaction times. Figure 7.2 illustrates this difference in thickness for anhydrite crystals that have been in contact with 0.05M Na_2CO_3 aqueous solutions during 3 days. While the carbonate layer formed on {010} surface is ~20 µm thick, it has a thickness of ~70 µm on {001} (Figure 7.2a). Its thickness on {100} is ~25 µm (Figure 7.2b).

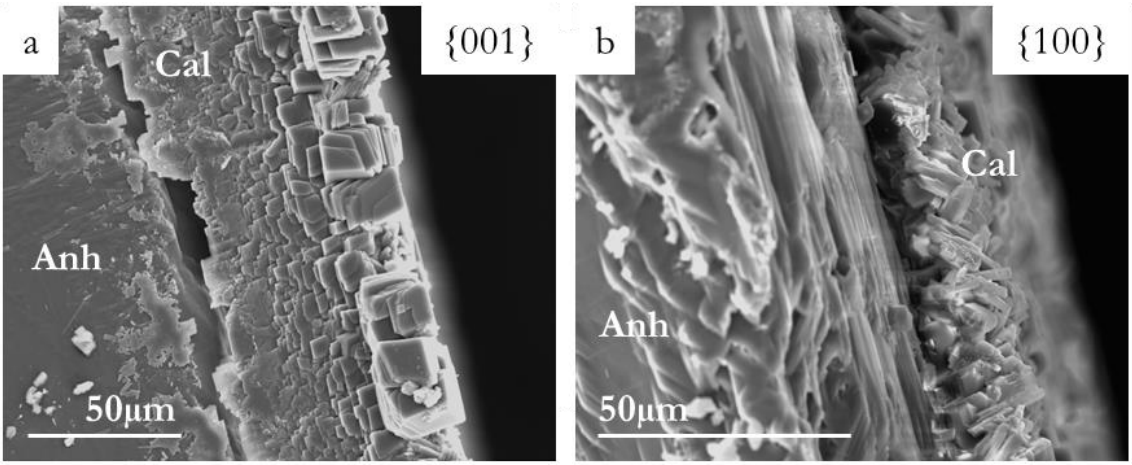

Figure 7.2. SEM micrographs of anhydrite single crystals after interaction with a 0.05M Na_2CO_3 aqueous solution during 3 days. The crystals have been cut parallel to {001} and {100} surfaces, respectively.

7.1.2. Influence of the carbonate concentration of the aqueous solution in the carbonation reaction pathway

Observations conducted on the three cleavage surfaces that bound the anhydrite single crystals used in the interaction experiments evidence that when the concentration of carbonate in the aqueous solution is high (0.5M), the carbonation reaction involves the formation of the stable calcium carbonate polymorph calcite in all the faces, with only trace amounts of vaterite forming on {001} surfaces. This vaterite appears as aggregates that rapidly dissolve to transform into calcite (Figure 5.1c). In contrast, during the interaction of anhydrite single crystals with 0.05M Na_2CO_3 aqueous solutions the reaction pathway followed by the carbonation reaction is significantly more complex. This reaction pathway is characterized by the simultaneous formation of calcite single crystals and vaterite aggregates on all anhydrite cleavage surfaces soon after anhydrite crystals are in contact with the carbonate aqueous solution. Although calcite is the dominant $CaCO_3$ phase in all the cases, the formation of both polymorphs on anhydrite {100}, {010} and {001} after only 1 hour interaction with the 0.05M Na_2CO_3 aqueous solution is apparent in the SEM micrographs shown in Figure 7.3.

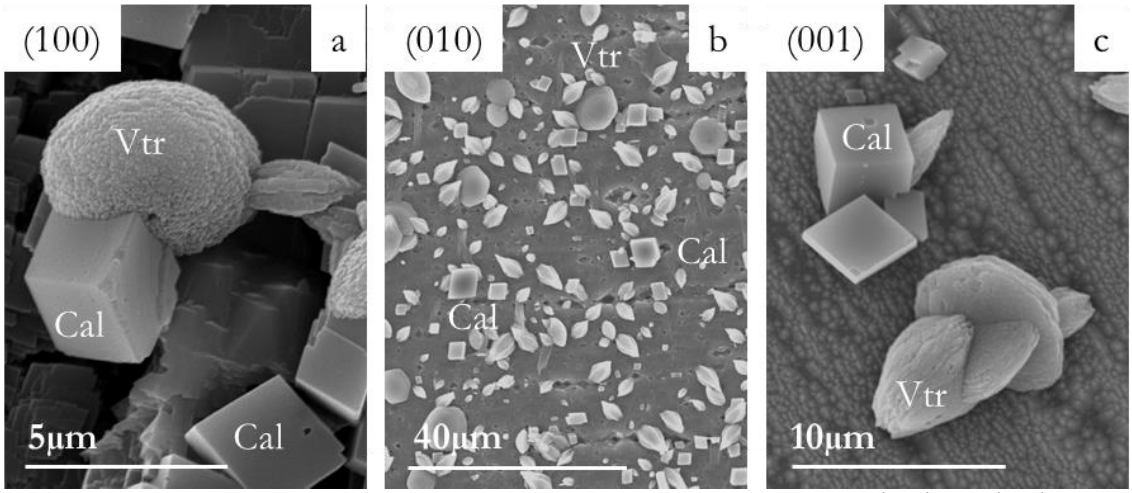

Figure 7.3. SEM micrographs of surfaces of anhydrite single crystals parallel to (a) {100}, (b) {010} and (c) {001} planes after interaction with a 0.05M Na_2CO_3 aqueous solution during 1 hour.

Furthermore, as the interaction progresses, the formation of a new phase, the $CaCO_3$ polymorph aragonite is observed. Crystals of this phase are first observed

after few hours of interaction on anhydrite {010}. Althought aragonite crystals appear later on {100} and {010} than on {001}, after 1 day interaction this phase is almost as abundant as calcite on these two other faces (Figure 7.4).

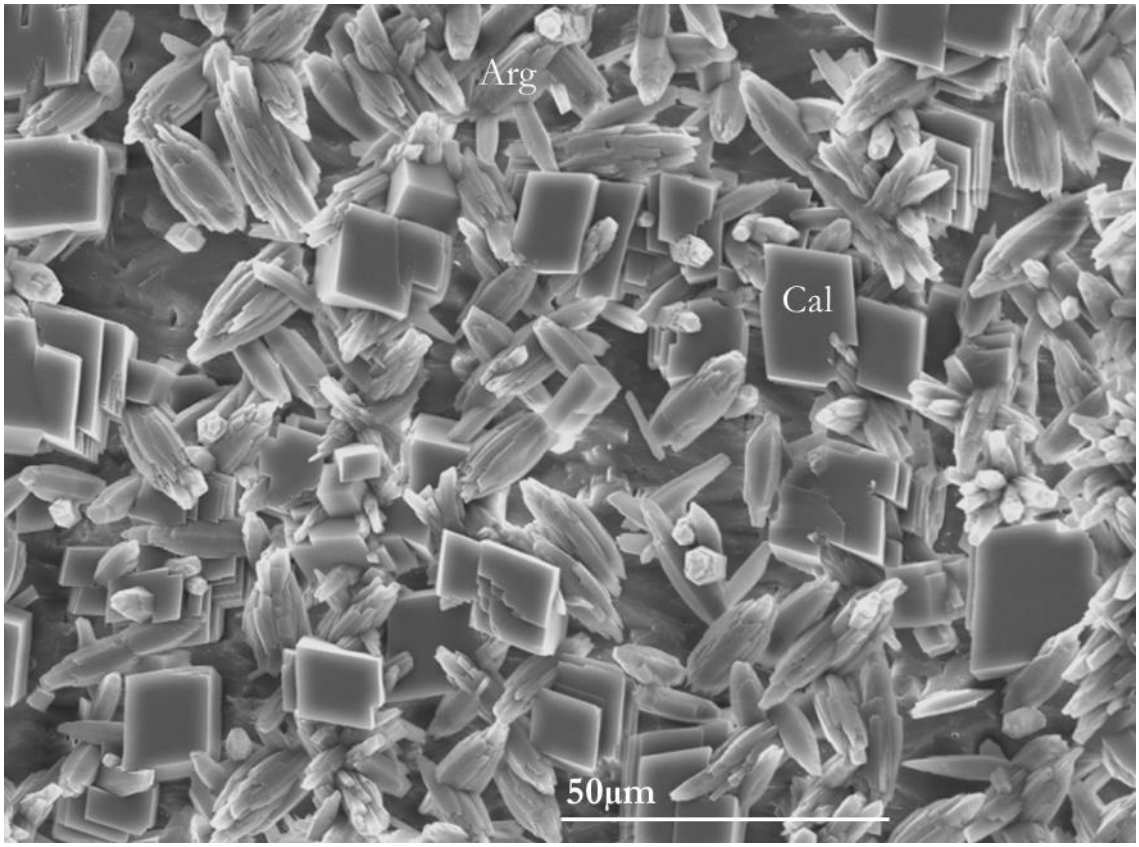

Figure 7.4. SEM micrographs of the {100} surface of an anhydrite single crystal that has been in contact with a 0.05M Na_2CO_3 aqueous solution during 24 hours. Note the presence of calcite single crystals and aragonite elongated crystals growing on this surface and the similar abundance of both phases. The pseudohexagonal section characteristic of aragonite twins can be observed on some of the elongated crystals.

It is interesting to note that, while vaterite crystal aggregates disappear from the surface of anhydrite crystals after 1 day interaction with 0.05M Na_2CO_3 aqueous solution, aragonite crystals remain as main components of the carbonate layer even after interaction periods as long as 7 days (Figure 7.5). It is also striking the morphological that can be observed in calcite crystals, whose habit is initially defined by cleavage rhombohedron {10$\bar{1}$4} but, as time passes by, either becomes elongated along the *c*-axis and develops new curved surfaces that seem to belong to the *c*-axis zone (Figure 7.5a) or develops numerous growth steps and show some signs of dissolution on {10$\bar{1}$4} (Figure 7.5b).

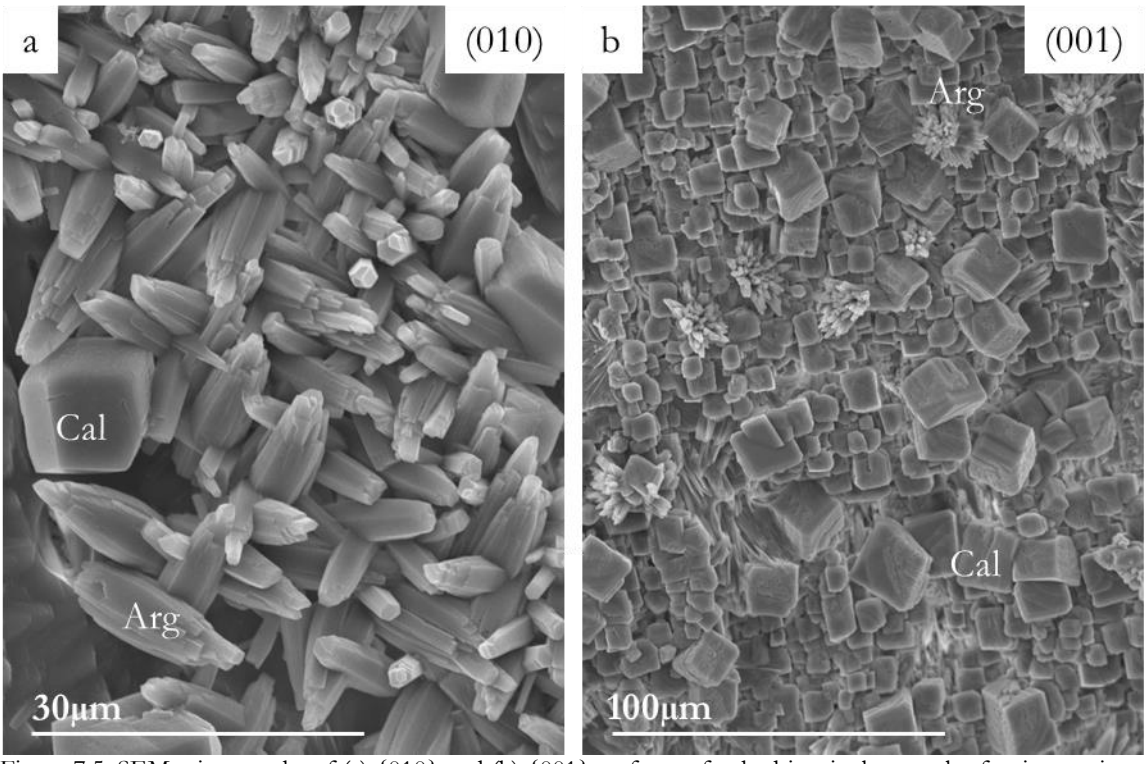

Figure 7.5. SEM micrographs of (a) {010} and (b) {001} surfaces of anhydrite single crystals after interaction with a 0.05M Na_2CO_3 aqueous solution during 7 days. Note the presence of calcite and aragonite growing on both surfaces. Calcite crystals show a habit that is bound by the {10$\bar{1}$4} rhombohedron (b) together with curved surfaced that seem to belong to the c-axis zone (a). Aragonite appears as elongated crystals that show the typical pseudohexagonal section of aragonite twin (a) or as sheaf-like aggregates that consist of needle-like crystals in radial arrangement (b).

Finally, it is interesting to note that both calcite and aragonite crystals grow oriented on anhydrite surfaces, as can clearly be seen in Figure 7.6. Furthermore, aragonite nucleates directly on calcite crystals.

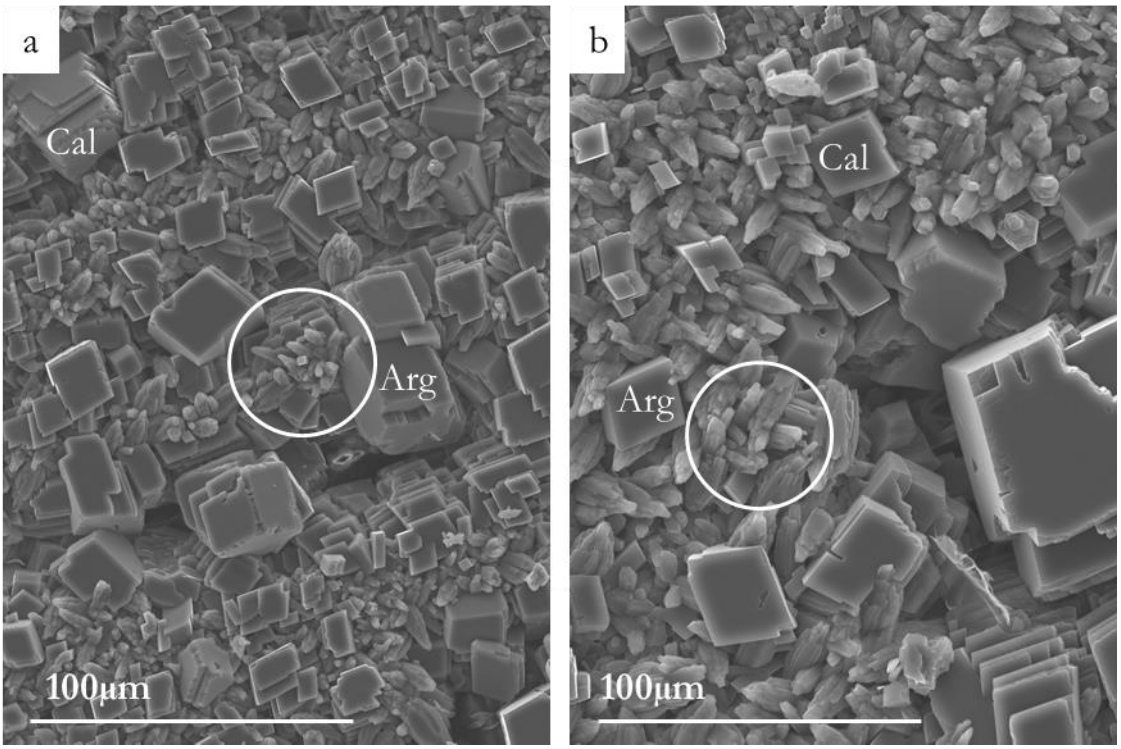

Figure 7.6. SEM micrographs of anhydrite single crystal surfaces after interaction with a 0.05M Na_2CO_3 aqueous solution during 5 days. Note the presence of calcite and aragonite crystals growing on these surfaces. The white circle in (a) highlights the growth of aragonite directly on the surface of calcite crystals. The oriented growth of both aragonite and calcite crystals can is evidenced in (b).

The amount of aragonite in the carbonate layer continues decreasing after 7 days interaction of anhydrite single crystals with 0.05M carbonate solutions. This decrease is concomitant to the increase of calcite in the carbonate layer. However, it is worthwhile to note that significant amounts of aragonite are still present in the carbonate layer after 14 days interaction, as can be seen in Figure 7.7. It is also important to note that calcite crystals, which are highly predominant in the carbonate layer, show morphologies in which edges and steps on $\{10\bar{1}4\}$ rhombohedron faces appear strongly lobbed.

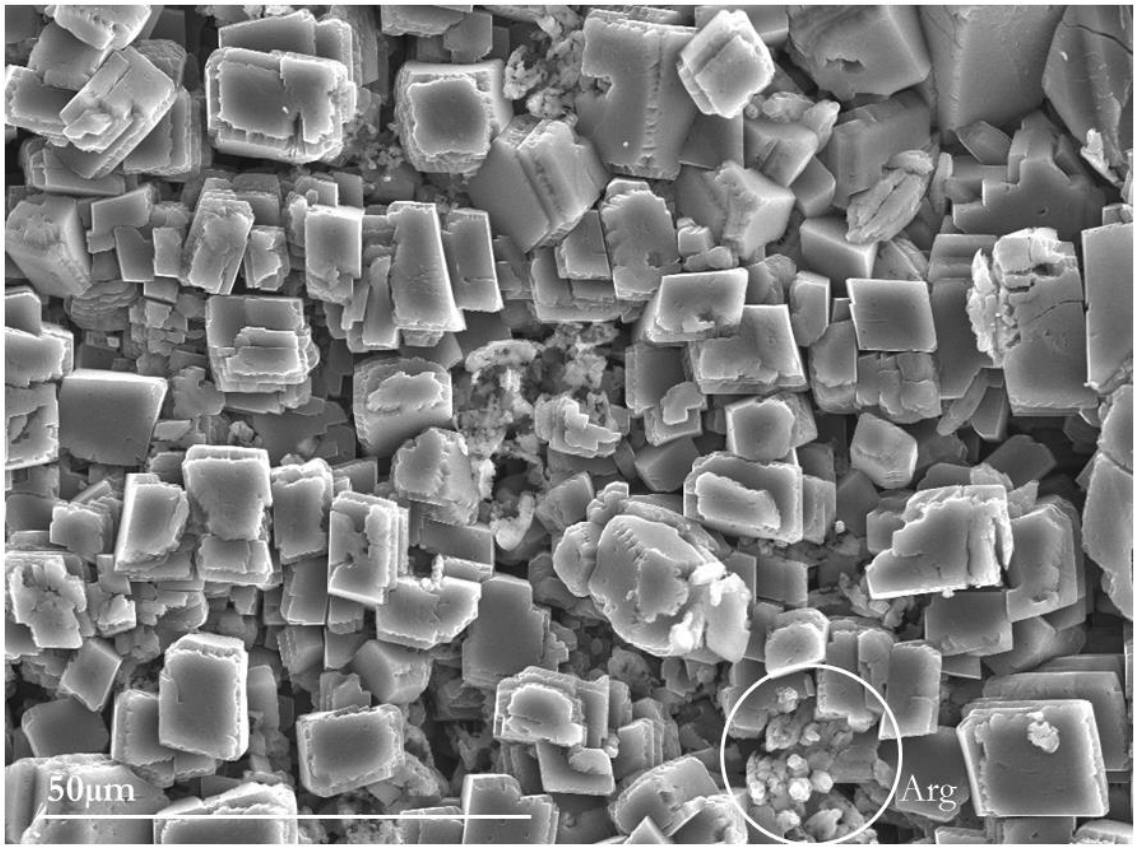

Figure 7.7. SEM micrograph of an anhydrite surface after interaction with a 0.05M Na_2CO_3 aqueous solution during 14 days. Note that calcite is the main $CaCO_3$ phase present, although very minor amounts of aragonite can also be seen. Calcite crystals shown are bound by the {10$\bar{1}$4} rhombohedron faces that show lobbed edges and steps.

7.1.3. Influence of the carbonate concentration of the aqueous solution in the textural characteristics of calcite pseudomorphs after anhydrite.

As has been explained in previous sections, the carbonation of anhydrite single crystal leads to the formation of pseudomorphs of $CaCO_3$. As can be seen in Figure 7.8, the external shape of anhydrite single crystals is accurately reproduced. This faithful reproduction includes the characteristics of bounding faces, edges and cleavage steps and extends to fine details of the surface as the striations that are typical feature of anhydrite {001} surfaces (Figure 7.8c).

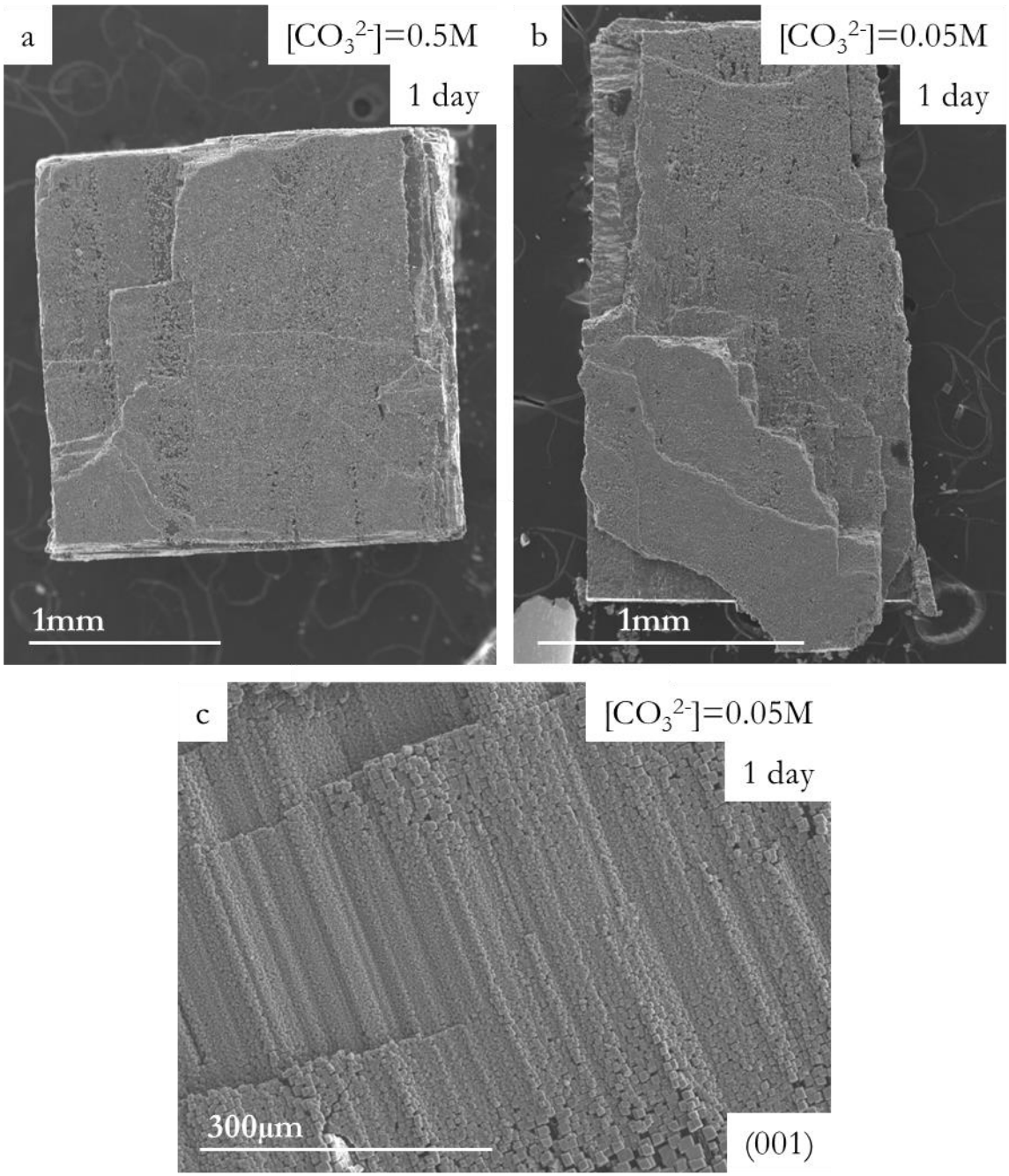

Figure 7.8. SEM micrographs of anhydrite single crystals after interaction with a Na_2CO_3 aqueous solution during 1 day: (a) 0.5 M; (b) 0.05M; (c) {001} surface of an anhydrite single crystal after interaction with a 0.05M Na_2CO_3 aqueous solution. The anhydrite crystals are partially replaced by $CaCO_3$. Note the perfect reproduction of the external shape of anhydrite crystals, including details of the surfaces like cleavage steps and striations characteristics.

Although $CaCO_3$ pseudomorphs always form regardless of the concentration of the carbonate aqueous solution that interacts with the primary anhydrite single crystal, the scale of the pseudomorphism is strongly affected by this parameter. This results in a much accurate reproduction of anhydrite surface characteristics when

the interaction takes place with more highly concentrated carbonate-bearing aqueous solutions. A detailed inspection of $CaCO_3$ pseudomorphs formed in contact with carbonate-bearing aqueous with different concentrations evidences that the size of the crystals building up the external rim of the carbonate layer anhydrite crystal is smaller the more concentrated the aqueous solution is, as can be seen in Figure 7.9. Thus, the average size of calcite crystals in this external rim is smaller than 5 micrometers when the carbonation takes place in contact with 0.5 Na_2CO_3 aqueous solution, while approaches 20 micrometers when the concentration of the solution is 0.05M.

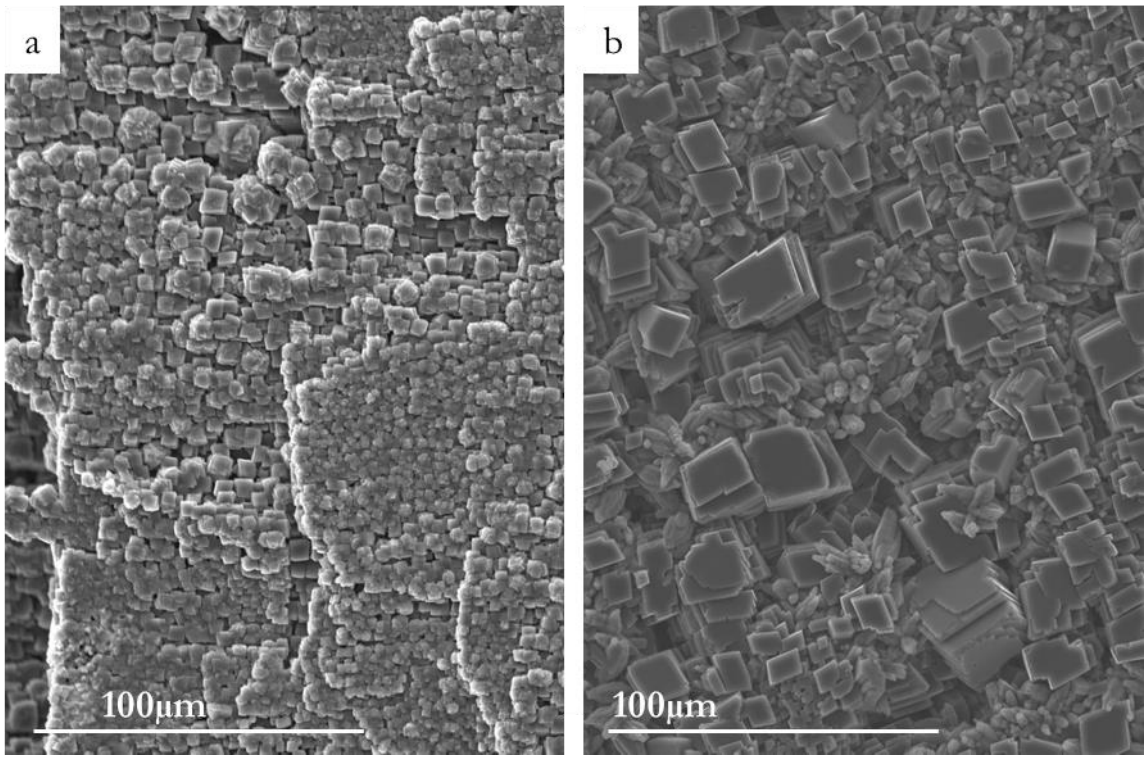

Figure 7.9. SEM micrographs of the surface of anhydrite single crystals after interaction with a (a) 0.5 M and a (b) 0.05M Na_2CO_3 aqueous solution during 5 days. Note the different sizes of the calcite crystals that constitute the external rim of the carbonate layer.

A main distinctive feature of $CaCO_3$ pseudomorphs formed after anhydrite interaction with 0.05M Na_2CO_3 aqueous solutions is their fragility. On handling them, the carbonate layer easily separates from the unreacted anhydrite core and breaks into pieces. This fragility contrast with the characteristics $CaCO_3$ pseudomorphs formed after reaction with 0.5M Na_2CO_3 aqueous solutions. In this

case, the adhesion between the carbonate layer and the anhydrite core is high at any stage of the mineral replacement process. To explore the reasons underlying this significant difference in fragility between $CaCO_3$ pseudomorphs formed in contact with carbonate aqueous solutions of different concentrations, the characteristics of the porosity contained within these pseudomorphs were in depth studied by comparing their CT scans. Figure 7.10 shows CT scans reconstructions obtained for a $CaCO_3$ pseudomorph formed after 24 hours interaction of an anhydrite single crystal with a 0.5M carbonate aqueous solution. In this reconstruction the interconnected porosity in the $CaCO_3$ pseudomorph appears color coded in green. As is apparent, all this porosity is contained within the carbonate layer, which appears with in different shades of gray.

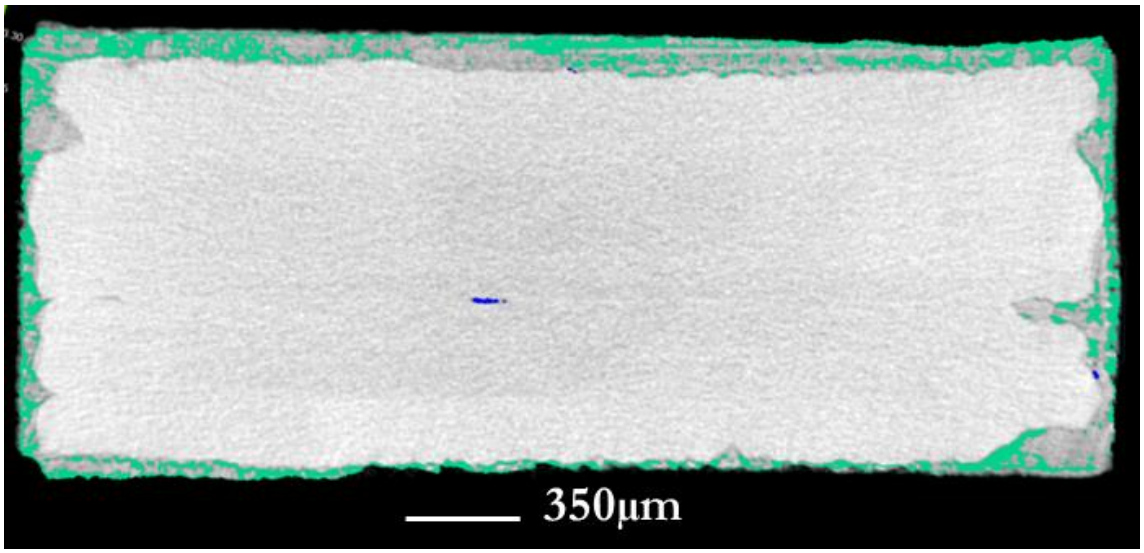

Figure 7.10. Reconstruction of the X-CT dataset of an anhydrite single crystal interacted during 1 day with the carbonate-bearing solution (0.5M Na_2CO_3). The interconnected porosity appears in green.

This carbonate layer is continuous and appears attached to the anhydrite unreacted core. This attachment between the carbonate layer and anhydrite core is maintained as the carbonate reaction progresses in contact with a 0.5M Na_2CO_3 aqueous solution, as is illustrated by the CT-reconstruction in Figure 7.11. This crystal corresponds to an anhydrite single crystal that has remained in contact the solution during 14 days. It is worthwhile to note the arrangement of the generated

porosity in columns perpendicular to one of the surfaces that bounded the original anhydrite crystal.

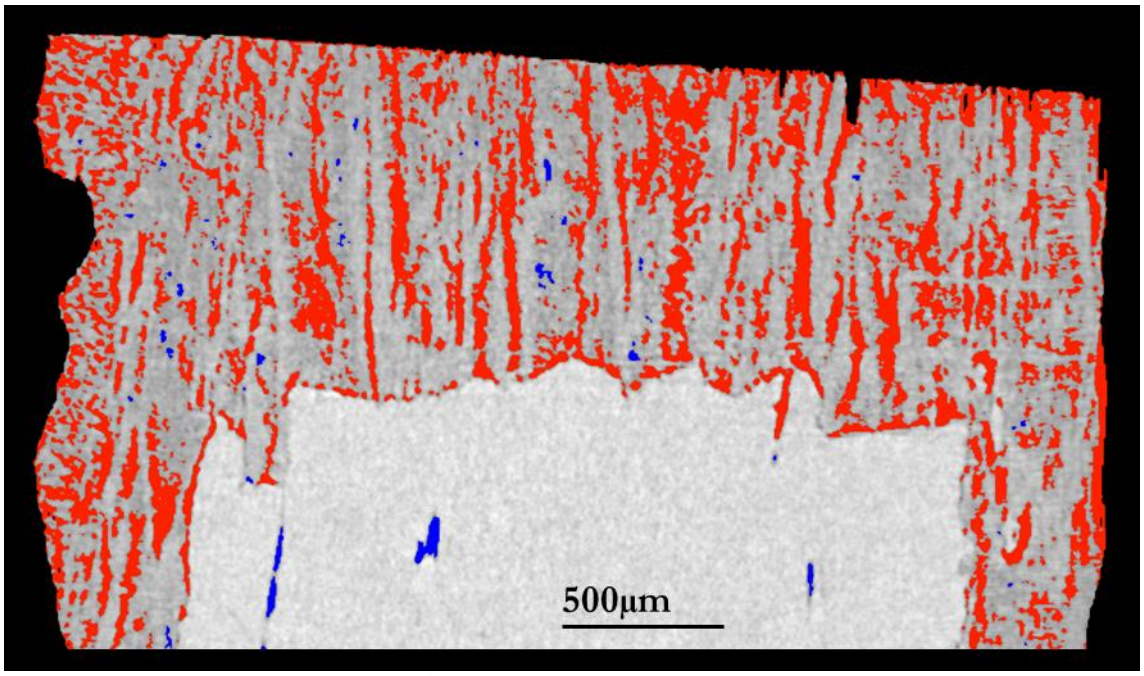

Figure 7.11. Reconstruction of the X-CT dataset of an anhydrite single crystal interacted during 14 days with the carbonate-bearing solution (0.5M Na_2CO_3). The interconnected porosity appears in red. Note the porosity within the carbonate layer arranged in columns that appear perpendicular to one of the external faces of the original anhydrite crystal.

The consistency of the carbonate layer in $CaCO_3$ pseudomorph formed after interaction of an anhydrite single crystal with 0.5M carbonate aqueous solutions contrast with the characteristics of this layer in pseudomorphs formed after reaction with a less concentrated solution. An example of the characteristics of both the carbonate layer and the distribution of porosity generated during the interaction of an anhydrite single crystal with a 0.05M Na_2CO_3 aqueous solution is shown in Figure 7.12. In the images, the generated porosity is marked in red and green. Although in this case the carbonate layer also appears quite continuous, most of the porosity generated appears concentrated in a gap that effectively separates the carbonate layer from the unreacted anhydrite core along its whole surface. The existence of this gap prevents the attachment of the carbonate layer to the anhydrite core.

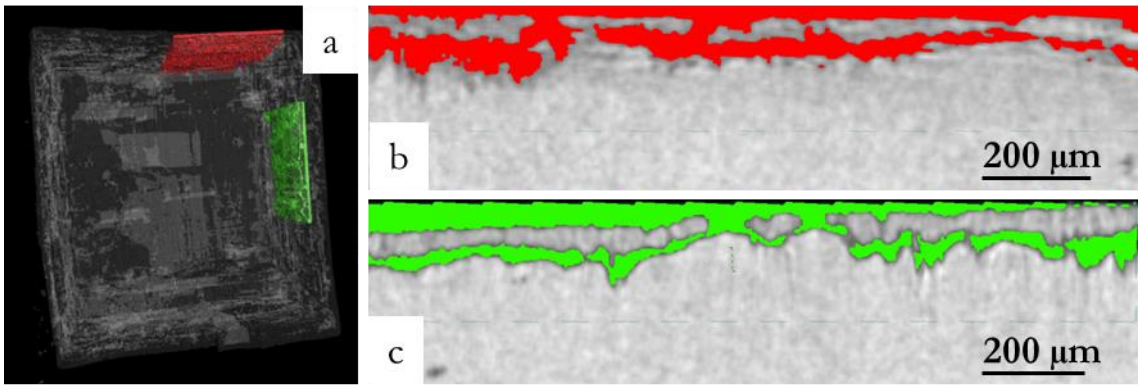

Figure 7.12. Reconstruction of the X-CT dataset of an anhydrite single crystal interacted during 1 day with the carbonate-bearing solution (0.05M Na_2CO_3). (a) Location of the regions of then anhydrite crystals explored (marked in red and green). (b, c) Detail of the interconnected porosity in red (b) and green (b). Note that most of the porosity concentrates in a gap that effectively separates the carbonate layer from the unreacted anhydrite core.

7.2. DISCUSSION

7.2.1. Kinetics of anhydrite carbonation

As it has been explained in previous chapters, the carbonation of anhydrite crystals shows the typical characteristics of ICDC. It involves the development of one or more solvent-mediated transformations (Cardew and Davey, 1985) that initiates as soon as the anhydrite crystal is in contact with a carbonate-bearing aqueous solution. Because this aqueous solution is undersaturated with respect to anhydrite, this phase starts to dissolve, releasing Ca^{2+} and SO_4^{2-} ions to the aqueous solution. Considering the solution volume/anhydrite crystal weight ratio, the concentration of CO_3^{2-} ions in the two carbonate bearing solutions is high enough to guarantee that the whole anhydrite crystal can be replaced by $CaCO_3$ phases. Furthermore, under the unstirred conditions in the experiments, when the dissolution-crystallization process starts, the concentration of Ca^{2+} and SO_4^{2-} ions will be much higher in the proximity of the anhydrite dissolving crystal than in the bulk solution. This means that, at this point, the supersaturation of the aqueous solution layer in direct contact with anhydrite surface with respect to $CaCO_3$ phases will be extremely high. This leads to the $CaCO_3$ phases nucleation on anhydrite surface. As soon as nucleation occurs, the solution will become depleted in Ca^{2+}, which will further promote the dissolution of anhydrite, initiating the dissolution-

crystallization loop (Putnis 2005; Putnis 2009; Putnis 2015; Putnis and Putnis, 2007; Ruiz-Agudo et al., 2014). Since any nucleation process has an energy barrier associated, the formation of $CaCO_3$ phases will occur earlier the faster this barrier can be overcome or, in other words, the higher the supersaturation rate is in the system (Putnis et al., 1995). There is a direct relationship between supersaturation rate and concentration (Prieto et al., 1993; Prieto et al., 1994; Putnis et al., 1995). Consequently, $CaCO_3$ nucleation will take place earlier when the initial carbonate concentration in the aqueous solution in contact with the anhydrite crystal is higher. In the present case, this is in contact with the 0.5M solution. Similarly, once the aqueous solution at the interface becomes depleted of Ca^{2+} ions due to $CaCO_3$ nucleation and growth, for the aqueous solution to reach again a supersaturation high enough to allow further growth of $CaCO_3$, it will be required that a higher amount of anhydrite dissolves when the concentration of carbonate in the aqueous solution is lower, this is 0.05M. Both factors, the larger supersaturation rate that is reached in a system where the initial concentration of carbonate is higher and the higher amount of anhydrite that needs to dissolve to reach an equal supersaturation when the concentration of carbonate is lower explains the much faster kinetics of anhydrite carbonation in contact with an carbonate aqueous solution with a concentration of 0.5M than with a concentration of 0.05M. Furthermore, since Ca^{2+} and CO_3^{2-} ions are both consumed during the growth of $CaCO_3$ phases, the concentration of CO_3^{2-} ions in the system will continuously drop as the carbonation reaction proceeds. This drop will be much more significant in the volume of aqueous solution located at the interface since mobility in the system is restricted and re-equilibration with the bulk solution can only take place by ion diffusion through the porosity network within the carbonate layer. The fact that a larger concentration gradient between the solution at the interface and the bulk together with the much larger amount of $CaCO_3$ that can precipitate before the solution at the interface becomes significantly depleted of CO_3^{2-} ions when the initial concentration of carbonate in the aqueous solution is higher, both further explain that the carbonation reaction can progress longer and at faster rate when the anhydrite crystal is in contact with a 0.5M carbonate solution. Indeed, in the case of a low initial concentration of carbonate, both the slower diffusion through the

porosity network and the earlier depletion of CO_3^{2-} ions in the solution at the interface can eventually lead to the complete stoppage of the carbonation reaction when in takes place in contact with a 0.05M carbonate solution, explaining that even after 14 days interaction, the maximum thickness of the carbonate layer around the unreacted anhydrite core hardly reaches 100 micrometers.

It is interesting the fact that the kinetics of anhydrite carbonation is surface-related. As has been pointed out, the carbonate layer is always significantly thicker on {001}, regardless the interaction time and the concentration of the solution, while it is similarly thick on both, {100} and {010}. These differences in the rate of advancement of the reaction front can be related to differences in the dissolution rate of the different surfaces. Indeed, Shindo et al. (2010) conducted in situ AFM observation of anhydrite dissolution in pure water. These authors found that dissolution occurs much faster on {001}, while the dissolution rates of {100} and {010} are similar.

7.2.2. Reaction pathway

As has been explained above, the reaction pathway followed during the anhydrite carbonation reaction strongly differs depending on the initial carbonate concentration in the aqueous solution. Thus, while when a 0.5M carbonate solution is used, it only involves the formation of calcite, accompanied by trace amounts of vaterite on {001} surface, during the interaction of anhydrite single crystals with a 0.05M carbonate solution, the carbonation reaction initiates with the precipitation of mixtures of calcite and vaterite, progresses simultaneously to the transformation of these mixtures into calcite and aragonite, with aragonite progressively becoming less abundant, to end with the carbonate layer being almost exclusively constituted by calcite. The formation of mixtures of calcite and vaterite has previously been observed during the early stages of the carbonation of gypsum (Fernández-Díaz et al., 2009) and has been attributed to kinetics effects derived from the high supersaturation levels that can be reached in the carbonate-bearing solution at the interface. Roncal-Herrero et al. (2017) gave a similar interpretation to the formation of vaterite accompanying calcite during the interaction of the fast dissolving

anhydrite {001} surface with 0.5M carbonate solutions. Indeed, it is well known that metastability phenomena are common during the crystallization of $CaCO_3$ from solution under far from equilibrium conditions (Radha and Navrotsky, 2010; Rahda et al., 2013; Sawada 1998). However, a kinetic effect related to the high supersaturation at nucleation time it is not a suitable explanation for the formation of vaterite during the interaction of anhydrite with 0.05M carbonate solutions, since it is to be expected that nucleation will take place under high supersaturations when the interactions occurs with a more concentrated solution (0.5M). Furthermore, it has been demonstrated by Cuesta et al. (2018) and Roncal-Herrero et al. (2017) that the existence of epitactic relationships between calcite and anhydrite reduce the energetic barrier for the nucleation of the former on the latter, to a high extent preventing the development of kinetics related metastability phenomena. Even more difficult to explain is the latter transformation of mixtures calcite and vaterite into mixtures of calcite and aragonite. Under the temperature conditions in the experiments (25ºC), solid state transformations between polymorphs are completely unfeasible due to their extreme sluggishness. Therefore, this transformation takes place via a dissolution-crystallization process. The driving force such a process is the lower solubility of aragonite compared to vaterite ($Ksp_{Arg} = 10^{-8.336}$, $Ksp_{Vtr} = 10^{-7.91}$ (Plummer and Busenberg, 1982)). However, for the solvent mediated transformation of vaterite into aragonite to proceed, first aragonite nuclei have to form. Since crystals of the less soluble, and consequently more stable, calcite are already present in the system ($Ksp_{Cal} = 10^{-8.48}$ (Plummer and Busenberg, 1982)) and the energy barrier that must be overcome for the formation of aragonite nuclei is much higher than the energy barrier for calcite growth, it stands to reason support that vaterite crystals should transform into calcite and aragonite should not form in the system at later stages of the carbonation process. In order to understand the possible factor underlying the reaction pathway observed the interaction of anhydrite single crystals with 0.05M carbonate solutions, one has to keep in mind that according to their solubility difference there is a thermodynamic driving force for the transformation of vaterite into aragonite, even it is smaller than that for the transformation vaterite into calcite. This driving force can dominate the process if the growth of calcite crystals becomes impossible because of the specific

physicochemical characteristics of the aqueous solution. This is what happens, for example, during calcite growth in the presence of high Mg^{2+}/Ca^{2+} ratios in the aqueous solution, where the calcite growth inhibition effect of this cation can lead to the eventual nucleation of aragonite (Astilleros et al., 2010; Fernandez-Díaz et al., 1996). A main difference between the composition of the aqueous solution at the interface depending on its initial concentration of carbonate is the evolution of the SO_4^{2-}/CO_3^{2-} ratio as the carbonation progresses. As soon as anhydrite dissolution starts, this ratio will rapidly become much higher in the case of the 0.05M carbonate solution. Vavouraki et al. (2008) conducted in situ AFM observations of the growth of calcite in the presence of different SO_4^{2-} concentrations. These authors found that the influence of SO_4^{2-} ions on calcite growth is very complex and strongly depends on its concentration in the aqueous solution. For a given supersaturation with respect to calcite, when the concentration of this oxyanion is low, no significant differences are observed with respect to the growth of calcite in the absence of SO_4^{2-}. However, an increase in SO_4^{2-} concentration leads to an acceleration of calcite growth, changes in calcite surface nanotopography and an increase of the thickness of growth steps. These features are attributed to the incorporation of a certain amount of SO_4^{2-} groups into calcite structure substituting CO_3^{2-} groups, this the formation of a $Ca(CO_3,SO_4)$ solid solution. This interpretation is supported by the higher thickness of growth steps, since the tetrahedron-sized SO_4^{2-} groups are significantly larger than the planar CO_3^{2-} groups. Furthermore, the faster growth rate can be explained by the higher supersaturation of the aqueous solution with respect to a sulfate-bearing calcite solid solution composition (Astilleros et al., 2003b; Prieto et al., 2007). Finally, Vavouraki et al. (2008) observed that a further increase of SO_4^{2-} concentration in the aqueous solution results in an important drop in growth rate and in the change of growth edges from parallel to crystallographic directions to curved and then to jagged edges, whose development was interpreted as arising from pinning. Furthermore, regardless the concentration of SO_4^{2-} ions in the solution, Vavouraki et al. (2008) observed the reproduction of the original nanotopography of calcite surfaces after successive growth layers were completed. This phenomenon, which has been denominated "template effect" (Astilleros et al., 2003a), is the consequence of the

misfit between the new growth layers that incorporate SO_4^{2-} ions and the underlying substrate. The growth of successive layers containing SO_4^{2-} ions occurs at progressively decreasing rate due to the accumulation of interfacial strain energy and can eventually result its complete stoppage. The "template effect" is accompanied by a change in the growth mechanism from layer growth to surface roughening though the formation of an increased number of new nuclei on top of previous nuclei.

The incorporation of a higher amount of SO_4^{2-} ions into calcite crystals that form from aqueous solutions with higher SO_4^{2-}/CO_3^{2-} ratios, as would be the case during the carbonation of anhydrite in contact with 0.05M carbonate solutions, can explain the formation aragonite after the strain energy accumulated prevents further growth of the sulfate-bearing calcite crystals. The adsorption of SO_4^{2-} groups onto calcite crystal surfaces could further contribute to their growth stoppage through their poisoning, as has widely been described for the case of Mg^{2+} (Morse and MacKenzie, 1990; Morse et al., 2007). Once this situation is reached, the system flows an alternative pathway to reduce its free energy, which involves the both, the transformation of vaterite into aragonite and the growth of aragonite crystals directly from the solution supersaturated with respect to this phase as a result of the continued dissolution of anhydrite. The incorporation of SO_4^{2-} ions into calcite also explains morphological changes in calcite morphology, with the development of jagged edges (Figures 7.6, 7.7), new curved surfaces (Figure 7.5a) and growth layer bunching (Figures 7.6, 7.7).

The influence of SO_4^{2-} ions in the polymorphism of $CaCO_3$ is more in depth investigated and discussed in Chapter 8.

7.2.3. Textural characteristics of calcite pseudomorphs after anhydrite

The concentration of the aqueous solution also has a strong influence in the characteristics of the calcite pseudomorph formed after anhydrite. This influence mainly regards the scale of pseudomorphism and the amount and distribution of porosity generated during the carbonation reaction. Regarding the scale of pseudomorphism, although a faithful reproduction of the external morphology is

achieved irrespective the carbonate concentration of the aqueous solution, the fine details of anhydrite crystal surfaces are much more poorly reproduced when the carbonate concentration is low. When the interaction takes place with a more highly concentrated solution (0.5M) the nucleation of calcite crystals on anhydrite surface takes place immediately due to the very high supersaturation reached with respect to this phase as soon as dissolution starts. Furthermore, this very high supersaturation determines that the number of calcite nuclei that form is very high. Consequently, they grow to form crystals that are small (5 μm). In contrast, when the interaction takes place with an aqueous solution that contains a lower carbonate concentration (0.05M), a higher volume of the anhydrite crystal has to dissolve before the energy barrier for nucleation is overcome. As a result, the finest details of the original anhydrite microtopography disappear before the first $CaCO_3$ nuclei form. Moreover, due to the lower carbonate concentration in the aqueous solution, the supersaturation rate will be lower than in the case of interaction with a 0.5 M carbonate solution, leading to nucleation taking place under lower supersaturation conditions. The consequence is the formation of a smaller number of nuclei that grow to be larger crystals (>20 μm) that reproduce the remaining features of anhydrite microtopography less accurately. Finally, the fact that different polymorphs form on anhydrite cleavage surfaces when they interact with a 0.05M carbonate solution and a sequence of dissolution-crystallization reactions involving these polymorphs take place simultaneously to the progress of the carbonation reaction can further contribute to the loss of anhydrite surface microtopographic details. A similar influence of the carbonate concentration in the aqueous solution and the degree of faithfulness of calcite pseudomorphs formed after gypsum was reported by Fernández-Díaz et al. (2009).

Regarding the development of porosity, it has been widely explained in previous chapters that the pseudomorphic carbonation of anhydrite is associated to a negative molar volume change. The preservation of the external shape of anhydrite crystals through the carbonation reaction requires the generation of an equivalent volume of porosity. This porosity has a transient character and its characteristics evolve along time. The most striking difference in the organization of

the porosity generated during anhydrite carbonation in contact with aqueous solutions with different carbonate concentrations regards the existence or absence of a gap between the carbonate layer and the unreacted anhydrite core. This gap is absent when the carbonation reaction takes place in contact with a solution with a high carbonate concentration (0.5M) but it is present when the carbonate concentration is low (0.05M). A similar gap has been observed to form between the hydrothermal alteration of crystalline titanate-based pyrochlore and interpreted as (Pöml et al., 2007). The development of a gap between the inward moving surface of the primary phase and the product has also been reported to take place during the carbonation of gypsum (Fernández-Díaz et al., 2009). In both systems, the volume of the gap increases as the reaction progresses. Furthermore, in the case of the carbonation of gypsum, considering an equivalent volume of gypsum affected by carbonation, this is larger when the reaction takes place in contact with a solution with a lower carbonate concentration, similarly, to observed here for the carbonation of anhydrite. The origin of this gap has to be interpreted as arising from a too large volume reduction during the carbonation reaction as to be compensated by microporosity distributed within the carbonate layer. In contact with less concentrated carbonate solutions, the volume of the primary phase that has to dissolve so that the liquid phase at the interface reaches a supersaturation high enough that allows calcite growth to proceed will be larger. Furthermore, this volume will progressively increase as the interfacial solution becomes progressively depleted of CO_3^{2-} ions. This explains the observed evolution of both, the observed differences between the porosity organization in calcite pseudomorphs formed after anhydrite (or gypsum) depending on the carbonate concentration in the aqueous solution, and the progressive enlargement of the gap as the carbonation reaction progresses, leading to the generation of extremely fragile pseudomorphs.

8. PRECIPITATION OF $CaCO_3$ POLYMORPHS FROM AQUEOUS SOLUTIONS: THE ROLE OF pH AND SULPHATE GROUPS

8. PRECIPITATION OF $CaCO_3$ POLYMORPHS FROM AQUEOUS SOLUTIONS: THE ROLE OF pH AND SULPHATE GROUPS

The different characteristics of the reaction pathways followed by the system when the carbonation of anhydrite single crystals takes place in contact with aqueous solutions that bear different carbonate concentrations (see Chapter 7) points to the evolution of the $(SO_4^{2-})/(CO_3^{2-})$ ratio playing a determining role in defining what $CaCO_3$ polymorph forms at different stages of the process. The precipitation experiments presented below have been conducted aiming to shed light on this possible influence of $(SO_4^{2-})/(CO_3^{2-})$ on $CaCO_3$ polymorphic selection.

8.1. RESULTS

8.1.1. Mineralogical evolution of the precipitation during ageing

The mineralogical evolution of the precipitates during ageing is summarized in Table 8.1 and illustrated in Figures 8.1 to 8.4.

The XRD and FTIR analyses of the precipitates evidence that soon after their formation (ageing time = 5 minutes) they mainly consist of vaterite, with calcite present as a minor phase. The amount of calcite in the precipitate at 5 minutes reaction progressively decreases as the initial $(SO_4^{2-})/(CO_3^{2-})$ ratio in the aqueous solution increases. This is clearly evidenced by the increase in the intensity of the peaks assigned to vaterite, and the decrease of those attributed to calcite in the diffraction patterns recorded in the samples corresponding to this ageing time (Figure 8.1a). Thus, the amount of calcite is significant in A0, where the initial $(SO_4^{2-})/(CO_3^{2-})$ ratio in the aqueous solution is 0, while no calcite is detected in experiment A22, where the initial $(SO_4^{2-})/(CO_3^{2-})$ ratio is 60.0. FTIR spectra show absorbance bands characteristics of vaterite and/or calcite, whereas the presence of aragonite is not detected (Figure 8.1b). A very weak band at ~ 1130 cm^{-1} (found in the spectrum of precipitates from experiments A5 – A22, but absent in that corresponding to the solids formed from sulphate-free solutions, A0) can be assigned to sulphate ions incorporated in the structure of vaterite and/or calcite.

Table 8.1. Mineral identity of the solid phases recovered in each experiment after different ageing times. Note that the phases in brackets indicate that they are very scarce but they are unequivocally identified at least in one of the analytical techniques used.

Exp.	$(SO_4^{2-})/(CO_3^{2-})$	5 minutes	10 hours	1 day	3 days	1 week	2 weeks
A0	0	Vtr, Cal	Vtr, Cal	Cal	Cal	Cal	Cal
A3	8.48	Vtr, Cal	Vtr, Cal	Vtr, Cal	Cal	Cal	Cal
A5	14.03	Vtr, Cal	Vtr, Cal	Vtr, Cal	Vtr, Cal	Vtr, Cal	Cal
A7	19.51	Vtr, Cal	Vtr, Cal	Vtr, Cal	Vtr, Cal	Cal, Vtr, Arg	Cal, Vtr, Arg
A15	41.78	Vtr, (Cal)	Vtr, (Cal)	Vtr, (Cal)	Vtr, (Cal)	Vtr, Arg, (Cal)	Vtr, Arg, (Cal)
A20	54.87	Vtr, (Cal)	Vtr, (Cal)	Vtr, (Arg), (Cal)	Vtr, Arg, (Cal)	Vtr, Arg, (Cal)	Vtr, Arg, Cal, (Gp)
A22	60.00	Vtr	Vtr	Vtr, (Arg)	Vtr, Arg	Vtr, Arg, Gp	Vtr, Arg, Gp
A25	67.61	Vtr	Vtr	Vtr, Arg	Vtr, Arg	Vtr, Arg, Gp	Vtr, Arg, Gp

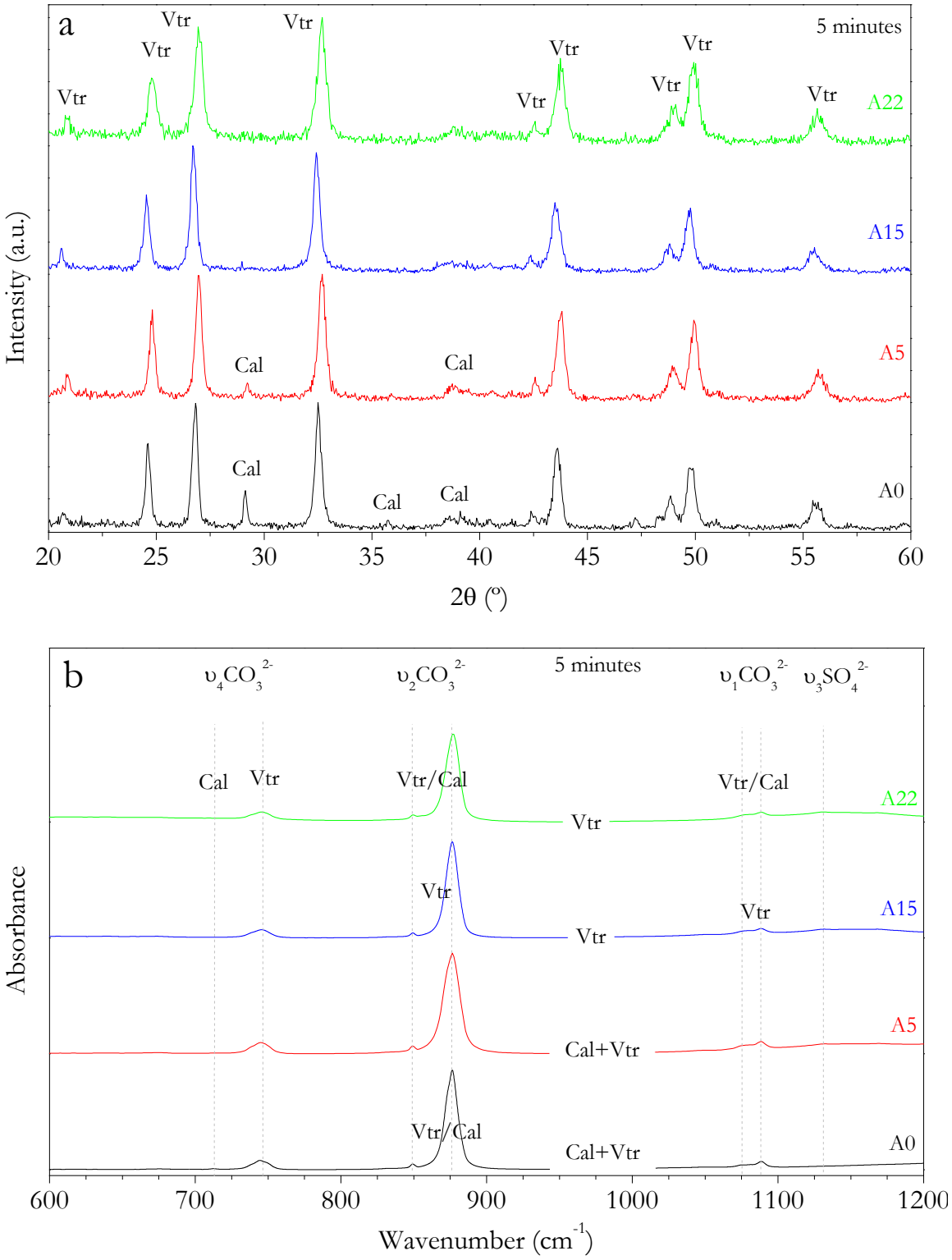

Figure 8.1. XRD patterns (a) and infrared spectra (b) of precipitates sampled after 5 minutes of reaction in the case of experiments A0, A5, A15 and A22, with initial $(SO_4^{2-})/(CO_3^{2-})$ ratios of 0, 14.0, 41.8 and 60.0, respectively.

Furthermore, the mineralogical composition of the precipitates evolves with ageing time, following trends whose characteristics vary depending on the initial $(SO_4^{2-})/(CO_3^{2-})$ ratio in the solution. The composition of precipitates formed in experiments A0 to A5,

where the initial $(SO_4^{2-})/(CO_3^{2-})$ ratio in the aqueous solution varies between 0 and 14.03, show a similar evolution trend. This trend is characterized by the progressive decrease of the amount of vaterite present in the precipitate as ageing progresses (Figure 8.2). This decrease takes place at a slower rate with increasing initial $(SO_4^{2-})/(CO_3^{2-})$ ratios in the aqueous solution, as confirmed by both, XRD (Figure 8.2a) and FTIR spectroscopy (Figure 8.2b). Thus, in the absence of SO_4^{2-} in the solution (A0 in Tables 8.1; $(SO_4^{2-})/(CO_3^{2-}) = 0$), the precipitate exclusively consists of calcite after 3 days of ageing. In experiment A3 ($(SO_4^{2-})/(CO_3^{2-}) = 8.48$), vaterite and calcite are detected after 3 days but calcite is the only $CaCO_3$ phase present in the precipitate after 7 days of ageing. In contrast, vaterite is still present in the precipitate formed in A5 ($(SO_4^{2-})/(CO_3^{2-}) = 14.0$) after 7 days of ageing (Figure 8.2; Table 8.1) but is undetected in the solid phase recovered after 14 days of reaction. This trend is observed in all these three experiments, i.e., vaterite can remain for longer ageing periods when the $(SO_4^{2-})/(CO_3^{2-})$ ratio increases.

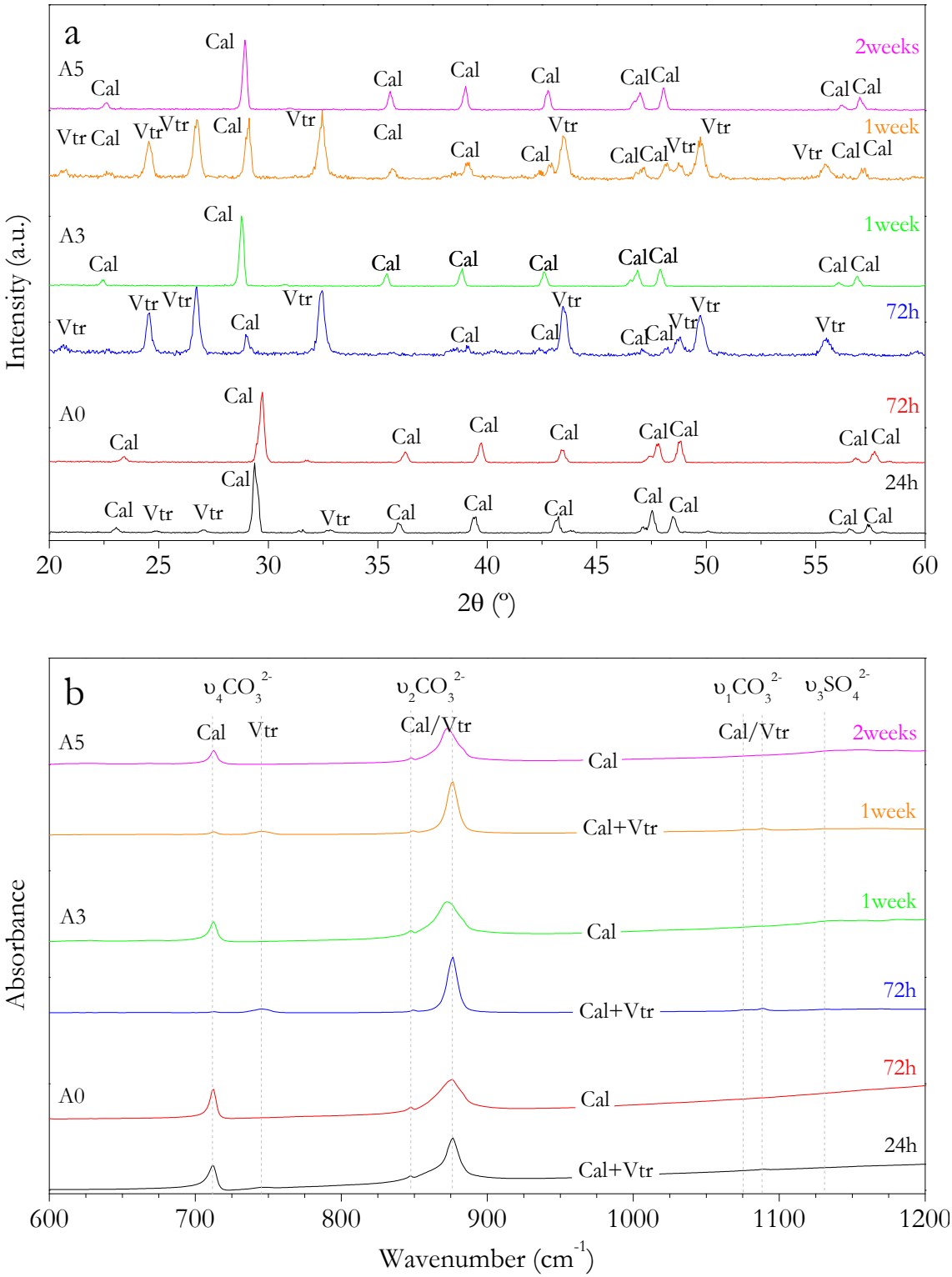

Figure 8.2. XRD patterns (a) and infrared spectra (b) of precipitates sampled from aqueous solutions with low $(SO_4^{2-})/(CO_3^{2-})$ ratios (A0 – A5) as a function of time.

A different mineralogical evolution trend is observed in experiments A7 to A20, where the initial $(SO_4^{2-})/(CO_3^{2-})$ ratio in the aqueous solution varies between 19.51 and 54.87 (Figure 8.3). In this case, the formation of aragonite is also observed during ageing. This $CaCO_3$ polymorph appears as a constituent of the precipitate formed after ageing times that are shorter as the initial $(SO_4^{2-})/(CO_3^{2-})$ ratio in the aqueous solution is higher. Thus, aragonite is detected in the precipitate formed in A7 and A15 after 7 days of ageing, while this phase is found much earlier in the precipitate formed in A20, after only 1 day of ageing. This evolution trend is particularly evident in the FTIR spectra, which show weak bands at ~ 699 cm^{-1} and 712 cm^{-1}; and at ~ 855 cm^{-1}, consistent with the positions of the υ_4 antisymmetric bending and υ_2 out-of-plane vibrations of carbonate ion in aragonite, respectively. This bands are absent in the precipitates formed after short times of ageing (72 h and shorter for A7 and A15, and 10 hours and shorter for A20). It is worthwhile to note that after 14 days of ageing these precipitates consist of the three $CaCO_3$ polymorphs, vaterite, aragonite and calcite, together with gypsum as a minor phase. Calcite is still the most abundant phase in A7, whereas vaterite is the most abundant one in A15 and A20 (Figure 8.3a). Bands at 1130, 628 and 608 cm^{-1}, particularly evident in the precipitate formed in A20 after 2 weeks of ageing can be assigned to sulphate ions incorporated into the lattice of the $CaCO_3$ polymorphs.

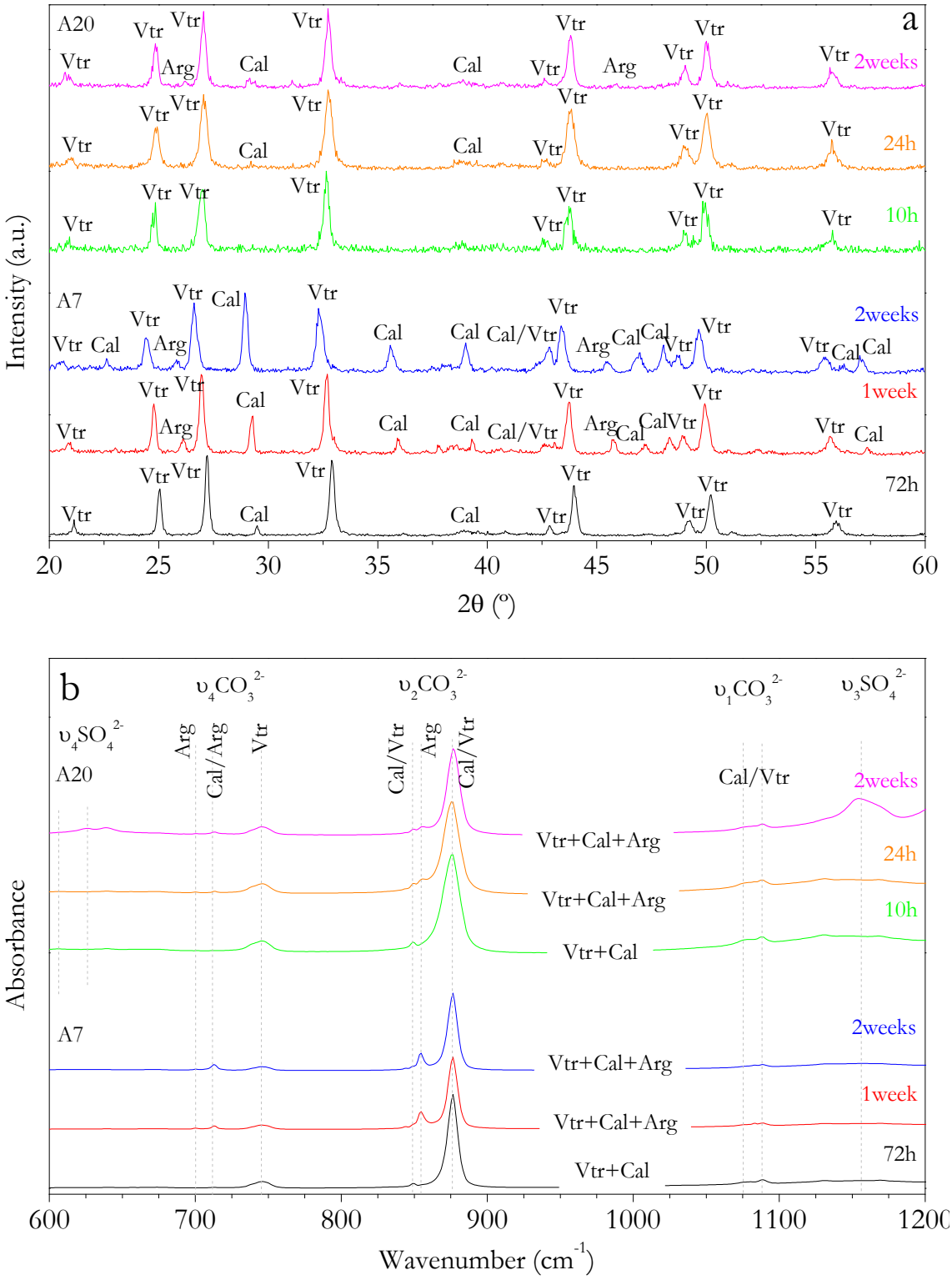

Figure 8.3. XRD patterns (a) and infrared spectra (b) of precipitates sampled from aqueous solutions with a $(SO_4^{2-})/(CO_3^{2-})$ ratios of 19.51 and 54.87 (A7 and A20) as a function of time.

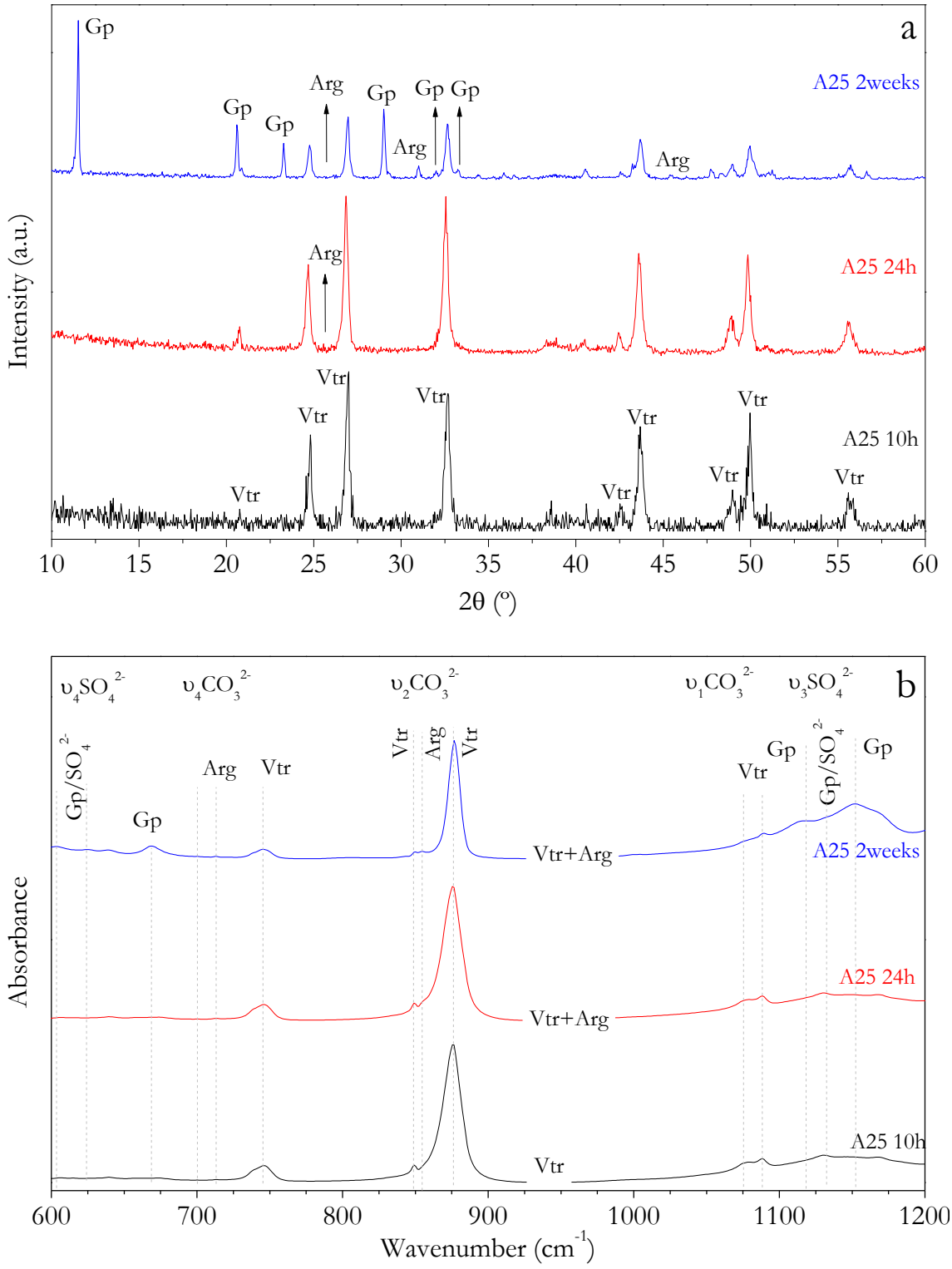

Figure 8.4. XRD patterns (a) and IR spectra (b) of precipitates sampled from aqueous solutions with the highest $(SO_4^{2-})/(CO_3^{2-})$ ratio (67.6) (A25) as a function of time.

Another mineralogical evolution trend is observed in experiments A22 and A25, where the initial $(SO_4^{2-})/(CO_3^{2-})$ ratio in the aqueous solution is 60.00 and 67.61, respectively (Figure 8.4). In both experiments, vaterite is the first and only phase that precipitates whereas calcite never does regardless the ageing time. It is also worthwhile to note that the formation of aragonite isobserved after 1 day of ageing. After 7 days gypsum precipitates and coexists with vaterite and aragonite.

8.1.2. Characterization of the precipitate and the aqueous solution

SEM micrographs in Figure 8.5 show that vaterite appears as cauliflower-like aggregates (Figures 8.5a-b) or radial aggregates that consist of lens-shaped crystallites (Figure 8.5c-d). As is apparent, no significant evolution of vaterite morphology is observed as a function of the initial $(SO_4^{2-})/(CO_3^{2-})$ ratio in the aqueous solution nor the ageing time. In contrast, calcite appears as single crystals whose morphology and size are highly dependable on both, reaction time and initial $(SO_4^{2-})/(CO_3^{2-})$ ratio in the solution. Thus, in experiment A0, where there is no sulphate in the solution, calcite crystals are bounded by flat $\{10\bar{1}4\}$ rhombohedron faces regardless the reaction time and show sizes in the 10-25 μm range (Figures 8.5a, c, e). In experiments A3 to A7, where the initial $(SO_4^{2-})/(CO_3^{2-})$ ratio varies between 8.5 and 19.5, calcite crystals that form early after the mixing of the aqueous solution also show the typical rhombohedron-like shape with flat $\{10\bar{1}4\}$ faces (Figure 8.5f). However, their morphology undergoes an evolution as ageing progresses. This evolution is characterized by a progressively increasing elongation along [001] (Figures 8.5 f-h) as well as the emergence of rough pseudofacets that lead to the development of a new form, the more acute $\{02\bar{2}1\}$ rhombohedron (see inset in Figure 8.5h). This evolution seems to be more marked in precipitates A7 and A5 than A3, which points to a positive relationship between higher initial $(SO_4^{2-})/(CO_3^{2-})$ ratio in the aqueous solution and more elongated and rougher-faced calcite crystals. Thus, after 14 days of ageing calcite crystals formed in experiment A3 show a length/width ratio around 2.4. This ratio is around 3.3 and 3.5 in calcite crystals formed in experiments A5 and A7, respectively (Figures 8.5i-j). As mentioned above, calcite crystals are hardly noticeable in experiments A15 to A20 and are absent in experiment A22 and A25 regardless the reaction time.

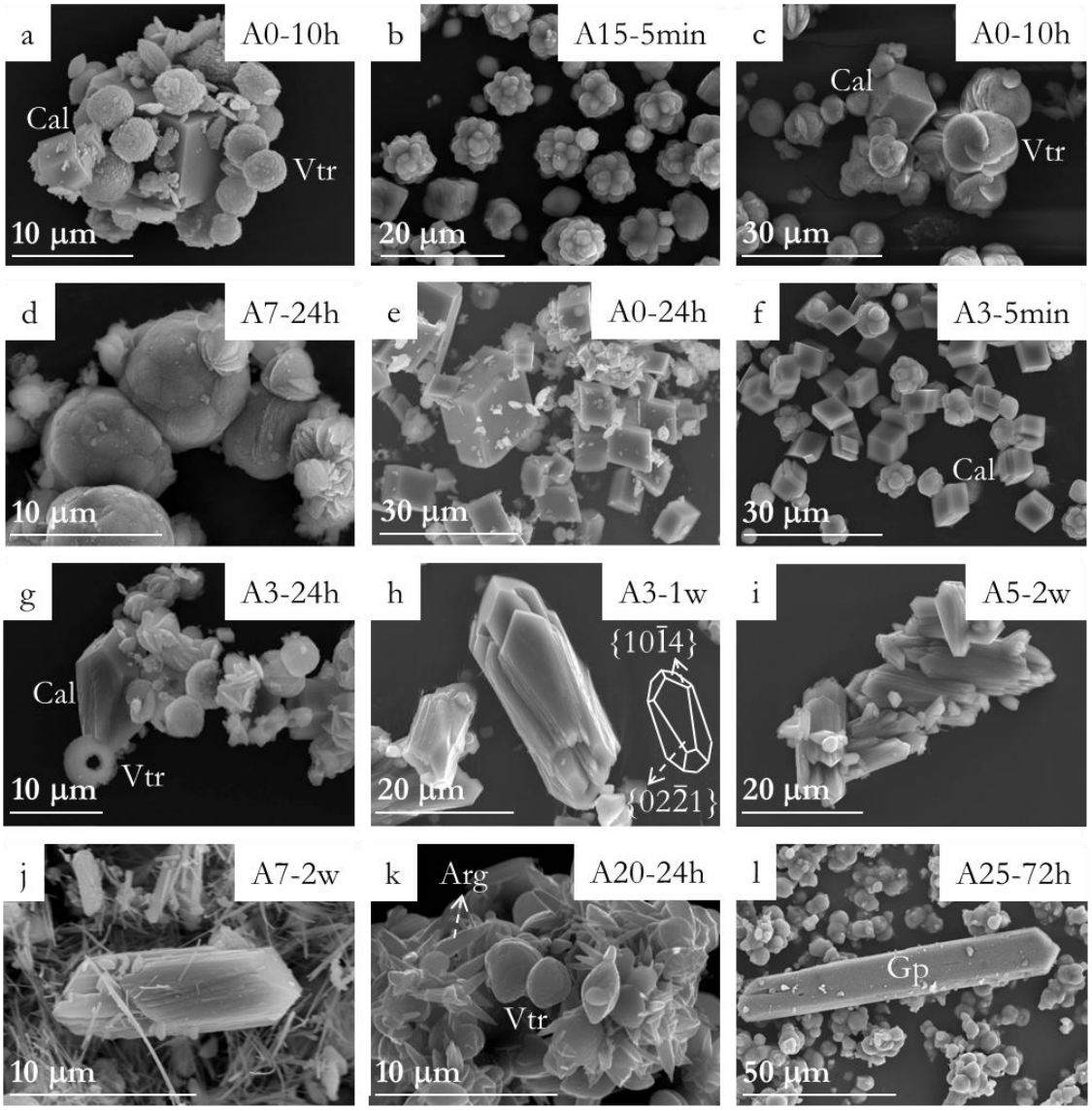

Figure 8.5. SEM images of precipitates recovered from solutions with different $(SO_4^{2-})/(CO_3^{2-})$ ratios after various elapsed times ranging from 5 minutes to 14 days. Vaterite appears as cauliflower-like aggregates (a-b) or lens-shaped crystallites (c-d). When there is no sulphate in the solution, calcite crystals are bounded by flat {10$\bar{1}$4} rhombohedral faces (a, c, e). In solutions with moderate concentration of sulphate calcite crystal habit undergoes an evolution characterized by progressive increase in elongation along [001] (f-j) and the emergence of the {02$\bar{2}$1} form (see inset in h). Aragonite appears as crystals with the so-called "morning-star" morphologies (k). Gypsum crystals exhibit tabular habits with the {010} form as the main face (l).

Aragonite is observed in experiments A7-A25 ($(SO_4^{2-})/(CO_3^{2-})$=19.51-67.61). In all cases, aragonite appears as crystals bounded by curved prismatic faces. These crystals grow on the surface of vaterite aggregates, forming so-called "morning-star" aggregates (Figure 8.5k). Finally, gypsum crystals, which are observed in experiments A22 and A25, typically exhibit tabular habits with the {010} form as the main face with an accentuated elongation along [001] (Figure 8.5l).

EDX analyses conducted on vaterite and calcite crystals evidence that they contain S in all the cases, except for those vaterite and calcite crystals formed in the absence of SO_4^{2-} (experiment A0) in the aqueous solution. For both, vaterite and calcite, a direct correlation between the [S] (% at) and the initial $(SO_4^{2-})/(CO_3^{2-})$ ratio in the aqueous solution is detected (Figure 8.6a). Thus, after 5 minutes reaction a [S] (% at) of 0.91 was measured in vaterite aggregates formed in experiment A3, while S/Ca ratio is as high as 1.54 and 3.23 in vaterite formed in experiments A7 and A25, respectively. A similar trend is observed in calcite crystals, whose S/Ca ratio after 5 minutes reaction is 2.81 in experiment A3, 4.48 in experiment A5 and 5.76 in experiment A20. It is interesting to note that for both, calcite and vaterite, for a given $(SO_4^{2-})/(CO_3^{2-})$ initial ratio, the highest S content is always detected in the precipitates with the shorter ageing (5 minutes reaction) and progressively decreases as ageing progresses. This evolution is depicted in Figure 8.6b for calcite formed in experiment A5. It is also striking that, regardless the initial $(SO_4^{2-})/(CO_3^{2-})$ ratio and the ageing time, calcite crystals always show higher S contents than vaterite aggregates. The small size of aragonite crystals formed in experiments A7 to A25 and gypsum crystals formed in experiments A22 and A25 prevented that EDX analyses could be conducted on them.

Finally, ICP-OES analyses of the S concentration in the aqueous solution show that at 5 minutes reaction, the concentration of S in the aqueous solution is progressively lower than the initial aqueous solution as the initial $(SO_4^{2-})/(CO_3^{2-})$ ratio in the aqueous solution increases (Figure 8.7a). Furthermore, the concentration of S in the aqueous solution varies with ageing time, following similar trends independently of the initial $(SO_4^{2-})/(CO_3^{2-})$ ratio in the solution (Figure 8.7b). Thus, the concentration of S in the aqueous solution is characterized by a rapid drop followed by a progressive increase as ageing progresses.

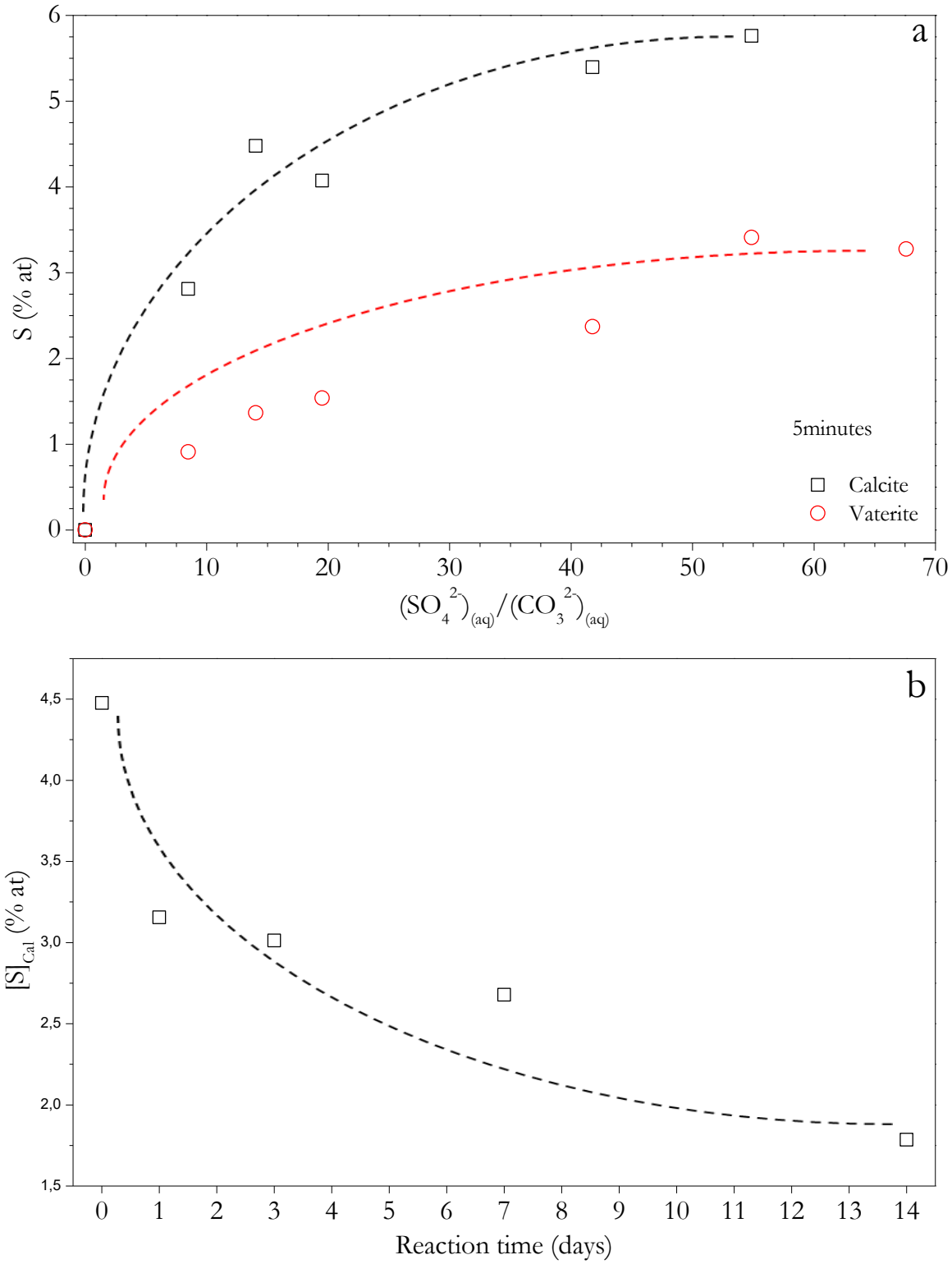

Figure 8.6. (a) Concentration of S (% at) in calcite and vaterite sampled after 5 minutes of reaction as a function of the initial $(SO_4^{2-})/(CO_3^{2-})$ ratio. (b) Variation of [S] (% at) with ageing in calcite crystals sampled from aqueous solutions with a $(SO_4^{2-})/(CO_3^{2-})$ ratio of 14.03 (A5).

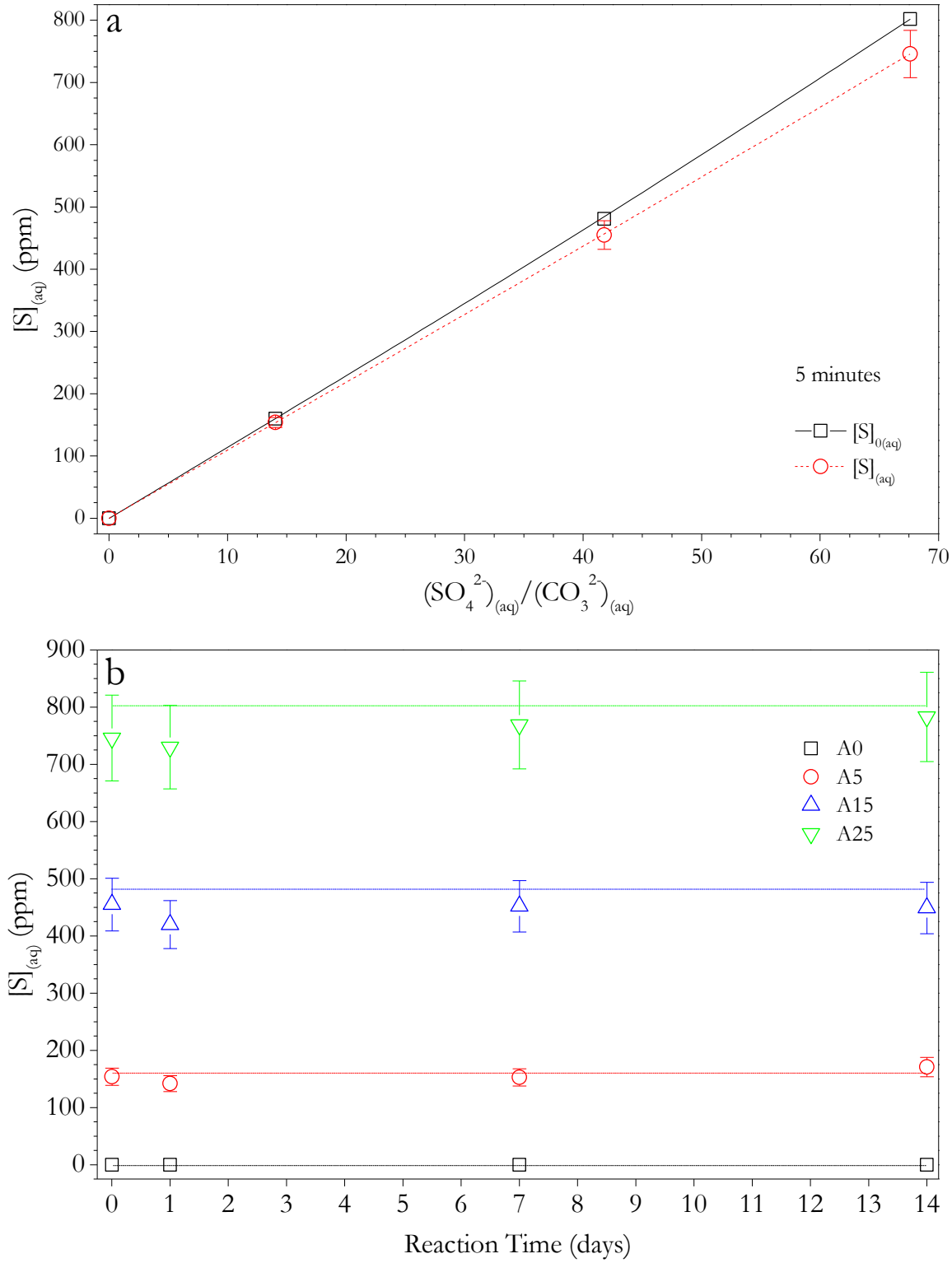

Figure 8.7. (a) Concentration of S (from ICP-OES analyses) in aqueous solutions sampled after 5 minutes of reaction as a function of the initial $(SO_4^{2-})/(CO_3^{2-})$ ratios (dashed lines). The initial concentrations of S in the solutions are connected by a solid line. (b) Evolution of the concentration of S (from ICP-OES) of aqueous solutions with initial $(SO_4^{2-})/(CO_3^{2-})$ ratios of 0 (A0), 14.3 (A5), 41.8 (A15) and 67.7 (A25), respectively.

8.2. DISCUSSION

The experimental results described in the previous section (XRD and FTIR analyses) show that the mineral composition of the precipitate recovered in each run varied as a function of two main factors: the high supersaturation of the parental aqueous solution, which controls the phases that are formed at the initial stages of crystallization, and the $(SO_4^{2-})/(CO_3^{2-})$ ratio in the parental solution, which influences the mineral evolution of the precipitates during ageing. After the mixing of the reactants, aqueous solutions are highly supersaturated with respect to all the crystalline $CaCO_3$ polymorphs and spontaneous precipitation takes place. According with the Ostwald step rule (Söhnel and Garside, 1992) the formation of the most soluble and disordered phase, is kinetically favoured (Sawada, 1997). However, under the conditions used in these experiments the precipitation of the amorphous calcium carbonate, the most soluble $CaCO_3$ phase, can be discarded since the aqueous solution is always undersaturated with respect to this phase ($SI_{ACC} \leq -0.1$). Therefore, kinetics factors promote the formation of vaterite as the first phase that precipitates immediately after the mixing of the parental solutions. After vaterite nucleation, the system can further reduce its free energy by the subsequent transformation of vaterite into calcite through a solvent mediated transformation (Cardew and Davey, 1985). In addition, a reduction of supersaturation resulting from the growth of vaterite promotes the nucleation of calcite. Therefore, as the system approaches to equilibrium, the most stable $CaCO_3$ phase, calcite, should become the prevailing phase at the expense of vaterite. The mineralogical evolution observed in experiments with the lower initial $(SO_4^{2-})/(CO_3^{2-})$ ratios (A0-A5) is in good agreement with this expected evolution. Furthermore, it is in good consonance with the precipitate mineralogical evolution upon ageing previously observed by, in similar mixing experiments conducted in more highly supersaturated systems ($SI_{Cal} \sim 3.7$) under higher pH (~10.9) (Fernández-Díaz et al., 2010). Our current results are further evidence that the presence of a high amount of sulphate ions in the aqueous media slows down or even inhibits the direct precipitation of calcite and transformation of vaterite into calcite, thereby contributing to the stabilization of vaterite with respect to calcite. The prolonged existence of vaterite as a major constituent of the precipitate is observed in all the experiments. The stabilization of vaterite is more evident the higher the $(SO_4^{2-})/(CO_3^{2-})$ ratio is in the aqueous solutions. Indeed, in experiments A22 and A25, where this ratio is

highest, vaterite does not transform into calcite even after 2 weeks of ageing. These results are again consistent with those previously reported by Fernández-Díaz et al. (2010), who notice that vaterite can remain as a major constituent phase for long ageing periods when $(SO_4^{2-})/(CO_3^{2-})$ ratios are higher than one. The stabilization of vaterite and the retardation of calcite crystallization in the presence of sulphate ions can be explained by a combination of both thermodynamics and kinetics factors. Computational modelling of the substitution of a small amount of carbonate groups by sulphate groups in the structures of vaterite and calcite (Arroyo-de Dompablo et al., 2015; Fernández-Díaz et al., 2010) showed that vaterite structure is much less disrupted by the isomorphic incorporation of AO_4^{2-} groups, including sulphate, chromate and selenate, than calcite structure. In the case of sulphate, the incorporation of this oxyanion results in an increment of calcite lattice energy, while it has the opposite effect on the lattice energy of vaterite. This different impact of sulphate isomorphic incorporation on the energetics of calcite and vaterite structures is especially relevant for the S content range up to 3% molar fraction, where it translate into an effective reduction of the energy difference between the two calcium carbonate polymorphs. The larger capability of vaterite to accommodate sulphate oxyanions in its structure compared to calcite seems to be in contradiction with the experimental evidence provided by the EDX analyses of calcite and vaterite grains in the precipitates obtained in these experiments. These analyses steadily show a higher S content in calcite crystals than in vaterite aggregates formed in the same experiment. This is so regardless the initial $(SO_4^{2-})/(CO_3^{2-})$ ratio and the ageing time (see Figure 8.6a). Similar results were reported by Fernández-Díaz et al. (2010) for precipitates formed under higher supersaturations and pHs. These authors explain the apparent contradiction between experimental results and energy-based expectations considering that the higher S contents measured in calcite most likely were the consequence of this phase forming later than vaterite. In such a scenario, calcite crystals would have grown from a CO_3^{2-} depleted medium after vaterite nucleation and, consequently, in a solution with a $(SO_4^{2-})/(CO_3^{2-})$ ratio significantly higher than the initial one.

Although the results of computer simulations of sulphate incorporation do not predict stability crossovers between vaterite and calcite, the approximation of the lattice

energy of both polymorphs can explain the increasingly larger duration of vaterite as precipitate component with growing initial sulphate concentration in the solution.

While the incorporation of impurities from the aqueous solution can change the lattice energy of the bulk crystal, surface-related phenomena like impurity adsorption can modify the surface chemistry of the different polymorphs, thereby changing their surface energies (Navrotsky, 2004). The impact of this phenomenon is particularly relevant in the case of small particles, where the surface/volume ratio is very high, and the effect of lattice energy in the stability of the different polymorphs is comparatively much less important than that of surface energy. A small increase of the surface energy of calcite nanoclusters and nanoparticles due to sulphate adsorption could dramatically increase the barrier for its nucleation, since such a barrier is proportional to the square of the surface energy. Were this to happen, the main outcome would also be a progressively slower transformation of vaterite into calcite as the $(SO_4^{2-})/(CO_3^{2-})$ ratio in the parent aqueous solutions increases. Kinetics arguments involving the adsorption of impurities have often been invoked to explain the stabilization of vaterite with respect to calcite and the retardation of calcite nucleation and growth. Phenomena observed during the precipitation of $CaCO_3$ from supersaturated aqueous solution bearing phosphate ions are an example (Katsifaras and Spanos, 1999). In this system, the stabilization of vaterite was rather attributed to the blocking of active sites for dissolution on the surface of this phase due to the adsorption of phosphate ions. A similar phosphate adsorption onto surface sites-related explanation was claimed to explain calcite growth inhibition. Indeed, a similar reasoning can be applied to explain the observed effect of sulphate ions. Another alternative thermodynamic and mechanistic argument has been invoked to explain the inhibition of calcite growth by the effect of sulphate ions. *In situ* AFM experiments of calcite growth performed using a fluid cell and flowing supersaturated sulphate-bearing aqueous solutions showed that a low concentration of sulphate in the aqueous solution (5 mM) is enough to decrease the rate of step spread on calcite surface (Vavouraki et al., 2008). These nanoscale AFM observations supported the interpretation that the trapping of sulphate ions by nanometric growing layers resulted in the generation of interfacial strain energy. Strain relaxation perpendicular to the growing layer introduces local variations in bond lengths, giving rise to local departures from calcite surface ideal nanotopography. The direct consequence of this phenomenon is a decrease of the step

advancement rate according to the so-called "template effect" model (Astilleros et al., 2002; Astilleros et al., 2003a; Astilleros et al., 2010), which is more marked the larger the amount of sulphate ions trapped within calcite monolayers.

An interesting result observed in experiments A7 to A25, where the initial $(SO_4^{2-})/(CO_3^{2-})$ ratio in the aqueous solution > 19.51, is the formation of aragonite. It takes place through the solvent-mediated transformation of vaterite and can also be explained invoking both, thermodynamic and kinetics arguments. For equivalent compositions of sulphate in the polymorphs, computer modelling of sulphate isomorphic incorporation predicts a significantly larger increment of aragonite lattice energy compared to that of both, calcite and vaterite. This result indicates that the substitution of carbonate groups by sulphate in aragonite structure is very unfavorable (Arroyo-de Dompablo et al., 2015; Fernández-Díaz et al., 2010). As a result, even when this polymorph forms from highly supersaturated solutions with very high $(SO_4^{2-})/(CO_3^{2-})$ ratios, it grows relatively sulphate-free compared to calcite. The direct consequence is a much more marked impact of the presence of sulphate in the growth medium on calcite stability. Indeed, the solubility of a sulphate-bearing calcite can overcome that of sulphate-free aragonite, as pointed out by Busenberg and Plummer (1985), who reported this to be the case for calcites with sulphate contents above 3 mole%. Such solubility crossover could explain the observation that, upon ageing of the vaterite precipitate, aragonite forms simultaneously to or, even, after the formation of the theoretically stable polymorph calcite when the concentration of sulphate in the aqueous solution is very high. This is the case in experiments A7 to A20. Unfortunately the small size of the aragonite crystals formed in these experiments has prevented to obtain EDX analysis evidence that could give full support to our interpretation, although the high concentration of sulphate measured in calcite crystals point in this direction (see Figure 8.6). On the other hand, the fact that sulphate incorporation into aragonite structure is very unfavorable, it can be concluded that an inhibitory effect of sulphate ions during the growth of aragonite will arguably be less effective than in the case of calcite, and so will be a hypothetical "template effect" mechanism.

Beside the precipitation of $CaCO_3$ polymorphs, gypsum was unequivocally detected after 7 days of interaction in the experiments with the highest $(SO_4^{2-})/(CO_3^{2-})$ ratios (A20-A25). The precipitation of this phase is not surprising since the initial

solutions are supersaturated with respect to this phase (SI_{Gp}~0.17-0.25). However, the early precipitation of $CaCO_3$ phases after mixing of the parent solutions necessarily depletes the solution in Ca^{2+} (and to a much lesser extent in SO_4^{2-}), leading to a very important reduction of aqueous phase SI_{Gp}. Thus, systems initially close to equilibrium with respect to gypsum, as is the case of the solution in experiment A15, will become undersaturated soon after the precipitation of $CaCO_3$ starts, making the formation of gypsum impossible. Those systems initially more highly supersaturated with respect to gypsum will either approach equilibrium or significantly less supersaturated, allowing gypsum precipitation to be prevented over large periods.

The presence of sulphate in the aqueous solutions and the ageing not only appears to be a critical factor controlling the mineralogy of the recovered precipitates, but it also affects the morphology of calcite single crystals. As mentioned in section 8.3.2, after short ageing time, calcite single crystals exhibit the typical rhombohedral idiomorphic shape (see Figures 8.5a,c,e), which progressively become blockier and elongated parallel to the *c* axis as ageing progresses. This elongation is clearly more pronounced as the $(SO_4^{2-})/(CO_3^{2-})$ ratio in the aqueous solution increases. Since there is a clear correlation between the concentration of sulphate in the aqueous solution and the amount of this anion that is incorporated into the calcite (and vaterite) structure, directly evidenced by EDX (see Figure 8.6a) and supported by ICP analysis (Figure 8.7a), we can conclude that the modification of calcite crystal habit is a direct result of the incorporation/sorption of this anion. The effect of several ions on calcite habit has been profusely discussed in the literature. In particular, the elongation of calcite crystals has been interpreted as resulting of a significant lowering of the surface energy of certain faces other than $\{10\bar{1}4\}$ due to a preferential sorption of foreign ions on these faces (Titiloye et al., 1993). It has also been attributed to a modification of calcite surface nanotopography due to step-specific impurity interactions (Davis et al., 2004). These interactions contribute to the stabilization of new crystal faces that become prevalent during growth. In the case under consideration here, the habit of calcite crystals grown in presence of sulphate, we observe the stabilization of the $\{02\bar{2}1\}$ form. The resulting habit strikingly resembles those of calcite crystals grown in the presence of small cations such as Mg^{2+}, Co^{2+} or Mn^{2+} (Fernández-Díaz et al., 2006).

Finally, the progressive decrease of S content in both the calcite and vaterite precipitates with reaction time (Figure 8.6b), which is in good agreement with a parallel progressive increase of sulphate concentration in the aqueous solution (Figure 8.7b), points to the precipitate undergoing of recrystallization processes through a dissolution-precipitation mechanism. The driving force for this recrystallization process could be the reduction of the extra energy associated to an excess of sulphate incorporated in calcite and vaterite structures under the influence of the high supersaturations dominating the early staged of the precipitation process. The progress of this recrystallization process leads to a chemical purification of the precipitates that further contributes to the stabilization of calcite as ageing progresses.

9. EXPERIMENTOS TIPO BATCH

9. EXPERIMENTOS TIPO BATCH

Con el fin de estudiar la evolución fisicoquímica del sistema anhidrita-disolución carbonatada a lo largo del tiempo y analizar en detalle las fases minerales que se forman, se llevaron a cabo experimentos de tipo "batch". En estos experimentos se pusieron en contacto fragmentos recién exfoliados de anhidrita de un tamaño de $1.6 \leq x \leq 2.0$mm con disoluciones que contenían dos concentraciones distintas de carbonato, 0.05M y 0.5M, de acuerdo con lo expuesto en el capítulo 4. La evolución del sistema se siguió mediante el análisis y estudio de la mineralogía de la fase sólida y la concentración de las especies químicas en la fase líquida. A la hora de interpretar los datos de composición de la fase líquida y comparar los resultados obtenidos en estos experimentos con los correspondientes a los experimentos de interacción con monocristal, se tendrá en cuenta que en estos últimos experimentos el equilibrio fase líquida-mineral se restringe al volumen de disolución localizado en la interfase donde tiene lugar la reacción, mientras que en los experimentos de tipo "batch" el equilibrio se alcanza con respecto a todo el volumen de la disolución.

El estudio de la interacción de anhidrita con disoluciones carbonatas se ha extendido también al caso del yeso, con la intención de analizar el efecto de la presencia de cristales de una fase distinta en el sistema, así como el efecto de la dilución de la disolución acuosa que se asocia a la disolución del yeso, al liberar las moléculas de agua presentes en su estructura a la fase líquida.

9.1 RESULTADOS

9.1.1. Evolución de la fase sólida durante la interacción de anhidrita con disoluciones de carbonato

9.1.1.1 Concentración inicial de carbonato 0.05M

Los difractogramas de las muestras sólidas recuperadas tras la reacción entre los cristales de anhidrita y una disolución de carbonato de concentración 0.05M durante tiempos progresivamente más largos no muestran ninguna evolución mineralógica por lo que se refiere a las fases presentes en el sistema (Figura 9.1). Así,

a todos los tiempos considerados, las fases presentes son anhidrita y calcita. Las fases vaterita y aragonito no se identifican en ninguno de los difractogramas obtenidos. También es significativo que no se observan variaciones importantes en la intensidad relativa de las reflexiones correspondientes a anhidrita y calcita. Puesto que el tiempo de interacción más corto considerado ha sido de 24 horas, se puede concluir que la reacción se ha completado durante ese periodo.

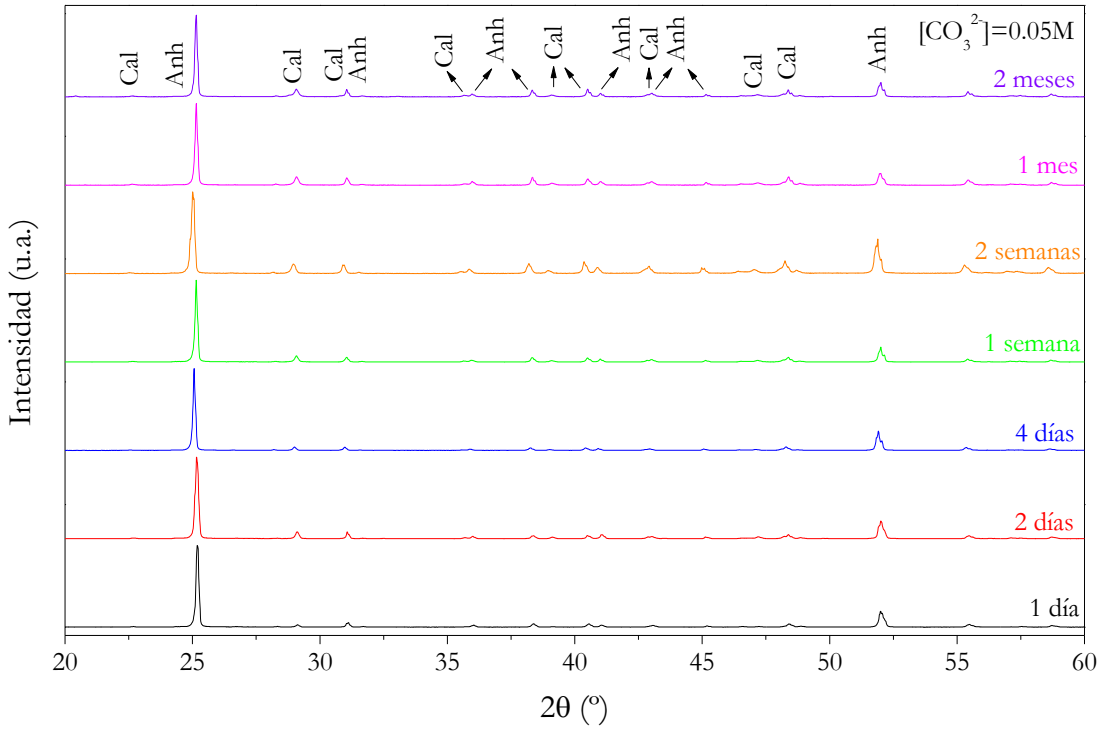

Figura 9.1. Difractogramas obtenidos de la muestras sólidas separadas en los experimentos tipo batch tras la interacción de fragmentos de anhidrita con disoluciones de carbonato (0.05M), a distintos tiempos de reacción. Las fases presenten son la calcita y la anhidrita.

El análisis de las muestras sólidas obtenidas en los experimentos de interacción de anhidrita con una disolución de carbonato de concentración 0.05M mediante espectroscopia Raman confirma las conclusiones derivadas del análisis mediante difracción de rayos X. Efectivamente, para todos los tiempos considerados, en los espectros Raman sólo se identifican bandas que corresponden a los modos vibracionales de las fases anhidrita y calcita (Figura 9.2). En el intervalo mostrado (250 cm^{-1} - 900 cm^{-1}), se identifican las siguientes bandas que pueden asignarse a la calcita: una banda a 282 cm^{-1} y a 712 cm^{-1}; la anhidrita a 417 cm^{-1}, 500 cm^{-1}, 610 cm^{-}

^{1} y 628 cm^{-1}. Es importante señalar que fuera del intervalo mostrado aparece una banda muy intensa a 1085 cm^{-1}, común a calcita y a aragonito. El estudio se centra en el intervalo 250 cm^{-1} - 900 cm^{-1} por ser suficiente para la distinción de los polimorfos. La ausencia de otras bandas correspondientes a la vaterita y al aragonito en este intervalo es consistente con los resultados derivados de los difractogramas de rayos X y descarta la presencia de dichas fases.

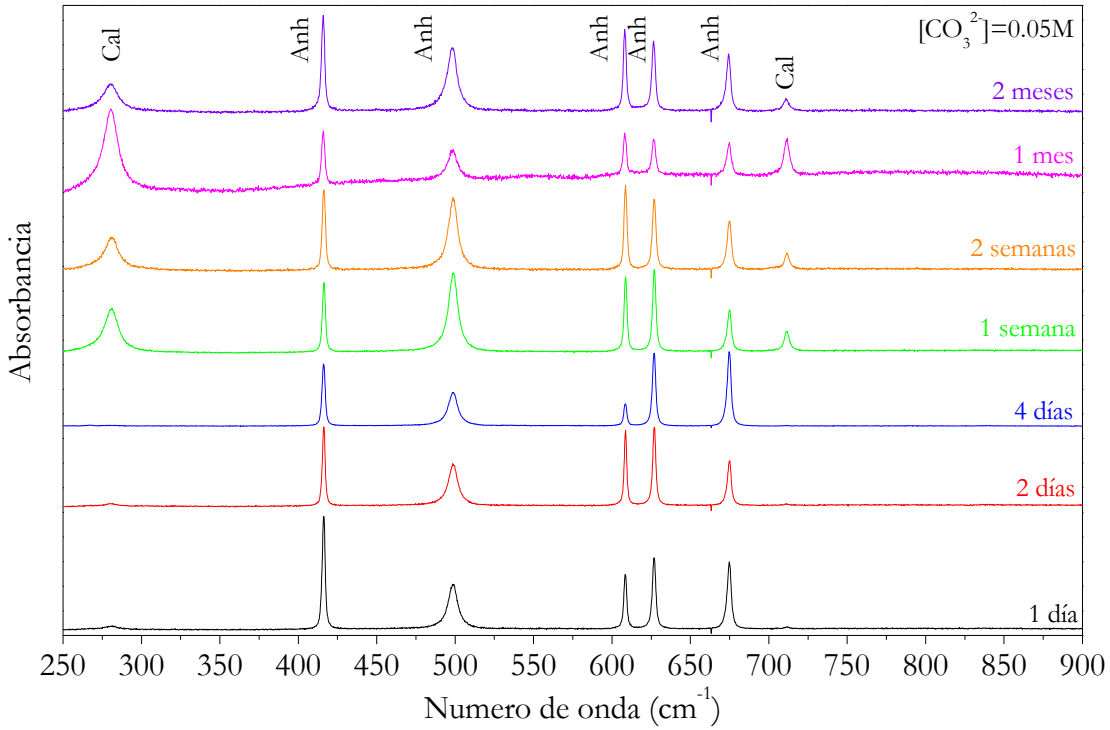

Figura 9.2. Espectros Raman entre 250 cm^{-1} y 900 cm^{-1} obtenidos de las muestras sólidas separadas en los experimentos tipo batch, tras la interacción de fragmentos de anhidrita con disoluciones de carbonato (0.05M), a distintos tiempos de reacción. Las fases presenten son la calcita y la anhidrita.

Las conclusiones derivadas de los análisis de DRX y espectroscopia Raman son confirmadas por las imágenes de SEM de las muestras sólidas, en las cuales, de acuerdo con criterios morfológicos, el único polimorfo del $CaCO_3$ que es posible identificar es la calcita. Los cristales de calcita muestran el típico hábito romboédrico, limitado por la forma $\{10\bar{1}4\}$ (Figura 9.3).

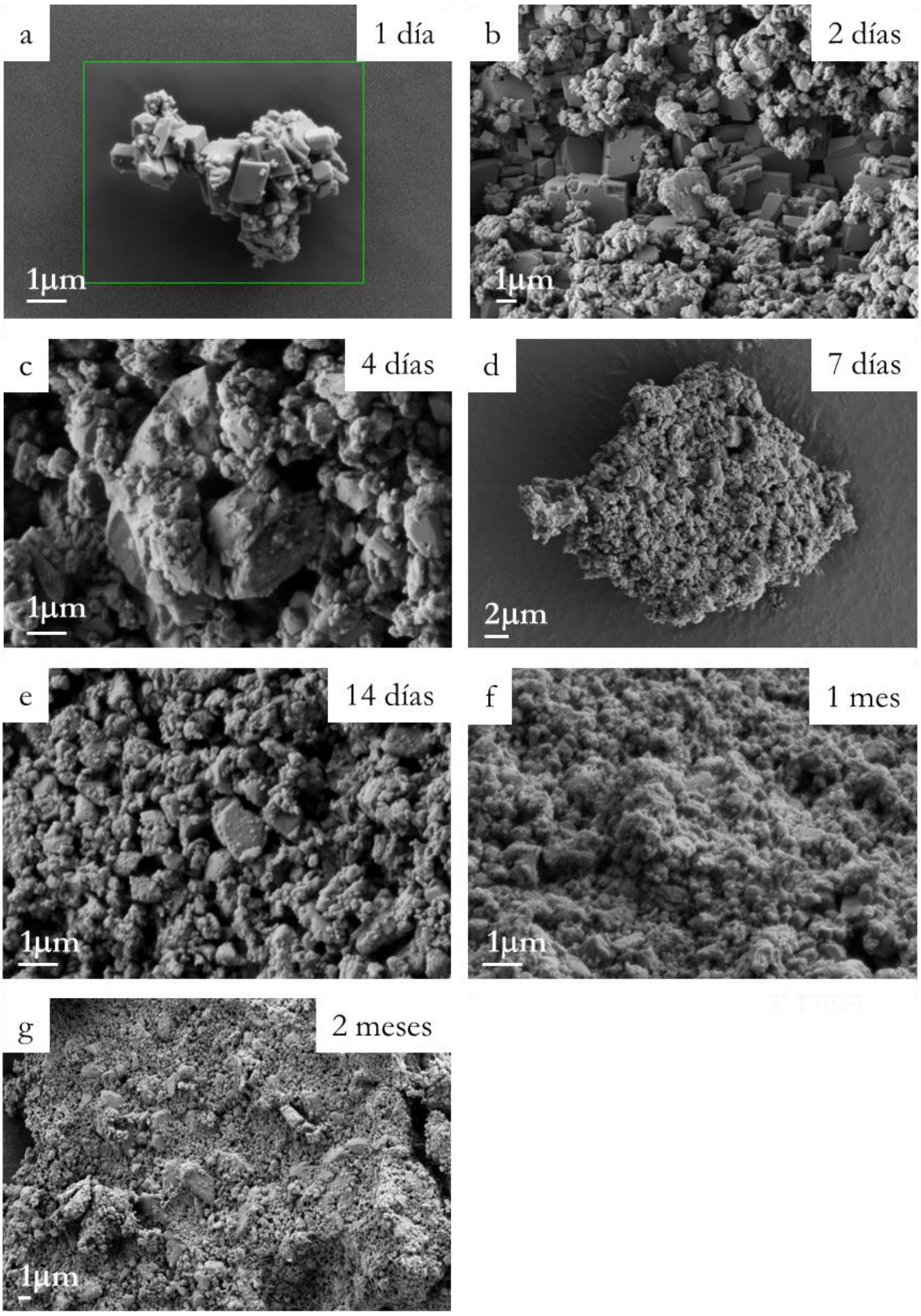

Figura 9.3. Imágenes de SEM de la superficie de la anhidrita tras hacerla reaccionar con una disolución de carbonato 0.05M durante distintos tiempos. En todas las imágenes, el único polimorfo del $CaCO_3$ que se observa es la calcita.

9.1.1.2 Concentración inicial de carbonato 0.5M

Los difractogramas de las muestras sólidas recuperadas tras la reacción entre los cristales de anhidrita y una disolución de carbonato de concentración 0.5M durante tiempos progresivamente más largos muestran una evolución del sistema ligeramente distinta de la observada cuando la interacción tiene lugar con la disolución de carbonato menos concentrada (0.05M) (Figura 9.4). El primer hecho distintivo es que la intensidad de los picos de anhidrita disminuye drásticamente en los difractogramas obtenidos a los 4 días y una semana de interacción hasta desaparecer por completo en los difractogramas obtenidos a partir de ese momento. Por lo que se refiere a las fases del $CaCO_3$, se observa la presencia de calcita a todos los tiempos de interacción considerados. Además, la presencia de un pico muy débil a $2\theta = 26.7°$ en los difractogramas correspondientes a tiempos de interacción inferiores o iguales a una semana apunta a la presencia inicial de vaterita en el sistema.

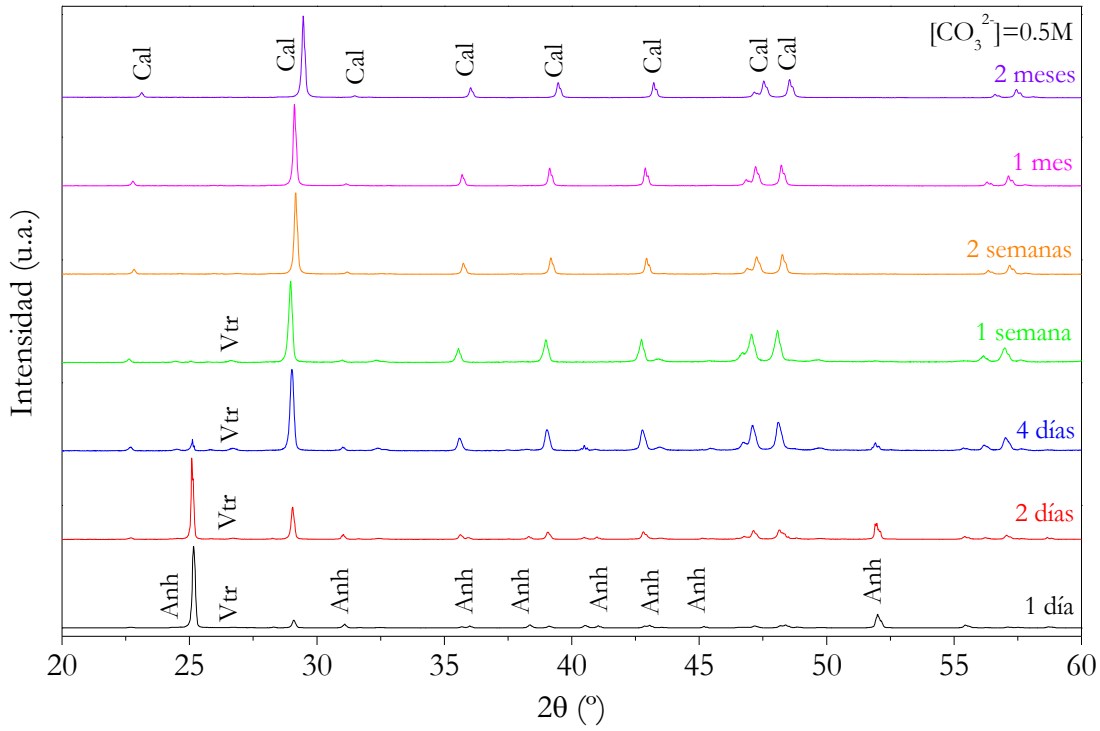

Figura 9.4. Difractogramas de las muestras sólidas recuperadas en los experimentos tipo batch de interacción de fragmentos de anhidrita con una disolución de carbonato de 0.5M, tras distintos tiempos de reacción. Aparecen las fases anhidrita, calcita y vaterita.

Los espectros Raman de las muestras sólidas recuperadas de estos experimentos se muestran en la Figura 9.5. El análisis de estos espectros apoya que la calcita es la única fase mineral presente en el sistema tras 4 días de interacción con la solución carbonatada y que para tiempos más cortos, sólo se puede confirmar la presencia de anhidrita y calcita. En el intervalo mostrado (250 cm^{-1} - 900 cm^{-1}), la calcita muestra bandas a 282 cm^{-1} y a 712 cm^{-1}, mientras que se pueden atribuir a la anhidrita a 417 cm^{-1}, 500 cm^{-1}, 610 cm^{-1} y 628 cm^{-1}. Al igual que ocurría en los experimentos realizados con una concentración de carbonato menor, fuera del intervalo mostrado aparece una banda muy intensa a 1085 cm^{-1}, común a calcita y a aragonito. Aunque tanto vaterita y como aragonito tienen bandas entre 700 cm^{-1} y 900 cm^{-1}, en los espectros estudiados no se observa ninguna banda que se pueda atribuir a estas fases.

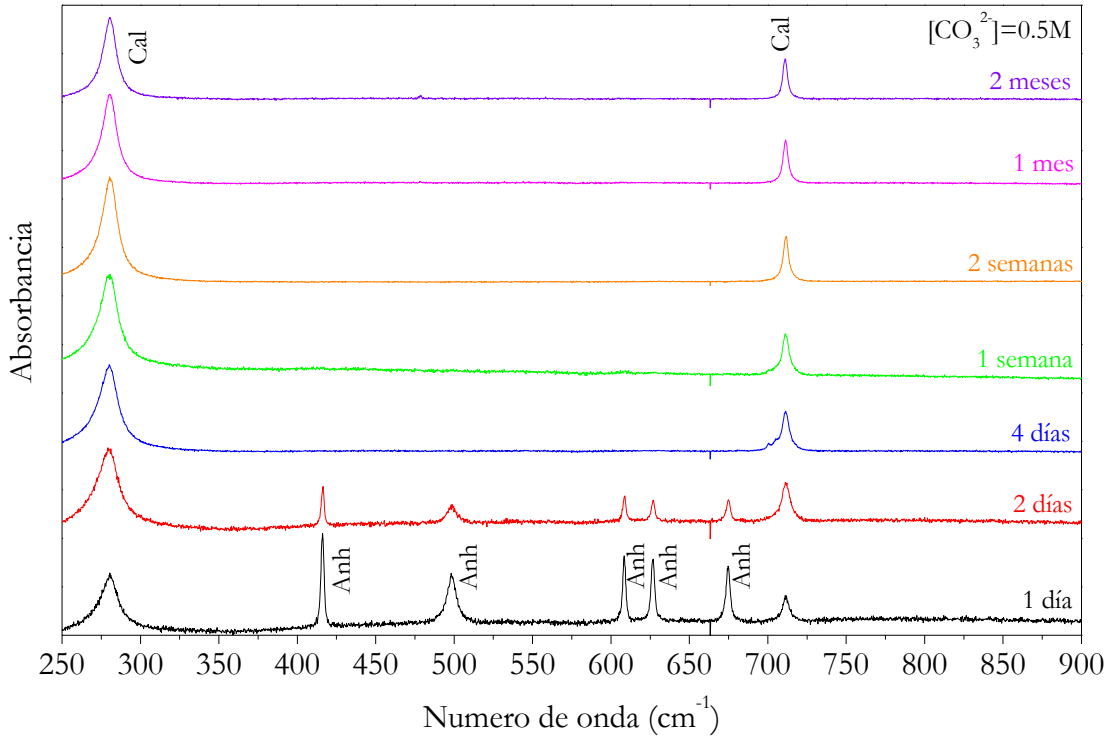

Figura 9.5. Espectros Raman entre 250 cm^{-1} y 900 cm^{-1} obtenidos en de la muestras sólidas recuperadas en los experimentos tipo batch de interacción de fragmentos de anhidrita con una disolución de carbonato de 0.5M, tras distintos tiempos de reacción. Se observan las fases calcita y anhidrita.

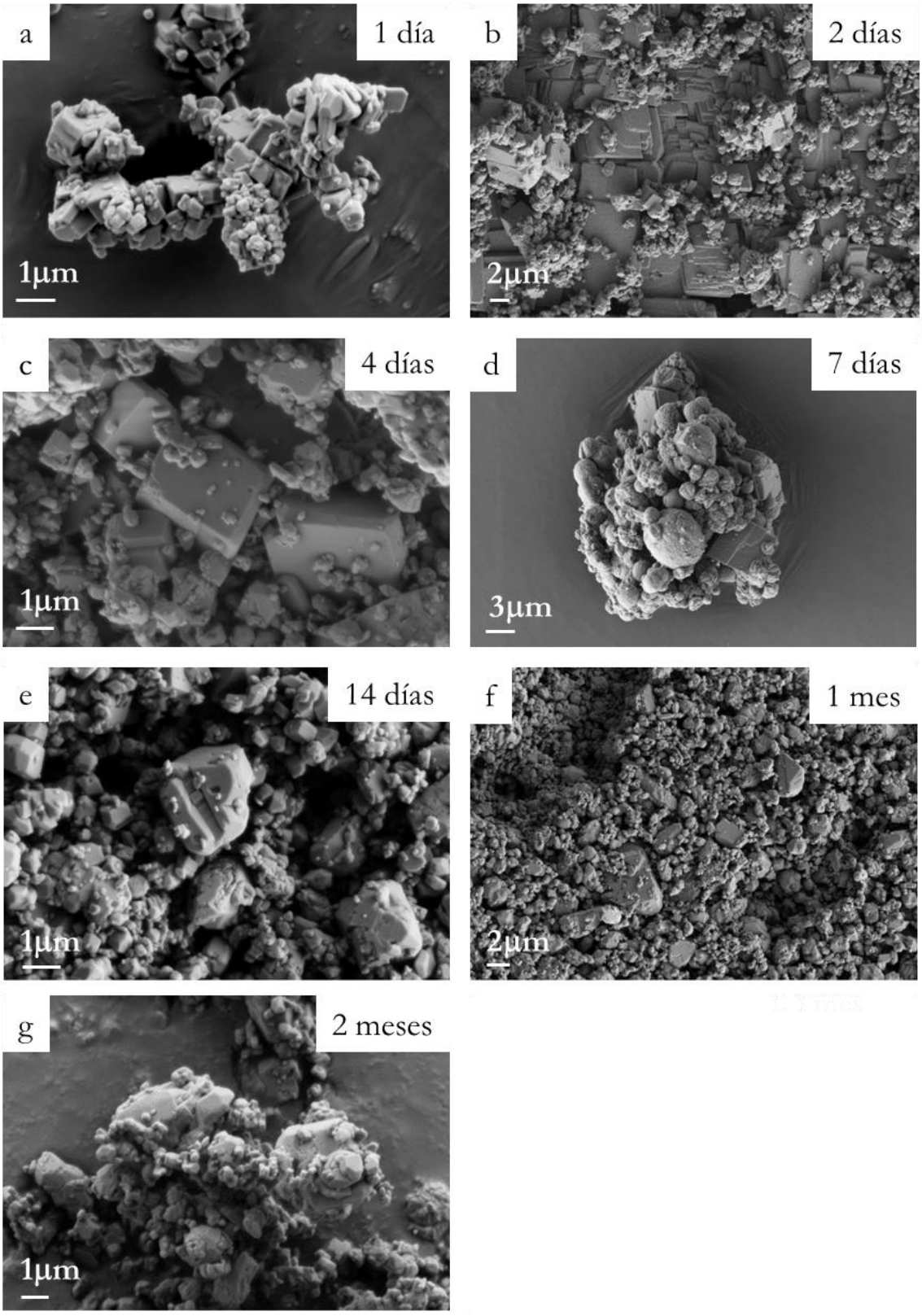

Figura 9.6. Imágenes de SEM de la superficie de la anhidrita tras hacerla reaccionar con una disolución de carbonato 0.5M durante distintos tiempos. En todas las imágenes, el único polimorfo del $CaCO_3$ que se observa es la calcita. Además, tras 7 días de reacción se observa vaterita.

El estudio mediante SEM de las muestras sólidas obtenidas en estos experimentos confirma la presencia de calcita en el sistema desde los primeros momentos de la interacción. En la imagen d de la Figura 9.6, que corresponde a una semana de interacción entre los cristales de anhidrita y la disolución carbonatada con concentración 0.5M se pueden observar formas globulares que pueden atribuirse a la presencia de una pequeña cantidad de vaterita, en consistencia con las conclusiones derivadas del análisis de DRX.

9.1.2. Evolución fisicoquímica de la fase líquida durante la interacción de anhidrita son disoluciones carbonatadas

El estudio de la evolución fisicoquímica de la fase liquida durante su interacción con cristales de anhidrita se ha realizado atendiendo a los cambios que se producen en el pH y en las concentraciones de S, Ca y Na.

9.1.2.1. Evolución del pH

La evolución del pH durante la interacción de cristales de anhidrita con las dos disoluciones carbonatadas consideradas se muestra en la Figura 9.7. Como puede observarse, en ambos casos el pH disminuye muy rápidamente al comienzo del proceso, pero este descenso se ralentiza según avanza la reacción. El resultado es una progresiva reducción de la basicidad de la fase líquida, que en el caso de los experimentos en los que la concentración inicial de carbonato es de 0.05M, el pH final que se alcanza se aproxima a la neutralidad. Por el contrario, cuando la concentración inicial de carbonato es 0.5M el descenso que se observa en el pH de la disolución es mucho menor, manteniéndose en valores próximos a 11 una vez transcurridas 12 horas desde el inicio de la interacción. Por tanto, cuanto mayor es la concentración de carbonato de la que se parte, menos disminuye el pH, y más alcalina es la disolución final.

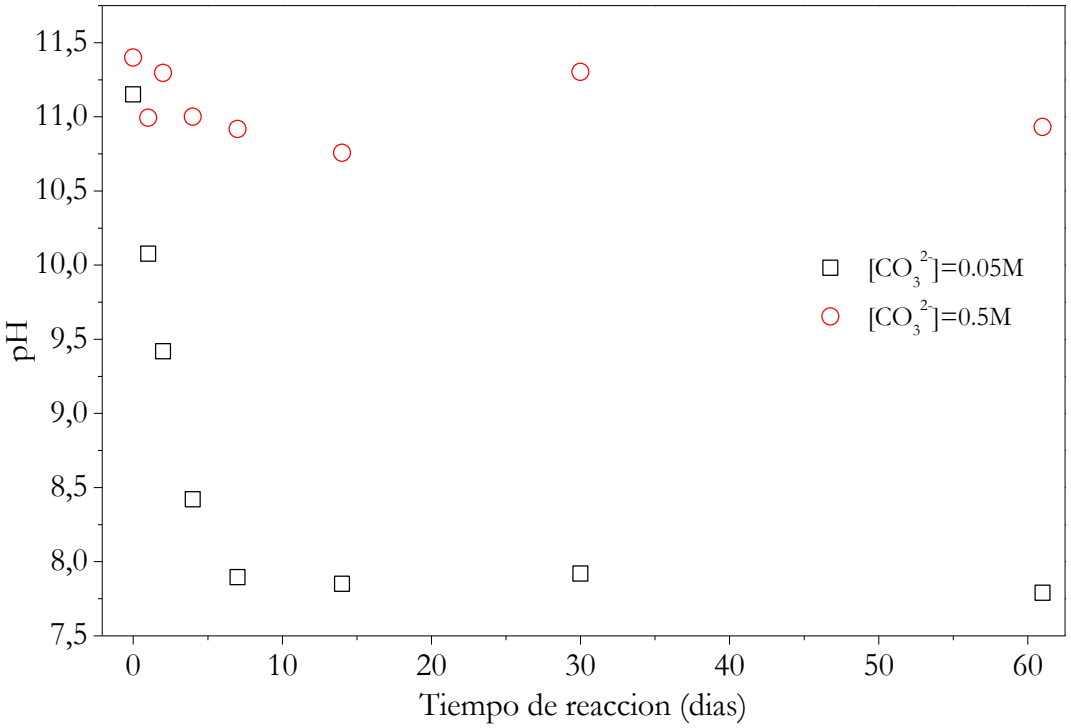

Figura 9.7. Evolución del pH a lo largo de la interacción de fragmentos de anhidrita con disoluciones carbonatas de concentración 0.05M y 0.5M.

9.1.2.2. Evolución de la concentración de S, Ca, Na en la fase líquida

Los análisis de ICP-MS de las disoluciones acuosas recuperadas de los experimentos de tipo "batch" realizados con cristales de anhidrita aportan información sobre la evolución de la concentración de Na, S y Ca en el sistema a lo largo del tiempo. Como se puede ver en la figura 9.8, la concentración Na en la fase líquida se mantiene constante durante todo el proceso. Por el contrario, la concentración de S sufre un aumento rápido durante las etapas iniciales del proceso, hasta alcanzar un valor que se mantiene aproximadamente constante tras un tiempo de reacción de una semana, cuando la concentración inicial de carbonato en la disolución es de 0.5M, y de dos semanas, cuando la concentración inicial de carbonato en la disolución es de 0.05M.

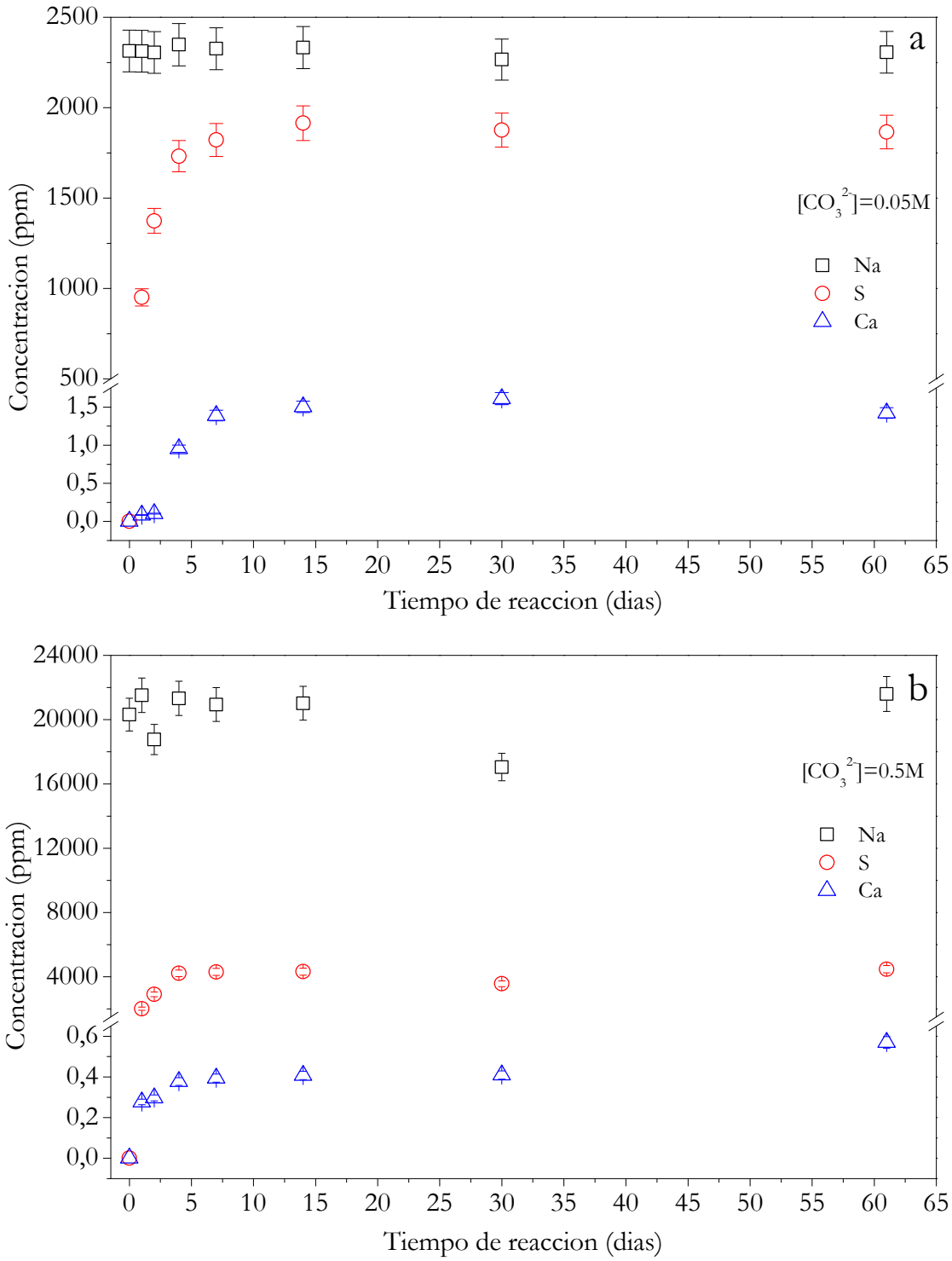

Figura 9.8. Evolución de la concentración de Na, S y Ca (ppm) a lo largo de la interacción de fragmentos de anhidrita con disoluciones carbonatas. Concentración inicial de carbonato (a) 0.05M y (b) 0.5M

Es de destacar que el aumento inicial de la concentración S se produce más rápidamente y alcanza valores finales mucho más altos cuando la concentración inicial de carbonato en la disolución acuosa es mayor, como se puede observar en la Figura 9.9.

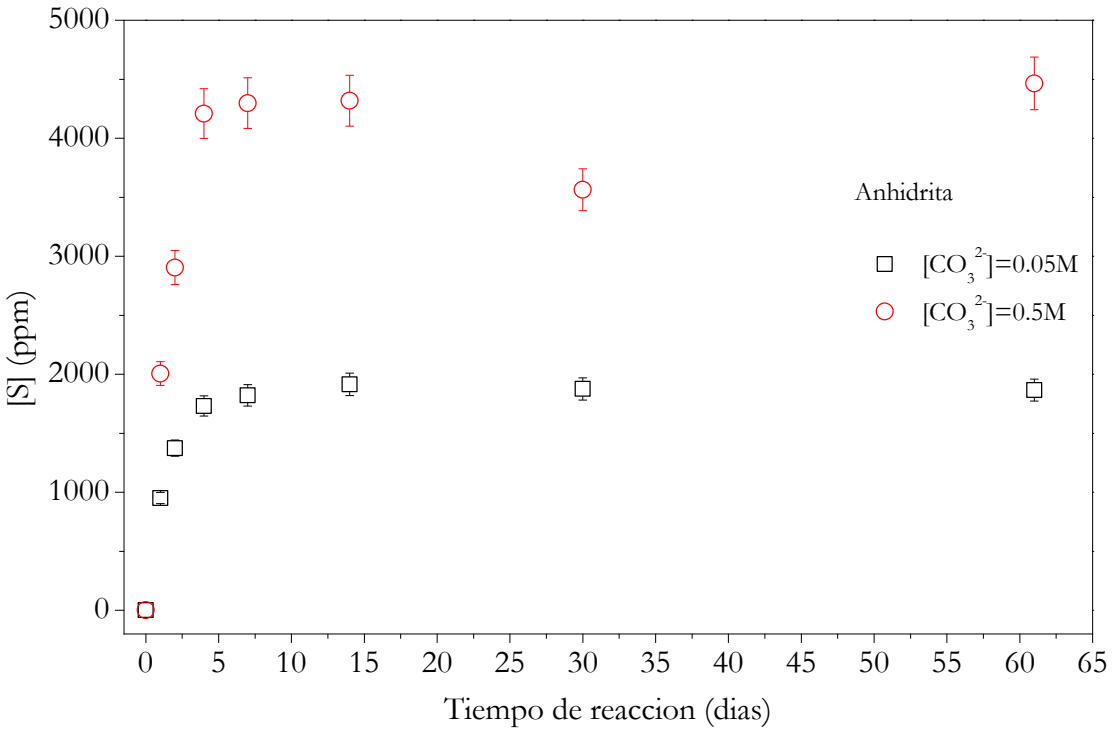

Figura 9.9. Comparación entre la evolución de la concentración de S (ppm) en la fase líquida dependiendo de la concentración inicial de carbonato (0.05M y 0.5M) en la disolución acuosa que interacciona con los cristales de anhidrita.

Por otra parte, la concentración de Ca en la disolución sigue un comportamiento similar al observado para el S, caracterizándose por un aumento inicial rápido hasta alcanzar un valor que se mantiene estable tras un tiempo de interacción de una semana cuando la concentración inicial de carbonato en la disolución es de 0.5M, y de dos semanas, cuando la concentración inicial de carbonato en la disolución es de 0.05M. De forma inversa a lo que se observa para la evolución de la concentración de S, la concentración de Ca en la fase líquida aumenta más rápido y alcanza un valor más alto cuando la concentración inicial de carbonato en la disolución es menor (Figura 9.10).

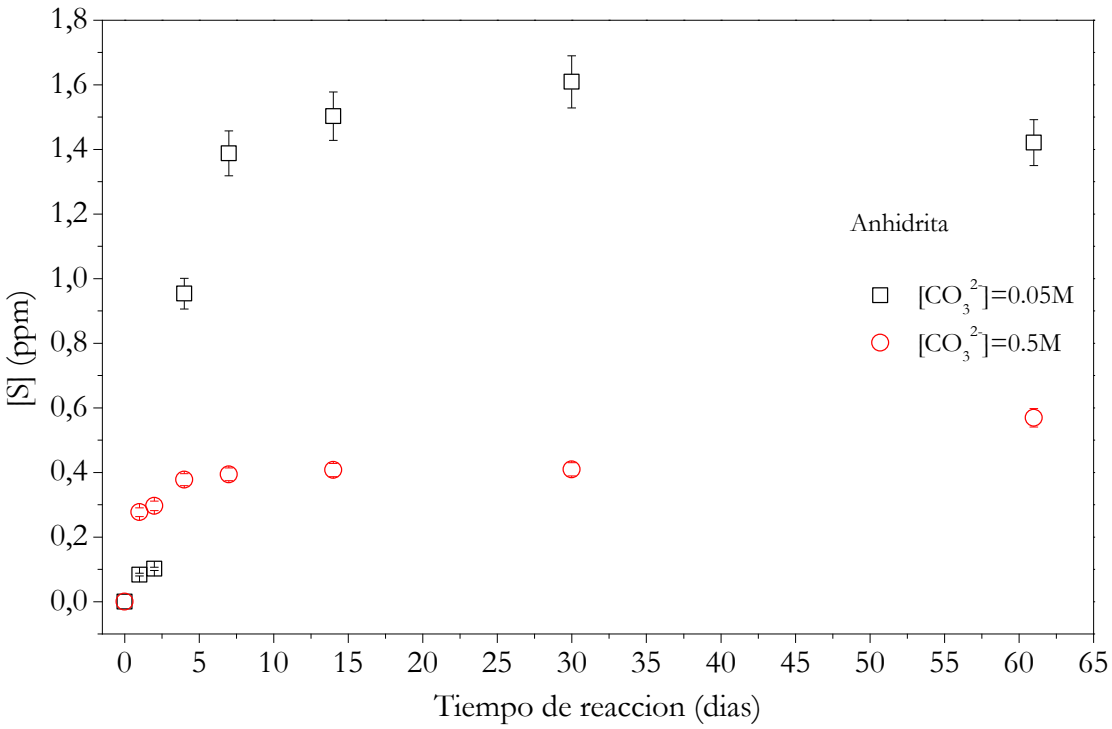

Figura 9.10. Comparación entre la evolución de la concentración de Ca (ppm) en la fase líquida dependiendo de la concentración inicial de carbonato (0.05M y 0.5M) en la disolución acuosa que interacciona con los cristales de anhidrita.

9.1.3. Evolución de la fase sólida durante la interacción de yeso con disoluciones de carbonato

9.1.3.1. Concentración inicial de carbonato 0.05M

Los difractogramas de las muestras sólidas recuperadas de los experimentos de interacción entre cristales de yeso y una disolución de carbonato de concentración 0.05M se muestran en la Figura 9.11. El análisis de estos difractogramas indica que el comportamiento de este sistema es muy similar al observado en el caso de la interacción de anhidrita. Al igual que ocurría entonces, la fase mineral de partida, en este caso, el yeso, se mantiene presente en el sistema a lo largo de toda la interacción. Por lo que se refiere a los polimorfos del $CaCO_3$ que se forman en el sistema como consecuencia de la interacción, el análisis de DRX sólo indica la presencia de calcita. Picos de difracción que pueden atribuirse a esta fase aparecen en los difractogramas a partir de un tiempo de interacción de 1 hora. En ninguno de los difractogramas se encuentran picos que se puedan asignar a otros polimorfos del $CaCO_3$. Aunque en alguno de los difractogramas se ha encontrado algún pico que se

puede atribuir a la anhidrita, la presencia de esta fase se interpreta como debida a una contaminación. Por tanto, a lo largo de todo el proceso de interacción, de acuerdo con los resultados del análisis de difracción de rayos X, las únicas fases presentes en el sistema son yeso y calcita.

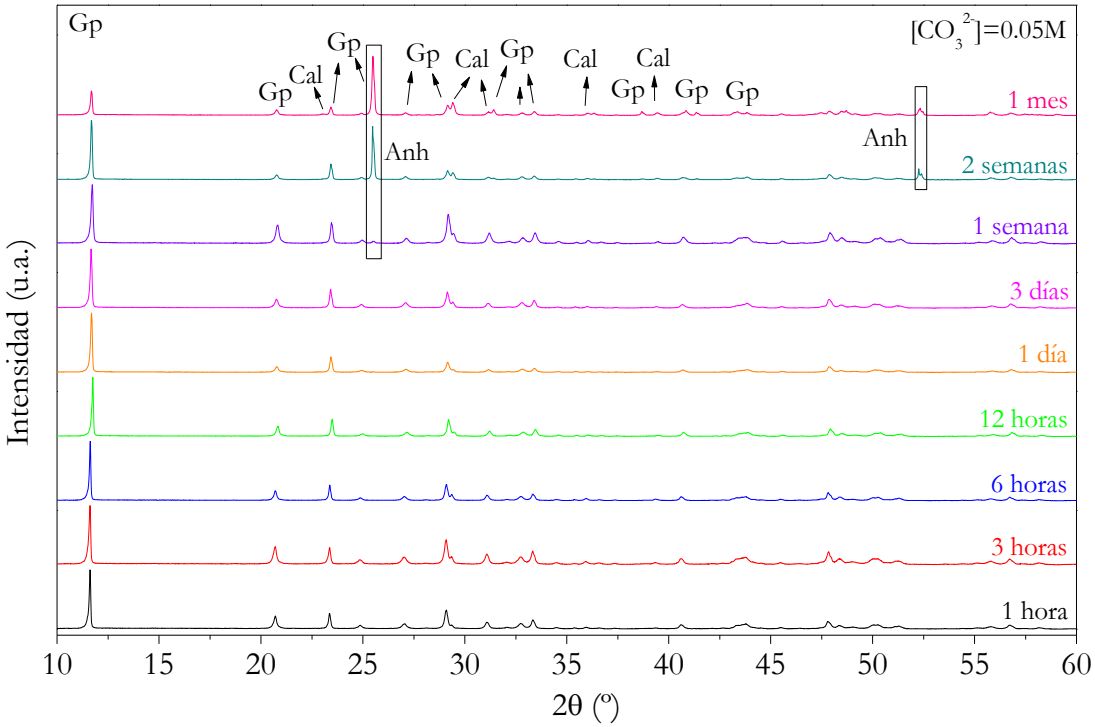

Figura 9.11. Difractogramas de las muestras sólidas recuperadas de los experimentos tipo "batch" correspondientes a la interacción entre cristales de yeso y una disolución de carbonato de concentración 0.05M, tras distintos tiempos de reacción. Todos los picos de difracción se pueden atribuir a yeso o calcita, con la excepción de algunos picos presentes en los difractogramas correspondientes a la muestra sólida recuperada en los experimentos correspondientes a tiempos de interacción más larga. Estos picos se pueden atribuir a la fase anhidrita y se interpretan como una contaminación.

Los resultados de los análisis de DRX son confirmados por los espectros Raman de las muestras sólidas. Estos espectros, que se muestran en la Figura 9.12, confirman a yeso y calcita como las únicas fases minerales presentes en el sistema, independientemente del tiempo de interacción considerado. Como se indica en la figura 7.12, se atribuyen al yeso las bandas que se localizan a números de onda de 415 cm^{-1}, 494 cm^{-1}, 628 cm^{-1} y 671 cm^{-1}. Por otro lado, en la región del espectro situada entre 3300 cm^{-1} and 3600 cm^{-1} se observan dos bandas anchas que se pueden atribuir a las moléculas de agua presentes en la estructura de esta fase

mineral. Finalmente, las bandas que aparecen a 282 cm^{-1} y a 712 cm^{-1} confirman la presencia de calcita. Además, se observa una banda a 752 cm^{-1} que sería consistente con la presencia de vaterita. En ninguno de los espectros que se muestran en la Figura 9.12 se observa la presencia de bandas que pudiera confirmar la presencia de aragonito en algún momento de la interacción.

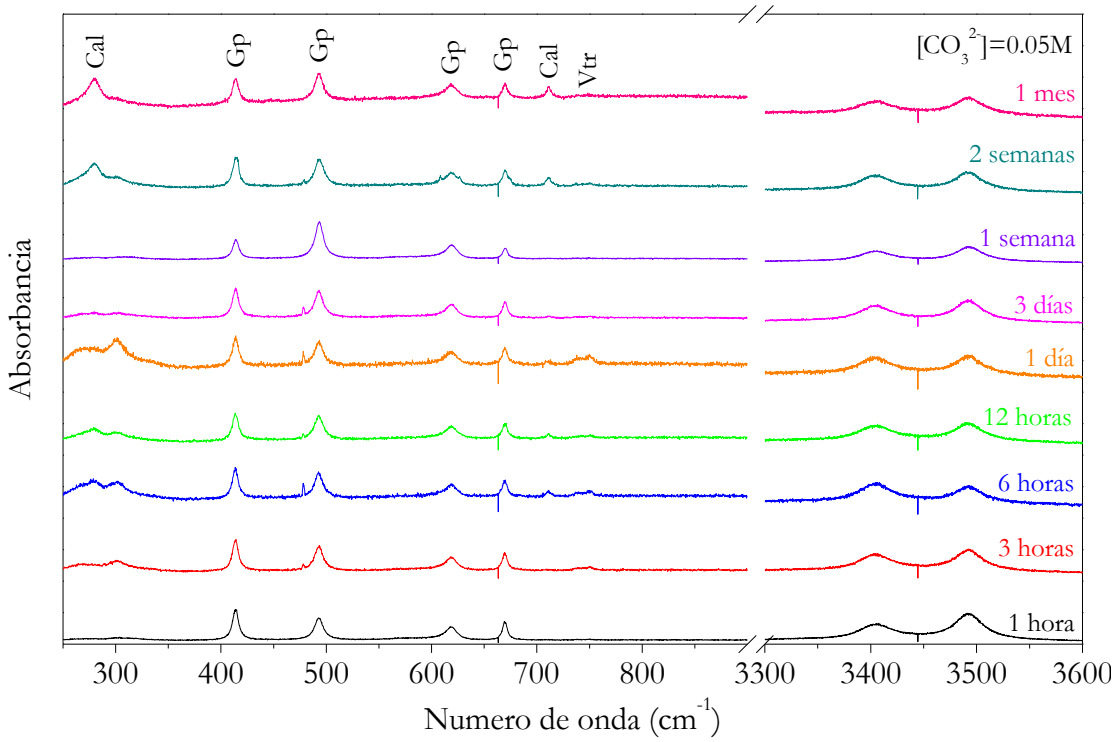

Figura 9.12. Espectros Raman de las muestras sólidas recuperadas de los experimentos tipo "batch" correspondientes a la interacción entre cristales de yeso y una disolución de carbonato de concentración 0.05M, tras distintos tiempos de reacción. Se muestran las regiones del espectro situadas entre 250 cm^{-1} y 900 cm^{-1}, y de 3300 cm^{-1} and 3600 cm^{-1}. Las bandas presentes en estos espectros se pueden atribuir a las fases yeso, calcita y vaterita.

La observación mediante SEM de las muestras sólidas correspondientes a estos experimentos tipo "batch" indica una evolución de fases presentes en el sistema a lo largo del proceso de interacción más compleja que lo que se puede concluir a partir del análisis de DRX y de los espectros Raman. Como se puede observar en las imágenes que se muestran en la Figura 9.13, la interacción de

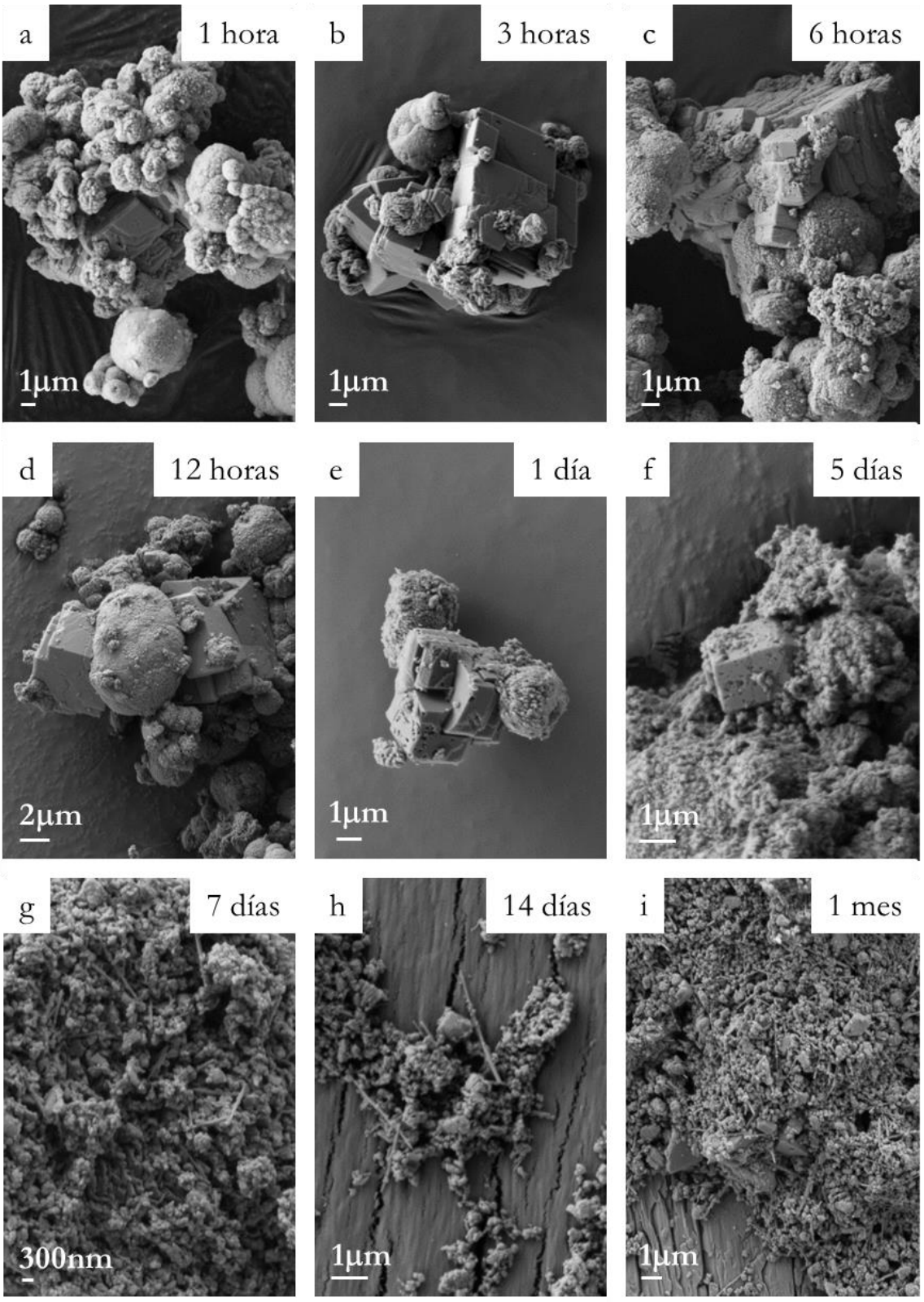

Figura 9.13. Imágenes de SEM de la superficie de cristales de yeso tras reaccionar con una disolución de carbonato 0.05M durante distintos tiempos. En todas las imágenes se puede identificar la presencia de cristales de calcita y vaterita. En las imágenes (g), (h) e (i) se observa también la presencia de unos fragmentos aciculares que pueden deberse a fragmentos de yeso desprendidos de los cristales tras la agitación mecánica.

cristales de yeso con la disolución carbonatada (0.05M) conduce a la formación de calcita desde el tiempo de interacción más corto de los considerados. Los cristales de calcita muestran su típico hábito limitado por las caras del romboedro $\{10\bar{1}4\}$. Es interesante observar que esta morfología va apareciendo peor definida conforme avanza la interacción, con la aparición de algunas superficies y aristas curvas los cristales de calcita, así como de signos de disolución sobre sus caras de romboedro. Junto a los cristales de calcita, desde el tiempo más corto de interacción considerado, también se observa la presencia de agregados cristalinos de morfología globular. Algunos de estos agregados aparecen huecos. De acuerdo con sus características morfológicas, estos agregados se interpretan como vaterita. Esta fase estaría presente en el sistema a todos los tiempos de reacción considerados, coexistiendo con la calcita, además de con el yeso. A tiempos de interacción prolongados (más de 7 días) también se observan unos filamentos en la fase sólida, que pueden atribuirse a fragmentos de yeso desprendidos tras la agitación producida durante la reacción.

9.1.3.2 Concentración inicial de carbonato 0.5M

Los difractogramas de las muestras sólidas recuperadas de los experimentos de interacción entre cristales de yeso y una disolución de carbonato de concentración 0.05M se muestran en la Figura 9.14. El análisis de estos difractogramas indica que el yeso deja de estar presente en el sistema tras 6 horas de interacción con la disolución carbonatada (su característico pico a $2\theta = 11.72°$ no aparece en los difractogramas a partir de ese tiempo). Además, confirma la presencia de calcita en el sistema todos los tiempos de interacción considerados, siendo además la fase mayoritaria tras 6 horas de interacción. En los difractogramas no se observa ningún pico que pueda ser atribuido al aragonito o a la vaterita.

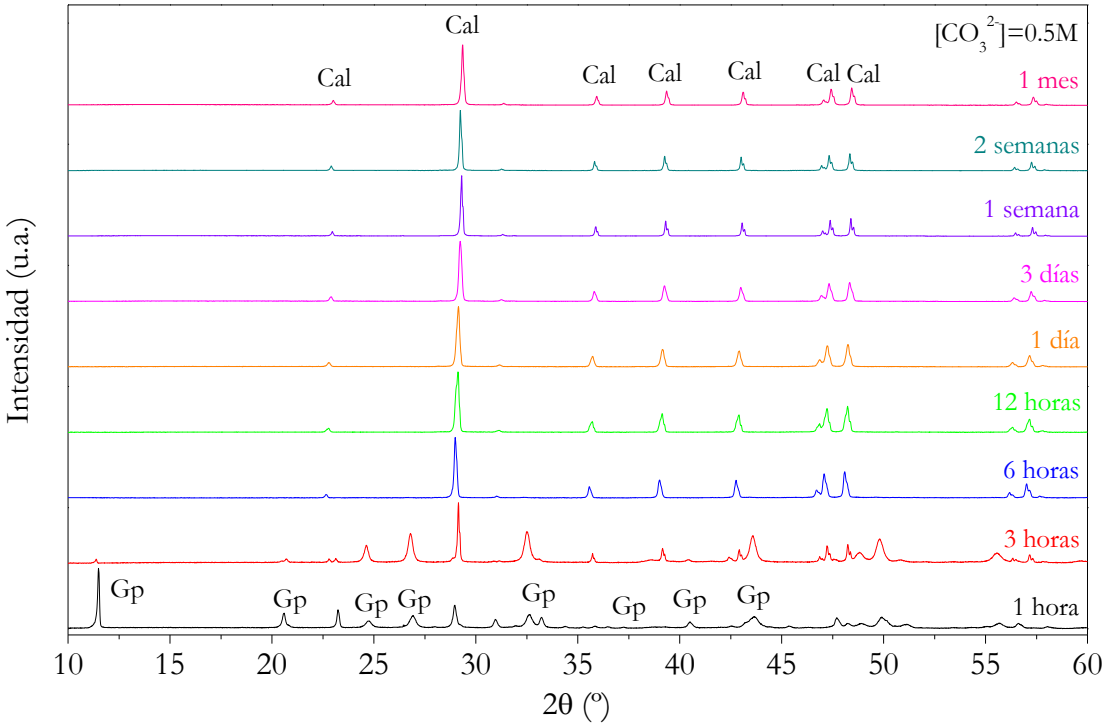

Figura 9.14. Difractogramas de las muestras sólidas recuperadas de los experimentos tipo "batch" correspondientes a la interacción entre cristales de yeso y una disolución de carbonato de concentración 0.5M, tras distintos tiempos de reacción. Todos los picos de difracción se pueden atribuir a yeso o calcita.

El análisis de los espectros Raman de las muestras sólidas obtenidas en estos experimentos (Figura 9.15) apoya los resultados de la DRX. En el espectro correspondiente a 1 y 3 horas de interacción se encuentran bandas a 415 cm^{-1}, 494 cm^{-1}, 628 cm^{-1} y 671 cm^{-1}, además dos bandas anchas en la región entre 3300 cm^{-1} and 3600 cm^{-1}. Todas estas bandas se pueden atribuir al yeso, incluidas sus bandas de agua. Estas bandas no se encuentran presentes en ninguno de los espectros correspondientes a tiempos de interacción más largos, indicando que o bien esta fase ya ha desaparecido del sistema o bien es muy minoritaria. En todos los espectros correspondientes a tiempos de interacción superiores a 1 hora se encuentran dos bandas muy bien definidas a 282 cm^{-1} y a 712 cm^{-1}. Ambas bandas se pueden atribuir a la calcita. En ninguno de los espectros en la Figura 9.15 se observa la presencia de otras bandas que pudieran apoyar la formación de algún otro polimorfo del $CaCO_3$.

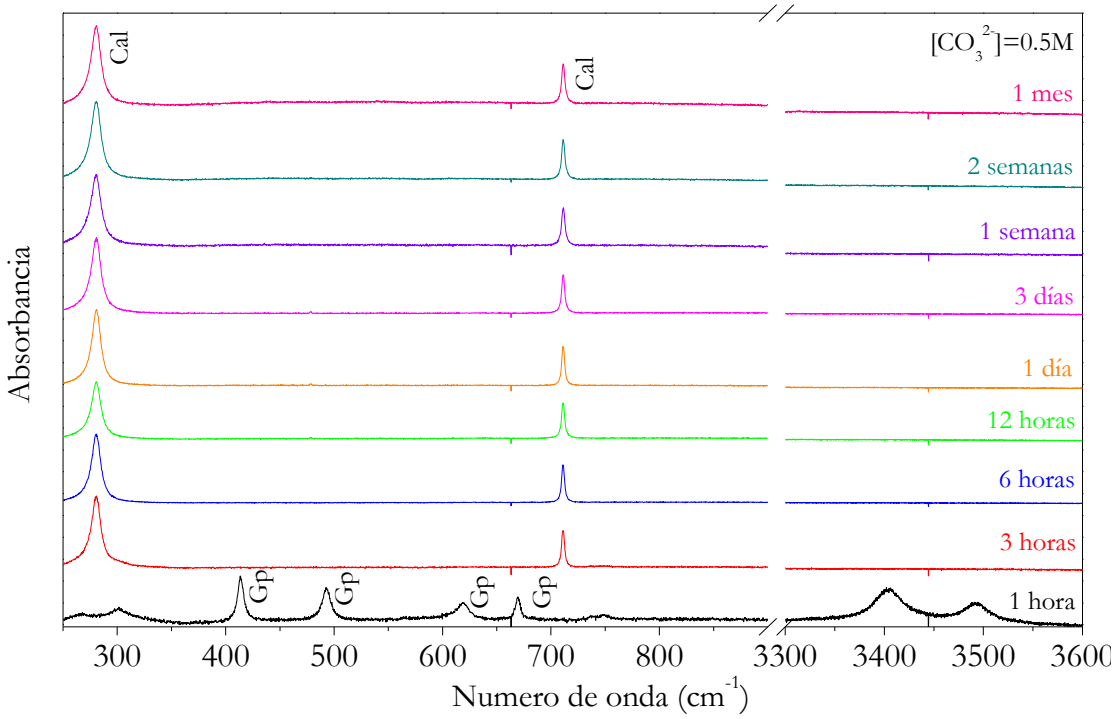

Figura 9.15. Espectros Raman de las muestras sólidas recuperadas de los experimentos tipo "batch" correspondientes a la interacción entre cristales de yeso y una disolución de carbonato de concentración 0.5M, tras distintos tiempos de reacción. Se muestran las regiones del espectro situadas entre 250 cm^{-1} y 900 cm^{-1}, y entre 3300 cm^{-1} y 3600 cm^{-1}. Las bandas presentes en estos espectros se pueden atribuir a las fases yeso (espectro de 1 y 3 horas) y calcita (espectros desde 3 horas).

También en este caso la observación mediante SEM de las muestras sólidas recuperadas de estos experimentos tipo "batch" indica una evolución de las fases presentes en el sistema más compleja que la deducida a partir del análisis de DRX y de los espectros Raman. Como se muestra en la Figura 9.16, en la que aparecen imágenes de SEM de la muestra sólida tras reaccionar los fragmentos de yeso con una disolución de carbonato de concentración 0.5M, a todos los tiempos se observa la presencia en la muestra sólida de cristales con hábito romboédrico, que se pueden interpretar como calcita. Es llamativa la aparición de signos de disolución sobre las caras de los cristales de calcita. Por otro lado, en las imágenes correspondientes a tiempos de interacción de hasta 5 días (Figura 9.16a-f) se observa la presencia de agregados cristalinos globulares junto a la calcita. Estos agregados, que son muy abundantes a tiempos de interacción cortos (1 y 3 horas; Figura 9.16 a, b), se pueden atribuir a vaterita. Además, en las muestras correspondientes a 1 y 2 semanas de interacción (Figura 9.16 g, h), aunque no se observa la presencia de agregados

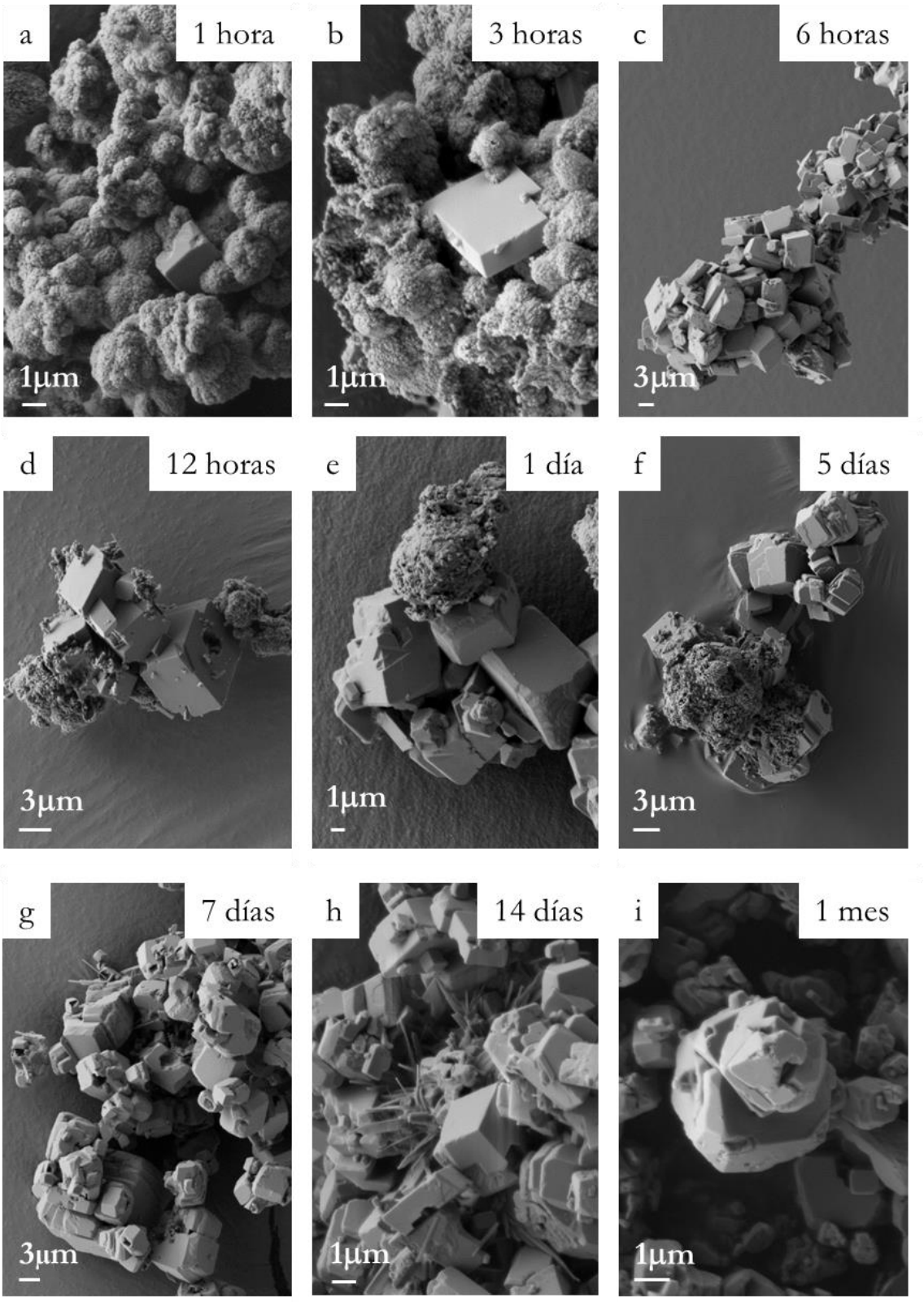

Figura 9.16. Imágenes de SEM de la superficie de cristales de yeso tras reaccionar con una disolución de carbonato 0.5M durante distintos tiempos. En todas las imágenes se puede identificar la presencia de cristales de calcita. Además, se observa la presencia de agregados cristalinos que se pueden atribuir a vaterita en las imágenes (a), b), (c), (d), (e) y (f). En las imágenes (g) y (h) se observa la presencia junto a la calcita de unos agregados formados por cristales alargados y de sección pesudohexagonal que se interpretan como aragonito.

globulares de vaterita, si se observan agregados formados por cristales alargados en disposición fibroso radial. De acuerdo con criterios morfológicos, estos agregados se podrían interpretar como correspondientes a aragonito. Tras 1 mes de interacción, en la muestra sólida sólo se observa la presencia de cristales de calcita, aunque con una morfología en la que se distinguen otras formas además de la de romboedro {10$\bar{1}$4}.

9.1.4. Evolución fisicoquímica de la fase líquida durante la interacción de yeso con disoluciones carbonatadas.

9.1.4.1. Evolución del pH

La evolución del pH durante la interacción de cristales de yeso con las dos disoluciones carbonatadas consideradas se muestra en la Figura 7.17. Este parámetro sufre una evolución similar a la observada en el caso de la interacción con cristales de anhidrita. Así, el pH sufre una rápida caída tras un tiempo de interacción corto. Esta caída es mucho más marcada para la disolución con menor concentración inicial de carbonato (0.05M), aproximándose su pH a 8 tras sólo 2 horas de interacción con los cristales de yeso, y manteniéndose aproximadamente constante este valor para tiempo de interacción más largos. En el caso de la disolución con mayor concentración inicial de carbonato (0.5M), la caída del pH, además de menos marcada, es algo más lenta, requiriéndose tiempos de interacción más largos hasta que se alcanza un estado estable en el valor del pH, que se aproxima a 11. Imagen 9.17.

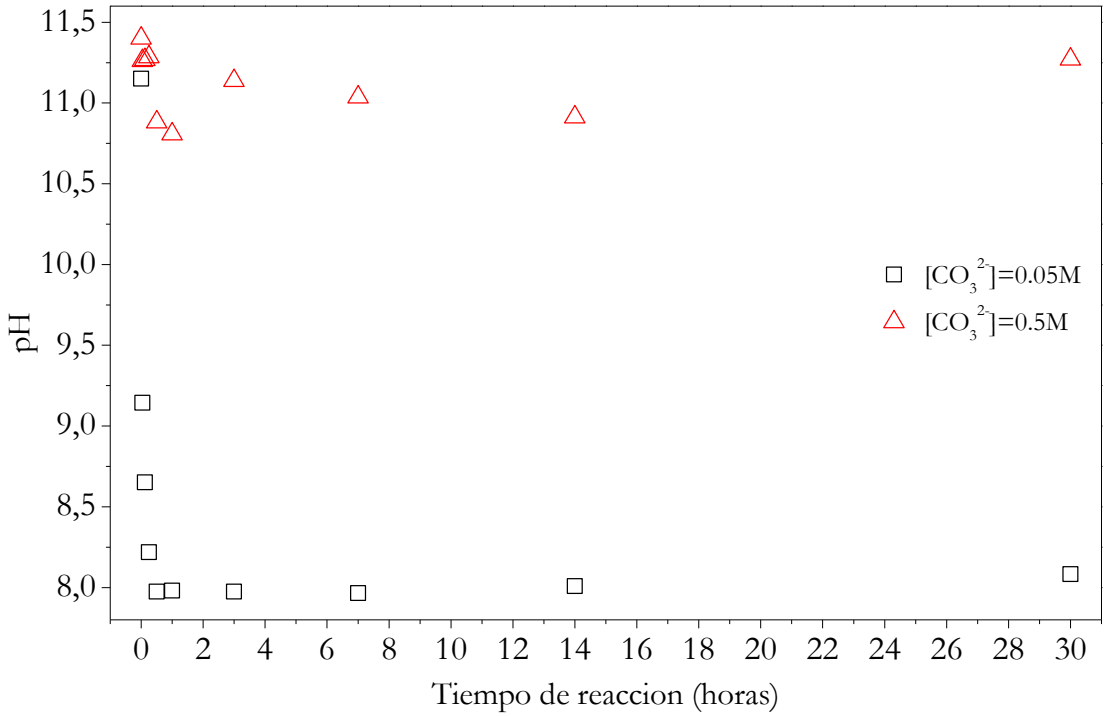

Figura 9.17. Evolución del pH a lo largo de la interacción de cristales de yeso con disoluciones carbonatas de concentración 0.05M y 0.5M.

9.1.4.2. Evolución de la concentración de S, Ca, Na en la fase líquida

La evolución seguida por la concentración de Na, S y Ca a lo largo de la interacción entre los cristales de yeso y las disoluciones carbonatadas es similar a la observada en el caso de los cristales de anhidrita. Así, en el caso del Na, tal como se puede ver en la figura 9.18, la concentración Na en la fase líquida se mantiene constante durante todo el proceso.

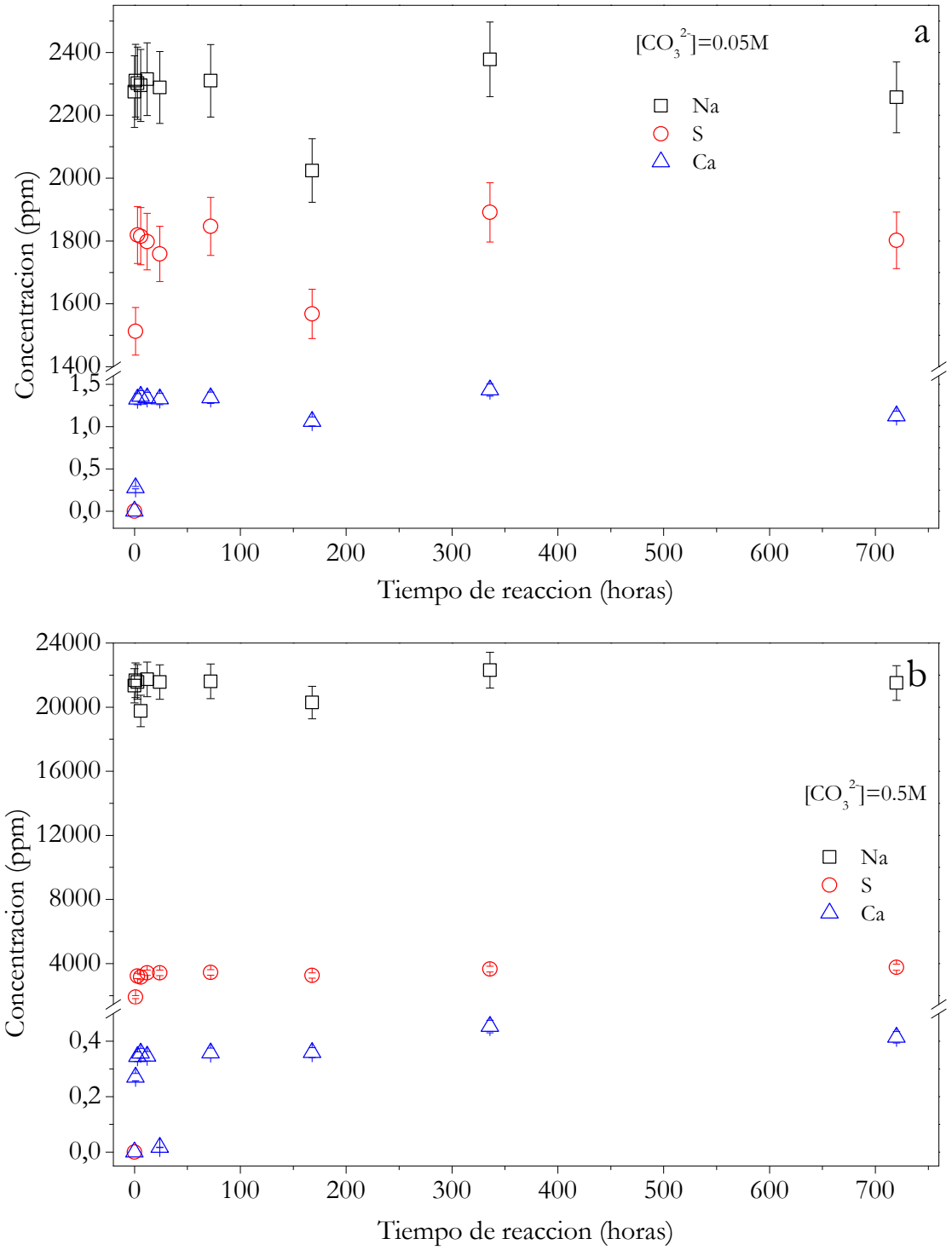

Figura 9.18. Evolución de la concentración de Na, S y Ca (ppm) a lo largo de la interacción de cristales de yeso con disoluciones carbonatas de concentración 0.05M y 0.5M. Concentración inicial de carbonato (a) 0.05M y (b) 0.5M.

Al igual que se ha descrito para el caso de la anhidrita, la evolución de la concentración de concentración de S se caracteriza por un rápido aumento inicial, hasta que se alcanza un estado estable tras un tiempo de interacción de tan sólo

unos pocos minutos. En este caso no se observan diferencias significativas en el tiempo para el cual se alcanza ese estado estable dependiendo de la concentración inicial de carbonato en la disolución, pero el valor de la concentración correspondiente a ese estado estable es mucho más alto cuando la interacción se produce con la disolución con mayor concentración inicial de carbonato (Figura 9.19).

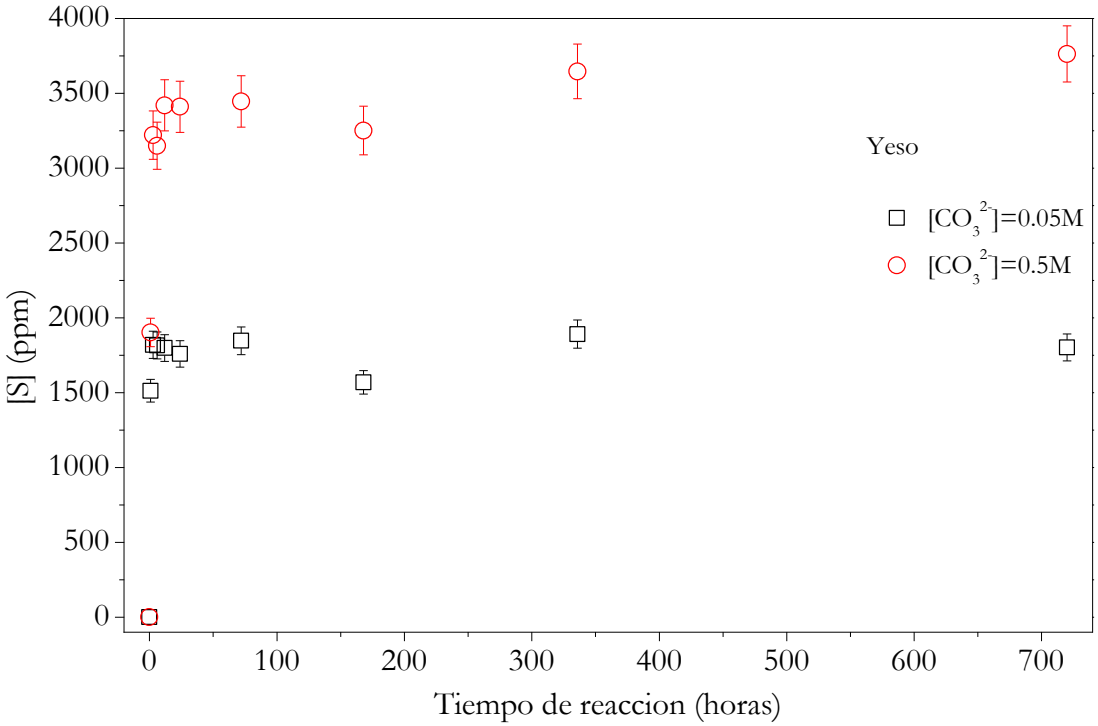

Figura 9.19. Comparación entre la evolución de la concentración de S (ppm) en la fase líquida dependiendo de la concentración inicial de carbonato (0.05M y 0.5M) en la disolución acuosa que interacciona con los cristales de yeso.

Por lo que se refiere a la evolución de la concentración de Ca, esta es paralela a la del S, con un aumento inicial muy rápido, aunque alcanzándose concentraciones significativamente menores que las del S, seguido por una situación de estado estable. Es de destacar que las concentraciones que corresponden a ese estado estable son mucho más altas cuando la interacción de los cristales de yeso tiene lugar con la disolución con menor concentración inicial de carbonato (0.05M) (Figura 9.20), al contrario de lo que se observa para el S (Figura 9.19).

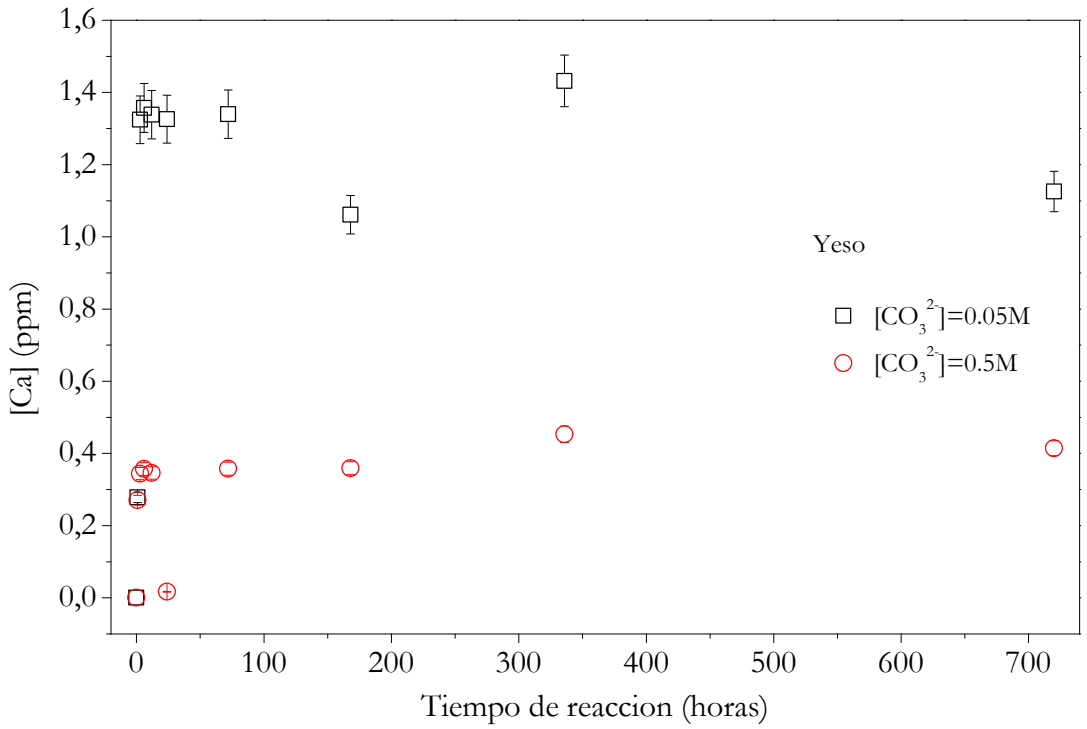

Figura 9.20. Comparación entre la evolución de la concentración de Ca (ppm) en la fase líquida dependiendo de la concentración inicial de carbonato (0.05M y 0.5M) en la disolución acuosa que interacciona con los cristales de yeso.

9.2. DISCUSIÓN

En todos los experimentos llevados a cabo se detectó la presencia de fase(s) de $CaCO_3$ tras los primeros momentos de interacción mineral – fluido. Por otra parte, los diferentes análisis químicos realizados en las disoluciones acuosas mostraron una reducción del pH y de la concentración de Ca^{2+} en las disoluciones acuosas acompañadas de un aumento progresivo de la concentración de SO_4^{2-}, a medida que trascurre la interacción mineral – fluido. Todo ello debe interpretarse como el resultado de una reacción acoplada de disolución-precipitación que implica la disolución de anhidrita y yeso y la precipitación subsiguiente de la fase(s) de $CaCO_3$ de manera similar a la descrita en otros capítulos, de acuerdo con las siguientes reacciones:

$$CaSO_4 \cdot nH_2O_{(s)} \xrightarrow{mH_2O_{(l)}} Ca^{2+} + SO_4^{2-} + (n+m)H_2O_{(l)} \quad (1)$$

$$CO_3^{2-}{}_{(aq)} + Ca^{2+}{}_{(aq)} \rightarrow CaCO_{3(s)} \quad (2)$$

Las reacciones (1) y (2) describen el comportamiento de los sistemas estudiados de una manera demasiado general sin atender a sus peculiaridades ni a su evolución temporal. Sin embargo, se han observados diferencias significativas en los distintos experimentos realizados, que dependen tanto de la concentración inicial de Na_2CO_3 (0.05M y 0.5M) como de la fase mineral utilizada (anhidrita o yeso).

En los experimentos realizados a baja concentración de Na_2CO_3 (0.05M) el mineral de partida está presente durante todo el proceso (2 meses en el caso de la anhidrita y 1 mes en el caso del yeso), ya que éste está en exceso, y el CO_3^{2-} se agota antes que el yeso y la anhidrita. En estos casos, se observan picos de difracción y bandas en Raman de las fases anhidrita y yeso en todo momento. Sin embargo, cuando la concentración de Na_2CO_3 es diez veces mayor (0.5M) se observa cómo los picos de difracción y las bandas de Raman correspondientes a la anhidrita o al yeso desaparecen en todos los difractogramas y espectros obtenidos a partir de 2 semanas y 6 horas, respectivamente.

La ausencia de la anhidrita y del yeso a partir de un tiempo de interacción determinado en los experimentos realizados a altas concentraciones de Na_2CO_3, es el resultado de un exceso de CO_3^{2-} en la disolución acuosa en relación con la fase mineral que conduciría a la precipitación de distintas fases de $CaCO_3$ y, como consecuencia, un rápido consumo de todo el Ca^{2+} procedente de la disolución de las fase mineral que haría desplazar rápidamente la reacción (1) hacia los productos de acuerdo con el principio de Le Châtelier. En esta situación la solución acuosa nunca podría llegar a equilibrarse por completo con respecto a las fases primarias yeso o anhidrita. Por el contrario, en los experimentos en los que se ha empleando concentraciones bajas de Na_2CO_3 (0.05M) no hay suficiente carbonato que pudiera reaccionar con el exceso del ion Ca^{2+} procedente de la disolución de la anhidrita o el yeso. Como consecuencia, el carbonato se consumía por completo y la disolución acuosa tendería hacia el equilibrio con respecto a la fase sólida primaria correspondiente. Este comportamiento se refleja perfectamente en los análisis de la disolución acuosa que muestran, que una vez concluidos los experimentos: a) el pH se mantiene siempre muy elevado (~11) en los experimentos en los que se emplearon altas concentraciones de Na_2CO_3 (0.5M), lo que implica una elevada

concentración de CO_3^{2-} (exceso) en la disolución acuosa, mientras que el pH disminuye considerablemente (~ 8) en los experimentos con una baja concentración de Na_2CO_3 de partida (0.05M) (Figuras 9.7 y 9.17), independientemente de la fase mineral inicial considerada; b) La concentración del ion Ca^{2+} es menor en los experimentos en los que se emplearon mayores concentraciones de Na_2CO_3 (0.5M) lo que implica que el Ca^{2+} se ha ido eliminando a medida que interaccionaba con el carbonato de la disolución (Figuras 9.10 y 9.20); c) Al contrario de lo que ocurre con el Ca^{2+}, la concentración del S es mayor en los experimentos en los que se emplearon concentraciones de Na_2CO_3 más altas (0.5M). Este comportamiento se puede explicar si tenemos en cuenta que este elemento apenas se incorpora en la fase(s) de $CaCO_3$ que precipitan, por lo que prácticamente todo el azufre contenido en las fases primarias pasa directamente a la disolución. Cuando se emplean concentraciones de Na_2CO_3 más bajas (0.05M) la fase primaria no se disuelve en su totalidad y, por tanto, la concentración de S en las disoluciones deberán ser necesariamente más bajas. (Figuras 9.9 y 9.19).

Otro aspecto relevante es el hecho de que la cinética de la reacción es más lenta cuando la fase primaria que reacciona es anhidrita. Así, se ha observado cómo los picos y las bandas correspondientes a la anhidrita desaparecen más lentamente (2 semanas) que los del yeso (6 horas) en los difractogramas y espectros Raman obtenidos en los experimentos en los que se emplearon altas concentraciones de Na_2CO_3. Ello se justifica debido a la mayor reactividad de esta fase en comparación con el yeso. Experimentos realizados con fragmentos de yeso y anhidrita han demostrado que la anhidrita se disuelve del orden de dos órdenes de magnitud más lentamente que el yeso (Jeschke and Draybrot, 2002; Jeschke et al., 2001). Estos resultados han sido también corroborados por estudios de microscopia de fuerza atómica (AFM) que han confirmado una rápida disolución de las superficies de cristales de yeso en comparación con las de la anhidrita (Bosbach et al., 1995; Shindo et al., 1996). Como veremos más adelante, las diferencias en la cinética de disolución de ambas fases puede explicar también las diferencias observadas en los caminos de reacción. Como resultado de la mayor reactividad del yeso, las pendientes de las curvas que muestran la evolución tanto del pH como de las

concentraciones de Ca y S son mucho más acusadas que en caso de la anhidrita, por lo que el factor limitante que condiciona la velocidad del proceso de disolución-precipitación está claramente controlado por la cinética de disolución de la fase primaria considerada. Por otra parte, la concentración inicial de los reactivos juega un papel menos relevante que la naturaleza de la fase primaria, si bien, como es de esperar, la velocidad de la reacción es ligeramente más rápida en aquellos experimentos en los que se emplearon concentraciones de Na_2CO_3 más altas.

Un último aspecto que debe discutirse es el de los caminos de reacción observados en los distintos experimentos realizados. Los resultados descritos en el apartado anterior muestran que la composición mineral de los precipitados recuperados en los distintos experimentos y su evolución temporal dependen fundamentalmente de la sobresaturación umbral que se alcanza en los distintos experimentos (Prieto et al., 1990). Esta sobresaturación umbral depende a su vez de tres factores fundamentales: a) la concentración inicial de Na_2CO_3 empleada, b) la reactividad de las fases consideradas y c) la existencia de relaciones estructurales entre la fase primaria y los distintos polimorfos de $CaCO_3$ que pueden formarse. En líneas generales, una baja concentración de Na_2CO_3, baja reactividad de la fase primaria considerada y la existencia de reacciones estructurales entre las fases implicadas va dar lugar a soluciones acuosas poco sobresaturadas con respecto a los posibles polimorfos que puedan formarse. Otro factor a considerar y que pueden jugar un papel relevante en los caminos de reacción es la relación SO_4^{2-}/CO_3^{2-} existente en la disolución acuosa. Como veremos, todos estos factores se interrelacionan entre sí siendo a veces complicado establecer qué factor o factores predominan sobre los otros.

Los polimorfos formados y los caminos de reacción se recogen en la tabla 9.1). En los experimentos de interacción de fragmentos de anhidrita con disoluciones de Na_2CO_3 poco concentradas (0.05M), la sobresaturación umbral alcanzada debe ser relativamente baja debido a la lenta cinética de disolución de la anhidrita. Bajo estas condiciones, la fase termodinámicamente estable, en este caso la calcita, es la fase que más probabilidades tiene de formarse. Además, como se ha discutido en el capítulo 5, la existencia de relaciones epitaxiales entre la calcita y la anhidrita

facilitaría la formación de esta fase al reducir la barrera energética para la nucleación, aun en condiciones de agitación mecánica continuada. En contraposición, la relación SO_4^{2-}/CO_3^{2-} en el momento de la nucleación sería presumiblemente elevada pero posiblemente no lo suficiente como para inhibir la formación de calcita y favorecer la precipitación de vaterita, como ocurría en los experimentos de precipitación directa (ver capítulo 8). Por otra parte, no es de descartar que en estas condiciones la disolución acuosa esté subsaturada con respecto a esta fase, por lo que su precipitación estaría termodinámicamente impedida. En los experimentos de interacción de la anhidrita con disoluciones más concentradas de Na_2CO_3, la sobresaturación umbral en el momento de nucleación sería algo mayor lo que justificaría la precipitación de pequeñas cantidades de vaterita de acuerdo con la regla de Ostwald (Shönel and Garside, 1992). La vaterita metaestable se transformaría posteriormente a calcita. Resultados similares se han observado en experimentos de interacción con monocristal realizados en medios acuosa sin agitación mecánica (Roncal-Herrero et al., 2017). El yeso se diferencia de la calcita en dos aspectos relevantes. En primer lugar, y tal como hemos visto, su reactividad es bastante mayor que la de la anhidrita, lo que facilita que la sobresaturación umbral alcanzada por la disolución acuosa en el momento de la nucleación sea más elevada. Por otra parte, no existen relaciones estructurales evidentes que puedan justificar el crecimiento epitaxial de calcita u otro polimorfo de $CaCO_3$ sobre su superficie. Bajo estas condiciones, los caminos de reacción observados son algo complejos y diferentes a los observados utilizando fragmentos de anhidrita. Así, partiendo de concentraciones bajas de Na_2CO_3 (0.05M), se observa, además de cristales de calcita, pequeños precipitados de vaterita en las imágenes de SEM (y como bandas muy débiles en los espectros Raman) que permanecen estables incluso en los experimentos de interacción de más larga duración (30 días). La estabilidad de la vaterita se vería también favorecida por una elevada relación SO_4^{2-}/CO_3^{2-} en la disolución acuosa, de manera similar a como se ha discutido en los experimentos de precipitación (ver capítulo 8). Por último, en los experimentos de mayor concentración de Na_2CO_3 (0.5M), se observa, además de calcita y vaterita, la formación de cristales de aragonito entre 1 y dos semanas de interacción. En esas condiciones la concentración de sulfato en la disolución acuosa es muy elevada

(todo el yeso se ha disuelto) lo que favorecería la inhibición de la calcita y, por tanto, la precipitación de aragonito.

Tabla 9.1. Resumen de los polimorfos formados en las reacciones de carbonatación con concentraciones de carbonato 0.05M y 0.5M, y partiendo de yeso y anhidrita.

	Anhidrita	Yeso
$[CO_3^{2-}]_0$=0.05M	Anh+Cal	Gp+Cal+Vtr
$[CO_3^{2-}]_0$=0.5M	Anh+Cal+Vtr → Cal	Gp+Vtr+Cal → Vtr+Cal → Cal+Arg

CONCLUSIONS

CONCLUSIONS

- The carbonation of anhydrite has a topotactic character that implies the epitactic nucleation of calcite on the three main cleavage planes of anhydrite, (100), (010) and (001).
- The development of this epitaxy is promoted by the character F of all the surfaces involved, the $\{10\bar{1}4\}$ surface, in the case of calcite, and the (100), (010) and (001) surfaces, in the case of anhydrite.
- The fact that the directions of parallelism between the structures of calcite and anhydrite contained in the planes of epitaxies ($<\bar{4}41>_{Cal}$ || $[100]_{Anh}$, $[010]_{Anh}$, $[001]_{Anh}$; $[010]_{Cal}$ || $<110>_{Anh}$, $<101>_{Anh}$, $<011>_{Anh}$), not only have similar repetition periods, but also coincide with periodic bound chains (PBC) within the structures of both phases, also contributes to the development of the epitaxy.
- The goodness of matching through the interface is moderate, which determines that the epitactic growth of calcite on the three main cleavage planes of the anhydrite takes place through a Volmer-Weber mechanism.
- This mechanism involves the formation of 3D nuclei of calcite with orientations that are related through the symmetry elements of the anhydrite substrate.
- The growth of these nuclei leads to their coalescence, which results in the formation of induced twins by the substrate.
- As a result of the different orientation of the calcite nuclei, the epitactic layer that covers the anhydrite crystals contains a certain volume of microporosity that is intrinsic to the Volmer-Weber growth mechanism and that prevents the sealing of the surface of the anhydrite by the calcite crystals, allowing the progress of the carbonation reaction from the initial moments.
- The carbonation process rate increases with the carbonate concentration in the fluid phase.
- Regardless of the carbonate concentration of the fluid phase, the carbonation of anhydrite in contact with carbonated solutions occurs through dissolution-

crystallization reactions whose speed is coupled through the interface between the primary and secondary phases(s).

- These dissolution-crystallization reactions lead to the formation of pseudomorphs that contain a large volume of porosity generated during carbonation and which, by compensating for the negative change in molar volume and solubility of the solid phases associated with the reaction, allow it to preserve the external shape of anhydrite crystals.
- The calcite pseudomorphs formed as a consequence of the carbonation of anhydrite show a good preservation of the microtopographic characteristics of the original surfaces of the anhydrite.
- This preservation is better when the concentration of carbonate in the fluid phase is higher, which is explained as a result of a more perfect coupling of the dissolution rates of anhydrite and precipitation of $CaCO_3$ during the carbonation process.
- The characteristics of the porosity generated during the carbonation of anhydrite undergo a spatio-temporal evolution.
- This evolution begins with the development of three well-differentiated regions within the replaced layer, according to the characteristics of the porosity they contain: The region directly in contact with the carbonated solution has a width of less than 100 μm and contains little porosity. The intermediate region is the one that occupies most of the carbonated layer and contains porosity organized in large channels. Finally, the region closest to the interface with the anhydrite nucleus is narrow and contains an organized porosity in small homogeneously distributed pores.
- The evolution of the porosity is the result of a process of "Ostwald ripening" during which the channels grow at the expense of small pores.
- This "Ostwald Ripening" results, ultimately, in the formation of a network of channels distributed along three mutually perpendicular directions.
- In the whole of the channels network, the system constituted by those that are oriented along the direction [001] of the anhydrite appears much better developed and is the only one identifiable in large regions of the pseudomorphs,

which points to a some degree of structural control in the development of porosity.

- The concentration of carbonate in the aqueous solution affects the characteristics of the generated porosity, which represents a greater volume of the total volume of anhydrite replaced and is concentrated in a gap, located at the interface in the primary and secondary phases(s) and whose dimensions increase as the carbonation process advances.
- The concentration of carbonate in the aqueous solution affects the reaction pathways followed by the carbonation process, which only involves the formation of calcite and trace amounts of vaterite when the carbonate concentration is high (0.5M), while it is more complex when the carbonate concentration is low (0.05M).
- In contact with aqueous solutions containing little amount of carbonate, the carbonation of anhydrite proceeds, first, through the formation of mixtures of calcite and vaterite, which are subsequently replaced by calcite and aragonite, the presence of this latter phase being progressively reduced in the carbonated layer with the passage of time.
- Changes in the reaction path during the anhydrite carbonation process are a consequence of the evolution of the $[SO_4^{2-}]/[CO_3^{2-}]$ ratio in the aqueous solution at the interface.
- Precipitation experiments performed to analyze this influence indicate that high ratios inhibit the nucleation and growth of calcite and promote the formation of metastable polymorphs, vaterite and aragonite, increasing the amount of aragonite and reducing the amount of vaterite during aging of the precipitates.
- The results of the precipitation experiments suggest that the $[SO_4^{2-}]/[CO_3^{2-}]$ ratio in the aqueous solution has an influence similar to that of the $[Mg^{2+}]/[Ca^{2+}]$ ratio on the $CaCO_3$ polymorphism.
- This influence is attributed to the combination of kinetic and thermodynamic effects, associated with the different adsorption on the surface and incorporation in the structure of the SO_4^{2-} groups depending on the polymorph.

- The results of batch experiments of interaction between carbonated solutions and fragments of anhydrite and gypsum crystals show that the reaction paths differ in systems with restricted mobility and agitation.

CONCLUSIONES

CONCLUSIONES

- La carbonatación de anhidrita tiene un carácter topotáctico que implica la nucleación epitaxial de calcita sobre los tres planos de exfoliación principales de la anhidrita, (100), (010) y (001).
- El desarrollo de esta epitaxia está favorecido por el carácter F de todas las superficies implicadas, la superficie $\{10\bar{1}4\}$, en el caso de la calcita, y las superficies (100), (010) y (001), en el caso de la anhidrita.
- El hecho de que las direcciones de paralelismo entre las estructuras de calcita y anhidrita contenidas en los planos de epitaxias ($<\bar{4}41>_{Cal}$ || $[100]_{Anh}$, $[010]_{Anh}$, $[001]_{Anh}$; $[010]_{Cal}$ || $<110>_{Anh}$, $<101>_{Anh}$, $<011>_{Anh}$), no sólo tienen periodos de repetición similares, sino que coinciden con cadenas de enlace periódico (PBC) dentro de las estructuras de ambas fases, también contribuye al desarrollo de la epitaxia.
- La bondad del ajuste a través de la interfase es moderada, lo que determina que el crecimiento epitaxial de calcita sobre los tres planos de exfoliación principales de la anhidrita se produzca a través de un mecanismo Volmer-Weber.
- Este mecanismo implica la formación de núcleos 3D de calcita con orientaciones que se relacionan a través de los elementos de simetría del sustrato de anhidrita.
- El crecimiento de estos núcleos conduce a su coalescencia, que tiene como resultado la formación de "maclas inducidas por el sustrato.
- Como consecuencia de la distinta orientación de los núcleos de calcita, la capa epitaxial que recubre la anhidrita contiene un cierto volumen de microporosidad que es intrínseco al mecanismo de crecimiento Volmer-Weber y que previene el sellado de la superficie de la anhidrita por los cristales de calcita, permitiendo el progreso de la reacción de carbonatación desde los momentos iniciales de la misma.
- La velocidad del proceso de carbonatación aumenta con la concentración de carbonato en la fase fluida.
- Independientemente de la concentración de carbonato de la fase fluida, la carbonatación de anhidrita en contacto con disoluciones carbonatadas se

produce a través de reacciones de disolución-cristalización cuya velocidad se acoplada a través de la interfase entre las fases primaria y secundaria(s).

- Estas reacciones de disolución-cristalización conducen a la formación de pseudomorfos que contienen un gran volumen de porosidad generado durante la carbonatación y que, al compensar el cambio negativo de volumen molar y de solubilidad de las fases sólidas asociado a la reacción, permite que se preserve la forma externa de los cristales de anhidrita.
- Los pseudomorfos de calcita formados como consecuencia de la carbonatación de anhidrita muestran una buena preservación de las características microtopográficas de las superficies originales de la anhidrita.
- Esta preservación es mejor cuando la concentración de carbonato en la fase fluida es más alta, lo que se explica como resultado de un acoplamiento más perfecto de las velocidades de disolución de anhidrita y de precipitación de $CaCO_3$ durante el proceso de carbonatación.
- Las características de la porosidad generada durante la carbonatación de anhidrita sufren una evolución espaciotemporal.
- Esta evolución se inicia con el desarrollo de tres regiones bien diferenciadas dentro de la capa reemplazada, de acuerdo con las características de la porosidad que contienen: La región directamente en contacto con la disolución carbonatada tiene una anchura inferior a 100 μm y contiene poca porosidad. La región intermedia es la que ocupa la mayor parte de la capa carbonatada y contiene porosidad organizada en grandes canales. Finalmente, la región más próxima a la interfase con el núcleo de anhidrita es estrecha y contiene una porosidad organizada en poros pequeños homogéneamente distribuidos.
- La evolución de la porosidad es el resultado de un proceso de "Ostwald ripening" durante el cual los canales crecen a expensas de los poros pequeños.
- Este proceso de "Ostwald ripening" resulta, en última instancia, en la formación de un entramado de canales distribuidos a lo largo de tres direcciones mutuamente perpendiculares.
- En el conjunto del entramado de canales, el sistema constituido por aquellos que se orientan a lo largo de la dirección [001] de la anhidrita aparece mucho mejor

desarrollado y es el único identificable en grandes regiones de los pseudomorfos, lo que apunta a un cierto grado de control estructural en el desarrollo de la porosidad.

- La concentración de carbonato en la disolución acuosa afecta a las características de la porosidad generada, que representa un volumen mayor del total del volumen de anhidrita reemplazado y se concentra en un hueco, localizado en la interfase en las fases primaria y secundaria(s) y cuyas dimensiones aumentan al avanzar el proceso de carbonatación.
- La concentración de carbonato en la disolución acuosa afecta al camino de reacción que sigue el proceso de carbonatación, que sólo involucra la formación de calcita y cantidades traza de vaterita cuando la concentración de carbonato es alta (0.5M), mientras que es más complejo cuando la concentración de carbonato es baja (0.05M).
- En contacto con disoluciones acuosas que contienen poco carbonato, la carbonatación de anhidrita procede, primero, a través de la formación de mezclas de calcita y vaterita, que son posteriormente sustituidas por calcita y aragonito, reduciéndose progresivamente la presencia de esta última fase en la capa carbonatada con el paso del tiempo.
- Los cambios en el camino de reacción durante el proceso de carbonatación de anhidrita son consecuencia de la evolución de la relación $[SO_4^{2-}]/[CO_3^{2-}]$ en la disolución acuosa en la interfase.
- Los experimentos de precipitación realizados para analizar esta influencia indican que relaciones altas inhiben la nucleación y crecimiento de calcita y promueven la formación de los polimorfos metaestables, vaterita y aragonito, incrementándose la cantidad de aragonito y reduciéndose la de vaterita durante el envejecimiento de los precipitados.
- Los resultados de los experimentos de precipitación apuntan a que la relación $[SO_4^{2-}]/[CO_3^{2-}]$ en la disolución acuosa tiene una influencia similar a la de la relación $[Mg^{2+}]/[Ca^{2+}]$ sobre el polimorfismo del $CaCO_3$.

- Esta influencia se atribuye a la combinación de efectos cinéticos y termodinámicos, asociados a la diferente adsorción de sobre la superficie e incorporación en la estructura de los grupos SO_4^{2-} dependiendo el polimorfo.
- Los resultados de experimentos tipo batch de interacción entre disoluciones carbonatadas y fragmentos de cristales de anhidrita y yeso evidencian que los caminos de reacción difieren en sistemas con movilidad restringida y con agitación.

BIBLIOGRAFÍA

BIBLIOGRAFÍA

- Alonso-Zarza, A. M.; Sánchez Moya, Y.; Bustillo Revuelta, M. A.; Sopeña, A.; Delgado Huertas, A. Silicification and dolomitization of anhydrite nodules in argillaceous terrestrial deposits: an example of meteoric-dominated diagenesis from the Triassic of central Spain. Sedimentology. 2002, 49, 303-317. DOI: https://doi.org/10.1046/j.1365-3091.2002.00442.x

- Altree-Williams, A.; Pring, A.; Ngothai, Y.; Brugger, J. The carbonatation of anhydrite: kinetics and reaction pathways. ACS Earth and Space Chemistry. 2017, 1, 89-100

- Altree-Williams, A.; Pring, A.; Ngothai, Y.; Brugger, J. Textural and compositional complexities resulting from coupled dissolution–reprecipitation reactions in geomaterials. Earth-Science Reviews. 2015, 150, 628-651. DOI: https://doi.org/10.1016/j.earscirev.2015.08.013

- Anadón, P.; Rosell L.; Talbot, M.R. Carbonate replacement of lacustrine gypsum deposits in two Neogene continental basins, eastern Spain. Sedimentary Geology. 1992, 78**,** 201-216. https://doi.org/10.1016/0037-0738(92)90020-R

- Anthony, J.W.; Bideaux, R.A.; Bladh, K.W.; Nichols, M.C. Eds., Handbook of Mineralogy, Volume V. Mineralogical Society of America, Chantilly, 2003, VA 20151-1110, USA. http://www.handbookofmineralogy.org/

- Aquilano, D.; Bruno, M.; Massaro, F. R.; Rubbo, M. Theoretical equilibrium shape of calcite. 2. [$\bar{4}$41] zone and its role in biomineralization. Crystal Growth and Desing. 2011, 11, 3985-3993. DOI: 10.1021/cg2005584

- Aquilano, D.; Rubbo, M.; Catti, M.; Pavese, A.; Ugliengo, P. Theoretical equilibrium and growth morphology of anhydrite ($CaSO_4$) crystals. Journal of Crystal Growth. 1992, 125, 519-532. DOI: https://doi.org/10.1016/0022-0248(92)90292-Q

- Arroyo-de Dompablo, M. E.; Fernández-González, M. A.; Fernández-Díaz, L. Computational investigation of the influence of tetrahedral oxoanions (sulphate, selenate and chromate) on the stability of calcium carbonate polymorphs. Royal Society of Chemistry Advances. 2015, 5, 59845-59852. DOI: 10.1039/C5RA08574H

- Astilleros, J.M.; Fernández-Díaz, L.; Putnis, A. The role of magnesium in the growth of calcite: An AFM study. Chemical Geology. 2010, 271, 52-58. DOI: 10.1016/j.chemgeo.2009.12.011

- Astilleros, J. M.; Pina, C. M.; Fernández-Díaz, L.; Prieto, M.; Putnis, A. Nanoscale phenomena during the growth of solid solutions on calcite {10$\bar{1}$4} surfaces. Chemical Geology. 2006, 225, 322-335. DOI: https://doi.org/10.1016/j.chemgeo.2005.08.025

- Astilleros, J. M.; Pina, C. M.; Fernández-Díaz, L.; Putnis, A. Nanoscale growth of solids crystallising from multicomponent aqueous solutions. Surface Science. 2003a, L767-L773. DOI: https://doi.org/10.1016/j.susc.2003.08.031

- Astilleros, J.M., Pina, C.M., Fernández-Díaz, L., Putnis, A. Supersaturation functions in binary solid solution-aqueous solution systems. Geochimica et Cosmochimica Acta. 2003b, 67, 1601-1608. DOI: https://doi.org/10.1016/S0016-7037(02)01166-3

- Astilleros, J.M.; Pina, C.M., Fernández-Díaz, L.; Putnis, A. Molecular-scale surface processes during the growth of calcite in the presence of manganese. Geochimica et Cosmochimica Acta. 2002, 66, 3177-3189. DOI: 10.1016/S0016-7037(02)00892-X

- Azam, S. Study on the geological and engineering aspects of anhydrite/gypsum transition in the Arabian Gulf coastal deposits. Bulletin of engineering geology and the environment. 2007, 66, 177-185. DOI: https://doi.org/10.1007/s10064-006-0053-2

- Balan, E.; Aufort, J.; Pouillé, S.; Dabos, M.; Blanchard, M.; Lazzeri, M.; Rollion-Bard, C.; Blamart, D. Infrared spectroscopic study of sulfate-bearing calcite from deep-sea bamboo coral. European Journal of Mineralogy. 2017, 29, 397-408. DOI: https://doi.org/10.1127/ejm/2017/0029-2611

- Balan, E.; Blanchard, M.; Pinilla, C.; Lazzeri, M. First-principles modeling of sulfate incorporation and $^{34}S/^{32}S$ isotopic fractionation in different calcium carbonates. Chemical Geology. 2014, 374, 84-91. DOI: https://doi.org/10.1016/j.chemgeo.2014.03.004

- Baldasari, A.; Speer, J.A. Witherite composition physical properties, and genesis. American Mineralogist. 1979, 64, 742-747

- Beaudoin, N., Hamilton, A., Koehn, D., Shipton, Z. K., & Kelka, U. Reaction-induced porosity fingering: Replacement dynamic and porosity evolution in the KBr-KCl system. Geochimica et Cosmochimica Acta. 2018, 232, 163-180. DOI: https://doi.org/10.1016/j.gca.2018.04.026

- Becker, U.; Risthaus, P.; Brandt, F.; Bosbach, D. Thermodynamic properties and crystal growth behavior of the hashemite ($BaSO_4$–$BaCrO_4$) solid solution. Chemical geology. 2006, 225, 244-255. DOI: https://doi.org/10.1016/j.susc.2007.09.021

- Blount, C. W. Barite solubility and thermodynamic quantities up to 300º C and 1400 bars. Am. Mineral. 1977, 62, 942-957.

- Bosbach, D., Jordan, G., Rammensee, W. Crystal growth and dissolution kinetics of gypsum and fluorite: An in situ Scanning Force Microscope study. European Journal of Mineralogy. 1995, 7, 267-276. DOI: 10.1127/ejm/7/2/0267

- Böttcher, M. E.; Gehlken, P. L.; Fernández-González, Á.; Prieto, M. Characterization of synthetic $BaCO_3$-$SrCO_3$ (witherite-strontianite) solid-solution by Fourier transform infrared spectroscopy. European Journal of Mineralogy. 1997, 9, 519-528. DOI: 10.1127/ejm/9/3/0519

- Bots, P.; Benning, L. G.; Rodriguez-Blanco, J. D.; Roncal-Herrero, T.; Shaw, S. Mechanistic insights into the crystallization of amorphous calcium carbonate (ACC). Crystal Growth & Design. 2012, 12, 3806-3814. DOI: 10.1021/cg300676b

- Bots, P., Benning, L.G.; Rickaby, R.E.M.; Shaw, S. The role of SO_4 in the switch from calcite to aragonite seas. Geology. 2011, 39, 331- 334. DOI: 10.1130/G3161.9

- Brice, W. R.; Chang, L. L. Subsolidus phase relations in aragonite-type carbonates. III. The systems $MgCO_3$-$CaCO_3$-$BaCO_3$, $MgCO_3$-$CaCO_3$-$SrCO_3$, and $MgCO_3$-$SrCO_3$-$BaCO_3$. American Mineralogist: Journal of Earth and Planetary Materials. 1973, 58, 979-985

- Busenberg, E.; Plummer, L. N. The solubility of $BaCO_{3(cr)}$ (witherite) in CO_2-H_20 solutions between 0 and 90° C, evaluation of the association constants of $BaHCO_3^{+}{}_{(aq)}$ and $BaCO_3^{0}{}_{(aq)}$ between 5 and 80° C, and a preliminary evaluation of the thermodynamic properties of $Ba^{2+}{}_{(aq)}$. Geochimica et Cosmochimica Acta. 1986, 50, 2225-2233. DOI: https://doi.org/10.1016/0016-7037(86)90077-3

- Busenberg, E.; Plummer, L. N. Kinetic and thermodynamic factors controlling the distribution of SO_4^{2-} and Na^+ in calcites and selected aragonites. Geochimica et Cosmochimica Acta. 1985, 49, 713-725. DOI: 10.1016-0016-7073(85)90166-8

- Busenberg, E.; Plummer, L. N. The solubility of strontianite ($SrCO_3$) in CO_2-H_2O solutions between 2 and 91° C, the association constants of $SrHCO_3^{+}{}_{(aq)}$ and $SrCO_3^{0}{}_{(aq)}$ between 5 and 80° C, and an evaluation of the thermodynamic properties of $Sr^{2+}{}_{(aq)}$ and $SrCO_{3(cr)}$ at 25° C and 1 atm total pressure. Geochimica et Cosmochimica Acta. 1984, 48, 2021-2035. DOI: https://doi.org/10.1016/0016-7037(84)90383-1

- Cañaveras, J.C.; Sánchez-Moral, S.; Sanz-Rubio, E.; Hoyos M. Meteoric calcitization of magnesite in Miocene lacustrine deposits (Calatayud Basin, NE

Spain). Sedimentary Geology. 1998, 119, 183-194. DOI: https://doi.org/10.1016/S0037-0738(98)00063-3

- Cañaveras, J.C.; Sánchez-Moral, S.; Calvo, J.P.; Hoyos, M.; Ordoñez S. Dedolomites associated with karstification, an example of early dedolomitization in lacustrine sequences from the Tertiary of the Madrid Bassin, Central Spain. Carbonate and Evaporites. 1996, 11, 85-103. DOI: https://doi.org/10.1007/BF03175788

- Cardew, P.T.; Davey, R.J. The Kinetics of Solvent-Mediated Phase Transformations. Proceedings of the Royal Society of London Series A-Mathematical and Physical Sciences. 1985, 398, 415-428. DOI: 10.1098/rspa.1985.0043

- Carlson, W. D. The polymorphs of $CaCO_3$ and the aragonite-calcite transformation. Reviews in Mineralogy, 1983, 11, 191-225.

- Casella, L. A.; He, S.; Griesshaber, E.; Fernández-Díaz, L.; Greiner, M.; Harper, E. M., Jackson D. J.; Ziegler A.; Mavromatis, V.; Dietzel M.; Eisenhauer, A.; Veintemillas-Verdaguer, S.; Brans, Uwe.; Schmahl, W. W. Hydrothermal alteration of aragonitic biocarbonates: assessment of micro-and nanostructural dissolution–reprecipitation and constraints of diagenetic overprint from quantitative statistical grain-area analysis. Biogeosciences. 2018, 15, 7451-7484. DOI: https://doi.org/10.5194/bg-15-7451-2018

- Chang, L.L.Y.; Howie, R.A.; Zussman, J. Rock-forming minerals. Non-silicates: Sulphates, carbonates, Phosphates, Halides. Vol 5B. The Geological Society London. 1998, 383. DOI: 10.1351/pac199769050921

- Chang, L.L.Y. Subsolidus phase relations in aragonite-type carbonates .1. System $CaCO_3$-$SrCO_3$-$BaCO_3$. American Mineralogist. 1971, 56, 1660–1673

- Chavagnac, V.; Ceuleneer, G.; Monnin, C.; Lansac, B.; Hoareau, G.; Boulart, C. Mineralogical assemblages forming at hyperalkaline warm springs hosted on

ultramafic rocks: A case study of Oman and Ligurian ophiolites. Geochemistry, Geophysics, Geosystems. 2013, 14, 2474 -2495. DOI: 10.1002/ggge.20147

- Chernov, A. A. Nucleation and Epitaxy. In Modern Crystallography III. Crystal Growth; Springer Series on Solid-State Science 36; Springer-Verlag: Berlin Heidelberg, 1984, 48−103

- Cody, R. D.; Hull, A. B. Experimental growth of primary anhydrite at low temperatures and water salinities. Geology. 1980, 8, 505-509. DOI: https://doi.org/10.1130/0091-7613(1980)8<505:EGOPAA>2.0.CO;2

- Cruz, J.A.; Sánchez-Pastor, N.; Gigler, A.M.; Fernández-Díaz, L. Vaterite Stability in the Presence of Chromate. Spectroscopy Letters. 2011, 44, 495- 499. DOI: 10.1080/00387010.2011.610408

- Cuesta Mayorga, I.; Astilleros, J. M.; Fernández-Díaz, L.; Morales, J.; Prieto, M., Roncal-Herrero, T.; Benning, L. G. Epitactic overgrowths of calcite ($CaCO_3$) on anhydrite ($CaSO_4$) cleavage surfaces. Crystal Growth & Design. 2018, 18, 1666-1675. DOI: 10.1021/acs.cgd.7b01610

- Davis, K.J.; Wasylenki, L.E.; Dove, P.M.; De Yoreo, J.J. Morphological consequences of differential Mg^{2+} incorporation at structurally distinct steps on calcite. American Mineralogist. 2004, 89, 714-720. DOI: 10.2138/am-2004-5-605

- De Leeuw, N.; Parker, S. Atomistic simulation of the effect of molecular adsorption of water on the surface structure and energies of calcite surfaces. Journal of the Chemical Society, Faraday Transactions. 1997, 93, 467-475

- De Yoreo, J.J.; Gilbert, P.U.P.A.; Sommerdijk, N.A.J.M.; Penn, R.L.; Whitelam, S.; Joester, D.; Zhang, H.; Rimer, J.D.; Navrotsky, A.; Banfield, J.F.; Wallace, A.F.; Michel, F.M.; Meldrum, F.C.; Cölfen, H.; Dove, P.M. Crystallization by particle attachment in synthetic, biogenic, and geologic environments. Science. 2015, 349, 492-502. DOI: 10.1126/science.aaa6760

- Deer W. A.; Howie R. A.; Zussman J. An introduction to the rock forming minerals. 1992. 2nd Edition. Pearson Prentice Hall

- Dejonghe, L.; Demaiffe, D.; Weis, D. Strontium isotope geochemistry of anhydrites and calcite pseudomorphs after anhydrite from Paleozoic formations in Belgium. Chemical Geology. 1998, 144, 63-71. DOI: https://doi.org/10.1016/S0009-2541(97)00110-1

- Dydo, P.; Turek, M.; Ciba, J. Scaling analysis of nanofiltration systems fed with saturated calcium sulfate solutions in the presence of carbonate ions. Desalination. 2003, 159, 245-251. DOI: https://doi.org/10.1016/S0011-9164(03)90076-2

- Effenberger, H.; Mereiter, K.; Zemann, J. Crystal structure refinements of magnesite, calcite, rhodochrosite, siderite, smithonite, and dolomite, with discussion of some aspects of the stereochemistry of calcite type carbonates. Zeitschriff Kristallographie - Crystalline Materials. 1981, 156, 233-243. DOI: https://doi.org/10.1524/zkri.1981.156.14.233

- Falini, G.; Gazzano, M.; Ripamonti, A. Crystallization of calcium carbonate in presence of magnesium and polyelectrolytes. Journal of Crystal Growth. 1994, 137, 577-584. DOI: 10.1016/0022-0248(94)91001-4

- Fernández-Díaz, L.; Fernández-González, A.; Prieto, M. The role of sulfate groups in controlling $CaCO_3$ polymorphism. Geochimica et Cosmochimica Acta. 2010, 74, 6064-6076. DOI: https://doi.org/10.1016/j.gca.2010.08.010

- Fernández-Díaz, L.; Pina, C. M.; Astilleros, J. M.; Sánchez-Pastor, N. The carbonatation of gypsum: Pathways and pseudomorph formation. American Mineralogist. 2009, 94, 1223-1234. DOI: 10.2138/am.2009.3194

- Fernández-Díaz, L.; Astilleros, J.M.; Pina, C.M. The morphology of calcite crystals grown in a porous medium doped with divalent cations. Chemical Geology. 2006, 225, 314-321. DOI: 10.1016/j.chemgeo.2005.08.024

- Fernández-Díaz, L.; Putnis, A.; Prieto, M.; Putnis, C.V. The role of magnesium in the crystallization of calcite and aragonite in a porous medium. Journal of Sedimentary Research. 1996, 66, 482-491. DOI: 10.1306/D4268388-2B26-11D7-8648000102C1865D

- Fernández-González, A. Cristalización de soluciones sólidas completas en sistemas acuosos difusión-reacción. Ph. D. Thesis, University of Oviedo. 1996, 241

- Fernández-González, Á.; Fernández-Díaz, L. Growth of calcium carbonate in the presence of Se(VI) in silica hydrogel. American Mineralogist. 2013, 98, 1824-1833. DOI: 10.2138/am.2013.4397

- Flörke, O. W. Die Kristallarten des SiO_2 und ihr Umwandlungsverhalten. Berichte der Deutschen Keramischen Gesellschaft. 1961, 38, 89-97

- Freyer, D.; Voigt, W. Crystallization and phase stability of $CaSO_4$ and $CaSO_4$ based salts. Monatshefte für Chemie/Chemical Monthly. 2003, 134, 693-719. DOI: https://doi.org/10.1007/s00706-003-0590-3

- Frisia, S.; Borsato, A.; Fairchild, I. J.; Susini, J. Variations in atmospheric sulphate recorded in stalagmites by synchrotron micro-XRF and XANES analyses. Earth and Planetary Science Letters. 2005, 235, 729-740. DOI: https://doi.org/10.1016/j.epsl.2005.03.026

- Gal, A.; Habraken, W.; Gur, D.; Fratzl, P.; Weiner, S.; Addadi, L. Calcite Crystal Growth by a Solid-State Transformation of Stabilized Amorphous Calcium Carbonate Nanospheres in a Hydrogel. Angewandte Chemie. 2013, 125, 4967-4970. DOI: 10.1002/ange.201210329

- Gebauer, D.; Gunawidjaja, P. N.; Ko, J. Y.; Bacsik, Z.; Aziz, B.; Liu, L.; Hu, Y.; Bergström, L.; Tai, C.; Sham, T.; Edén, M.; Hedin, N. Proto-Calcite and Proto-Vaterite in Amorphous Calcium Carbonates. Angewandte Chemie International Edition. 2010, 49, 8889-8891. DOI: 10.1002/anie.201003220

- Gislason, S. R.; Oelkers, E. H. Carbon storage in basalt. Science. 2014, 344, 373-374. DOI: 10.1126/science.1250828

- Godelitsas, A.; Astilleros, J. M. Dissolution, sorption/(re)-precipitation, formation of solid solutions and crystal growth phenomena on mineral surfaces: implications for the removal of toxic metals from the environment. European Mineralogical Union and the Mineralogical Society of Great Britain and Ireland. 2010, 10, 289-324. DOI: 10.1180/EMU-notes.10.8

- González-López, J.; Fernández-González, Á.; Jiménez, A. Precipitation behaviour in the system Ca^{2+}-Co^{2+}-CO_3^{2-}-H_2O at ambient conditions — Amorphous phases and $CaCO_3$ polymorphs. Chemical Geology. 2018, 482, 91-100. DOI: 10.1016/j.chemgeo.2018.02.003

- Grasby, S.E. Naturally precipitating vaterite (μ-CaCO3) spheres: unusual carbonates formed in an extreme environment. Geochimica et Cosmochimica Acta. 2003, 67, 1659-1666. DOI: 10.1016/S0016-7037(00)01304-2

- Griesshaber, E.; Kelm, K.; Sehrbrock, A.; Mader, W.; Mutterlose, J.; Brand, U.; Schmahl, W. W. Amorphous calcium carbonate in the shell material of the brachiopod Megerlia truncata. European Journal of Mineralogy. 2009, 21, 715-723. DOI: 10.1127/0935-1221/2009/0021-1950

- Hanor, J. S. A model for the origin of large carbonate-and evaporite-hosted celestine ($SrSO_4$) deposits. Journal of Sedimentary Research. 2004, 74, 168-175. DOI: https://doi.org/10.1306/092203740168

- Hartman, P.; Perdok, W. On the relations between structure and morphology of crystals. I. Acta Crystallographica. 1955a, 8, 49-52. DOI: https://doi.org/10.1107/S0365110X55000121

- Hartman, P.; Perdok, W. On the relations between structure and morphology of crystals. II. Acta Crystallographica. 1955b, 8, 521-524. DOI: https://doi.org/10.1107/S0365110X55001679

- Hawthorne, F. C.; Ferguson, R. B. Anhydrous sulphates. II. Refinement of the crystal structure of anhydrite. Canadian Mineralogist. 1975, 13, 289-292

- Hawthorne, F. C.; Krivovichev, S. V.; Burns, P. C. The crystal chemistry of sulfate minerals. Reviews in Mineralogy and Geochemistry, 2000, 40, 1-112. DOI: https://doi.org/10.2138/rmg.2000.40.1

- Heijnen, W. M. M. The morphology of gel grown calcite. Neues Jahrbuch für Mineralogie-Monatshefte. 1985, 8, 357-371

- Hövelmann, J.; Austrheim, H.; Jamtveit, B. Microstructure and porosity evolution during experimental carbonation of a natural peridotite. Chemical Geology. 2012, 334, 254-265. DOI: https://doi.org/10.1016/j.chemgeo.2012.10.025

- Hu, Y.-B.; Wolthers, M.; Wolf-Gladrow, D.A.; Nehrke, G. Effect of pH and Phosphate on Calcium Carbonate Polymorphs Precipitated at near-Freezing Temperature. Crystal Growth and Desing. 2015, 15, 1596-1601. DOI: 10.1021/cg500829p

- Hua, B.; Deng, B.; Thornton, E.C.; Yang, J.; Amonette, J.E. Incorporation of Chromate into Calcium Carbonate Structure During Coprecipitation. Water Air and Soil Pollution. 2007, 179, 381- 390. DOI: 10.1007/s11270-006-9242-7

- Jeschke, A.A., and Dreybrodt, W. Pitfalls in the determination of empirical dissolution rate equations of minerals from experimental data and a way out: an iterative procedure to find valid rate equations, applied to Ca-carbonates and –sulphates. Chemical Geology. 2002, 192, 183-194. DOI: https://doi.org/10.1016/S0009-2541(02)00135-3

- Jeschke, A.A., Vosbeck, K., and Dreybrodt, W. Surface controlled dissolution rates of gypsum in aqueous solutions exhibit nonlinear dissolution rates. Geochimica et Cosmochimica Acta. 2001, 65, 27-34. DOI: https://doi.org/10.1016/S0016-7037(00)00510-X

- Jonas, L., John, T., King, H. E., Geisler, T., & Putnis, A. The role of grain boundaries and transient porosity in rocks as fluid pathways for reaction front propagation. Earth and Planetary Science Letters. 2014, 386, 64-74. DOI: https://doi.org/10.1016/j.epsl.2013.10.050

- Jonas, L., John, T., & Putnis, A. Influence of temperature and Cl on the hydrothermal replacement of calcite by apatite and the development of porous microstructures. American Mineralogist. 2013, 98, 1516-1525. DOI: https://doi.org/10.2138/am.2013.4288

- Jroundi, F.; Gonzalez-Muñoz, M.T.; Garcia-Bueno, A.; Rodriguez-Navarro, C. Consolidation of archaeological gypsum plaster by bacterial biomineralization of calcium carbonate. Acta Biomaterialia. 2014, 10, 3844 -3854. DOI: 10.1016/j.actbio.2014.03.007

- Katsifaras, A.; Spanos, N. Effect of inorganic phosphate ions on the spontaneous precipitation of vaterite and on the transformation of vaterite to calcite. Journal of Crystal Growth. 1999, 204, 183-190. DOI: 10.1016/S0022-0248(99)00174-8

- Kelemen, P. B.; Hirth, G. Reaction-driven cracking during retrograde metamorphism: Olivine hydration and carbonation. Earth and Planetary Science Letters. 2012, 345, 81-89. DOI: https://doi.org/10.1016/j.epsl.2012.06.018

- Kelemen, P. B.; Matter, J. In situ carbonation of peridotite for CO_2 storage. Proceedings of the National Academy of Sciences of the United States of America. 2008, 105, 17295-17300. DOI: www.pnas.orgcgidoi10.1073pnas.0805794105

- Kendall, A. C. Late diagenetic calcitization of anhydrite from the Mississippian of Saskatchewan, western Canada. Sedimentology. 2001, 48, 29-55. DOI: https://doi.org/10.1111/j.1365-3091.2001.00350.x

- Kile, D.E.; Eberl, D.D.; Hoch, A.R.; Reddy, M.M. An assessment of calcite crystal growth mechanisms based on crystal size distributions. Geochimica et

Cosmochimica Acta. 2000, 64, 2937-2950. DOI: 10.1016/S0016-7037(00)00394-X

- King, H. E.; Plümper, O.; Putnis, A. Effect of secondary phase formation on the carbonation of olivine. Environmental Science and Technology. 2010, 44, 6503-6509. DOI: 10.1021/es9038193

- Klinkenberg, M.; Weber, J.; Barthel, J.; Vinograd, V.; Poonoosamy, J.; Kruth, M.; Bosbach, D.; Brandt, F. The solid solution–aqueous solution system (Sr, Ba, Ra) SO_4 + H_2O: A combined experimental and theoretical study of phase equilibria at Sr-rich compositions. Chemical Geology, 2018, 497, 1-17. DOI: https://doi.org/10.1016/j.chemgeo.2018.08.009

- Kostov, I.; Kostov, R. I. Crystal habits of minerals. Bulgarian Academic Monographs 1. Pensoft Publishers and Prof. Marin Drinov. Academic Publishing House: Sofia. 1999, 307-308

- Kowacz, M.; Putnis, C.V.; Putnis, A. The Control of Solution Composition on Ligand-Promoted Dissolution: DTPA−Barite Interactions. Crystal Growth and Desing. 2009, 9, 5266-5272. DOI: 10.1021/cg9007894

- Kuhn T.; Herzig P. M.; Hannington M. D.; Garbe-Schönberg D.; P Stoffers. Origin of fluids and anhydrite precipitation in the sediment-hosted Grimsey hydrothermal field north of Iceland. Chemical Geology. 2003, 202, 5-21. DOI : 10.1016/S0009-2541(03)00207-9

- KrystalShaper. Available online: http://www.jcrystal.com/ (accessed on 10 February 2019)

- Lippmann, F. Sedimentary Carbonate Minerals; Springer-Verlag Berlin Heidelberg, 1973; pp 228. DOI: 454 10.1007/987-3-642-65474-9

- Lowenstam, H. A.; Weiner, S. On biomineralization; Oxford University Press. New York, 1989; pp 324

- Mann, S. Biomineralization. Principles and concepts in bioinorganic materials chemistry; Oxford University Press, Inc. New York, 2001; pp 198

- Massaro, F. R.; Pastero, L.; Costa, E.; Sgualdino, G.; Aquilano, D. Single and twinned Li_2CO_3 crystals (zabuyelite) epitaxially grown on {0001} and {10$\bar{1}$4} forms of $CaCO_3$ (calcite) crystals. Crystal Growth and Desing. 2008, 8, 2041-2046. DOI: 10.1021/cg8001515

- Matter, J. M.; Stute, M.; Snæbjörnsdottir, S.Ó.; Oelkers, E. H.; Gislason, S. R.; Aradottir, E. S.; Sigfusson, B.; Gunnarsson, I.; Sigurdardottir, H.; Gunnlaugsson, E.; Axelsson, G.; Alfredsson, H. A.; Wolff-Boenisch, D.; Mesfin, K.; de la Reguera Taya, D. F.; Hall, J.; Dideriksen, K.; Broecker, W. S. Rapid carbon mineralization for permanent disposal of anthropogenic carbon dioxide emissions. Science. 2016, 352, 1312-1314. DOI: 10.1126/science.aad8132

- Matter, J. M.; Kelemen, P. B. Permanent storage of carbon dioxide in geological reservoirs by mineral carbonation. Nature Geoscience. 2009, 2, 837-841. DOI: https://doi.org/10.1038/ngeo683

- Meldrum, F.C.; Cölfen, H. Controlling Mineral Morphologies and Structures in Biological and Synthetic Systems. Chemical Reviews. 2008, 108, 4332-4432. DOI: 10.1021/cr8002856

- Morales, J.; Astilleros, J. M.; Jiménez, A.; Göttlicher, J.; Steininger, R.; Fernández-Díaz, L. Uptake of dissolved lead by anhydrite surfaces. Applied Geochemistry. 2014, 40, 89-96. DOI: https://doi.org/10.1016/j.apgeochem.2013.11.002

- Morales, J.; Astilleros, J. M.; Fernández-Díaz, L.; Álvarez-Lloret, P.; Jiménez, A. Anglesite ($PbSO_4$) epitactic overgrowths and substrate induced twinning on anhydrite ($CaSO_4$) cleavage surfaces. Journal of Crystal Growth. 2013, 380, 130-137. DOI: https://doi.org/10.1016/j.jcrysgro.2013.06.010

- Morse, J.W.; Arvidson, R.S.; Lüttge, A. Calcium carbonate formation and dissolution. Chemical Reviews. 2007, 107, 342-381. DOI: 10.1021/cr050358j

- Morse, J.W.; Mackenzie, F.T. Geochemistry of sedimentary carbonates. Elsevier, Amsterdam, The Netherlands, 1990

- Munz, I. A.; Brandvoll, Ø.; Haug, T. A.; Iden, K.; Smeets, R.; Kihle, J.; Johansen, H. Mechanisms and rates of plagioclase carbonation reactions. Geochimica et Cosmochimica Acta. 2012, 77, 27-51. DOI: https://doi.org/10.1016/j.gca.2011.10.036

- Navrotsky, A. Energetic clues to pathways to biomineralization: Precursors, clusters, and nanoparticles. Proceedings of the National Academy of Sciences. USA. 2004, 101, 12096–12101. DOI: 10.1076/pnas.0404778101

- Oelkers, E. H.; Gislason, S. R.; Matter, J. Mineral Carbonation of CO_2. Elements. 2008, 4, 333-337. DOI: 10.2113/gselements.4.5.333

- Ogino, T.; Suzuki, T.; Sawada, K. The formation and transformation mechanism of calcium carbonate in water. Geochimica et Cosmochimica Acta. 1987, 51, 2757-2768. DOI: 10.1016/0016-7037(87)90155-4

- Olajire, A. A. A review of mineral carbonation technology in sequestration of CO_2. Journal of Petroleum Science and Engineering. 2013, 109, 364-392. DOI: https://doi.org/10.1016/j.petrol.2013.03.013

- Ortoleva, P., Merino, E., Moore, C., & Chadam, J. Geochemical self-organization I; reaction-transport feedbacks and modeling approach. American Journal of science. 1987, 287, 979-1007.

- Palmer, D. CrystalMaker, v 1.0.4; CrystalMaker Software Ltd: Begbroke, Oxfordshire, England, 2005

- Paquette, J.; Reeder, R. Relationship between surface structure, growth mechanism, and trace element incorporation in calcite. Geochimica et Cosmochimica Acta. 1995, 59, 735-749. DOI: https://doi.org/10.1016/0016-7037(95)00004-J

- Parkhurst, D.L.; Appelo, C.A.J. User's guide to PHREEQC (Version 2): a computer program for speciation, batch-reaction, one-dimensional transport, and inverse geochemical calculations; Water-Resources Investigations Report. 2010, 99-4259; USGS: Denver, CO, USA

- Pedrosa, E. T., Putnis, C. V., & Putnis, A. The pseudomorphic replacement of marble by apatite: The role of fluid composition. Chemical Geology. 2016a, 425, 1-11. DOI: https://doi.org/10.1016/j.chemgeo.2016.01.022

- Pedrosa, E. T., Putnis, C. V., Renard, F., Burgos-Cara, A., Laurich, B., & Putnis, A. Porosity generated during the fluid-mediated replacement of calcite by fluorite. Crystal engineering communications. 2016b, 18, 6867-6874. DOI: 10.1039/C6CE01150K

- Perdikouri, C.; Piazolo, S.; Kasioptas, A.; Schmidt, B. C.; Putnis, A. Hydrothermal replacement of aragonite by calcite: interplay between replacement, fracturing and growth. European Journal of Mineralogy. 2013, 25, 123-136. DOI: https://doi.org/10.1127/0935-1221/2013/0025-2261

- Pérez-Garrido, C.; Astilleros, J. M.; Fernández-Díaz, L.; Prieto, M. In situ AFM study of the interaction between calcite $\{10\bar{1}4\}$ surfaces and supersaturated Mn^{2+}-CO_3^{2-} aqueous solutions. Journal of Crystal Growth. 2009, 311, 4730-4739. DOI: https://doi.org/10.1016/j.jcrysgro.2009.09.017

- Pérez-Garrido, C.; Fernández-Díaz, L.; Pina, C. M.; Prieto, M. In situ AFM observations of the interaction between calcite surfaces $(10\bar{1}4)$ and Cd-bearing aqueous solutions. Surface Science. 2007, 601, 5499-5509. DOI: https://doi.org/10.1016/j.susc.2007.09.021

- Perrin, J.; Rivard, C.; Vielzeuf, D.; Laporte, D.; Fonquernie, C.; Ricolleau, A.; Cotte, M.; Floquet, N. The coordination of sulfur in synthetic and biogenic Mg calcites: The red coral case. Geochimica et Cosmochimica Acta. 2017, 197, 226-244. DOI: https://doi.org/10.1016/j.gca.2016.10.017

- Peuble, S.; Andreani, M.; Gouze, P.; Pollet-Villard, M. ; Reynard, B.; Van de Moortele, B. Multi-scale characterization of the incipient carbonation of peridotite. Chemical Geology. 2018, 476, 150-160. DOI: https://doi.org/10.1016/j.chemgeo.2017.11.013

- Pierre, C.; Rouchy, J. M. Carbonate replacements after sulfate evaporites in the middle Miocene of Egypt. Journal of Sedimentary Research. 1988, 58, 446-456. DOI: https://doi.org/10.1306/212F8DB9-2B24-11D7-8648000102C1865D

- Pinto, A. J.; Jiménez, A.; Prieto, M. Interaction of phosphate bearing solutions with gypsum: Epitaxy and induced twinning of brushite ($CaHPO_4 \cdot 2H_2O$) on the gypsum cleavage surface. American Mineralogist. 2009, 94, 313-322. DOI: https://doi.org/10.2138/am.2009.3046

- Plummer, L.N.; Busenberg, E. The solubilities of calcite, aragonite and vaterite in CO_2-H_2O solutions between 0 and 90° C, and an evaluation of the aqueous model for the system $CaCO_3$-CO_2-H_2O. Geochimica et Cosmochimica Acta. 1982, 46, 1011 -1040. DOI: 10.1016/0016-7037(82)90056-4

- Plümper, O.; Røyne, A.; Magrasó A.; Jamtveit, B. The interface-scale mechanism of reaction-induced fracturing during serpentinization. Geology. 2012, 40, 1103–1106. DOI: https://doi.org/10.1130/G33390.1

- Pohl, W. L. Economic Geology: principles and practice. 2011. Wiley Blackwell. http://bcs.wiley.com/he-bcs/Books?action=index&bcsId=6365&itemId=1444336622

- Pollok, K..; Putnis, C.V.; and Putnis, A. Mineral replacement reactions in solid solution-aqueous solution systems: Volume changes, reactions paths and end-points using the example of model salt systems. American Journal of Science. 2011, 311, 211-223. DOI: 10.2475/03.2011.02

- Power, I. M.; Wilson, S. A.; Dipple, G. M. Serpentinite carbonation for CO_2 sequestration. Elements. 2013, 9, 115-121. DOI: https://doi.org/10.2113/gselements.9.2.115

- Pöml, P.;, Menneken, M.; Stephan, T.; Niedermeier, D. R. D.; Geisler, T.; Putnis, A. Mechanism of hydrothermal alteration of natural self-irradiated and synthetic crystalline titanate-based pyrochlore. Geochimica et Cosmochimica Acta. 2007, 71, 3311-3322. DOI: https://doi.org/10.1016/j.gca.2007.03.031

- Prieto, M.; Astilleros, J. M.; Fernández-Díaz, L. Environmental remediation by crystallization of solid solutions. Elements. 2013, 9, 195-201. DOI: https://doi.org/10.2113/gselements.9.3.195

- Prieto, M., Astilleros, J.M., Pina, C.M., Fernández-Díaz, L., Putnis, A. Comment: supersaturation in binary solid solution-aqueous solution systems. American Journal of Science. 2007, 307, 1034–1045. DOI: 10.2475/07.2007.04

- Prieto, M.; Cubillas P.; Fernández-González, A. Uptake of dissolved Cd by biogenic and abiogenic aragonite: a comparison with sorption onto calcite. Geochimica et Cosmochimica Acta. 2003, 67, 3859-3869. DOI: https://doi.org/10.1016/S0016-7037(03)00309-0

- Prieto, M.; Fernández-González, A.; Fernández-Díaz, L. Nucleation, growth, and zoning phenomena in crystallizing (Ba,Sr)CO_3, Ba(SO_4,CrO_4), (Ba,Sr)SO_4, and (Cd,Ca)CO_3 solid solutions from aqueous solutions. Geochimica et Cosmochimica Acta. 1997, 61, 3383-3397. DOI: https://doi.org/10.1016/S0016-7037(97)00160-9

- Prieto, M., Putnis, A., Fernández-Díaz, L., & López-Andrés, S. Metastability in diffusing-reacting systems. Journal of Crystal Growth. 1994, 142, 225-235. DOI: https://doi.org/10.1016/0022-0248(94)90291-7

- Prieto, M., Putnis, A.; Fernández-Díaz, L. Crystallization of solid-solutions from aqueous-solutions in a porous-medium: Zoning in (Ba,Sr)SO_4. Geological magazine. 1993, 130, 289-299. DOI: https://doi.org/10.1017/S0016756800019981

- Prieto, M., Putnis, A., & Fernandez-Diaz, L. Factors controlling the kinetics of crystallization: supersaturation evolution in a porous medium. Application to

barite crystallization. Geological Magazine. 1990, 127, 485-495. DOI: https://doi.org/10.1017/S0016756800015417

- Putnis, A. Transient porosity resulting from fluid–mineral interaction and its consequences. Reviews in Mineralogy and Geochemistry. 2015, 80, 1-23. DOI : https://doi.org/10.2138/rmg.2015.80.01

- Putnis, A. Mineral replacement reactions. Reviews in mineralogy and geochemistry. 2009, 70, 87-124

- Putnis, A. Mineral replacement reactions: from macroscopic observations to microscopic mechanisms. Mineralogical Magazine. 2002, 66, 689-708. DOI: https://doi.org/10.1180/0026461026650056

- Putnis, A.; Putnis, C. V. The mechanism of reequilibration of solids in the presence of a fluid phase. Journal of Solid State Chemistry. 2007, 180, 1783-1786

- Putnis, A., Prieto, M., & Fernandez-Diaz, L. Fluid supersaturation and crystallization in porous media. Geological Magazine. 1995, 132, 1-13. DOI: https://doi.org/10.1017/S0016756800011389

- Putnis, C. V., Tsukamoto, K., & Nishimura, Y. Direct observations of pseudomorphism: compositional and textural evolution at a fluid-solid interface. American Mineralogist. 2005, 90, 1909-1912. DOI: https://doi.org/10.2138/am.2005.1990

- Qian, G.; Xia, F.; Brugger, J.; Skinner, W.M.; Bel, J.; Chen, G.; Pring A. Replacement of pyrrhotite by pyrite and marcasite under hydrothermal conditions up to 220° C: An experimental study of reaction textures and mechanisms. American Mineralogist. 2011, 96, 1878-1893. DOI: https://doi.org/10.2138/am.2011.3691

- Qian G.; Brugger J.; Skinner W.M.; Chend G.; Pring A. An experimental study of the mechanism of the replacement of magnetite by pyrite up to 300 °C. Geochimica et Cosmochimica Acta. 2010, 74, 5610-5630. DOI: https://doi.org/10.1016/j.gca.2010.06.035

- Radha, A.V.; Navrotsky, A. Thermodynamics of Carbonates. Reviews in Mineralogy and Geochemistry. 2013, 77, 73-121. DOI: 10.2138/rmg.2013.77.3

- Radha, A.V.; Forbes, T.Z.; Killian, C.E.; Gilbert, P.U.P.A.; Navrotsky, A. Transformation and crystallization energetics of synthetic and biogenic amorphous calcium carbonate. Proceedings of the National Academy of Sciences. 2010, 107, 16438–16443. DOI: 10.1073/pnas.1009959107

- Raufaste, C., Jamtveit, B., John, T., Meakin, P., & Dysthe, D. K. The mechanism of porosity formation during solvent-mediated phase transformations. Proceedings of the Royal Society A: Mathematical, Physical and Engineering Sciences. 2010, 467, 1408-1426. DOI: https://doi.org/10.1098/rspa.2010.0469

- Reardon, E.J.; Armstrong, D.K. Celestite ($SrSO_{4(s)}$ solubility in water, sea water and NaCl solution. Geochimica et Cosmochimica Acta. 1987, 51, 63-72. DOI: https://doi.org/10.1016/0016-7037(87)90007-X

- Reddy, M.M.; Wang, K. Crystallization of calcium carbonate in the presence of metal ions: I. Inhibition by magnesium ion at pH 8.8 and 25° C. Journal of Crystal Growth. 1980, 50, 470-480. DOI: 10.1016/0022-0248(80)90095-0

- Reddy, M.M.; Nancollas, G.H. The crystallization of calcium carbonate. IV. The effect of magnesium, strontium and sulfate ions. Journal of Crystal Growth. 1976, 35, 33-38. DOI: 10.1016/0022-0248(76)90240-2

- Redfern, S.; Parker, S. Atomistic simulation of the effects of calcium and strontium defects on the surface structure and stability of $BaSO_4$. Journal of the Chemical Society, Faraday Transactions. 1998, 94, 1947-1952

- Renard, F., Gratier, J. P., Ortoleva, P., Brosse, E., & Bazin, B. Self-organization during reactive fluid flow in a porous medium. Geophysical Research Letters. 1998, 25, 385-388.

- Rendón-Angeles, J. C.; Matamoros-Veloza, Z.; López-Cuevas, J.; Pech-Canul, M. I.; Yanagisawa, K. Stability and direct conversion of mineral barite crystals in

carbonated hydrothermal fluids. Journal of Materials Science. 2008, 43, 2189-2197. DOI: https://doi.org/10.1007/s10853-007-2044-5

- Riechers, S. L.; Kerisit, S. N. Anisotropic growth of otavite on calcite: Implications for heteroepitaxial growth mechanisms. Crystal Growth and Desing. 2018, 18, 159-170. DOI: 10.1021/acs.cgd.7b01055

- Rodríguez, J.D.; Jiménez, A.; Prieto, M.; Torre, L.; García-Granda, S. Interaction of gypsum with As(V)-bearing aqueous solutions: Surface precipitation of guerinite, sainfeldite, and $Ca_2NaH(AsO_4)_2 \cdot 6H_2O$, a synthetic arsenate. American Mineralogist. 2008, 93, 928-939. DOI: https://doi.org/10.2138/am.2008.2750

- Rodríguez-Blanco, J. D.; Jiménez, A.; Prieto, M. Oriented overgrowth of pharmacolite ($CaHAsO_4 \cdot 2H_2O$) on gypsum ($CaSO_4 \cdot 2H_2O$). Crystal Growth and Desing. 2007, 7, 2756-2763. DOI: 10.1021/cg070222+

- Rodriguez-Blanco, J. D.; Shaw, S.; Bots, P.; Roncal-Herrero, T.; Benning, L.G. The role of pH and Mg on the stability and crystallization of amorphous calcium carbonate. Journal of Alloys and Compounds. 2012, 536, S477-S479. DOI: 10.1016/j.jallcom.2011.11.057

- Roncal-Herrero, T.; Astilleros, J. M.; Bots, P.; Rodríguez-Blanco, J. D.; Prieto, M.; Benning, L. G.; Fernández-Díaz, L. Reaction pathways and textural aspects of the replacement of anhydrite by calcite at 25° C. American Mineralogist. 2017, 102, 1270-1278. DOI: http://doi.org/10.2138/am-2017-5963CCBY

- Rouchy, J.M.; Taberner, C.; Blanc-Valleron, M.M.; Sprovieri, R.; Russell, M.; Pierre, C.; Di Stefano, E.; Pueyo, J.J.; Caruso, A.; Dinarés, J.; Gomis-Coll, E.; Cespuglio, G.; Wolff, G.; Ditchfield, P.; Santisteban, C.; Pestrea, S.; Combourieu-Nebout, N.; Santisteban, S.; Grimalt, J.O. Sedimentary and diagenetic markers of the restriction in a marine basin: the Lorca basin (SE Spain) during the Messinian. Sedimentary Geology 1998, 121, 23-55. DOI: https://doi.org/10.1016/S0037-0738(98)00071-2

- Rouchy, J.M.; Bernet-Rollande, M.C.; Maurin, A.F. Descriptive petrography of evaporites: application in the field, subsurface, and laboratory. In: French oil and gas industry association, ed. Evaporitic sequences in the petroleum exploration: Volume 1 Geological Methods, edition Technip. 1994

- Rudge, J. F.; Kelemen, P. B; Spiegelman, M. A simple model of reaction-induced cracking applied to serpentinization and carbonation of peridotite. Earth and Planetary Science Letters. 2010, 291, 215-227. DOI: https://doi.org/10.1016/j.epsl.2010.01.016

- Ruiz-Agudo, E.; Álvarez-Lloret, P.; Ibáñez-Velasco, A.; Ortega-Huertas, M. Crystallographic Control in the Replacement of Calcite by Calcium Sulphates. Crystal Growth and Design. 2016, 16, 4950-4959. DOI: 10.1021/acs.cgd.6b00522

- Ruiz-Agudo, E.; Putnis, C. V.; Putnis, A. Coupled dissolution and precipitation at mineral−fluid interfaces. Chemical Geololy. 2014, 383, 132-146. DOI: https://doi.org/10.1016/j.chemgeo.2014.06.007

- Sánchez-Pastor, N.; Gigler, A.M.; Cruz, J.A.; Park, S.-H.; Jordan, G.; Fernández-Díaz, L. Growth of Calcium Carbonate in the Presence of Cr(VI). Crystal Growth and Desing. 2011, 11, 3081-3089. DOI: 10.1021/cg200357c

- Sánchez-Pastor, N. Cristalización secuencial de sulfatos y carbonatos de bario y estroncio a partir de soluciones acuosas: Relaciones entre morfología cristalina, composición química y fenómenos de superficie a escala molecular. Ph. D. Thesis, University Complutense. 2007, 178

- Sánchez-Pastor, N.; Pina C.M.; Fernández-Díaz, L. A combined in situ AFM and SEM study of the interaction between celestite (001) surfaces and carbonate-bearing aqueous solutions. Surface Science. 2007a, 601, 2973-2982. DOI: https://doi.org/10.1016/j.susc.2007.05.002

- Sánchez-Pastor, N.; Pina C.M.; Fernández-Díaz, L. Interaction between barite and celestite cleavage surfaces and carbonate bearing aqueous solutions. Geochimica et Cosmochimica Acta. 2007b, 71, A872

- Sanz-Rubio, E., Sánchez-Moral, S., Cañaveras, J. C., Calvo, J. P., & Rouchy, J. M. Calcitization of Mg–Ca carbonate and Ca sulphate deposits in a continental Tertiary basin (Calatayud Basin, NE Spain). Sedimentary Geology, 2001, 140, 123-142. DOI: https://doi.org/10.1016/S0037-0738(00)00175-5

- Sawada, K. Mechanisms of crystal growth of ionic crystals in solution. Formation, transformation, and growth inhibition of calcium carbonates. In H. Ohtaki, Ed., Crystallization Processes. 1998, 39-68.

- Sawada, K. The mechanisms of crystallization and transformation of calcium carbonates Pure and Applied Chemistry. 1997, 69, 921-928. DOI: 10.1351/pac199769050921

- Sheikholeslami, R.; Ong, H. W. K. Kinetics and thermodynamics of calcium carbonate and calcium sulfate at salinities up to 1.5 M. Desalination. 2003, 157, 217-234. DOI: https://doi.org/10.1016/S0011-9164(03)00401-6

- Shindo, H.; Igarashi, T.; Karino, W.; Seo, A.; Yamanobe-Hada, M.; Haga, M. Stabilities of crystal faces of anhydrite ($CaSO_4$) compared by AFM observation of facet formation processes in aqueous solutions. Journal of Crystal Growth. 2010, 312, 573-579. DOI: 10.1016/j.jcrysgro.2009.12.001

- Shindo, H.; Seo, A.; Watabe, T. Structures of the $CaSO_4$ (001) surface studied with atomic force microscopy in air and in solution. Physical Chemistry Chemical Physics. 2001, 3, 230-234. DOI: 10.1039/b007614g

- Shindo, H., Seo, A., Itasaka, M., Odaki, T., & Tanaka, K. Stability of surface atomic structures of ionic crystals studied by atomic force microscopy observation of various faces of $CaSO_4$ crystal in solutions. Journal of Vacuum Science & Technology B: Microelectronics and Nanometer Structures

Processing, Measurement, and Phenomena. 1996, 14, 1365-1368. DOI: https://doi.org/10.1116/1.589099

- Shtukenberg, A. G.; Astilleros, J. M.; Putnis, A. Nanoscale observations of epitaxial growth of hashemite on Barite (001). Surface Science. 2005, 590, 212-223. DOI: https://doi.org/10.1016/j.susc.2005.06.013

- Smyth, J.R.S., and McCormick, T.C. Crystallographic Data for Minerals, in: Mineral Physics & Crystallography: A Handbook of Physic Contrasts. 1995, pp 1-17. Washington DC American Geophysical Union

- Söhnel, O.; Garside, J. Precipitation: Basic Principles and Industrial Applications; Butterworth-Heinemann, 1992

- Söhnel, O.; Mullin, J.W. Influence of mixing on batch precipitation. Crystal Research and Technology. 1987, 22, 1235-1240. DOI: 10.1002/crat.2170221004

- Speer, J.A. Crystal chemistry and phase relations of orthorhombic carbonates. Reviews in Mineralogy and Geochemistry. 1983, 145-190. URI: http://eprints.uni-kiel.de/id/eprint/29352

- Speer J.A.; Hensley-Dunn M. Strontianite composition and physical properties. American Mineralogist. 1976, 61, 1001-1004

- Stafford, K. W.; Ulmer-Scholle, D.; Rosales-Lagarde, L. Hypogene calcitization: Evaporite diagenesis in the western Delaware Basin. Carbonates and Evaporites. 2008, 23, 89-103. DOI: https://doi.org/10.1007/BF03176155

- Stanley, S.M.; Hardie, L.A. Secular oscillations in the carbonate mineralogy of reef-building and sediment-producing organisms driven by tectonically forced shifts in seawater chemistry. Palaeogeography, Palaeoclimatology, Palaeoecology. 1998, 144, 3- 19. DOI: 10.1016/S0031-0182(98)00109-6

- Suárez-Orduña R.; Rendón-Angeles J. C.; Yanagisawa K. Kinetic study of the conversion of mineral celestite to strontianite under alkaline hydrothermal

conditions. International Journal of Mineral Processing. 2007, 83, 12-18. DOI: https://doi.org/10.1016/j.minpro.2007.03.003

- Suárez-Orduña R.; Rendón-Angeles J. C.; López-Cuevas J.; Yanagisawa K. The conversion of mineral celestite to strontianite under alkaline hydrothermal conditions. Journal of Physics: Condensed Matter. 2004, 16, S1331–S1344. DOI: https://doi.org/10.1088/0953-8984/16/14/046

- Tang, Y.; Zhang, F.; Cao, Z.; Jing, W.; Chen, Y. Crystallization of $CaCO_3$ in the presence of sulfate and additives: Experimental and molecular dynamics simulation studies. Journal of colloid and interface science. 2012, 377, 430-437. DOI: https://doi.org/10.1016/j.jcis.2012.02.069

- Titiloye, J.O., Parker, S.C. and Mann, S. Atomistic Simulation of Calcite Surfaces and the Influence of Growth Additives on Their Morphology. Journal of Crystal Growth. 1993, 131, 553-545. DOI: 10.1016/0022-0248(93)90205-B

- Tollefsen, E.; Stockmann, G.; Skelton, A.; Mörth, C.-M.; Dupraz, C.; Sturkell, E. Chemical controls on ikaite formation. Mineralogical Magazine. 2018, 82, 1119-1129. DOI: 10.1180/mgm.2018.110

- Tucker, M.E. Sedimentary Petrology: An introduction to the Origin of Sedimentary Rocks, 3rd ed.; Blackwell Science Ltd. Oxford, UK, 2001

- Ulven, O. I.; Beinlich, A.; Hövelmann, J.; Austrheim, H.; Jamtveit, B. Subarctic physicochemical weathering of serpentinized peridotite. Earth and Planetary Science Letters. 2017, 468, 11-26. DOI: https://doi.org/10.1016/j.epsl.2017.03.030

- Van der Merwe, J. H. The role of lattice misfit in epitaxy. Critical Reviews in Solid State and Materials Sciences. 1978, 7, 209-231. DOI: https://doi.org/10.1080/10408437808243439

- Vavouraki, A.I.; Putnis, C.V.; Putnis, A.; Koutsoukos, P.G. An Atomic Force Microscopy study of the growth of calcite in the presence of sodium sulfate. Chemical Geology. 2008, 253, 243-251. DOI: 10.1016/j.chemgeo.2008.05.013

- Wagterveld, R.M.; Yu, M.; Miedema, H.; Witkamp, G.J. Polymorphic change from vaterite to aragonite under influence of sulfate: The "morning star" habit. Journal of Crystal Growth. 2014, 387, 29- 35. DOI: 10.1016/j.jcrysgro.2013.10.044

- Weber, J.; Barthel, J.; Klinkenberg, M.; Bosbach, D.; Kruth, M.; Brandt, F. Retention of ^{226}Ra by barite: The role of internal porosity. Chemical Geology. 2017, 466, 722-732. DOI: https://doi.org/10.1016/j.chemgeo.2017.07.021

- Warren, J. K. Evaporites: Sediments, Resources and Hydrocarbons. Springer: Berlin Heidelberg. 2006. 539-542. ISBN: 13 978-3-540-26011-0

- Weiner, S.; Dove, P. M. An overview of biomineralization processes and the problem of the vital effect. Reviews in Mineralogy and Geochemistry. 2003, 54, 1-29. DOI: 10.2113/0540001

- Xia, F.; Brugger J.;Chen, G.; Ngothai, Y.; O'Neill, B.; Putnis, A.; Pring, A. Mechanism and kinetics of pseudomorphic mineral replacement reactions: A case study of the replacement of pentlandite by violarite. Geochimica el Cosmochimica Acta. 2009a, 73, 1945-1969. DOI: https://doi.org/10.1016/j.gca.2009.01.007

- Xia, F.; Brugger J.; Ngothai, Y.; O'Neill, B.; Chen, G.; Pring, A. Three-dimensional ordered arrays of zeolite nanocrystals with uniform size and orientation by a pseudomorphic coupled dissolution-reprecipitation replacement route. Crystal Growth & Design. 2009b, 9, 4902-4906. DOI: 10.1021/cg900691a

- Zhao, J.; Brugger, J.; Guorong C.; Ngothai, Y.; Pring, A. The replacement of chalcopyrite by bornite under hydrothermal conditions. American Mineralogist. 2014, 99, 343-354. DOI: https://doi.org/10.2138/am.2014.4628

- Zhu, W.; Fusseis, F.; Lisabeth, H.; Xing, T.; Xiao, X.; De Andrade, V.; Karato, S. I. Experimental evidence of reaction induced fracturing during olivine carbonation. Geophysical Research Letters. 2016, 43, 9535-9543. DOI: https://doi.org/10.1002/2016GL070834

ANEXOS

EUROPEAN CRISTALLOGRAPHIC ASSOCIATION 2016

Calcite ($CaCO_3$) epitactic overgrowths on anhydrite ($CaSO_4$) cleavage surfaces

Fernandez-Diaz Lurdes[1,2], Iris Cuesta[1,2], José Manuel Astilleros[1,2], Manuel Prieto[3]

1. Department of Crystallography and Mineralogy, Complutense University of Madrid. Spain
2. Department of Geomaterials, Institute of Geosciences (UCM, CSIC). Spain.
3. Department of Geology, University of Oviedo, Spain

email: ishtar@ucm.es

The mineral replacement of calcium sulfate minerals by calcium carbonate (product phase is a common phenomenon in a wide range of Earth's surface and subsurface environments and often leads to the formation of pseudomorphs. The mineral replacement process is usually triggered by presence of carbonate-rich aqueous solutions in the system and involves the coupling of dissolution and crystallization reactions, according to reaction pathways that mainly depends on the specific calcium sulfate mineral and the concentration of carbonate in the aqueous solution. When the calcium sulfate mineral is anhydrite ($CaSO_4$), the initial stages of mineral replacement reaction are characterized by the simultaneous formation of dissolution pits on anhydrite crystal surfaces and the oriented nucleation of calcite ($CaCO_3$) crystals on these surfaces. The progress of the coupled dissolution-crystallization reactions eventually results in the formation of calcite pseudomorphs after anhydrite. In this work we investigate the crystallographic relationships observed during the development of these reactions between calcite crystals and the three main anhydrite cleavage surfaces, (100), (010) and (001). In all the investigated anhydrite cleavage surfaces, calcite crystals dispose one of their {104} faces in contact and parallel to the substrate. In the case of anhydrite (100) surface the better matching occurs with $[001]_{Anh}$, $[011]_{Anh}$ ∥ $<-441>_{Cal}$, $<010>_{Cal}$. As a consequence, most calcite crystals show this orientation. However, for a few calcite crystals the matching occurs so that $[010]_{Anh}$, $[011]_{Anh}$ ∥ $<-441>_{Cal}$, $<010>_{Cal}$. Although this second matching is characterized by a slightly higher misfit, this still is within the limits required for epitactic nucleation from solution. On anhydrite (010) surface, calcite crystals are oriented according to a similar pattern as observed on (100) surface. Most calcite crystals appear oriented so that $[001]_{Anh}$, $[101]_{Anh}$ ∥ $<-441>_{Cal}$, 2 x $<010>_{Cal}$. This orientation provides an excellent matching between the structures of both phases. However, also in this case a small number of calcite crystals are oriented with $[100]_{Anh}$, $[101]_{Anh}$ ∥ $<-441>_{Cal}$, 2 x $<010>_{Cal}$. Calcite crystals grown on anhydrite (001) also shown two main orientations, with $[100]_{Anh}$, $[110]_{Anh}$ ∥ $<-441>_{Cal}$, $<010>_{Cal}$ and $[100]_{Anh}$, $[010]_{Anh}$ ∥ $[-441]_{Cal}$, $[48\text{-}1]_{Cal}$.

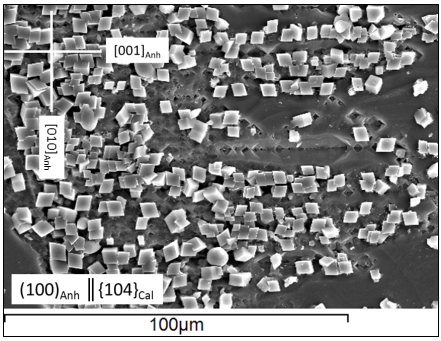

Figure 1. Calcite crystals growing on anhydrite (100) surface. Calcite crystals dispose one of their {104} faces in contact with the substrate. Most of calcite crystals are oriented with $[001]_{Anh}$ and $[011]_{Anh}$ parallel to $<-441>_{Cal}$ and $<010>_{Cal}$.

Keywords: Anhydrite, calcite, epitaxy, pseudomorph, mineral replacement

EUROPEAN MINERALOGICAL CONFERENCE 2016

CARBONATION OF GYPSUM AND ANHYDRITE: INFLUENCE OF THE CARBONATE BEARING SOLUTION CONCENTRATION ON ITS REACTION PATWAYS AND POROSITY.

Cuesta-Mayorga I.*[1,4], Astilleros J.M.[1,2], Roncal-Herrero T.[3],Grattoni C.A.[4],Fernández-Díaz L.[1,2], & Benning L.G.[4,5].

[1] Departamento de Cristalografía y Mineralogía, Universidad Complutense de Madrid, Spain
[2]Institute of Geosciences, Consejo Superior de Investigaciones Científicas, Universidad Complutense de Madrid, Spain
[3] Department of Physics, University of York, York, United Kingdom
[4] School of Earth and Environment, University of Leeds, Leeds, United Kingdom
[5]GeoForschungsZentrum GFZ, Potsdam, Germany
*corresponding email: iriscuesta@ucm.es

Carbonation, pseudomorphism, porosity

Gypsum ($CaSO_4 \cdot 2H_2O$) and anhydrite ($CaSO_4$) are among the most abundant non-silicates minerals in the Earth crust. Their interaction with carbonate-bearing solutions has led to the formation of large volumes of diagenetic carbonate deposits. This process involves the dissolution of the primary sulfates and their pseudomorphic transformation into $CaCO_3$ polymorphs. This occurs via a dissolution and repreciptation mechanism, yet the resulting carbonate polymorphs are different for each sulfate precursor phase. We have previously shown that reacting 0.5M Na_2CO_3 solutions with anhydrite leads to the precipitation of mostly calcite with traces of vaterite. However, the same reaction but in the presence of gypsum occurs via the sequential formation and transformation of amorphous calcium carbonate (ACC), vaterite and calcite (Fernández-Díaz L., 2009). These initial data suggested that such carbonation reactions of gypsum and anhydrite result in both cases in the generation of high amounts of porosity, accompanied by wide, prominent gaps between the parent sulfate and the product carbonates in the case of the carbonation of gypsum. However, a quantitative and time resolved assessment of the reactions was lacking.

In this work we present the results of an experimental study where we addressed the effect of initial aqueous carbonate concentration (0.5, 0.25 and 0.05M Na_2CO_3) on the carbonation of calcium sulfate phases. Our aims were to quantify in a time resolved (over 12 days) manner (i) any changes in reaction pathways and (ii) the generation and evolution of porosity during both anhydrite and gypsum carbonation reactions. We have characterized the changes in $CaCO_3$ polymorphs by combining scanning electron microscopy (SEM), glancing X-ray diffraction and Raman and Fourier transform infrared spectroscopy (FTIR) analyses. The generation and evolution of porosity was quantified over time using mercury porosimetry, computed tomography (CT), BET-surface area and nuclear magnetic resonance (NMR). The results reveal that when reacted with low concentration carbonate solutions (0.05M) both gypsum and anhydrite transform to mixtures of aragonite and calcite, and not as shown above to mainly calcite. Furthermore, the total porosity is inversely proportional to the carbonate concentration. Interestingly, in the case of anhydrite this higher porosity includes the development of a gap, similar to that previously observed for gypsum. Regardless of the initial carbonate concentration and for both calcium sulfates, the sizes of the newly-formed pores rapidly increase at the beginning of the process, but steadily decrease

over the 12 days of reaction. These observations indicate that the reactant concentration plays a crucial role in the carbonation of gypsum and anhydrite. This factor may have influenced the porosity features of many diagenetic limestones and could have important consequences for industrial applications such as oil recovery and CO_2 sequestration.

Fernández-Díaz L., Pina C.M., Astilleros J.M., Sánchez-Pastor N. (2009): The carbonatation of gypsum: Pathways and pseudomorph formation. *Am. Min.* **94**, 1223-1234.

SEM 2017

Estudio Preliminar de los Caminos de Reacción y la Incorporación de Sulfato Durante la Carbonatación de Yeso y Anhidrita a Temperatura Ambiente

/ IRIS CUESTA MAYORGA (1), JOSE MANUEL ASTILLEROS GARCÍA-MONGE (1,2), TERESA RONCAL-HERRERO (3), LURDES FERNÁNDEZ DÍAZ (1,2), LIANE G. BENNING (4,5).*

(1) Departamento de Cristalografía y Mineralogía. Universidad Complutense de Madrid. 28040, Madrid (España)
(2) Instituto de Geociencias (UCM-CSIC). Facultad de CC. Geológicas, Madrid (España)
(3) School of Electronic and Electrical Engineering, University of Leeds, Leeds (Reino Unido)
(4) School of Earth and Environment, University of Leeds, Leeds (Reino Unido)
(5) Interface Geochemistry. German Research Centre for Geosciences (GFZ). Potsdam (Alemania)

INTRODUCCIÓN

Las reacciones que dan lugar al reemplazamiento de un mineral por otro tienen lugar en una amplia variedad de ambientes geológicos y se producen bajo condiciones fisicoquímicas muy diversas. Estas reacciones a menudo implican la disolución de la fase mineral original, como resultado de su interacción con un fluido acuoso, y la precipitación casi simultánea de la fase producto (transformaciones vía solvente). El acople entre la cinética de ambos procesos, disolución y precipitación, no sólo determina la preservación de rasgos microtexturales de la fase mineral original (Putnis, 2002; Fernández-Díaz et al, 2009), tanto de la superficie como del interior del mismo, sino que también, en circunstancias favorables, puede conducir a que se preserve parcialmente el quimismo de la disolución acuosa como consecuencia de la incorporación de los distintos iones disueltos en la fase o fases producto durante su precipitación. Este trabajo se enmarca en un proyecto más amplio enfocado al estudio experimental del reemplazamiento de sulfatos minerales, yeso ($CaSO_4{\cdot}2H_2O$) y anhidrita ($CaSO_4$), por carbonatos de calcio. Debido a la solubilidad relativamente elevada de estos dos minerales ($K_{sp,yeso} = 10^{-4,58}$, $K_{sp,anhidrita} = 10^{-4,36}$) (Parkhurst & Appelo, 1999), las rocas que los contienen sufren a menudo procesos de carbonatación como resultado de su interacción con aguas carbonatadas tanto en ambientes sedimentarios como diagenéticos (Warren, 2016).

El objetivo de este trabajo experimental es doble. Por una parte se pretende estudiar los caminos de reacción que sigue el sistema durante la interacción de pequeños fragmentos de yeso y anhidrita con disoluciones carbonatadas (0,05M y 0,5M de Na_2CO_3), prestando especial atención al efecto que tienen sobre estos caminos de reacción tanto la fase mineral de partida (yeso o anhidrita) como a la concentración de los reactivos. También pretendemos estudiar la posible incorporación de SO_4^{2-} en la estructura de los distintos polimorfos de $CaCO_3$ (calcita y vaterita) precipitados durante el proceso de carbonatación. Este aspecto es relevante ya que a lo largo de las reacciones de reemplazamiento, la relación SO_4^{2-}/CO_3^{2-} en los polimorfos puede verse modificada, y con ella, la solubilidad y estabilidad relativo de estos polimorfos, así como las condiciones de equilibro del sistema. (Arroyo-de Dompablo M.E. et al., 2015).

EXPERIMENTAL

En los experimentos llevados a cabo se emplearon fragmentos de yeso y de anhidrita, de un tamaño comprendido entre 1,6<x<1,0mm, procedentes de Teruel y de Naica (México), respectivamente. Se prepararon una batería de experimentos en los que se hicieron reaccionar 0,50g de mineral con 25mL de disoluciones carbonatadas (Na_2CO_3 0,5M y 0,05M), en matraces Erlenmeyer de 100mL que se mantuvieron cerrados.

Los experimentos se llevaron a cabo a temperatura ambiente (22±1ºC) y con agitación orbital constante (200rpm). Los tiempos de interacción mineral-disolución acuosa variaron dependiendo de la fase mineral de partida. En el caso del yeso fueron de 1 hora (h), 3 h, 6 h, 12 h, 1 día (d), 3 d, 1 semana (s), 2 s y 1 mes (m); mientras que en los experimentos realizados con la anhidrita fueron de 1 d, 2 d, 4 d, 1 s, 2 s, 1 m y 2 m. Cada experimento se llevó a cabo por triplicado.

Transcurrido el tiempo de interacción, las fases sólidas y acuosas se separaron por filtración a vacío. Las disoluciones se conservaron refrigeradas en recipientes de vidrio y posteriormente se analizaron mediante ICP-OES y ICP-MS con el fin de determinar las concentraciones de S, Na, y Ca. También se monitorizó la evolución del pH de las soluciones.

Las fases sólidas se caracterizaron mediante difracción de rayos X (DRX) y microRaman, ambas técnicas aplicadas sobre muestras en polvo. Por otra parte, las características morfológicas y texturales de los fragmentos extraídos se observaron mediante el microscopía electrónica de barrido (MEB).

RESULTADOS Y DISCUSIÓN

La precipitación de las fases

Palabras clave: Reemplazamiento mineral, calcita, vaterita, camino de reacción

Keywords: Mineral replacement, calcite, vaterite, reaction *pathways*

* Corresponding Author: iriscuesta@ucm.es

carbonatadas se produjo tras la rápida reacción del $CO_3^{2-}{}_{(aq)}$ con el $Ca^{2+}{}_{(aq)}$ procedente la disolución del mineral de partida, yeso o anhidrita, de acuerdo con las siguientes reacciones:

$$CaSO_4 \cdot nH_2O_{(s)} \rightarrow$$
$$\rightarrow Ca^{2+}{}_{(aq)} + SO_4^{2-}{}_{(aq)} + nH_2O_{(l)} \quad (1)$$
$$Ca^{2+}{}_{(aq)} + CO_3^{2-}{}_{(aq)} \rightarrow CaCO_{3(s)} \quad (2)$$

Los análisis realizados mediante DRX y Raman sobre los fragmentos sólidos extraídos en los experimentos en los que se hizo interaccionar yeso con las disoluciones carbonatadas menos concentradas ($[Na_2CO_3]$=0,05M) mostraron picos de difracción y bandas en los espectros Raman correspondientes al yeso, incluso para los tiempos de interacción más largos. Por otra parte, los difractogramas y espectros obtenidos en todos los fragmentos analizados mostraron la presencia de vaterita, lo que implicaría que esta fase se forma en los primeros instantes de la reacción y persiste durante largos periodos de interacción (al menos un mes). Agregados con morfologías compatibles con esta fase mineral también fueron observados en todas las imágenes de MEB. Además de vaterita, también se detectó la presencia de calcita en todos los difractogramas e imágenes de MEB, aunque los espectros de Raman mostraron la presencia de esta fase solo a partir de las 6 h de interacción. Por último, el aragonito sólo se observó en las imágenes de MEB obtenidas sobre muestras extraídas tras periodos de interacción relativamente largos (3 d o más de interacción) (Figs. 1a y 2a). Sin embargo, debido a su escasez, esta fase no se detectó en ninguno de los espectros ni difractogramas.

En los experimentos de interacción de yeso con las disoluciones más concentradas ($[Na_2CO_3]$=0,5M), esta fase fue detectada únicamente en los espectros y difractogramas obtenidos tras los tiempos de interacción relativamente cortos (3 h o menos), lo que indica que la reacción de carbonatación se ha completado. Los caminos de reacción siguen un patrón muy similar al descrito en los experimentos llevados a cabo a bajas concentraciones: la calcita y vaterita aparece desde los primeros momentos de la reacción y coexisten a lo largo de todo el proceso. La principal diferencia radica en la tardía aparición del aragonito que solamente se observó en las imágenes de MEB obtenidas sobre muestras correspondientes a 1 s o más de interacción (Fig. 1a).

La cinética de reacción fue algo más lenta cuando se emplearon fragmentos de anhidrita, ya que los difractogramas

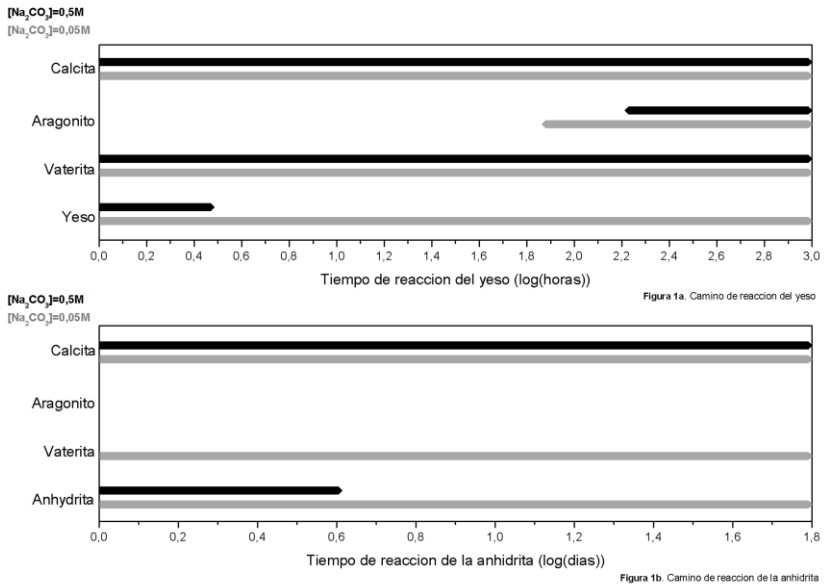

fig 1. *Representación esquemática de los caminos de reacción observados durante la interacción de (**a**) yeso y (**b**) anhidrita con soluciones de Na_2CO_3.*

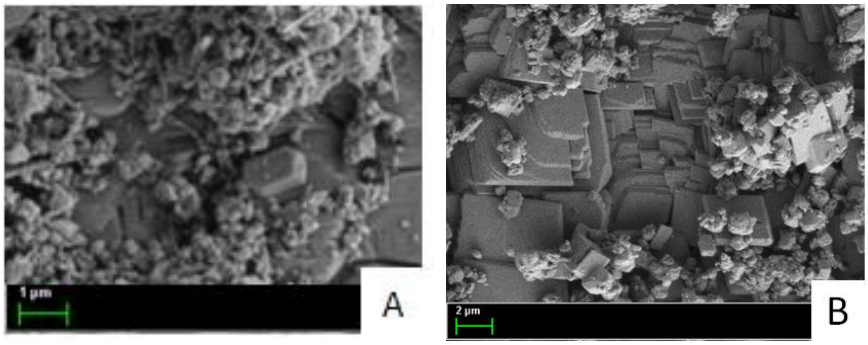

fig 2. *a) Imagen de MEB de una muestra sólida extraída después de un mes de interacción de un fragmento de yeso con una solución carbonatada ($[Na_2CO_3]$=0,05M). Pueden observarse cristales y agregados de los tres polimorfos de $CaCO_3$ (calcita, vaterita y aragonito). b) Cristales romboédricos de calcita crecidos epitaxialmente sobre un substrato de anhidrita tras dos días de interacción con soluciones carbonatadas ($[Na_2CO_3]$=0,5M).*

indicaron la persistencia de esta fase hasta transcurridos al menos 4d desde el inicio del experimento cuando la interacción se produjo con disoluciones carbonatadas muy concentradas, $[Na_2CO_3]$=0,5M. Sin embargo, en este caso los caminos de reacción variaron con la concentración de reactivo empleada. Así, cuando se utilizaron concentraciones de carbonato más bajas ($[Na_2CO_3]$=0,05M) se detectó la presencia de calcita y vaterita en todas las muestras analizadas. Esto, al igual que en los experimentos realizados utilizando yeso como reactante, implica la rápida formación de estas fases y su persistencia a lo largo de periodos prolongados de tiempo. Sin embargo, en este caso la calcita aparece claramente como el producto mayoritario de la reacción y los cristales de esta fase crecen orientados sobre la superficie de la anhidrita en evidente relación epitaxial. Por otra parte no se detectó la presencia de aragonito en ningún momento de la reacción, ni en difractogramas rayos X ni en los espectros Raman. Tampoco se observaron cristales cuya morfología pudiera ser compatible con esta fase en las imágenes de MEB. Por último, la interacción de los fragmentos de anhidrita con disoluciones altamente concentradas ($[Na_2CO_3]$=0,5M) dio como resultado únicamente la formación de cristales de calcita orientados epitaxialmente sobre el substrato de anhidrita (Figs. 1b y 2b).

La diferencia en los caminos de reacción observados puede justificarse atendiendo a distintos factores:
a) La formación de una epitaxia de calcita sobre anhidrita tiene como consecuencia la reducción de la barrera energética para la nucleación, lo que favorece la formación de este polimorfo de $CaCO_3$ sobre los fragmentos de anhidrita, previniendo así la cristalización de otros polimorfos metaestables. En el caso del yeso, al no tener lugar el crecimiento epitaxial de ningún polimorfo de $CaCO_3$ sobre su superficie, factores probablemente

cinéticos conducen a la formación de vaterita y, en un corto periodo de tiempo, también de aragonito.

b) La formación de vaterita puede deberse a la alta reactividad de las superficies consideradas, que se disuelven rápidamente, conduciendo a que se alcancen también rápidamente altos niveles de sobresaturación y la formación de fases metaestables.

c) La relación SO_4^{2-}/CO_3^{2-} en las disoluciones acuosas tiende a aumentar a medida que transcurre el tiempo de interacción. Dicho incremento es mucho más acusado cuando las disoluciones acuosas de partida están mucho menos concentradas en CO_3^{2-}. En estas circunstancias, la formación de aragonito se ve favorecida debido al efecto inhibidor que ejerce el sulfato sobre el crecimiento de calcita (Fernandez-Díaz et al., 2010).

A partir del análisis de los picos de los difractogramas correspondientes a la calcita y a la vaterita resulta posible extraer conclusiones interesantes. En primer lugar, en picos representativos de esta fase (Fig. 3) se detecta un importante desplazamiento hacia valores de espaciado mayores que los teóricos, lo que indica un aumento del tamaño de la celda unidad. Este incremento de los parámetros de red puede deberse a la incorporación de SO_4^{2-} en la estructura de la calcita. Por otra parte la posición de los picos parece oscilar a lo largo del tiempo. Esto se podría explicar como consecuencia de procesos de reequilibrio que implicarían la disolución-recristalización de calcita con distintas concentraciones de sulfato en su estructura.

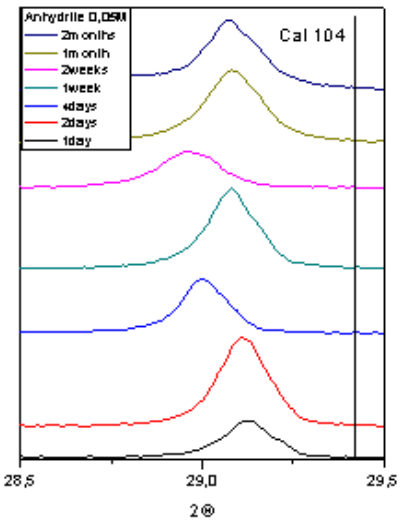

***fig 3**. Detalle de la posición de pico de difracción correspondiente al plano (104) de la calcita en el precipitado formado tras la interacción de cristales de anhidrita con una disolución acuosa de 0,05M Na_2CO_3 durante distintos periodos de tiempo.*

En los difractogramas de vaterita (Fig. 4) los picos aparecen mucho próximos a los valores teóricos. Esto podría indicar una menor incorporación de sulfato en la estructura de esta fase, aunque también es posible que la estructura de la vaterita se vea mucho menos distorsionada por la incorporación de dicho grupo aniónico. Esta segunda interpretación se ve apoyada por los resultados de los estudios de modelado computacional llevados a cabo por Fernández-Díaz et al. (2010) y Arroyo-de Dompablo (2015).

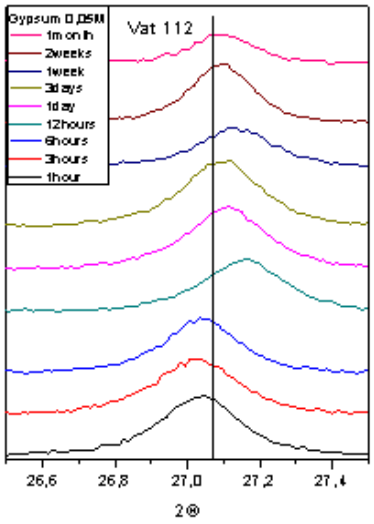

***fig 4**. Detalle de la posición de pico de difracción correspondiente al plano (112) de la vaterita en el precipitado formado tras la interacción de cristales de yeso con una disolución acuosa de 0,05M Na_2CO_3 durante distintos periodos de tiempo.*

AGRADECIMIENTOS

Este trabajo ha sido financiado por el Ministerio de Economía y Competitividad a través de los siguientes proyectos y contratos: CGL2013-47988-C2-01-P, BES-2014-070279 y CGL2016-77138-C2-1-P. Tanto los experimentos de interacción como la mayor parte de la caracterización de las muestras se han realizado en el GFZ (Deutsche GeoForschungsZentrum), en Potsdam, Alemania. Los autores agradecen la ayuda prestada por Anja Schleicher en la caracterización de las muestras mediante difracción de rayos X.

REFERENCIAS

Arroyo-de Dompablo, M.E, Fernández-González, M. A, Fernández-Díaz, L. (2015): Computational investigation of the influence of tetrahedral oxoanions (sulphate, selenate and chromate) on the stability of calcium carbonate polymorphs. RSC Adv. ***5****, 59845-59852.*

Fernandez-Díaz, L, Fernández-González, A., Prieto, M. (2010): The role of sulfate groups in controlling $CaCO_3$ polymorphism. Geochim. Cosmochim. Acta ***74****, 6064-6076.*

Pina, C.M., Astilleros, J.M., Sánchez-Pastor, N. (2009): The carbonatation of gypsum: Pathways and pseudomorph formation. Am. Mineral ***94****, 1223-1234.*

Parkhurst, D.L. & Appelo, C.A.J. (1999): User's guide to PHREEQC (Version2). A computer program for speciation, batch-reaction, one-dimensional transport and inverse geochemical calculations; Water-Resources Investigations Report, US. Geological Survey 99–4259.

Putnis, A. (2002): Mineral replacement reactions: from macroscopic observations to microscopic mechanisms. Mineral Mag. ***66****, 689-708.*

Warren J. K. (2016): Evaporites: A geological compendium. 2º edition. Springer, Berlin. 1807 p.

GEOBREMEN 2017

CARBONATION OF GYPSUM AND ANHYDRITE: INFLUENCE OF THE CARBONATE BEARING SOLUTION CONCENTRATION ON ITS REACTION PATWAYS AND POROSITY.

Cuesta-Mayorga I.*[1,4], Astilleros J.M.[1,2], Roncal-Herrero T.[3],Grattoni C.A.[4],Fernández-Díaz L.[1,2], & Benning L.G.[4,5].

[1] Departamento de Cristalografía y Mineralogía, Universidad Complutense de Madrid, Spain
[2]Institute of Geosciences, Consejo Superior de Investigaciones Científicas, Universidad Complutense de Madrid, Spain
[3] Department of Physics, University of York, York, United Kingdom
[4] School of Earth and Environment, University of Leeds, Leeds, United Kingdom
[5]GeoForschungsZentrum GFZ, Potsdam, Germany
*corresponding email: iriscuesta@ucm.es

Carbonation, pseudomorphism, porosity

Gypsum ($CaSO_4 \cdot 2H_2O$) and anhydrite ($CaSO_4$) are among the most abundant non-silicates minerals in the Earth crust. Their interaction with carbonate-bearing solutions has led to the formation of large volumes of diagenetic carbonate deposits. This process involves the dissolution of the primary sulfates and their pseudomorphic transformation into $CaCO_3$ polymorphs. This occurs via a dissolution and repreciptation mechanism, yet the resulting carbonate polymorphs are different for each sulfate precursor phase. We have previously shown that reacting 0.5M Na_2CO_3 solutions with anhydrite leads to the precipitation of mostly calcite with traces of vaterite. However, the same reaction but in the presence of gypsum occurs via the sequential formation and transformation of amorphous calcium carbonate (ACC), vaterite and calcite (Fernández-Díaz L., 2009). These initial data suggested that such carbonation reactions of gypsum and anhydrite result in both cases in the generation of high amounts of porosity, accompanied by wide, prominent gaps between the parent sulfate and the product carbonates in the case of the carbonation of gypsum. However, a quantitative and time resolved assessment of the reactions was lacking.

In this work we present the results of an experimental study where we addressed the effect of initial aqueous carbonate concentration (0.5, 0.25 and 0.05M Na_2CO_3) on the carbonation of calcium sulfate phases. Our aims were to quantify in a time resolved (over 12 days) manner (i) any changes in reaction pathways and (ii) the generation and evolution of porosity during both anhydrite and gypsum carbonation reactions. We have characterized the changes in $CaCO_3$ polymorphs by combining scanning electron microscopy (SEM), glancing X-ray diffraction and Raman and Fourier transform infrared spectroscopy (FTIR) analyses. The generation and evolution of porosity was quantified over time using mercury porosimetry, computed tomography (CT), BET-surface area and nuclear magnetic resonance (NMR). The results reveal that when reacted with low concentration carbonate solutions (0.05M) both gypsum and anhydrite transform to mixtures of aragonite and calcite, and not as shown above to mainly calcite. Furthermore, the total porosity is inversely proportional to the carbonate concentration. Interestingly, in the case of anhydrite this higher porosity includes the development of a gap, similar to that previously observed for gypsum. Regardless of the initial carbonate concentration and for both calcium sulfates, the sizes of the newly-formed pores rapidly increase at the beginning of the process, but steadily decrease

over the 12 days of reaction. These observations indicate that the reactant concentration plays a crucial role in the carbonation of gypsum and anhydrite. This factor may have influenced the porosity features of many diagenetic limestones and could have important consequences for industrial applications such as oil recovery and CO_2 sequestration.

Fernández-Díaz L., Pina C.M., Astilleros J.M., Sánchez-Pastor N. (2009): The carbonatation of gypsum: Pathways and pseudomorph formation. *Am. Min.* **94**, 1223-1234.

SEM 2018

Precipitación de polimorfos de $CaCO_3$ en presencia de sulfato.

Iris Cuesta Mayorga (1, 2*), José Manuel Astilleros García-Monge (1, 2), Lurdes Fernández Díaz (1, 2).

(1) Departamento de Mineralogía y petrología. Universidad Complutense de Madrid, 28040, Madrid (España).
(2) Instituto de Geociencias (UCM-CSIC). Calle del Dr. Severo Ochoa, 7, 28040 Madrid (España).
* corresponding author: iriscuesta@ucm.es

Palabras Clave: $CaCO_3$, Polimorfismo, Sulfato. | **Key Words:** $CaCO_3$, Polymorphism, Sulphate.

INTRODUCCIÓN

La precipitación polimórfica del $CaCO_3$ a partir de disoluciones acuosas es un problema clave en numerosas disciplinas, desde la geología hasta la ingeniería química y la biología. La formación de los distintos polimorfos de un compuesto en unas condiciones determinadas depende de factores termodinámicos y cinéticos. En el caso particular del $CaCO_3$, las tres principales fases anhidras que pueden cristalizar a temperatura ambiente son la calcita (Cal), el aragonito (Arg) y la vaterita (Vtr), siendo el Arg estable en condiciones de alta presión, y la Vtr metaestable. Aun así, los tres polimorfos pueden formarse simultáneamente. Uno de los factores que más influyen en la selección polimórfica es la presencia de iones extraños en el medio de cristalización. Dicha influencia puede tener carácter cinético (inhibiendo la formación de una fase y permitiendo que una fase alternativa se forme) o termodinámico (incorporándose en la estructura de los polimorfos y modificando sus energías dando lugar a cruces de estabilidad) (Fernández-Díaz et al., 2010). Estas sustituciones pueden ser isomórficas. Este es caso de la sustitución de grupos SO_4^{2-} en la posición grupos CO_3^{2-} en las estructuras de los distintos polimorfos de $CaCO_3$. Dicha sustitución puede modificar la estabilidad relativa de estos polimorfos (Fernández-Díaz et al., 2010; Tang et al., 2012; Wagterveld et al., 2014).

En trabajos anteriores se ha constatado a través de experimentos de carbonatación, de envejecimiento de precipitados en condiciones de alta basicidad (pH=10,9) que la incorporación SO_4^{2-} favorece la estabilización de la Vtr. Esta influencia del SO_4^{2-} es especialmente relevante dada la abundancia de este oxianión en la naturaleza, especialmente en ambientes evaporíticos.

En este trabajo presentamos los resultados de experimentos de envejecimiento de precipitados de $CaCO_3$ formados a partir de disoluciones con relaciones $[SO_4^{2-}]/[CO_3^{2-}]$ entre 0 y 67,6) en condiciones próximas a la neutralidad (pH=7,6), las cuales son representativas de una mayor variedad de ambientes naturales que las condiciones de alta basicidad estudiadas anteriormente. El objetivo del trabajo es mejorar nuestra comprensión de la influencia del SO_4^{2-} en el polimorfismo del $CaCO_3$.

EXPERIMENTAL

Los precipitados se prepararon por mezcla de disoluciones ($CaCl_2$, $NaHCO_3$, y Na_2SO_4) y se mantuvieron en contacto con la fase líquida durante el envejecimiento. El volumen de las disoluciones fue de 100 mL. Todos ellos se llevaron a cabo con agitación y a temperatura ambiente (22±1º C). Las concentraciones empleadas vienen detalladas en la Tabla 1.

Exp	$CaCl_2$ (M)	$NaHCO_3$ (M)	Na_2SO_4 (M)	$[SO_4^{2-}]/[CO_3^{2-}]$
A0	0,05	0,05	---	0
A3	0,04	0,05	0,003	8,48
A5	0,04	0,05	0,005	14,03
A7	0,04	0,05	0,007	19,51
A15	0,05	0,05	0,015	41,78
A20	0,05	0,05	0,020	54,87
A22	0,05	0,05	0,022	60.00
A25	0,05	0,05	0,025	67,61

Tabla 1. *Concentraciones de cada reactivo empleadas en los experimentos y ratio $[SO_4^{2-}]/[CO_3^{2-}]$ calculado a partir de los valores de obtenidos mediante la simulación con PhreeqC.*

Se consideraron períodos de envejecimiento de 5 minutos, 10 horas, 1 día, 3 días, 1 semana y 2 semanas. Trascurridos estos tiempos, los precipitados se separaron de la fase acuosa por filtración a través de membranas de acetato de celulosa (0,45 µm), se secaron en estufa, y se caracterizaron por difracción de rayos X (DRX), espectroscopia IR (Espectroscopia IR), y espectroscopia de rayos X de energía dispersiva (EDS). Las características morfológicas de los cristales constituyentes de los precipitados de estudiaron mediante el microscopía electrónica de barrido (MEB).

RESULTADOS Y DISCUSIÓN

La reacción que resume los procesos que tienen lugar durante la precipitación y el envejecimiento de los sólidos formados es la siguiente:

$Ca^{2+} + CO_3^{2-} + SO_4^{2-} \rightarrow Ca(CO_3)_{1-x}(SO_4)_x + CaSO_4$.

En el momento de la mezcla de disoluciones, en todos los experimentos el sistema está sobresaturado (SI>0) con respecto a los tres polimorfos de $CaCO_3$ (Vtr, Cal, Arg), y con respecto al yeso ($CaSO_4 \cdot 2H_2O$) (Gp) en los experimentos A15-A25.

La evolución mineralógica de los precipitados a lo largo del envejecimiento depende directamente de la relación $[SO_4^{2-}]/[CO_3^{2-}]$ inicial en la disolución. En todos los casos, en las primeras etapas del proceso, el precipitado está constituido casi exclusivamente por Vtr. La formación de este polimorfo se debe al control cinético, debido a la alta sobresaturación. La Vtr se transforma en Cal (en los experimentos A0-A5) en el proceso de envejecimiento, siendo éste el único polimorfo presente tras dos semanas de reacción. Esta transformación se retrasa progresivamente al aumentar $[SO_4^{2-}]/[CO_3^{2-}]$. En los experimentos A7-A20, una parte de la Vtr se transforma en Cal, pero a tiempos largos de envejecimiento se observa la precipitación de Arg. Tras 2 semanas, el precipitado está formado por tres polimorfos (Vtr, Cal, Arg), siendo la Cal minoritaria. En los experimentos A22, A25 no se observa Cal. Vtr, Arg y Gp forman el precipitado tras 2 semanas de reacción.

La morfología de la Cal evoluciona desde típico hábito romboédrico con caras $\{10\bar{1}4\}$, a cristales cada vez más alargados según [001] (Figura 1).

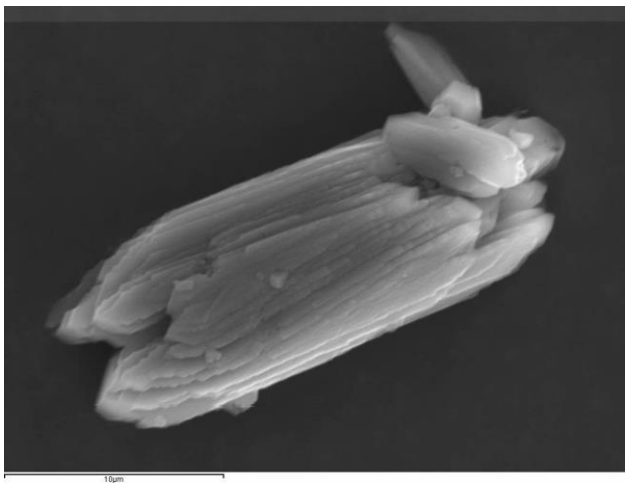

Figura 1*. Cristales alargados de Cal en el experimento A5 tras 2 semanas de envejecimiento. Los análisis de EDS indican un contenido en S de 1,79% at.*

Los análisis de EDS confirman la incorporación de S en la Cal y Vtr. La cantidad de S incorporada, aumenta con el ratio $[SO_4^{2-}]/[CO_3^{2-}]$ inicial presente en la disolución. Sin embargo, la pendiente de dichas curvas disminuye al aumentar el ratio $[SO_4^{2-}]/[CO_3^{2-}]$ inicial (Figura 2). Este comportamiento parece indicar que existe un límite para la incorporación de grupos SO_4^{2-} en la estructura de Vtr y Cal, incluso cuando ésta está favorecida por encima de su valor de equilibrio por el efecto de la alta sobresaturación. Los análisis de EDS indican que la cantidad de S en la Cal es siempre mayor que el de la Vtr, lo que puede estar relacionado con que la Cal precipita más tarde que la Vtr, a partir de una disolución con una relación $[SO_4^{2-}]/[CO_3^{2-}]$ mayor que la inicial. A lo largo del proceso de envejecimiento, el contenido de S en la Cal y Vtr disminuye progresivamente.

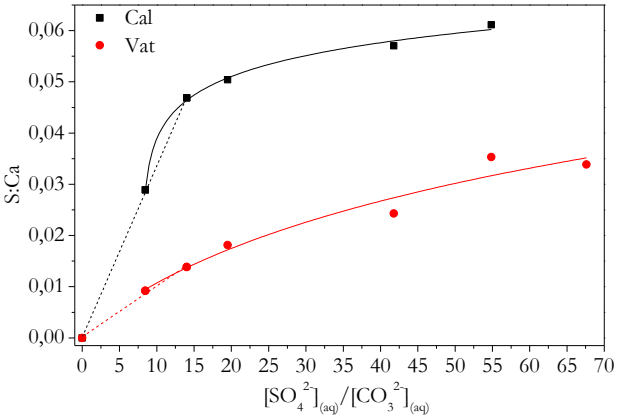

Figura 2*. Relación atómica S:Ca en función de $[SO_4^{2-}]/[CO_3^{2-}]$ inicial. Tanto la Cal (cuadrados negros) como la Vtr (círculos rojos) muestran la misma tendencia. Para valores de $[SO_4^{2-}] \leq 0{,}005M$, la tendencia es lineal (líneas discontinuas). Para valores $[SO_4^{2-}] \geq 0{,}003M$ la tendencia observada es logarítmica (líneas continuas).*

CONCLUSIONES

Los resultados experimentales muestran cómo la presencia de SO_4^{2-} en el medio de cristalización, y en condiciones cercanas a la neutralidad, favorece:

- La formación de Vtr e inhibe su transformación en otros polimorfos.
- La disolución de la Vtr y su transformación en Arg vía disolución-cristalización durante el proceso de envejecimiento.

En las condiciones tratadas en este trabajo, la presencia de SO_4^{2-} ejerce una influencia de carácter termodinámico en la selección polimórfica de $CaCO_3$.

REFERENCIAS

Fernández-Díaz, L., Fernández-González, A., Prieto, M. (2010): The role of sulfate groups in controlling $CaCO_3$ polymorphism. Geochimica et Cosmochimica Acta, **74**, 6064-6076. DOI: 10.1016/j.gca.2010.08.010.

Tang, Y., Zhang, F., Cao, Z., Jing, W., Chen, Y., (2012): Crystallization of $CaCO_3$ in the presence of sulfates and additives: Experimental and molecular dynamics simulation studies. Journal of Colloid and Interface Science, **377**, 430-437. DOI: 10.1016/j.jcis.2012.02.069.

Wagterveld R.M., Yu, M., Witkamp, G. J., (2014): Polymorphic change from vaterita to aragonite under influence of sulfate: The "morning start" habit. Journal of Crystal Growth, **387**, 29-35. DOI: 10.1016/j.jcrysgro.2013.10.044

Epitactic overgrowth of calcite ($CaCO_3$) on anhydrite ($CaSO_4$) cleavage surfaces

CRYSTAL GROWTH & DESIGN

Article

Cite This: Cryst. Growth Des. 2018, 18, 1666−1675

pubs.acs.org/crystal

Epitactic Overgrowths of Calcite ($CaCO_3$) on Anhydrite ($CaSO_4$) Cleavage Surfaces

Iris Cuesta Mayorga,[†,‡] José Manuel Astilleros,*[,†,‡] Lurdes Fernández-Díaz,[†,‡] Juan Morales,[§] Manuel Prieto,[∥] Teresa Roncal-Herrero,[⊥] and Liane G. Benning[#,¶,△]

[†]Departamento de Mineralogía y Petrología, Universidad Complutense de Madrid, C/José Antonio Novais 2, Madrid 28040, Spain

[‡]Instituto de Geociencias (CSIC, UCM), C/José Antonio Novais 2, Madrid 28040, Spain

[§]Instituto de Geología Económica Aplicada, Universidad de Concepción, Casilla 160-C, Concepción, Chile

[∥]Departamento de Geología. Universidad de Oviedo, C/Jesús Arias de Velasco, s/n, Oviedo 33005, Spain

[⊥]School of Chemical and Process Engineering and [△]School of Earth and Environment, University of Leeds, LS2 9JT, Leeds, United Kingdom

[#]GFZ, German Research Center for Geosciences, Potsdam, 14473 Germany

[¶]Department of Earth Sciences, Free University of Berlin, 12249, Berlin, Germany

ABSTRACT: We investigate the crystallographic relationships between calcite crystals overgrown on the three main anhydrite cleavage surfaces, (100), (010), and (001), as a result of the interaction between anhydrite surfaces with carbonate-rich aqueous solutions (0.5 mol/L Na_2CO_3). Scanning electron microscope (SEM) images and energy back scattered diffraction (EBSD) analyses reveal that this interaction always leads to oriented nucleation and growth of calcite crystals, characterized by a parallelism between the calcite $\{10\bar{1}4\}$ faces and the corresponding anhydrite cleavage surface. A high density of oriented calcite crystals was observed on the $(001)_{Anh}$ face, while the calcite crystal density was significantly lower on the $(100)_{Anh}$ and $(010)_{Anh}$ faces. On all investigated anhydrite cleavage surfaces, calcite $\{10\bar{1}4\}$ showed at least two excellent matching orientations, both defined by the parallelism between $\langle\bar{4}41\rangle_{Cal}$ and one of the three crystallographic axes of anhydrite. As a result, two different populations of calcite crystals coexisted on the same substrate. In each population four groups of differently orientated crystals could be distinguished, related by symmetric operators inherent to the anhydrite substrates. The coalescence of these differently oriented crystals leads to the formation of twins. The calcite epitactic overgrowth contains an intrinsic intergranular porosity that makes the passivation of anhydrite crystals very unlikely. This characteristic together with the negative molar volume change involved in the anhydrite carbonation reaction makes anhydrite a material suitable to be used in the design of CO_2 capture strategies.

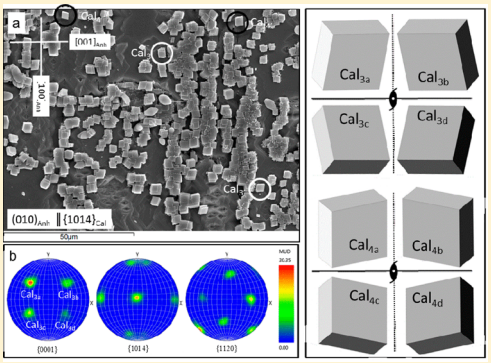

INTRODUCTION

The increasing concern about climate change effects and the overwhelming evidence that connect it to a steady increase in carbon dioxide (CO_2) levels in the atmosphere due to human activities have triggered the search for methods to reduce the volume of industrial carbon dioxide emissions.[1] Some of these methods are inspired by natural processes, which are continuously operating on Earth and which over millions of years have played a major role in regulating atmospheric CO_2 levels.[1] These processes frequently involve the reaction between CO_2-bearing fluids and mineral components released during weathering which can lead to long-lasting CO_2 removal and storage through the precipitation of thermodynamically stable mineral carbonates such as calcite.[2] For example, the efficiency of anthropogenic CO_2 removal through precipitation of $CaCO_3$ phases has been demonstrated through the injection of waters charged with dissolved carbon dioxide of anthropogenic origin into basaltic and peridotitic rocks. Such *in situ* field tests have yielded promising results regarding both the kinetics and the efficiency of the CO_2 removal.[3−5] In a similar fashion, sedimentary evaporitic rocks that make up the huge gypsum ($CaSO_4{\cdot}2H_2O$) and anhydrite ($CaSO_4$) deposits around the world are also highly susceptible for transforming into carbonate minerals upon interaction with water rich in dissolved CO_2. Such sedimentary deposits have been naturally carbonated since Precambrian times, leading to the formation of large volumes of diagenetic limestones in sedimentary basins.[6−9]

In all such systems, in the modern context of CO_2 sequestration through mineral carbonation, the kinetics of the prevalent carbonation reaction is a major concern when assessing the viability and efficiency of CO_2 removal.[10] Mineral

Received: November 20, 2017
Revised: February 7, 2018
Published: February 12, 2018

DOI: 10.1021/acs.cgd.7b01610
Cryst. Growth Des. 2018, 18, 1666−1675

carbonation commonly involves the nucleation of secondary $CaCO_3$ phases on the surface of primary minerals and, for the carbonation reaction to progress, a continuous interaction between the CO_2-bearing fluid phase and the interfaces between primary and secondary phases is required. The reaction progress is strongly controlled by the existence of crystallographic relationships between the original phase and the carbonated end product. This is so because textural overgrowth characteristics that develop on the surface of primary minerals will govern the resulting reaction progress.[11] A direct consequence of this is the slowing down of the kinetics of the reaction. In a recent study we have reported on the carbonation of anhydrite as a result of its interaction with carbonate-rich aqueous solution,[11] and showed how such interactions lead to the complete transformation of single crystals of anhydrite into aggregates of calcite crystals.

It is well-known that the kinetics of anhydrite carbonation is significantly more sluggish than that of gypsum.[11,12] This can partially be explained by the higher reactivity of gypsum surfaces compared to anhydrite surfaces, but also by the existence of epitactic relationships between the calcite overgrowth and the anhydrite substrate, which have not been detected during the carbonation of gypsum under similar conditions.

We hypothesize that the structural elements that enable the development of epitactic relationships between anhydrite and calcite govern the rates and pathways of the carbonation reactions. To assess this, we present here data on the epitatic growth of calcite on the three most common faces in the habit of natural anhydrite crystals: (100), (010), and (001). Our aim is to determine the following: (a) the structural elements that enable the development of epitactic relationships between both phases and (b) the connection between the degree of epitactic fit and those textural characteristics of the calcite overgrowth. A quantitative understanding of the structural factors that control the formation of calcite epitactic overgrowths will enable us to predictively assess the viability of using the carbonation of different calcium-bearing minerals as a means to sequester and store carbon dioxide in a more stable phase as it could be calcite.

1. MATERIALS AND METHODS

We reacted carbonate-rich aqueous solutions with natural, pale blue anhydrite crystals from Naica (Chihuahua, Mexico). Such crystals were freshly cleaved parallel to the (100), (010), and (001) faces using a razor blade prior to each experiment, to obtain fragments with sizes of approximately 3 × 3 × 1 mm^3. In each case, the largest area corresponded to the surface to be studied. We focused our study in these three particular surfaces because they are the most frequent ones in the habit of natural anhydrite crystals[13] and cleavage along them is perfect. The orientation of the sections was determined by observing the interference figures in polarized light microscopy.

Individual anhydrite fragments were placed into glass reactors filled with 5 mL of a commercial 0.5 mol/L Na_2CO_3 solution (pH ≈ 11.4; Fluka) and the reactors were then hermetically sealed. After set periods of time (between 15 min and 4 days), each anhydrite crystal was removed from the solutions and washed with Milli-Q water (resistivity of 18.2 MΩ.cm at 25 °C) to remove any excess salts and rapidly dried using absorbent paper. All experiments were carried out in a thermostatic chamber at 25 ± 0.5 °C and atmospheric pressure. These conditions are within the range of temperatures and pressures which are relevant for the development of anhydrite carbonation processes in Nature.

The morphological and textural characteristics of the initial anhydrite surfaces and of any formed secondary phases resulting from their interaction with the carbonate-rich solution were imaged with a scanning electron microscope (SEM; JEOL JSM 6400, 40 kV). The mineralogy of the formed secondary phases was identified using glancing incidence X-ray diffraction (GIXRD) (PANalytical X'Pert PRO MRD equipped with a Cu Kα X-ray source). Diffraction patterns, collected with a 0.5° incidence to minimize the presence of peaks coming from the bulk of the anhydrite substrate, were matched to files from the ICDD-PDF2 database for anhydrite (00−037−1796) and for the $CaCO_3$ polymorphs calcite (01−071−3699), aragonite (00−001−0628), and vaterite (00−024−0030). Electron backscatter diffraction (EBSD) analyses provided information on crystallographic relationships between the anhydrite substrate and newly formed phase(s). In all the analyses, anhydrite fragments were placed directly on the sample holder without polishing them. EBSD measurements were conducted by means of a ZEISS (EVO 15 MA) SEM equipped with an HKL Nordlys detector (Oxford), using a 17 kV accelerating voltage of the primary beam and a ∼14 mm working distance. The EBSD data were postprocessed using the Aztec (Oxford Instruments) and CHANNEL 5 software. The geometry of the beam-sampler-detector was fixed to a ∼70° tilt. Pole figures obtained from EBSD maps show the degree of co-orientation of the overgrown crystals and the substrate. In all measurements, anhydrite surfaces were oriented prior to setting them in the sampler holder.

CrystalMaker software[14] was used to plot crystal structure projections and to measure repeating periods along different crystallographic directions as well as angles between directions.

2. RESULTS

SEM micrographs of anhydrite (100), (010), and (001) surfaces after interaction with a carbonate-bearing aqueous solution evidence the formation of an overgrowth, which appears as a more or less continuous layer (Figure 1). The degree of coverage of the anhydrite surfaces by the overgrowth increases with time. However, for a given time the degree of coverage varies and depends on the anhydrite surface. In all cases the (001) face always showed the highest degree of coverage. The overgrowths mostly consisted of evenly sized (3−5 μm), euhedral lozenge-shaped microcrystals (Figure 1). In some cases, a few sphere-like aggregates could also be distinguished in the overgrowths formed on anhydrite (010) and (001) surfaces at early stages of reaction (Figure 1c). GIXRD analyses showed that calcite was the main overgrowth component on all anhydrite faces considered, while vaterite was a very minor constituent on the (001) faces. Moreover, although minor vaterite was also observed on the anhydrite (010) surface after a few minutes interaction, this phase was much less abundant than on $(001)_{Anh}$ and was almost absent on $(100)_{Anh}$ regardless the time of interaction.

Thus, we can safely assert that the lozenge-like morphologies correspond to calcite and the sphere-like morphologies correspond to vaterite.[11] According to the angles between faces and edges measured on the SEM micrographs, the habit of calcite crystals is always dominated by the $\{10\bar{1}4\}$ rhombohedron. The calcite crystals grow oriented on the anhydrite substrate, defining an epitactic relationship regardless of the orientation of the substrate. Nevertheless, marked differences in specific epitactic relationships between calcite and the anhydrite (100), (010), and (001) surfaces were observed.

2.1. Calcite Overgrowth on Anhydrite (100) and (010).

The microtopography of anhydrite (100) surfaces is characterized by large and very flat terraces, bounded by macrosteps that run parallel to the [010] and [001] directions (Figure 1a). Post reaction with the carbonate-rich aqueous solution, the anhydrite (100) surfaces developed clear signs of dissolution, in the form of etch pits along [001] (Figure 1a). The orientation

DOI: 10.1021/acs.cgd.7b01610
Cryst. Growth Des. 2018, 18, 1666−1675

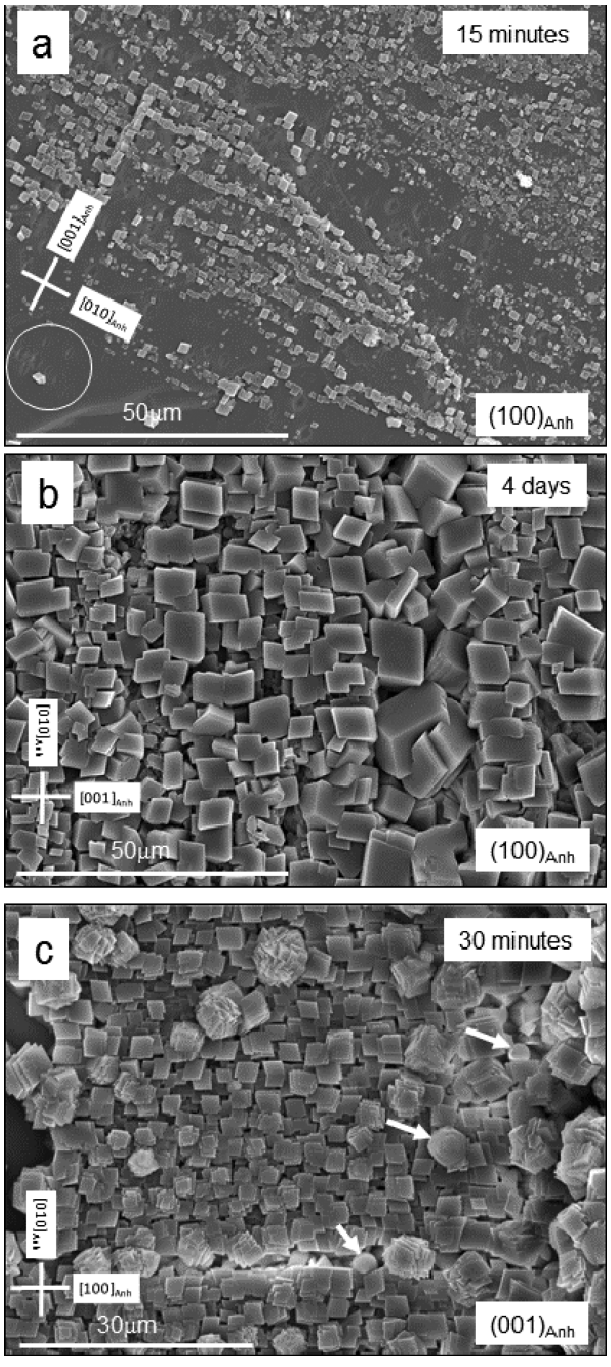

Figure 1. SEM images obtained after 15 min (a), 4 days (b), and 30 min (c) of exposure of anhydrite (100) and (001) surfaces to 0.5 M Na_2CO_3 solutions. The anhydrite surface is covered by a more or less discontinuous layer of small calcite crystals specifically oriented with respect to the substrate. (a) Etch pit orientation (encircled area) enables the identification of the main crystallographic directions on the anhydrite surfaces. (c) Some sphere-like aggregates of vaterite can be distinguished in the overgrowths formed on anhydrite (001) surface (see white arrows).

and morphology of these etch pits helped us confirm the main crystallographic directions. In addition, the dissolution of the surface was accompanied by the growth of new calcite crystals, which formed preferentially on edges and surface defects of the anhydrite (Figure 1a). After 15 min of interaction, around a third of the (100) anhydrite substrate was covered (Figure 1a) by calcite crystals while after 5 h the substrate was fully covered.[11] Such a homogeneous calcite layer on the anhydrite (100) surface after 4 days of reaction (Figure 1b) consists of evenly sized calcite crystals (~5 μm or larger), whose habit is bounded by $\{10\bar{1}4\}$ faces. These calcite crystals appear oriented with respect to the anhydrite substrate in a way that one of the calcite rhombohedron faces is always in contact with the anhydrite (100) plane, defining the epitactic relationship $(100)_{Anh}\|\{10\bar{1}4\}_{Cal}$ (Figure 2a). Moreover, in the majority of these oriented calcite crystals (from here on denoted as Cal_1), one of their $\langle\bar{4}41\rangle_{Cal}$ edges (either $[\bar{4}41]_{Cal}$ or its symmetry-equivalent $[48\bar{1}]$, both resulting from the intersection of the different faces of the $\{10\bar{1}4\}$ form) is oriented parallel to the [001] direction of the anhydrite substrate. A detailed inspection of the micrograph in Figure 2a reveals a second, much less numerous, population of crystals (from here on Cal_2), which are oriented with one of their $\langle\bar{4}41\rangle$ edges parallel to the $[010]_{Anh}$. Consequently, both calcite crystal populations (Cal_1 and Cal_2), are related to each other by a 11.9° rotation about the axis parallel to $[100]_{Anh}$.

The preferential orientations of these calcite crystal overgrowths in relation to the (100) anhydrite cleavage surface was clarified through EBSD analyses (Figure 2b). The pole-orientation density distribution figures (Figure 2a) obtained for the {0001}, $\{10\bar{1}4\}$, and $\{11\bar{2}0\}$ are consistent with the orientation deduced from the SEM photomicrographs for the larger population of calcite crystals (Cal_1). Moreover, EBSD analysis also showed a 4-fold increase in the number of poles, indicating the existence of four symmetry related orientations in Cal_1: Cal_{1a}, Cal_{1b}, Cal_{1c}, and Cal_{1d} (Figure 2c). This increase in the number of poles is the result of the existence of symmetric operators inherent to the anhydrite structure and normal to the (100) substrate plane. These are a twofold screw axis, mirror planes, glide planes, as well as a center of symmetry contained in this plane. Furthermore, the existence of a slight tilt of the pole positions with respect to the expected ones was also noticeable. This is most likely due to a small displacement of the anhydrite crystal in the sample holder during sample preparation for EBSD analyses.

The Cal_2 crystals were far rarer and thus their pole figures are not as clearly recognizable in the EBSD analysis (Figure 2b). However, the slight dispersion around the pole positions could reflect a slight misorientation of the Cal_1 crystals and/or the presence of this smaller population of Cal_2 crystals. This is particularly because the Cal_2 crystals are only slightly rotated (~11.9°) with respect to the major Cal_1 population. Nevertheless, similarly to the Cal_1 crystals, we could define four symmetry related orientations for calcite crystals of the Cal_2 population: Cal_{2a}, Cal_{2b}, Cal_{2c}, and Cal_{2d} (Figure 2d).

Comparing SEM micrographs of different anhydrite surfaces evidence that (010) surfaces showed similar features to (100) surfaces (Figure 3a). Both surfaces were dominated by large and very flat terraces, bounded by macrosteps that ran parallel to [100] and [001] directions. Moreover, calcite crystals formed on such surfaces were also bound by $\{10\bar{1}4\}$ faces and oriented with one of these faces parallel to the anhydrite (010) substrate ($(010)_{Anh}\|\{10\bar{1}4\}_{Cal}$). Furthermore, a majority of calcite crystals had a set of their $\langle\bar{4}41\rangle$ edges oriented parallel to the [001] direction of the anhydrite substrate (Cal_3), while a smaller population had these set of $\langle\bar{4}41\rangle$ edges parallel to the $[100]_{Anh}$ (Cal_4). Pole-orientation density distributions figures obtained by EBSD analyses along the $(010)_{Anh}$/calcite phase boundary again revealed similar features to those obtained for the $(100)_{Anh}$ (Figure 3b). Indeed, the presence of twofold and

DOI: 10.1021/acs.cgd.7b01610
Cryst. Growth Des. 2018, 18, 1666−1675

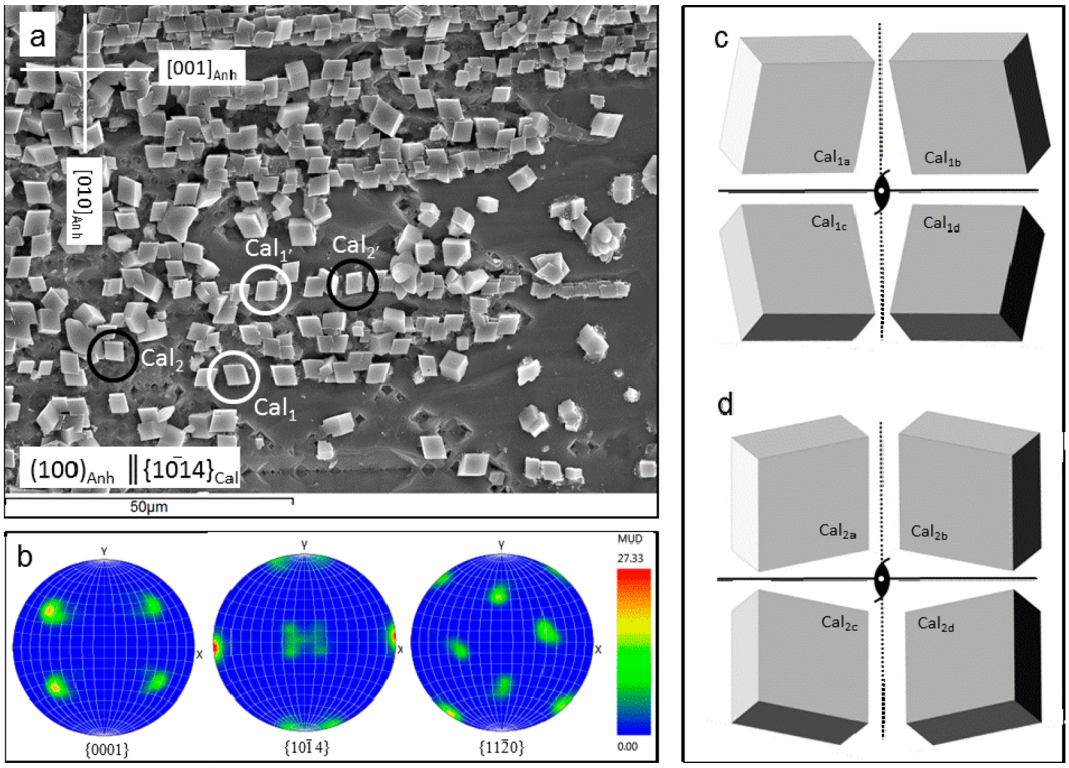

Figure 2. (a) SEM image of calcite crystals grown oriented on the (100) surface of an anhydrite cleaved crystal after 2 h of interaction. The epitaxy involves a matching of the plane (100) of anhydrite with the plane (10$\bar{1}$4) of calcite. The encircled crystals show four different orientations of calcite on the anhydrite substrate which are symmetrically related two by two: Cal_1-Cal_1' and Cal_2-Cal_2' with some of the ⟨$\bar{4}$41⟩ edges running parallel to the $[001]_{Anh}$ and $[010]_{Anh}$, respectively. (b) EBSD pole-orientation density distribution figures which show the crystallographic orientation relationships between the $(100)_{Anh}$ and the overgrown calcite crystals: $(100)_{Anh}\|(10\bar{1}4)_{Cal}$. The number of poles is four times higher than expected reflecting the four alternative orientations shown by the calcite crystals (c) Four alternative orientations, Cal_{1a}, Cal_{1b}, Cal_{1c}, and Cal_{1d}, can be deduced from the pole figures. They reflect the symmetry operators inherent to the anhydrite structure that are normal to the $(100)_{Anh}$ substrate. (c) Four alternative orientations envisaged for the Cal_2 population of crystals.

twofold screw axes, mirror and glide planes, as well as a symmetry center in the anhydrite structure determined the existence of four statistically equivalent orientations of calcite crystals with respect to the anhydrite (010) substrate for each one of the two alternative epitactic relationships defined above.

2.2. Calcite Overgrowth on Anhydrite (001). Anhydrite (001) surfaces were also characterized by flat terraces, bounded by macrosteps that ran parallel to the [100] and [010] directions. Post reaction of these surfaces with the carbonate-rich solutions revealed significantly higher average densities of calcite crystals than on the anhydrite (100) and (010) substrates. The anhydrite (001) substrate was almost completely covered by calcite crystals after 1 h of reaction with the solution.[11] However, at very early stages we observed the development of deep, dissolution-related grooves on the anhydrite (001) substrate, which were oriented parallel to [100] (Figure 4a). This enabled us to define the main crystallographic directions on this surface.[15] Similarly to our observations on both the (100) and (010) surfaces, on the (001) surface calcite crystals with the typical rhombohedron-like habit, bounded by the six faces of the {10$\bar{1}$4} form, are formed. The calcite crystals were oriented with one of their rhombohedron faces parallel to the anhydrite (001) substrate (defining the matching $(001)_{Anh}\|\{10\bar{1}4\}_{Cal}$). Some of these calcite crystals (Cal_5, Figure 4a) are oriented with a set of the ⟨$\bar{4}$41⟩ edges parallel to [100] in the anhydrite substrate. This defines the epitactic relationship $[100]_{Anh}\|\langle\bar{4}41\rangle_{Cal}$. However, a second population of calcite crystals (Cal_6) was slightly tilted (<12°) with respect to those that constitute the Cal_5 population. This tilting occurs in such a way that the ⟨$\bar{4}$41⟩ edges of the calcite run parallel to $[010]_{Anh}$, defining the relationship: $[010]_{Anh}\|\langle\bar{4}41\rangle_{Cal}$. On this (001) anhydrite substrate, the population of Cal_5 crystals was significantly larger than that of Cal_6 crystals. EBSD analyses of the adjacent anhydrite and calcite boundaries also yielded similar crystallographic orientations as those described for the (100) and (010) anhydrite surfaces (Figure 4b).

Finally, we also observed that the nucleation of calcite crystals on the anhydrite substrate with such different and symmetry related orientations often lead to the formation of substrate-induced twins as differently oriented calcite crystals grew and eventually coalesced (Figure 5).

3. DISCUSSION

We demonstrated that the density of calcite crystals formed upon interaction between specific anhydrite surfaces with carbonate-rich aqueous solutions was significantly higher at earlier stages of reaction on $(001)_{Anh}$ compared to on $(100)_{Anh}$ and $(010)_{Anh}$. This is a consequence of the significantly higher reactivity of the $(001)_{Anh}$ surfaces, which dissolves at a much faster rate than both $(100)_{Anh}$ and $(010)_{Anh}$.[16] Consequently, the rate at which Ca^{2+} ions were released from an anhydrite (001) substrate was also faster, resulting in a more rapid increase of local supersaturation in the vicinity of the $(001)_{Anh}$-aqueous solution interface compared to the interface between the aqueous solution and the other two anhydrite cleavage

DOI: 10.1021/acs.cgd.7b01610
Cryst. Growth Des. 2018, 18, 1666−1675

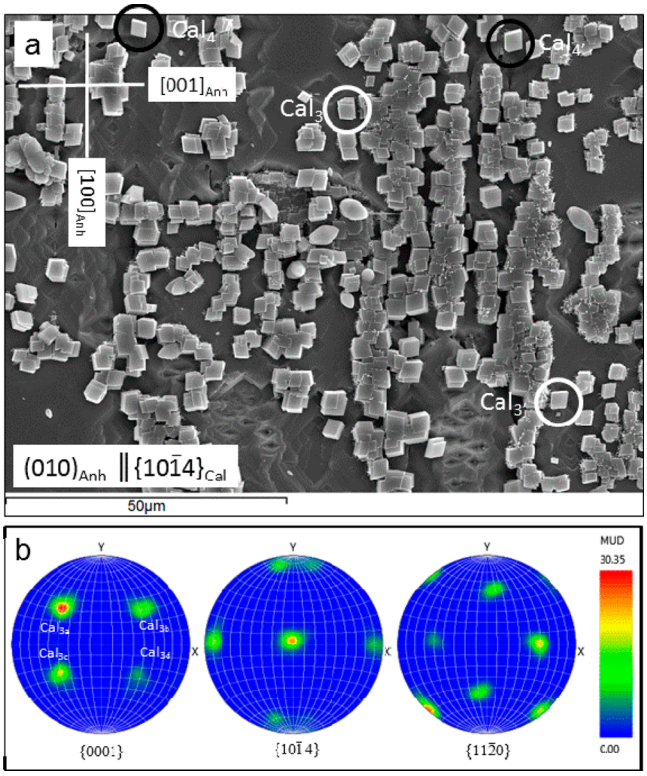

Figure 3. (a) SEM image of calcite crystals grown oriented on the anhydrite (010) surface after 2 h of interaction with the carbonate-rich aqueous solution. The epitaxy is defined by $(100)_{Anh}\|(10\bar{1}4)_{Cal}$. The encircled crystals show the four different orientations of calcite crystals on the anhydrite substrate, which are symmetrically related two by two: Cal_3-Cal_3' and Cal_4-Cal_4'. (b) EBSD pole-orientation density distribution figures. The number of poles is four times higher than expected, reflecting the four alternative orientations shown by the calcite crystals which constitute the Cal_3 population: Cal_{3a}, Cal_{3b}, Cal_{3c}, and Cal_{3d}.

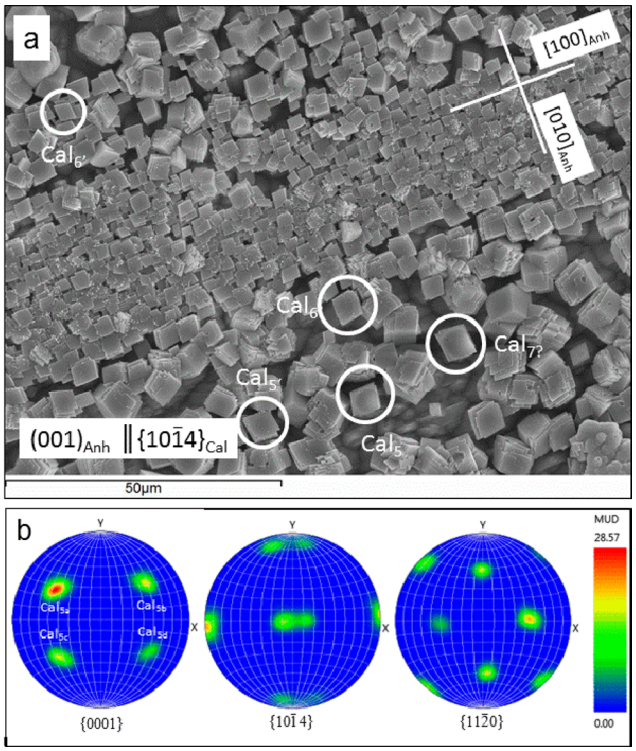

Figure 4. (a) SEM image of calcite crystals grown specifically oriented on the (001) surface of an anhydrite cleavage fragment. The epitaxy involves the matching of the plane (001) of anhydrite with the plane (10$\bar{1}$4) of calcite. The encircled crystals show alternative orientations of calcite on the anhydrite substrate. The density of the crystals is significantly higher than observed on $(100)_{Anh}$ and on $(010)_{Anh}$ for the same interaction time (2 h). (b) Pole-orientation density distribution figures obtained using EBDS. The number of poles is four times higher than expected, reflecting the four alternative orientations for the Cal_5 population: Cal_{5a}, Cal_{5b}, Cal_{5c}, and Cal_{5d}.

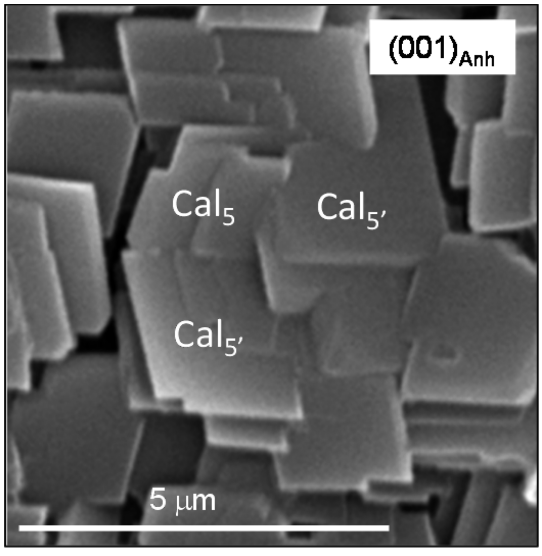

Figure 5. SEM image of substrate-induced calcite twins grown on an anhydrite (001) surface. This type of twins develops when two neighboring, differently oriented calcite crystals (Cal_5 and $Cal_{5'}$) belonging to the same epitactic population (Cal_5) grow to coalesce. The crystal individuals forming the twin are related one to other through a reflection operator belonging to the anhydrite substrate (see Figure 3c).

surfaces, (100) and (010). The nucleation of $CaCO_3$ at higher supersaturation levels can, in turn, explain both, the formation of a higher number of calcite nuclei as well as the formation of a small amount of metastable vaterite at the early stages of the reaction.[11]

Unsurprisingly the habit of all calcite crystals that grew on the three anhydrite surfaces was bounded by the {10$\bar{1}$4} form, that is, the cleavage rhombohedron. This form is the most stable one among the calcite forms because the four different periodic bond chains (PBCs) contained in a $d_{\{10\bar{1}4\}}$ slide provide it with a very strong F character.[17−19] These PBCs run parallel to [$\bar{4}$41], [48$\bar{1}$], [2$\bar{2}$1], and [010] directions in the calcite structure.[20] The two first directions mentioned above are relatively straight chains of carbonate−calcium−carbonate bonds, whereas PBCs parallel to the [2$\bar{2}$1] and [010] directions consist of undulating bond chains, also composed by carbonate−calcium−carbonate bonds (Figure 6).

Although the development of an epitaxy between an overgrowth and a substrate is not exclusively ruled by geometrical factors, the existence of geometrical similarities between the structures of the involved phases is a requirement for the epitaxy to be possible. These similarities are present in the structures of anhydrite and calcite, despite the fact that both phases crystallize in different crystal systems (anhydrite: space group *Amma*, a = 6.993 Å, b = 6.995 Å, and c = 6.245 Å; calcite: space group $R\bar{3}c$, a = 4.990 Å, and c = 17.061 Å).[21,22] The

DOI: 10.1021/acs.cgd.7b01610
Cryst. Growth Des. 2018, 18, 1666−1675

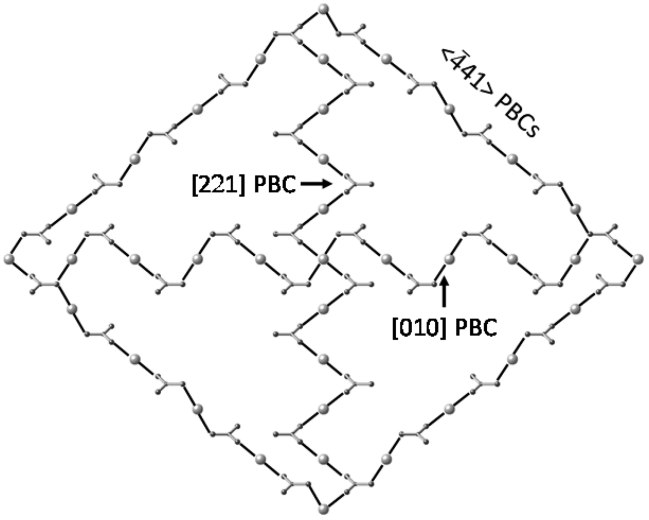

Figure 6. Schematic projection showing the three nonequivalent PBCs contained in the calcite $\{10\bar{1}4\}$ surface. The [221] direction runs parallel to the short diagonal of the rhombus defined by $\langle\bar{4}41\rangle$ directions. The [010] direction runs parallel to the long diagonal. Ca^{2+} cations are depicted by spheres, whereas ball and stick groups represent CO_3^{2-}.

structures of the $\{100\}_{Anh}$, $\{010\}_{Anh}$, and $\{001\}_{Anh}$ surfaces and the $\{10\bar{1}4\}$ form of calcite are based on chains of alternating oxyanion polyhedra and $[n]$-coordinated Ca^{2+}. These chains link to each other, forming layers. In the anhydrite structure three sulfate-calcium-sulfate bond chains can be distinguished.[23] These PBCs run parallel to the crystallographic axes. Consequently, they provide an F-character to the three main anhydrite surfaces since all of them contain two groups of coplanar PBCs. As a result of these crystallographic similarities, the formation of a $\{10\bar{1}4\}$ layer of calcite on any of the three anhydrite surfaces does not interrupt the SO_4−Ca sequence and can ideally continue and match the structure of anhydrite. Indeed, structural continuity "represents the master condition which has to be respected when two crystalline individuals grow within the twinning or epitaxial relationships".[24] Moreover, although the geometries of the sulfate (SO_4^{2-}, tetrahedron) and carbonate (CO_3^{2-}, triangle) oxyanions are different, both are identically charged and have a similar size, which contributes to make possible the development of epitatic relationships between both phases. As a matter of fact, it has been demonstrated that calcite can incorporate small amounts of sulfate substituting carbonate in its bulk structure.[25−29]

Beyond the structural similarities, the formation of the interface between layers of two different phases also requires a good matching of their lattice planes. The mismatch through the interface between the lattices of the two phases involved in the epitaxy can be described by the lattice misfit (mf), which is frequently expressed by means of the equation[30]

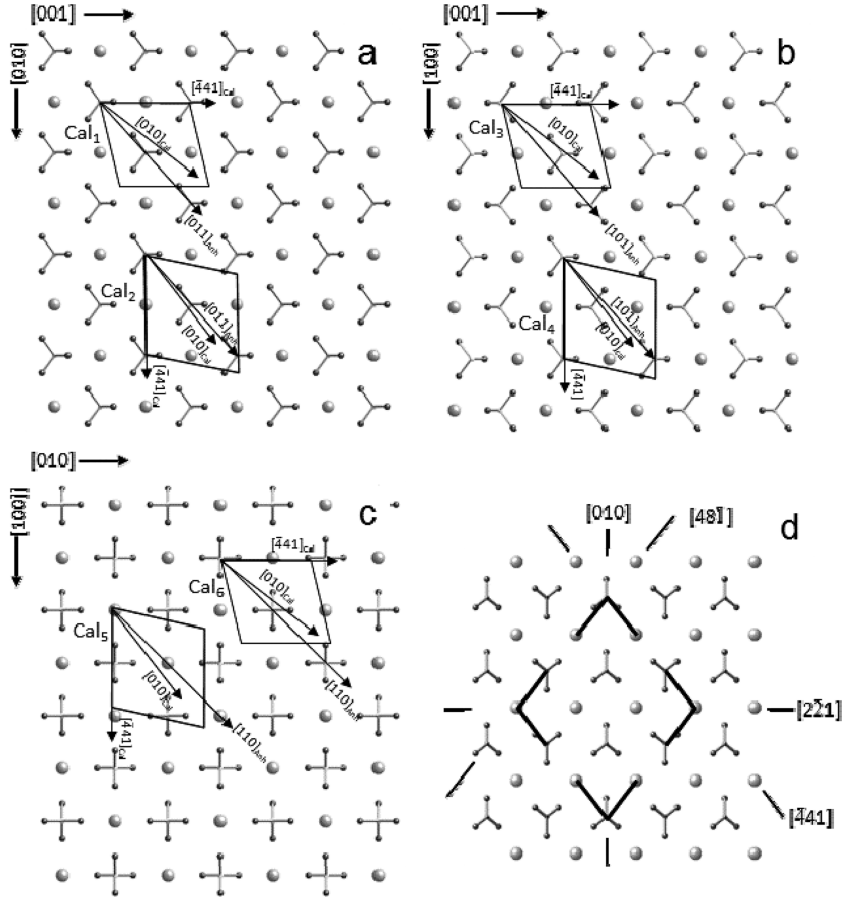

Figure 7. Projections of the crystal structures of a slice of (a) $(200)_{Anh}$, (b) $(020)_{Anh}$, and (c) $(002)_{Anh}$. The superimposed rhombus depicts the $(10\bar{1}4)$ face of the calcite rhombohedron projected in the same orientation as shown in the SEM images. (d) Schematic of the $(10\bar{1}4)_{Cal}$ surface of calcite showing the main directions. Ca^{2+} cations are depicted by spheres, whereas ball and stick groups represent SO_4^{2-} and CO_3^{2-}.

DOI: 10.1021/acs.cgd.7b01610
Cryst. Growth Des. 2018, 18, 1666−1675

Table 1. Epitactic Relationships between Anhydrite ($CaSO_4$) and Calcite ($CaCO_3$)

anhydrite ($CaSO_4$)		Calcite ($CaCO_3$)			misfit (%)	
contact plane	parameter (Å)	contact plane	parameter (Å)	calcite population	linear	angular
(100)	2 × [001] = 12.490	(10$\bar{1}$4)	⟨$\bar{4}$41⟩ = 12.850	1	2.88	–
	⟨011⟩ = 4.689		[010] = 4.990		6.42	∼9.20°
	2 × [010] = 13.990		⟨$\bar{4}$41⟩ = 12.850	2	−8.14	–
	⟨011⟩ = 4.689		[010] = 4.990		6.42	∼2.70°
(010)	2 × [001] = 12.490	(10$\bar{1}$4)	⟨$\bar{4}$41⟩ = 12.850	3	2.88	–
	⟨101⟩ = 9.376		2 × [010] = 9.980		6.44	∼9.20°
	2 × [100] = 13.986		⟨$\bar{4}$41⟩ = 12.850	4	−8.12	–
	⟨101⟩ = 9.376		2 × [010] = 9.980		6.44	∼2.70°
(001)	2 × [100] = 13.986	(10$\bar{1}$4)	⟨$\bar{4}$41⟩ = 12.850	5	−8.12	–
	⟨110⟩ = 9.891		2 × [010] = 9.980		0.90	∼5.50°
	2 × [010] = 13.990		⟨$\bar{4}$41⟩ = 12.850	6	−8.14	–
	⟨110⟩ = 9.891		2 × [010] = 9.980		0.90	∼5.50°
	⟨110⟩ = 9.891		2 × [010] = 9.980	7	0.90	–
	2 × [100] = 13.986		⟨$\bar{4}$41⟩ = 12.850		−8.12	∼5.50°
	2 × [010] = 13.990		⟨$\bar{4}$41⟩ = 12.850		−8.14	∼5.50°

$$mf(\%) = \frac{t_{[uvw]_{Cal}} - t_{[uvw]_{Anh}}}{t_{[uvw]_{Anh}}} \times 100 \quad (1)$$

where $t_{[uvw]}$ is the repeating period along the $[uvw]$ direction of the substrate (anhydrite) and overgrowth (calcite). Negative misfit values mean that the unit cell of the overgrowth is contracted along $[uvw]$ in comparison to the unit cell of the substrate ($t_{[uvw]_{Cal}} < t_{[uvw]_{Anh}}$), whereas a positive misfit value indicates an expansion of the overgrowth unit cell along the same direction. If the difference between the corresponding lattice constants mf is ≤10% to 12%, the lattice matching results in the formation of a coherent substrate−overgrowth interface. This is furthermore, accompanied by the generation of elastic strain and stress and the formation of an epitaxy.[31,32] Figure 7a−d display the projections of the structure of anhydrite on the (100), (010), and (001) planes and calcite on the (10$\bar{1}$4) plane. The superimposed lozenges on the anhydrite structure projections depict a calcite rhombohedron, bounded by ⟨$\bar{4}$41⟩ edges and with one of its (10$\bar{1}$4) faces siting on the projected anhydrite plane. These lozenges are oriented with a pair of their ⟨$\bar{4}$41⟩ edges parallel to a main direction in the anhydrite projection. This matches our observations from the SEM images and EBSD analyses results (Figures 2−4).

As explained above, in most of the calcite crystals (Cal_1 and Cal_3) the epitactic overgrowth of $\{10\bar{1}4\}_{Cal}$ on $(100)_{Anh}$ and $(010)_{Anh}$ was controlled by the parallelism between the $\langle\bar{4}41\rangle_{Cal}$ and $[001]_{Anh}$. For anhydrite, the distance between successive SO_4 groups along [001] is 6.245 Å, i.e., it coincides with the anhydrite c cell parameter. In the calcite structure, the distance between successive equivalent CO_3 groups (repeating period) is 12.850 Å, which is about twice the distance between successive SO_4 groups along $[001]_{Anh}$ (2 × 6.245 Å = 12.49 Å). Similar repeating periods guarantee a good matching between the two structures. Considering a 1:2 ratio between the repeating periods along $[001]_{Anh}$ and $\langle\bar{4}41\rangle_{Cal}$, the misfit is 2.88% (Table 1), which clearly lies within the limits required for epitactic nucleation from solution.[31] Thus, our data show that the excellent matching between both surfaces along these directions explains the development of an oriented overgrowth of calcite on both $(100)_{Anh}$ and $(010)_{Anh}$ surfaces. One additional pair of directions within these contact planes can also be defined in both anhydrite surfaces, $\langle011\rangle_{Anh}\|[010]_{Cal}$ and $\langle101\rangle_{Anh}\|[010]_{Cal}$. These pairs show relatively good matching with linear misfit close to 6.4% (see Table 1). However, an angular divergence between both directions of ∼9.20° does not support the possibility that matching along these directions contribute to the development of the epitaxies.

As we have shown in the SEM images (Figures 2a and 3a), there was a secondary, much less numerous population of calcite crystals, which included two crystal populations (Cal_2 and Cal_4), with one of their $\langle\bar{4}41\rangle_{Cal}$ aligned parallel to the [010] and [100] directions of the $(100)_{Anh}$ and $(010)_{Anh}$ surfaces, respectively. Since the a and b axes in the anhydrite structure are almost identical in length ($b - a$ = 0.002 Å), the linear misfits between the calcite and anhydrite structures along both of these directions are also very similar to ∼8% for both the $[010]_{Anh}\|\langle\bar{4}41\rangle_{Cal}$ and the $[100]_{Anh}\|\langle\bar{4}41\rangle_{Cal}$ alignments. It was also possible to define a second pair of alignments, with $\langle011\rangle_{Anh}\|[010]_{Cal}$ (Cal_2) and $\langle101\rangle_{Anh}\|[010]_{Cal}$ (Cal_4), which were identical to those described for Cal_1 and Cal_3, although with a lower angular divergence (∼2.7°). Although the matches described for Cal_2 and Cal_4 were not as good as those calculated for the Cal_1 and Cal_3 populations, they nevertheless still guarantee the development of an epitactic overgrowth of so oriented calcite crystals on the $(100)_{Anh}$ and $(010)_{Anh}$ surfaces. The good match between the two pair of directions in this second orientation explains, therefore, the development of two nonsymmetrically related populations of calcite crystals rotated by ∼12° with respect to each other. On anhydrite {001} surfaces we have suggested a match between $[100]_{Anh}\|\langle\bar{4}41\rangle_{Cal}$ and $\langle110\rangle_{Anh}\|[010]_{Cal}$ for Cal_5, and $[010]_{Anh}\|\langle\bar{4}41\rangle_{Cal}$ and $\langle110\rangle_{Anh}\|[010]_{Cal}$ for Cal_6 with a slightly better misfits for Cal_5 than Cal_6 (see Table 1). This higher fitting goodness explains the much larger population of Cal_5 crystals.

It is possible to evaluate epitaxy relationship solely on the basis of structural similarities and misfit values. However, as stated by the PBC theory, a minimum interface energy is achieved when, apart from a matching of parallel planes of the substrate and the overgrowth, there is a coincidence between the close-packed atomic rows (defined by the PBCs) contained in these planes.[31] In all the epitactic relationships defined above, the better match involves crystallographic directions parallel to PBCs in both calcite and anhydrite. This factor further favors the development of the oriented overgrowth. Indeed, other alternative epitactic relationships with low misfits

DOI: 10.1021/acs.cgd.7b01610
Cryst. Growth Des. 2018, 18, 1666−1675

values can be envisaged. For instance, the $[110]_{Anh}\|\langle 010\rangle_{Cal}$ alignment on $(001)_{Anh}$ exhibits an excellent match with a linear misfit of 0.90%. However, such an epitaxy is in principle energetically unfavorable with respect to the epitaxies defined above, since the $[110]_{Anh}$ is not parallel to any PBC in the anhydrite structure. Furthermore, although the $[010]_{Cal}$ direction corresponds to a PBC, this is a rough, high-energy, and thus less favorable PBC.[19] In Figure 7c, some crystals could be oriented following this orientation (Cal_7), although this is not clearly supported by SEM observations and EBSD analyses (Table 1).

The existence of epitactic relationships between anhydrite surfaces and calcite overgrowths can influence the kinetics of the carbonation reaction. It has been shown that under certain conditions the development of epitactic overgrowths can lead to *surface passivation*[33] and, as a result, to a slowdown or even full inhibition of any further dissolution−precipitation after the formation of a thin overgrowth. Such overgrowths are often only nanometer-thin, as in the cases of the epitactic overgrowths of otavite ($CdCO_3$) and rhodochrosite ($MnCO_3$) on a calcite {1014} substrate or of hashemite ($BaCrO_4$) on a barite ($BaSO_4$) (001) substrates.[32,34−37] Overgrowths can result from the development of two-dimensional, yet only a few nanometers high, nuclei. These spread rapidly on a substrate and coalesce according to a Frank−van der Merwe or Stranski−Krastanov epitactic growth mechanisms.[32−34] Depending on the goodness of the lattice misfit this commonly involves isostructural phases, which belong to the same mineral group. The formation of this type of overgrowths leads to the almost perfect preservation of the nanotopography of the surface of a substrate.[38,39] A second type of epitactic overgrowth involves the formation on a dissolving substrate of three-dimensional crystals, according to a Volmer−Weber growth mechanism. Commonly, the formation of 3-D crystals takes place when the primary and the secondary phases are non-isostructural but share some structural features and the matching through certain interfaces is good. In this case, even if the overgrowth completely carpets the substrate (like in the case of our calcite crystals growing on the anhydrite surfaces), the armoring is usually imperfect. The existence of hollows, left between differently oriented crystals in the overgrowth, allows a continuous communication between the aqueous solution and the substrate. This way, the progress of the dissolution−crystallization reaction is guaranteed, even if its kinetics is slowed down. Excellent examples of this type of epitaxy are the oriented growth of pharmacolite ($CaHAsO_4{\cdot}2H_2O$) on gypsum and of anglesite ($PbSO_4$) on anhydrite.[40,41] In the latter case, it was demonstrated that the formation of the overgrowth did not prevent the dissolution−precipitation reaction progressing until the complete replacement of anhydrite by anglesite.[42]

The anhydrite−calcite epitaxy described here clearly fits in this latter category. The coalescence of micrometer-sized blocky calcite crystals that are differently oriented on the anhydrite substrates will necessarily lead to the formation of a porous overgrowth. This will, nevertheless, fail to perfectly seal the substrate. The effect of this imperfect sealing is further enhanced by the fact that the replacement of anhydrite by calcite leads to a negative volume change, further contributing to an increase in the porosity of the overgrown calcite layer and explaining that anhydrite crystals in contact with carbonate-bearing solutions can become completely replaced by aggregates of calcite crystals in relatively short times (~15 days under the experimental conditions used in this work).[11]

It is worth highlighting that the existence of two or more equiprobable orientations of the calcite crystals on the anhydrite substrates leads to the development of so-called substrate-induced twinning.[43] The formation of such twins (Figure 5) is a consequence of the coalescence of individuals that are differently oriented with respect to the substrate, but whose orientations are related to each other by symmetry operators inherent to the substrate structure.[42,43] The twin law is, therefore, determined by the substrate symmetry. For instance, in the anhydrite−calcite epitaxy in this current study, individual crystal *a* can be related with individual crystal *d* through a center of symmetry which acts as a twin center (Figure 2c). The formation of substrate-induced twins is a general phenomenon, which has so far been reported to occur during pseudomorphic mineral replacement processes through interface coupled dissolution−crystallization reactions.[42,43]

4. CONCLUSIONS

We evidence here that the epitactic growth of a calcite overgrowth on the three main anhydrite cleavage surfaces, (100), (010), and (001), as a result of their interaction with carbonate-rich aqueous solutions is in all the cases facilitated by (1) the continuity of the anhydrite structure after the deposition of calcite nuclei regardless of substrate type, (2) the goodness of anhydrite-calcite matching through the interface, and (3) the F-character of the anhydrite and calcite surfaces, which guarantees that all crystallographic directions along which both structures show good matchings corresponds to PBCs. Furthermore, we can conclude that moderate goodness of some of the matches defined explain the epitactic growth of calcite on the three anhydrite substrates through a Volmer−Weber mechanism.

Calcite overgrowth consists of micrometric calcite crystals oriented in a number of different ways that produces a certain volume of intergranular porosity within the overgrowth, defined in the contact between differently oriented crystals. This porosity is the consequence of the imperfect assembly between differently oriented rhombohedron-like calcite crystals and is independent of that which will result from the molar volume change involved in the mineral carbonation reaction. Consequently, we can anticipate that, regardless of the molar volume change, mineral carbonation reactions which progress through the formation of micrometer-sized and nonevenly oriented epitactic overgrown crystals are likely to slow down the carbonation due to the progressive thickening of the overgrowth. However, the intrinsic intergranular porosity of this epitactic overgrowth makes unlikely that the transformation will be completely stopped by the overgrowth development. This situation is to be expected when (1) the epitactic overgrowth involves two nonisostructural phases, whose matching through the interface has a moderate goodness, and (2) the primary mineral phase contains symmetry operators normal to the primary-secondary phases interface.

So far, most experimental works were oriented to evaluate the viability of sequestering CO_2 through the carbonation of rock-forming silicate minerals, focusing on olivine and plagioclase.[44,45] In comparison, the carbonation of calcium sulfates, and particularly the carbonation of anhydrite, has significant advantages that render this process as potentially more effective for the capture and long-term storage of CO_2. First, the kinetics of the carbonation reaction is much faster in the case of anhydrite than in the case of olivine and plagioclase. Second, the carbonation of olivine is accompanied by a positive

DOI: 10.1021/acs.cgd.7b01610
Cryst. Growth Des. 2018, 18, 1666−1675

molar volume change, a passivation and self-limiting phenomena which have been reported to take place during the development of this reaction.[46−48] In contrast, anhydrite carbonation is accompanied by a negative molar volume change, which necessarily involves the generation of porosity. Third, the characteristics of calcite epitactic overgrowths, which contain an intrinsic intergranular porosity, irrespective the cleavage surface, that would prevent full passivation during anhydrite carbonation reactions. Finally, in the Earth's surface, anhydrite deposits are widespread and, in general, accessible. Therefore, we conclude that anhydrite carbonation appears as a potentially efficient process worth to be taken into consideration when designing strategies for the capture of CO_2 through solvent mediated mineral replacement reactions.

AUTHOR INFORMATION

Corresponding Author

*E-mail: jmastill@ucm.es. Phone: +34 913944876.

ORCID

José Manuel Astilleros: 0000-0002-4555-6243

Notes

The authors declare no competing financial interest.

ACKNOWLEDGMENTS

This study was supported by the MINECO (Spain) under projects CGL2013-47988-C2-1-P and CGL2016-77138- C2-1-P. I. Cuesta Mayorga acknowledges a FPI (BES-2014-070279) fellowship from the Spanish MINECO and L.G.B. acknowledges financial support from the Helmholtz Recruiting Initiative.

REFERENCES

(1) Oelkers, E. H.; Gislason, S. R.; Matter, J. Mineral Carbonation of CO_2. *Elements* **2008**, *4*, 333−337.

(2) Matter, J. M.; Stute, M.; Snæbjörnsdottir, S.Ó.; Oelkers, E. H.; Gislason, S. R.; Aradottir, E. S.; Sigfusson, B.; Gunnarsson, I.; Sigurdardottir, H.; Gunnlaugsson, E.; Axelsson, G.; Alfredsson, H. A.; Wolff-Boenisch, D.; Mesfin, K.; de la Reguera Taya, D. F.; Hall, J.; Dideriksen, K.; Broecker, W. S. Rapid carbon mineralization for permanent disposal of anthropogenic carbon dioxide emissions. *Science* **2016**, *352*, 1312−1314.

(3) Kelemen, P. B.; Matter, J. In situ carbonation of peridotite for CO_2 storage. *Proc. Natl. Acad. Sci. U. S. A.* **2008**, *105*, 17295−17300.

(4) Matter, J. M.; Kelemen, P. B. Permanent storage of carbon dioxide in geological reservoirs by mineral carbonation. *Nat. Geosci.* **2009**, *2*, 837−841.

(5) Gislason, S. R.; Oelkers, E. H. Carbon storage in basalt. *Science* **2014**, *344*, 373−374.

(6) Kendall, A. C. Late diagenetic calcitization of anhydrite from the Mississippian of Saskatchewan, western Canada. *Sedimentology* **2001**, *48*, 29−55.

(7) Alonso-Zarza, A. M.; Sánchez Moya, Y.; Bustillo Revuelta, M. A.; Sopeña, A.; Delgado Huertas, A. Silicification and dolomitization of anhydrite nodules in argillaceous terrestrial deposits: an example of meteoric-dominated diagenesis from the Triassic of central Spain. *Sedimentology* **2002**, *49*, 303−317.

(8) Warren, J. K. *Evaporites: Sediments, Resources and Hydrocarbons*; Springer: Berlin Heidelberg, 2006; pp 539−542.

(9) Stafford, K. W.; Ulmer-Scholle, D.; Rosales-Lagarde, L. Hypogene calcitization: Evaporite diagenesis in the western Delaware Basin. *Carbonates Evaporites* **2008**, *23*, 89−103.

(10) Ruiz-Agudo, E.; Putnis, C. V.; Putnis, A. Coupled dissolution and precipitation at mineral−fluid interfaces. *Chem. Geol.* **2014**, *383*, 132−146.

(11) Roncal-Herrero, T.; Astilleros, J. M.; Bots, P.; Rodríguez-Blanco, J. D.; Prieto, M.; Benning, L. G.; Fernández-Díaz, L. Reaction pathways and textural aspects of the replacement of anhydrite by calcite at 25° C. *Am. Mineral.* **2017**, *102*, 1270−1278.

(12) Fernández-Díaz, L.; Pina, C. M.; Astilleros, J. M.; Sánchez-Pastor, N. The carbonatation of gypsum: Pathways and pseudomorph formation. *Am. Mineral.* **2009**, *94*, 1223−1234.

(13) Kostov, I.; Kostov, R. I. Crystal habits of minerals. *Bulgarian Academic Monographs (1)*; Pensoft Publishers and Prof. Marin Drinov Academic Publishing House: Sofia, 1999; pp 307−308.

(14) Palmer, D. *CrystalMaker*, v 1.0.4; CrystalMaker Software Ltd: Begbroke, Oxfordshire, England, 2005.

(15) Shindo, H.; Seo, A.; Watabe, T. Structures of the $CaSO_4$ (001) surface studied with atomic force microscopy in air and in solution. *Phys. Chem. Chem. Phys.* **2001**, *3*, 230−234.

(16) Shindo, H.; Igarashi, T.; Karino, W.; Seo, A.; Yamanobe-Hada, M.; Haga, M. Stabilities of crystal faces of anhydrite ($CaSO_4$) compared by AFM observation of facet formation processes in aqueous solutions. *J. Cryst. Growth* **2010**, *312*, 573−579.

(17) Hartman, P.; Perdok, W. On the relations between structure and morphology of crystals. I. *Acta Crystallogr.* **1955**, *8*, 49−52.

(18) Paquette, J.; Reeder, R. Relationship between surface structure, growth mechanism, and trace element incorporation in calcite. *Geochim. Cosmochim. Acta* **1995**, *59*, 735−749.

(19) Aquilano, D.; Bruno, M.; Massaro, F. R.; Rubbo, M. Theoretical equilibrium shape of calcite. 2. [441] zone and its role in biomineralization. *Cryst. Growth Des.* **2011**, *11*, 3985−3993.

(20) Heijnen, W. M. M. The morphology of gel grown calcite. *Neues Jahrb. Mineral., Monatsh.* **1985**, *8*, 357−371.

(21) Hawthorne, F. C.; Ferguson, R. B. Anhydrous sulphates. II. Refinement of the crystal structure of anhydrite. *Can. Mineral.* **1975**, *13*, 289−292.

(22) Effenberger, H.; Mereiter, K.; Zemann, J. Crystal structure refinements of magnesite, calcite, rhodochrosite, siderite, smithonite, and dolomite, with discussion of some aspects of the stereochemistry of calcite type carbonates. *Z. Kristallogr. - Cryst. Mater.* **1981**, *156*, 233−243.

(23) Aquilano, D.; Rubbo, M.; Catti, M.; Pavese, A.; Ugliengo, P. Theoretical equilibrium and growth morphology of anhydrite ($CaSO_4$) crystals. *J. Cryst. Growth* **1992**, *125* (3−4), 519−532.

(24) Massaro, F. R.; Pastero, L.; Costa, E.; Sgualdino, G.; Aquilano, D. Single and twinned Li_2CO_3 crystals (zabuyelite) epitaxially grown on {0001} and {1014} forms of $CaCO_3$ (calcite) crystals. *Cryst. Growth Des.* **2008**, *8*, 2041−2046.

(25) Frisia, S.; Borsato, A.; Fairchild, I. J.; Susini, J. Variations in atmospheric sulphate recorded in stalagmites by synchrotron micro-XRF and XANES analyses. *Earth Planet. Sci. Lett.* **2005**, *235*, 729−740.

(26) Arroyo-de Dompablo, M. E.; Fernández-González, M. A.; Fernández-Díaz, L. Computational investigation of the influence of tetrahedral oxoanions (sulphate, selenate and chromate) on the stability of calcium carbonate polymorphs. *RSC Adv.* **2015**, *5*, 59845−59852.

(27) Fernández-Díaz, L.; Fernández-González, A.; Prieto, M. The role of sulfate groups in controlling $CaCO_3$ polymorphism. *Geochim. Cosmochim. Acta* **2010**, *74*, 6064−6076.

(28) Balan, E.; Aufort, J.; Pouillé, S.; Dabos, M.; Blanchard, M.; Lazzeri, M.; Rollion-Bard, C.; Blamart, D. Infrared spectroscopic study of sulfate-bearing calcite from deep-sea bamboo coral. *Eur. J. Mineral.* **2017**, *29*, 397.

(29) Perrin, J.; Rivard, C.; Vielzeuf, D.; Laporte, D.; Fonquernie, C.; Ricolleau, A.; Cotte, M.; Floquet, N. The coordination of sulfur in synthetic and biogenic Mg calcites: The red coral case. *Geochim. Cosmochim. Acta* **2017**, *197*, 226−244.

(30) Van der Merwe, J. H. The role of lattice misfit in epitaxy. *Crit. Rev. Solid State Mater. Sci.* **1978**, *7*, 209−231.

(31) Chernov, A. A. Nucleation and Epitaxy. In *Modern Crystallography III. Crystal Growth*; Springer Series on Solid-State Science 36; Springer-Verlag: Berlin Heidelberg, 1984; pp 48−103.

DOI: 10.1021/acs.cgd.7b01610
Cryst. Growth Des. 2018, 18, 1666−1675

(32) Shtukenberg, A. G.; Astilleros, J. M.; Putnis, A. Nanoscale observations of epitaxial growth of hashemite on Barite (001). *Surf. Sci.* **2005**, *590*, 212−223.
(33) Prieto, M.; Astilleros, J. M.; Fernández-Díaz, L. Environmental remediation by crystallization of solid solutions. *Elements* **2013**, *9*, 195−201.
(34) Pérez-Garrido, C.; Fernández-Díaz, L.; Pina, C. M.; Prieto, M. *Surf. Sci.* **2007**, *601*, 5499−5509.
(35) Pérez-Garrido, C.; Astilleros, J. M.; Fernández-Díaz, L.; Prieto, M. In situ AFM observations of the interaction between calcite (1014) surfaces and Cd-bearing aqueous solutions. *J. Cryst. Growth* **2009**, *311*, 4730−4739.
(36) Godelitsas, A.; Astilleros, J. M. Dissolution, sorption/(re)-precipitation, formation of solid solutions and crystal growth phenomena on mineral surfaces: implications for the removal of toxic metals from the environment. In *Ion partitioning in ambient-temperature aqueous systems*, Prieto, M.; Stoll, H., Eds.; EMU Notes in Mineralogy 10; European Mineralogical Union and the Mineralogical Society of Great Britain and Ireland: London, 2010; pp 289−324.
(37) Riechers, S. L.; Kerisit, S. N. Anisotropic growth of otavite on calcite: Implications for heteroepitaxial growth mechanisms. *Cryst. Growth Des.* **2018**, *18*, 159−170.
(38) Astilleros, J. M.; Pina, C. M.; Fernández-Díaz, L.; Putnis, A. Nanoscale growth of solids crystallising from multicomponent aqueous solutions. *Surf. Sci.* **2003**, *545*, L767.
(39) Astilleros, J. M.; Pina, C. M.; Fernández-Díaz, L.; Prieto, M.; Putnis, A. Nanoscale phenomena during the growth of solid solutions on calcite {1014} surfaces. *Chem. Geol.* **2006**, *225*, 322−335.
(40) Rodríguez-Blanco, J. D.; Jiménez, A.; Prieto, M. Oriented overgrowth of pharmacolite ($CaHAsO_4{\cdot}2H_2O$) on gypsum ($CaSO_4{\cdot}2H_2O$). *Cryst. Growth Des.* **2007**, *7*, 2756−2763.
(41) Morales, J.; Astilleros, J. M.; Fernández-Díaz, L.; Álvarez-Lloret, P.; Jiménez, A. Anglesite ($PbSO_4$) epitactic overgrowths and substrate-induced twinning on anhydrite ($CaSO_4$) cleavage surfaces. *J. Cryst. Growth* **2013**, *380*, 130−137.
(42) Morales, J.; Astilleros, J. M.; Jiménez, A.; Göttlicher, J.; Steininger, R.; Fernández-Díaz, L. Uptake of dissolved lead by anhydrite surfaces. *Appl. Geochem.* **2014**, *40*, 89−96.
(43) Pinto, A. J.; Jiménez, A.; Prieto, M. Interaction of phosphate-bearing solutions with gypsum: Epitaxy and induced twinning of brushite ($CaHPO_4{\cdot}2H_2O$) on the gypsum cleavage surface. *Am. Mineral.* **2009**, *94*, 313−322.
(44) King, H. E.; Plümper, O.; Putnis, A. Effect of secondary phase formation on the carbonation of olivine. *Environ. Sci. Technol.* **2010**, *44*, 6503−6509.
(45) Olajire, A. A. A review of mineral carbonation technology in sequestration of CO_2. *J. Pet. Sci. Eng.* **2013**, *109*, 364−392.
(46) Béarat, H.; McKelvy, M. J.; Chizmeshya, A. V. G.; Gormley, D.; Nunez, R.; Carpenter, R. W.; Squires, K.; Wolf, G. H. Carbon sequestration via aqueous olivine mineral carbonation: Role of passivating layer formation. *Environ. Sci. Technol.* **2006**, *40*, 4802−4808.
(47) Munz, I. A.; Brandvoll, Ø.; Haug, T. A.; Iden, K.; Smeets, R.; Kihle, J.; Johansen, H. Mechanisms and rates of plagioclase carbonation reactions. *Geochim. Cosmochim. Acta* **2012**, *77*, 27−51.
(48) Hövelmann, J.; Austrheim, H.; Jamtveit, B. Microstructure and porosity evolution during experimental carbonation of a natural peridotite. *Chem. Geol.* **2012**, *334*, 254−265.

DOI: 10.1021/acs.cgd.7b01610
Cryst. Growth Des. 2018, 18, 1666−1675

Precipitation of $CaCO_3$ polymorphs from aqueous solutions: The role of pH and sulphate groups

minerals

MDPI

Article

Precipitation of $CaCO_3$ Polymorphs from Aqueous Solutions: The Role of pH and Sulphate Groups

Iris Cuesta Mayorga [1,2], José Manuel Astilleros [1,2,*] and Lurdes Fernández-Díaz [1,2]

[1] Departamento de Mineralogía y Petrología, Universidad Complutense de Madrid, C/José Antonio Novais 2, Madrid 28040, Spain; iriscuesta@ucm.es (I.C.M.); lfdiaz@geo.ucm.es (L.F.D.)

[2] Instituto de Geociencias (CSIC, UCM), C/José Antonio Novais 2, Madrid 28040, Spain

* Correspondence: jmastill@ucm.es; Tel.: +34-913-944-876

Received: 15 February 2019; Accepted: 10 March 2019; Published: 13 March 2019

Abstract: In this work, we aimed to experimentally study the nucleation and growth of $CaCO_3$ phases precipitated from supersaturated aqueous solutions in the presence of varying concentrations of sulphate oxyanion. The experiments were conducted under pH conditions close to neutral (7.6) and by considering a wide range of initial $(SO_4^{2-})/(CO_3^{2-})$ ratios (0 to approx. 68) in the aqueous solution. We paid special attention to the evolution of the precipitates during ageing within a time framework of 14 days. The mineralogy, morphology, and composition of the precipitates were studied by X-ray diffraction, Fourier transform infrared spectroscopy, scanning electron microscopy, and EDX microanalysis. The concentration of sulphate ions in the reacted aqueous solution was studied by ICPs. The experimental results showed that the mineral composition of the precipitate recovered in each run varied with the $(SO_4^{2-})/(CO_3^{2-})$ ratio in the parental solution, which influenced the mineral evolution of the precipitates during ageing. We observed that high concentrations of sulphate in the aqueous solution stabilized the vaterite precipitates and inhibited calcite formation. Furthermore, aragonite never precipitated directly from the solution, and it was only formed via a dissolution-precipitation process in solutions with a high $(SO_4^{2-})/(CO_3^{2-})$ ratio after long reaction times. Finally, gypsum only precipitated after long ageing in those aqueous solutions with the highest concentration of sulphate. The reaction pathways during ageing, the morphology of the calcite crystals, and the composition of vaterite and calcite were discussed considering both kinetic and thermodynamic factors. These results showed a considerably more complex behavior of the system than that observed in experiments conducted under higher pHs and supersaturation levels and lower $(SO_4^{2-})/(CO_3^{2-})$ ratios in the aqueous phase.

Keywords: $CaCO_3$ polymorphs; sulphate; ageing process; aragonite; gypsum

1. Introduction

The presence of calcium carbonate mineral phases is ubiquitous in surface and subsurface environments in the Earth. Calcium carbonate phases in such environments range from amorphous to crystalline and from anhydrous (calcite, aragonite, and vaterite ($CaCO_3$)) to differently hydrated (monohydrocalcite ($CaCO_3{\cdot}H_2O$) and ikaite ($CaCO_3{\cdot}6H_2O$)) [1]. In these environments, the only stable phase of calcium carbonate is calcite, which appears as the main constituent of sedimentary carbonate rocks [1,2] and hard tissues in marine organisms [2–4]. However, all other phases can also form and often remain metastable over long periods due to kinetic factors and/or the influence of specific chemical species in a variety of bio-geological contexts [5–7]. Thus, amorphous $CaCO_3$ (ACC) plays a main role in the early stages of the formation of carbonate hard tissues, where it forms at far-from-equilibrium conditions and, following Ostwald's step rule, subsequently transforms into

other $CaCO_3$ phases through different reaction pathways [8–10]. In carbonate hard tissues, ACC can also remain stabilised in specific locations under the influence of organic molecules and/or inorganic foreign ions like magnesium [11] as a sort of $CaCO_3$ storage which can eventually be disposed for hard tissue-damage reparation [12]. The appearance of the hydrated forms of calcium carbonate ikaite and monohydrocalcite is restricted to very specific environments like near-freezing conditions aqueous environments where the presence of magnesium or phosphate ions has been proposed to promote their formation [13,14]. Kinetic effects facilitate the formation of vaterite in natural environments where this phase represents an intermediate step in the reaction pathway that leads from ACC to calcite following Ostwald's steps rule [15]. The seasonal formation and temporal stabilization of vaterite in evaporite-rich geological settings has also been linked to the influence of high concentrations of dissolved sulphate [16]. Finally, aragonite is the second most abundant $CaCO_3$ phase in surface and subsurface environments after calcite [17]. Aragonite also is a main component of carbonate biominerals, often coexisting with calcite in the same hard tissue [4,18,19]. The main role played by high Mg^{2+}/Ca^{2+} ratios in aqueous environments as the determining factor in the crystallization and stabilization of aragonite has been long known [5]. This role has been attributed to the inhibitory effect of dissolved magnesium on the growth of calcite [20–23]. Changes in the Mg^{2+}/Ca^{2+} ratio in seawater have been proposed to explain the recurrent calcite-aragonite switches in marine $CaCO_3$ biominerals along Earth's history [24]. Consequently, the influence of different foreign ions in the crystallization of $CaCO_3$ and, specifically, in its polymorph selection has long been a main topic of research in carbonate mineralogy. Understandably, most research efforts have been focused on shedding light on the role of magnesium and, to a lesser extent, that of other cations like Sr^{2+} or Co^{2+} [5,23,25–27]. However, much less attention has been paid to the influence of different anions on $CaCO_3$ polymorph selection, even though there exists strong evidences that this influence, especially that of tetrahedral oxyanions, could also be most relevant [28]. Indeed, as mentioned above, phosphate oxyanions have been linked to the formation of ikaite [13]. A combined role of sulphate and Mg^{2+} in the switch from calcite to aragonite seas has been claimed on both geochemical and experimental evidences [29]. The notion that sulphate (SO_4^{2-}), chromate (CrO_4^{2-}), and selenate (SeO_4^{2-}) promote the formation of vaterite and inhibit its transformation into calcite is supported by overwhelming experimental evidence [30–38]. Furthermore, this notion has been given theoretical support by computational studies that relate the effect of tetrahedral oxyanions on $CaCO_3$ polymorph selection to thermodynamic effects arising from the different impacts that their incorporation-substituting carbonate groups have on the structure of the three $CaCO_3$ polymorphs calcite, aragonite, and vaterite [28,31]. This incorporation produces a most significant disruption of the local structure of aragonite. Although less so, this disruption still is very marked in calcite, while the vaterite structure is the least disturbed by the isomorphic incorporation of tetrahedral oxyanions.

In an earlier work, the specific influence of the presence of sulphate oxyanions in the crystallization medium on the formation and evolution upon ageing of $CaCO_3$ precipitates was studied at high pHs (10.9) by conducting batch experiments [31]. High pH conditions are restricted to limited geological settings such as hyper alkaline lakes in connection to tectonic rifts [39]. Even though other authors have studied the influence of sulphate ions on the precipitation of $CaCO_3$ under lower pHs [37,38], these studies only explored a narrow range of SO_4^{2-}/CO_3^{2-} ratio conditions and a comprehensive study of close-to-neutrality conditions is still missing. In this study, we aim to improve our current understanding of the influence of sulphate oxyanions in $CaCO_3$ formation and evolution by filling this gap. We present here the results of precipitation experiments conducted under circa neutral conditions (initial pH = 7.6), closer to those commonly found in surface and subsurface waters, and by considering a wide range of initial SO_4^{2-}/CO_3^{2-} ratios (0 to approx. 68) in an aqueous solution. Furthermore, we study the evolution of the precipitates upon ageing within a time framework of 14 days, regarding its mineralogy, morphology, and composition of the different phases that constitute the precipitate at each stage. Different reaction pathways during ageing are unraveled depending on the initial $(SO_4^{2-})/(CO_3^{2-})$ ratio in the solution. These pathways are discussed considering both the kinetic and thermodynamic arguments. Our goal is to draw general

conclusions on the influence of sulphate oxyanions and the $(SO_4^{2-})/(CO_3^{2-})$ ratio in aqueous environments on the polymorphic selection of $CaCO_3$.

2. Materials and Methods

Stock solutions of $CaCl_2$ (1M, Fluka, Sigma-Aldrich, St. Louis, MO, USA), $NaHCO_3$ (99.7%, Panreac, Barcelona, Spain), and Na_2SO_4 (>99%, Sigma-Aldrich, St. Louis, MO, USA) were prepared with deionized water (Millipore, Burlington, MA, USA; resistivity = 18.2 MΩ·cm). The $CaCO_3$ precipitates were obtained by mixing 50 mL of a $CaCl_2$ solution with 50 mL of a stirred $NaHCO_3$ + Na_2SO_4 solution ($(SO_4^{2-})/(CO_3^{2-})$ = 0–67.6) in Erlenmeyer flasks (Pyrex). The flasks were immediately closed and kept at 25 ± 0.5 °C while continuously stirred by means of a magnetic stirrer. PHREEQC software [40] was used to calculate the solution speciation and supersaturation with respect to the different solid phases that can form in the system using the phreeqc.dat database. This database includes a Ksp of $10^{-8.48}$ for calcite, of $10^{-8.34}$ for aragonite, of $10^{-4.58}$ for gypsum, and of $10^{-4.36}$ for anhydrite. The Ksp of $10^{-7.91}$ for vaterite [41] and of $10^{-6.0}$ for ACC [42] were manually added to this database.

Table 1 shows the initial concentration of the reactants, the initial calculated pH, the activities of the relevant species, and the saturation indexes (SI) with respect to calcite (Cal), aragonite (Arg), vaterite (Vtr), gypsum (Gp), and anhydrite (Anh). In all the experiments, the solutions were initially highly supersaturated with respect to the three $CaCO_3$ polymorphs. In order to maintain the supersaturation at an approximately constant value with respect to the three $CaCO_3$ polymorphs ($SI_{Cal} \approx 2.35$, $SI_{Arg} \approx 2.2$, and $SI_{Vtr} \approx 1.8$), the $CaCl_2$ concentrations were adjusted. Only the solutions in experiments A15 to A25 were supersaturated with respect to gypsum ($SI_{Gp} \leq 0.25$). In all experiments, the solutions were undersaturated with respect to anhydrite. It is important to note that the mentioned SI values are those that would be reached if mixing were instantaneous and if no crystallization occurred before the complete homogenization of the solution were reached after mixing. This is an unlikely situation, and it can be assumed that some $CaCO_3$ precipitation will take place before a complete mixing of the reactant solutions [43–45]. This might lead to precipitates that are chemically inhomogeneous regarding their concentration of impurities.

Table 1. A summary of the initial fluid chemistry.

Experiment	Solution Composition (M)			Relevant Dissolved Species			Saturation Indexes					$(SO_4^{2-})/(CO_3^{2-})$
	$[CaCl_2]$	$[NaHCO_3]$	$[Na_2SO_4]$	pH	(CO_3^{2-})	(SO_4^{2-})	(Ca^{2+})	SI_{Cal}	SI_{Arg}	SI_{Vtr}	SI_{Gp}	SI_{Anh}	
A0	0.05	0.05	-	7.62	$5.81 \cdot 10^{-5}$	0	$1.38 \cdot 10^{-2}$	2.38	2.24	1.81	-	-	0
A3	0.04	0.05	0.003	7.66	$6.66 \cdot 10^{-5}$	$5.65 \cdot 10^{-4}$	$1.10 \cdot 10^{-2}$	2.34	2.20	1.77	−0.63	−0.93	8.48
A5	0.04	0.05	0.005	7.67	$6.71 \cdot 10^{-5}$	$9.42 \cdot 10^{-4}$	$1.08 \cdot 10^{-2}$	2.34	2.19	1.77	−0.42	−0.72	14.03
A7	0.04	0.05	0.007	7.67	$6.76 \cdot 10^{-5}$	$1.32 \cdot 10^{-3}$	$1.05 \cdot 10^{-2}$	2.33	2.19	1.76	−0.28	−0.58	19.51
A15	0.05	0.05	0.015	7.64	$6.11 \cdot 10^{-5}$	$2.55 \cdot 10^{-3}$	$1.20 \cdot 10^{-2}$	2.34	2.20	1.77	0.06	−0.24	41.78
A20	0.05	0.05	0.020	7.64	$6.18 \cdot 10^{-5}$	$3.39 \cdot 10^{-3}$	$1.15 \cdot 10^{-2}$	2.33	2.19	1.76	0.17	−0.13	54.87
A22	0.05	0.05	0.022	7.65	$6.21 \cdot 10^{-5}$	$3.73 \cdot 10^{-3}$	$1.13 \cdot 10^{-2}$	2.33	2.18	1.76	0.20	−0.10	60.00
A25	0.05	0.05	0.025	7.65	$6.25 \cdot 10^{-5}$	$4.23 \cdot 10^{-3}$	$1.10 \cdot 10^{-2}$	2.32	2.17	1.75	0.25	−0.05	67.61

Three independent runs were conducted for each experiment. The experimental runs were terminated after six different ageing times (5 min; 10 h; and 1, 3, 7, and 14 days). The precipitates were separated by filtering the aqueous phase through a 0.45-μm cellulose acetate membrane (Sartorius stedim; Albet), thoroughly rinsed with deionized water, subsequently rinsed with 10 mL of ethanol, and left to dry overnight at 30 °C in a drying chamber. The filtered aqueous solutions were stored in closed Pyrex flasks at 4 °C in a refrigerator until they were prepared for analysis.

2.1. Sample Characterization

The filtered solid phases recovered from each experiment were characterized by different techniques to determine their mineralogy, their chemical composition, and the morphology and size of their crystalline constituents. The precipitates were first analyzed by powder X-ray diffraction (XRD) to identify the mineral phases by means of a Panalytical X`Pert PRO MRD microprocessor-controlled X-ray diffractometer (version, Panalytical B.V., Almelo, The Netherlands). Most of the diffraction patterns were recorded between 20° and 60° and a few of them between 10° and 60° with a step size of 0.001° and using Cu Kα radiation. Diffractograms were processed with the X'Pert HighScore Plus (PANalytical B.V.) software. The diffraction patterns were compared to standard powder diffraction files from the ICDD-PDF2 data base (release 2007): 00–005–0586 for calcite, 01–080–2790 for aragonite, 04–017–8634 for vaterite, and 04–016–3025 for gypsum.

The precipitates were further analyzed by Fourier Transform Infrared (FTIR) spectroscopy using a BRUKER IFS 66v/S spectrophotometer (BRUKER, Billerica, MA, USA) equipped with a triglycine sulphate (TGS) detector. FTIR spectra were recorded on samples diluted in KBr by the co-addition of 64 scans, with a precision of 0.2 cm^{-1}. The morphology of the mineral phases of the precipitate was imaged using a JEOL JSM 6400 Scanning Electron Microscope (SEM) (JEOL Ltd., Akishima, Tokyo, Japan). Semiquantitative chemical analyses of the precipitates were obtained using an Oxford Instrument Energy Dispersive X-ray (EDX) detector. KristalShaper software [46] was used to model the habit of calcite crystals.

In order to determine the content of S in the aqueous solution from each experiment, the solutions were analyzed immediately after filtering using inductively coupled plasma-optical emission spectrometry (ICP-OES) (SPECTRO Arcos, SPECTRO, Kleve, Germany).

3. Results

3.1. Mineralogical Evolution of the Precipitation during Ageing

The mineralogical evolution of the precipitates during ageing is summarized in Table 2 and illustrated in Figures 1 to 4.

Table 2. The mineral identity of the solid phases recovered in each experiment after different ageing times: Note that the phases in brackets indicate that they are very scarce but that they are unequivocally identified at least in one of the analytical techniques used.

Exp	$(SO_4^{2-})/(CO_3^{2-})$	5 Min	10 H	1 Day	3 Days	7 Days	14 Days
A0	0	Vtr, Cal	Vtr, Cal	Vtr, Cal	Cal	Cal	Cal
A3	8.48	Vtr, Cal	Vtr, Cal	Vtr, Cal	Vtr, Cal	Cal	Cal
A5	14.03	Vtr, Cal	Vtr, Cal	Vtr, Cal	Vtr, Cal	Cal, Vtr	Cal
A7	19.51	Vtr, Cal	Vtr, Cal	Vtr, Cal	Vtr, Cal	Vtr, Cal, Arg	Cal, Vtr, Arg
A15	41.78	Vtr, (Cal)	Vtr, (Cal)	Vtr, (Cal)	Vtr, (Cal)	Vtr, Arg, (Cal)	Vtr, Arg, Cal
A20	54.87	Vtr, (Cal)	Vtr, (Cal)	Vtr, (Arg), (Cal)	Vtr, Arg, (Cal)	Vtr, Arg, (Cal)	Vtr, Arg, Cal, (Gp)
A22	60.00	Vtr	Vtr	Vtr, (Arg)	Vtr, Arg	Vtr, Arg, Gp	Vtr, Arg, Gp
A25	67.61	Vtr	Vtr	Vtr, Arg	Vtr, Arg	Vtr, Arg, Gp	Vtr, Arg, Gp

The XRD and FTIR analyses of the precipitates evidence that, soon after their formation (ageing time = 5 min), they mainly consist of vaterite, with calcite present as a minor phase. The amount of calcite in the precipitate in a 5 min reaction progressively decreases as the initial $(SO_4^{2-})/(CO_3^{2-})$ ratio in the aqueous solution increases. This is clearly evidenced by the increase in the intensity of the peaks assigned to vaterite and the decrease of those attributed to calcite in the diffraction patterns recorded in the samples corresponding to this ageing time (Figure 1a). Thus, the amount of calcite is significant in A0, where the initial $(SO_4^{2-})/(CO_3^{2-})$ ratio in the aqueous solution is 0, while no calcite is detected in experiment A22 when the initial $(SO_4^{2-})/(CO_3^{2-})$ ratio is 60.0. The FTIR spectra show absorbance band characteristics of vaterite and/or calcite, whereas the presence of aragonite is not detected (Figure 1b). A very weak band at approx. 1130 cm^{-1} (found in the spectrum of precipitates from experiments A5–A22 but absent in that corresponding to the solids formed from sulphate-free solution A0) can be assigned to sulphate ions incorporated in the structure of vaterite and/or calcite.

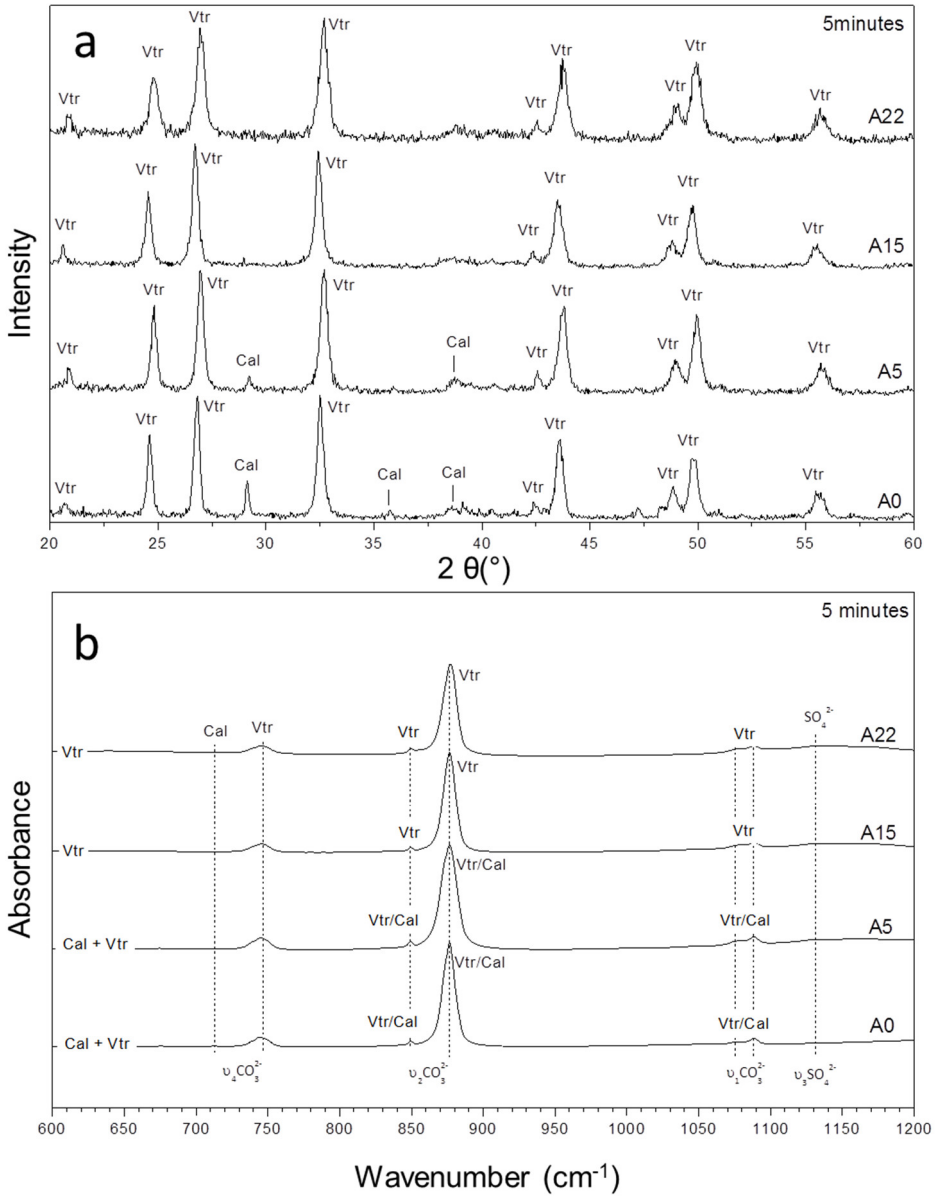

Figure 1. The XRD patterns (**a**) and infrared spectra (**b**) of precipitates sampled after 5 min of reaction in the case of experiments A0, A5, A15, and A22 with initial $(SO_4^{2-})/(CO_3^{2-})$ ratios of 0, 14.0, 41.8, and 60.0, respectively.

Furthermore, the mineralogical composition of the precipitates evolves with ageing time, following trends with characteristics varying depending on the initial $(SO_4^{2-})/(CO_3^{2-})$ ratio in the solution. The composition of precipitates formed in experiments A0 to A5, where the initial $(SO_4^{2-})/(CO_3^{2-})$ ratio in the aqueous solution varies between 0 and 14.03, shows a similar evolution trend. This trend is characterized by the progressive decrease of the amount of vaterite present in the precipitate as ageing progresses (Figure 2). This decrease takes place at a slower rate with increasing initial $(SO_4^{2-})/(CO_3^{2-})$ ratios in the aqueous solution, as confirmed by both XRD (Figure 2a) and FTIR spectroscopy (Figure 2b). Thus, in the absence of SO_4^{2-} in the solution (A0 in Tables 1 and 2; $(SO_4^{2-})/(CO_3^{2-}) = 0$), the precipitate exclusively consists of calcite after 3 days of ageing. In experiment A3 ($(SO_4^{2-})/(CO_3^{2-}) = 8.48$), vaterite and calcite are detected after 3 days but calcite is the only $CaCO_3$ phase present in the precipitate after 7 days of ageing. In contrast, vaterite is still present in the precipitate formed in A5 ($(SO_4^{2-})/(CO_3^{2-}) = 14.0$) after 7 days of ageing (Figure 2; Table 2) but is undetected in the solid phase recovered after 14 days of reaction. This trend is observed in all these

three experiments, i.e., vaterite can remain for longer ageing periods when the $(SO_4^{2-})/(CO_3^{2-})$ ratio increases.

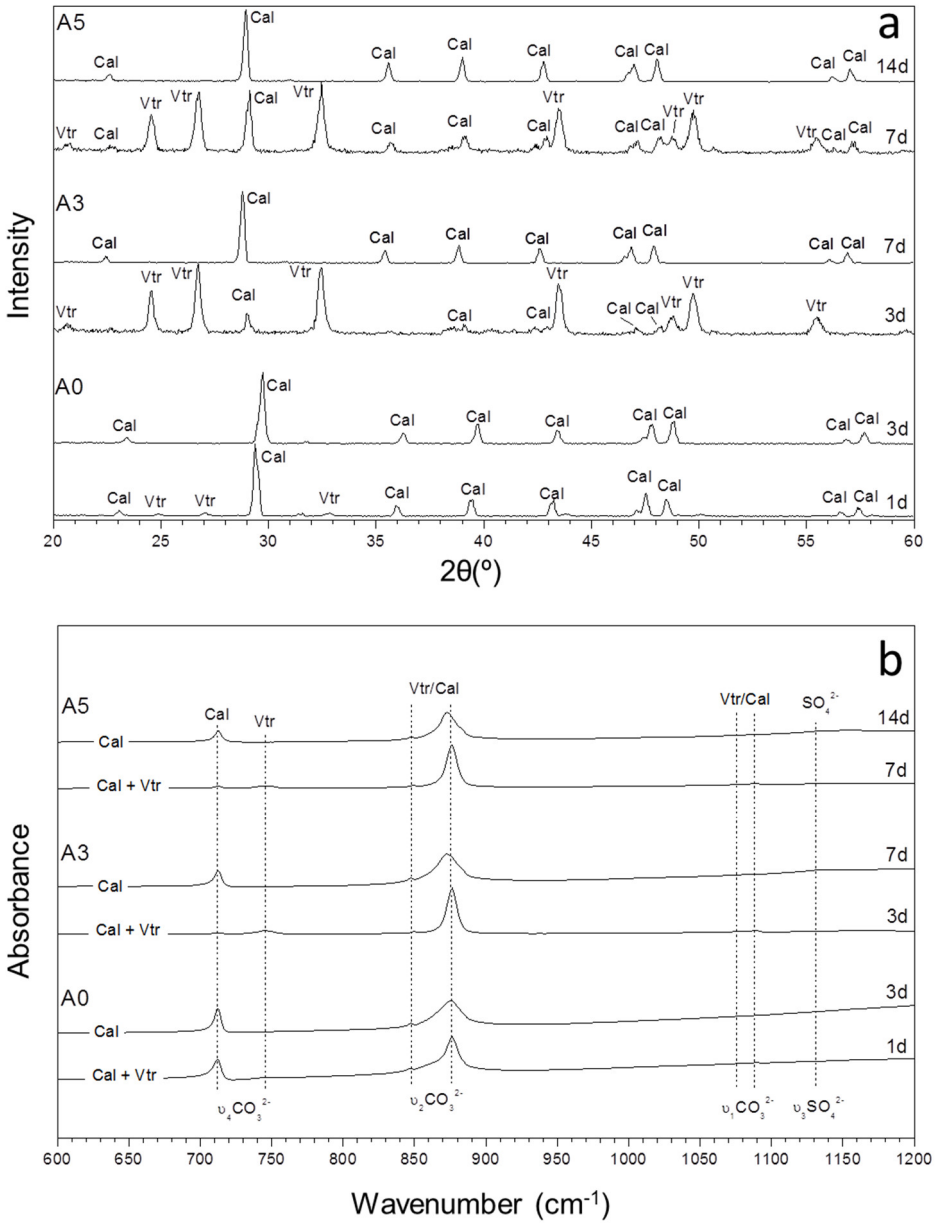

Figure 2. The XRD patterns (**a**) and infrared spectra (**b**) of precipitates sampled from aqueous solutions with low $(SO_4^{2-})/(CO_3^{2-})$ ratios (A0–A5) as a function of time.

A different mineralogical evolution trend is observed in experiments A7 to A20, where the initial $(SO_4^{2-})/(CO_3^{2-})$ ratio in the aqueous solution varies between 19.51 and 54.87 (Figure 3). In this case, the formation of aragonite is also observed during ageing. This $CaCO_3$ polymorph appears as a constituent of the precipitate formed after ageing times that are shorter, as the initial $(SO_4^{2-})/(CO_3^{2-})$ ratio in the aqueous solution is higher. Thus, aragonite is detected in the precipitate formed in A7 and A15 after 7 days of ageing, while this phase is found much earlier in the precipitate formed in A20 after only 1 day of ageing. This evolution trend is particularly evident in the FTIR spectra, which show weak bands at approx. 699 cm^{-1} and 712 cm^{-1} and at approx. 855 cm^{-1}, consistent with the positions of the υ_4 antisymmetric bending and υ_2 out-of-plane vibrations of carbonate ion in aragonite, respectively. These bands are absent in the precipitates formed after short times of ageing (3 days and shorter for A7 and A15 and 10 h and shorter for A20). It is worthwhile to note that after

14 days of ageing, these precipitates consist of the three $CaCO_3$ polymorphs, vaterite, aragonite, and calcite, together with gypsum as a minor phase. Calcite is still the most abundant phase in A7, whereas vaterite is the most abundant one in A15 and A20 (Figure 3a). Bands at 1130, 628, and 608 cm^{-1}, particularly evident in the precipitate formed in A20 after 14 days of ageing, can be assigned to sulphate ions incorporated into the lattice of the $CaCO_3$ polymorphs.

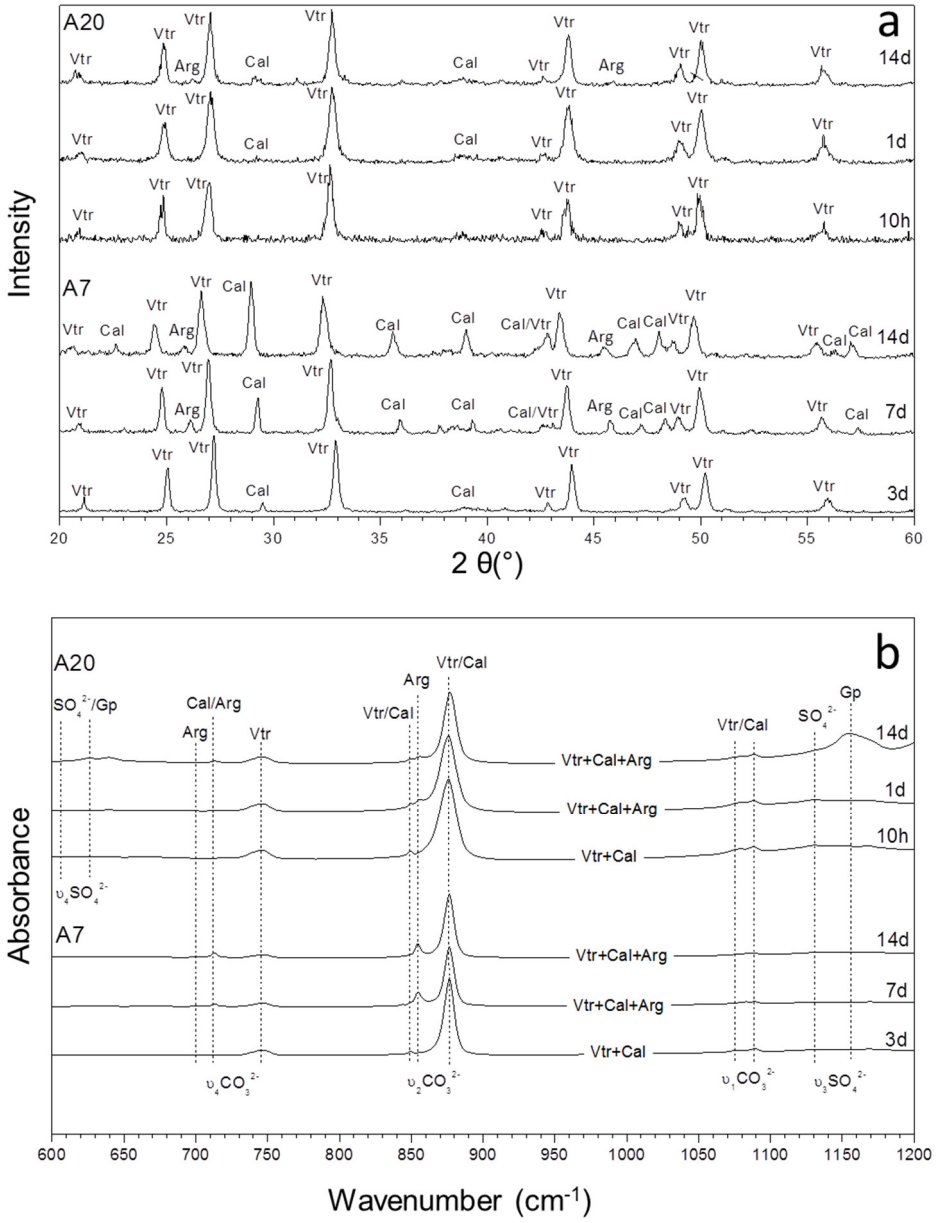

Figure 3. The XRD patterns (**a**) and infrared spectra (**b**) of precipitates sampled from aqueous solutions with $(SO_4^{2-})/(CO_3^{2-})$ ratios of 19.51 and 54.87 (A7 and A20) as a function of time.

Another mineralogical evolution trend is observed in experiments A22 and A25, where the initial $(SO_4^{2-})/(CO_3^{2-})$ ratios in the aqueous solution are 60.00 and 67.61, respectively (Figure 4). In these experiments, vaterite is always the first and only phase that precipitates whereas calcite, never forms part of the precipitate regardless of the ageing time. It also is worthwhile to note that the formation of aragonite is unequivocally observed after 1 day of ageing in both experiments A25 and A22. After 7 days, gypsum precipitates and coexists with vaterite and aragonite, also in both experiments.

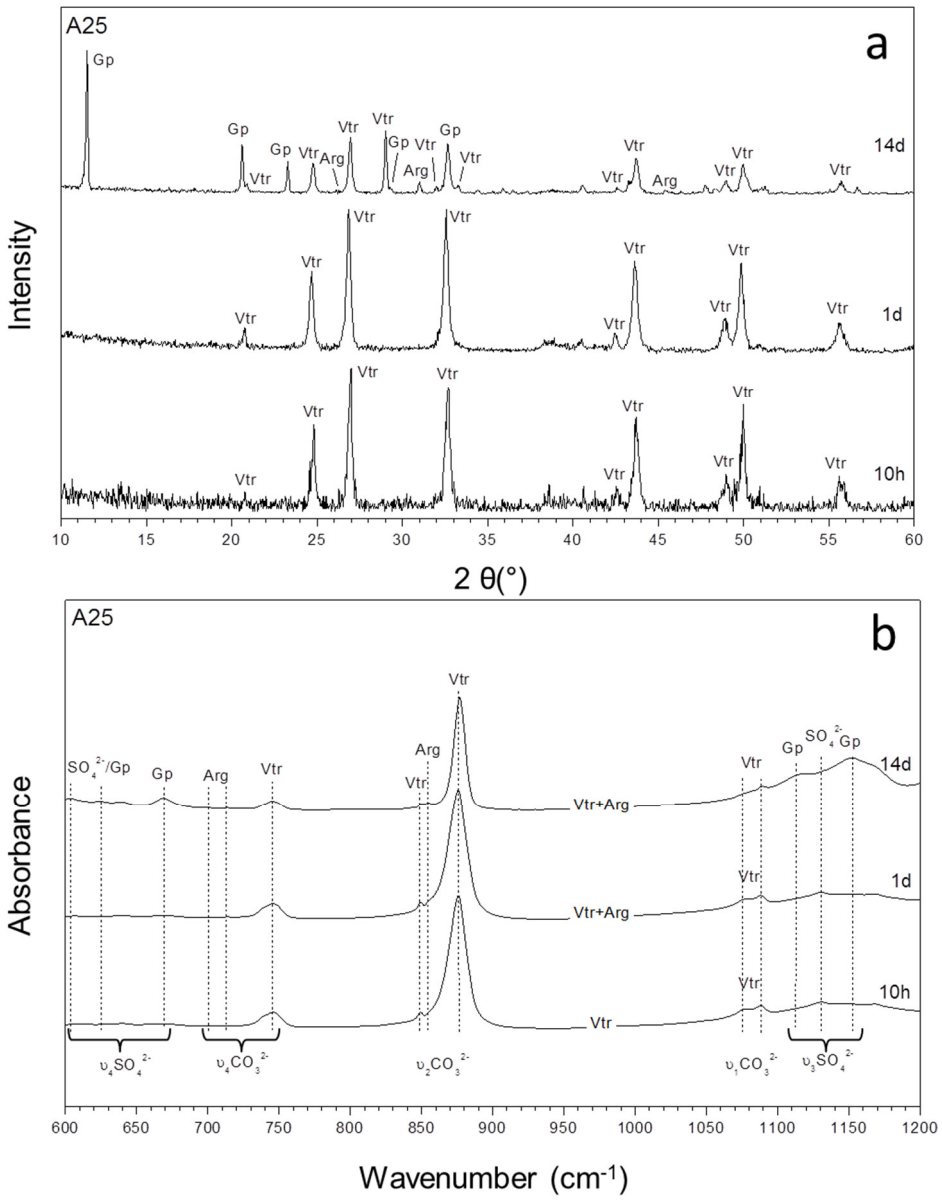

Figure 4. The XRD patterns (**a**) and infrared spectra (**b**) of precipitates sampled from aqueous solutions with the highest $(SO_4^{2-})/(CO_3^{2-})$ ratio (67.6) (A25) as a function of time.

3.2. Characterization of the Precipitate and the Aqueous Solution

The SEM micrographs in Figure 5 show that vaterite appears as cauliflower-like aggregates (Figures 5a,b) or radial aggregates that consist of lens-shaped crystallites (Figure 5c,d). As is apparent, no significant evolution of the vaterite morphology is observed as a function of the initial $(SO_4^{2-})/(CO_3^{2-})$ ratio in the aqueous solution or the ageing time. In contrast, calcite appears as single crystals with morphologies and sizes highly dependent on both reaction time and initial $(SO_4^{2-})/(CO_3^{2-})$ ratio in the solution. Thus, in experiment A0, where there is no sulphate in the solution, calcite crystals are bounded by flat {10−14} rhombohedron faces regardless of the reaction time and show sizes in the 10–25 μm range (Figures 5a,c,e). In experiments A3 to A7, where the initial $(SO_4^{2-})/(CO_3^{2-})$ ratio varies between 8.5 and 19.5, the calcite crystals that formed early after the mixing of the aqueous solution also show the typical rhombohedron-like shape with flat {10−14} faces (Figure 5f). However, their morphology undergoes an evolution as ageing progresses. This evolution is characterized by a progressively increasing elongation along [001] (Figures 5f–h) as well as by the emergence of rough pseudofacets that lead to the development of a new form, the more

acute {02–21} rhombohedrum (see inset in Figure 5h). This evolution seems to be more marked in precipitates A7 and A5 than A3, which points to a positive relationship between the higher initial $(SO_4^{2-})/(CO_3^{2-})$ ratio in the aqueous solution and more elongated and rougher-faced calcite crystals. Thus, after 14 days of ageing, calcite crystals formed in experiment A3 show a length/width ratio around 2.4. This ratio is around 3.3 and 3.5 in calcite crystals formed in experiments A5 and A7, respectively (Figures 5i,j). As mentioned above, calcite crystals are hardly noticeable in experiments A15 to A20 and are absent in experiment A22 and A25 regardless of the reaction time.

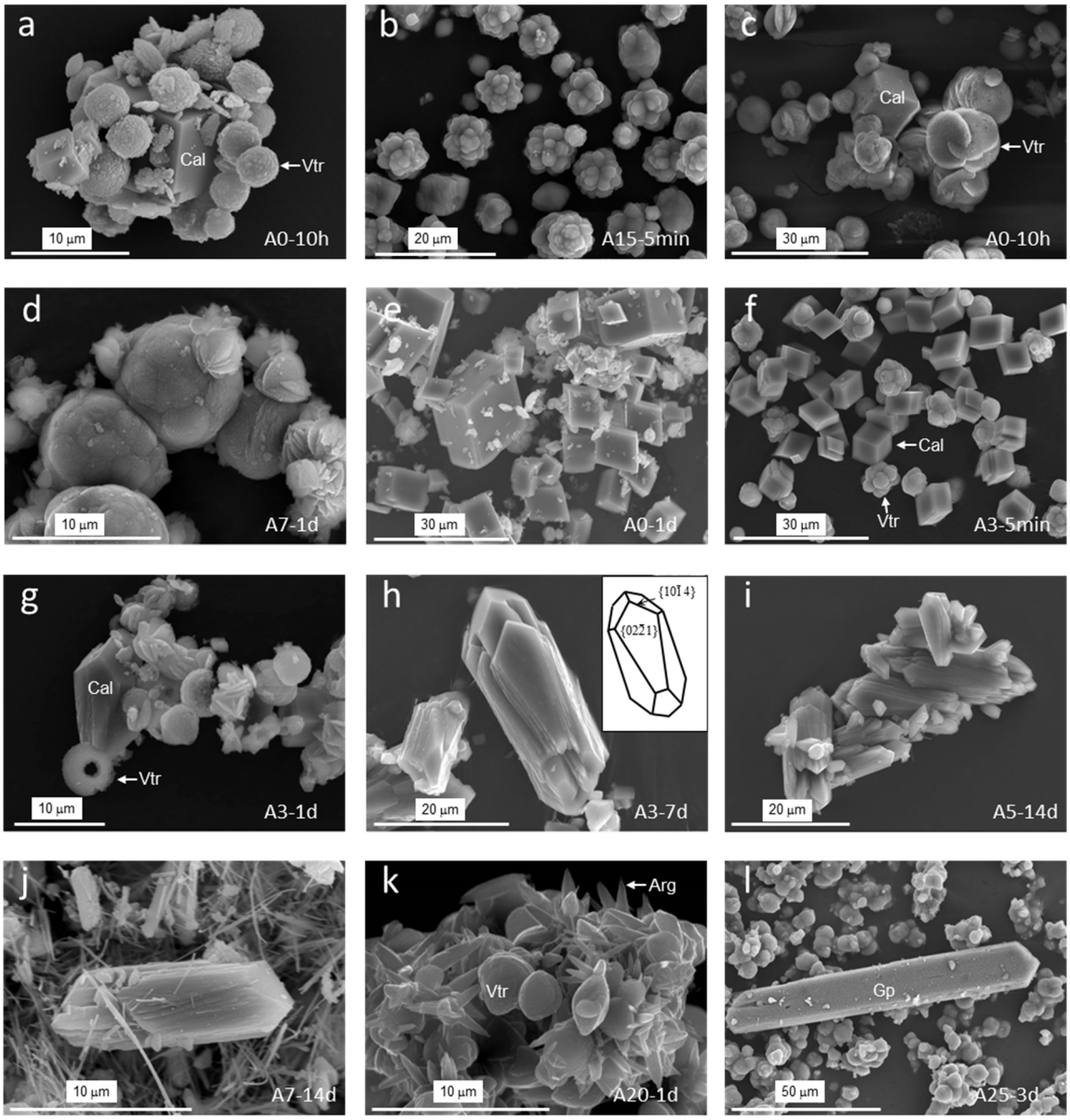

Figure 5. SEM images of the precipitates recovered from solutions with different $(SO_4^{2-})/(CO_3^{2-})$ ratios after various elapsed times ranging from 5 min to 14 days. Vaterite appears as cauliflower-like aggregates (**a**,**b**) or lens-shaped crystallites (**c**,**d**). When there is no sulphate in the solution, the calcite crystals are bounded by flat {10–14} rhombohedron faces (**a**,**c**,**e**). In solutions with a moderate concentration of sulphate, the calcite crystal habit undergoes an evolution characterized by a progressive increase in elongation along [001] (**f–j**) and by the emergence of the {02–21} form (see inset in **h**). Aragonite appears as crystals with the so-called "morning-star" morphologies (**k**). Gypsum crystals exhibit tabular habits with the {010} form as the main face (**l**).

Aragonite is observed in experiments A7–A25 ($(SO_4^{2-})/(CO_3^{2-})$ = 19.51–67.61). In all cases, aragonite appears as crystals bounded by curved prismatic faces. These crystals grow on the surface of vaterite aggregates, forming so-called "morning-star" aggregates (Figure 5k). Finally, gypsum crystals, which are observed in experiments A22 and A25, typically exhibit tabular habits with the {010} form as the main face with an accentuated elongation along [001] (Figure 5l).

EDX analyses conducted on vaterite and calcite crystals evidence that they contain S in all the cases, except for the vaterite and calcite crystals formed in the absence of SO_4^{2-} (experiment A0) in the aqueous solution. For both vaterite and calcite, a direct correlation between the [S] (% at) and the initial $(SO_4^{2-})/(CO_3^{2-})$ ratio in the aqueous solution is detected (Figure 6a). Thus, after 5 min of reaction, a [S] (% at) of 0.91 was measured in vaterite aggregates formed in experiment A3, while the S/Ca ratios were as high as 1.54 and 3.23 in vaterite formed in experiments A7 and A25, respectively. A similar trend was observed in calcite crystals, where the S/Ca ratio after 5 min of reaction were 2.81 in experiment A3, 4.48 in experiment A5, and 5.76 in experiment A20. It is interesting to note that for both calcite and vaterite for a given $(SO_4^{2-})/(CO_3^{2-})$ initial ratio, the highest S content is always detected in the precipitates with shorter ageing (5 min of reaction) and progressively decreases as ageing progresses. This evolution is depicted in Figure 6b for calcite formed in experiment A5. It is also striking that, regardless of the initial $(SO_4^{2-})/(CO_3^{2-})$ ratio and the ageing time, calcite crystals always show higher S contents than vaterite aggregates. The small size of aragonite crystals formed in experiments A7 to A25 and gypsum crystals formed in experiments A22 and A25 prevented EDX analyses from being conducted on them.

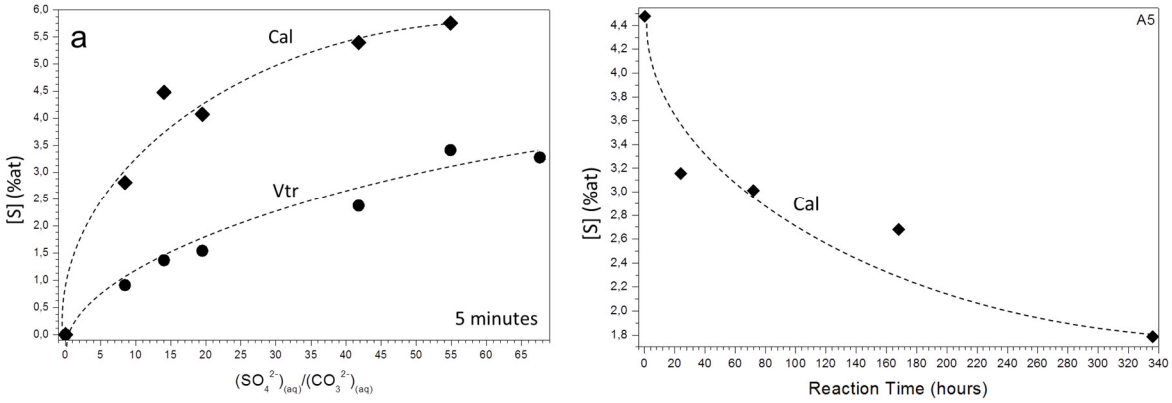

Figure 6. (**a**) The concentration of S (% at) in calcite and vaterite sampled after 5 min of reaction as a function of the initial $(SO_4^{2-})/(CO_3^{2-})$ ratio and (**b**) the variation of [S] (% at) with ageing in calcite crystals sampled from aqueous solutions with a $(SO_4^{2-})/(CO_3^{2-})$ ratio of 14.03 (A5).

Finally, ICP-OES analyses of the S concentration in the aqueous solution show that at 5 min of reaction, the concentration of S in the aqueous solution is progressively lower than the initial aqueous solution as the initial $(SO_4^{2-})/(CO_3^{2-})$ ratio in the aqueous solution increases (Figure 7a). Furthermore, the concentration of S in the aqueous solution varies with ageing time, following similar trends independently of the initial $(SO_4^{2-})/(CO_3^{2-})$ ratio in the solution (Figure 7b). Thus, the concentration of S in the aqueous solution is characterized by a rapid drop followed by a progressive increase as ageing progresses.

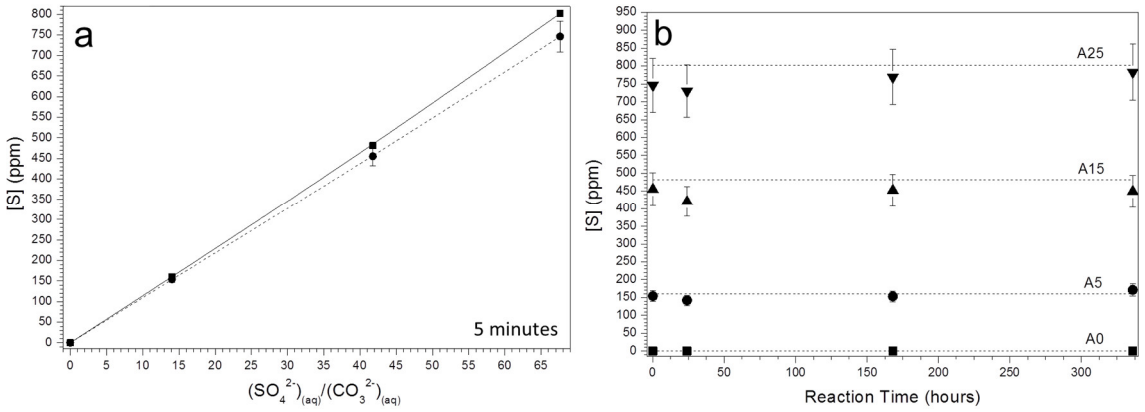

Figure 7. (**a**) The concentration of S (from inductively coupled plasma-optical emission spectrometry (ICP-OES) analyses) in aqueous solutions sampled after 5 min of reaction as a function of the initial $(SO_4^{2-})/(CO_3^{2-})$ ratios (dashed lines): The initial concentrations of S in the solutions are connected by a solid line. (**b**) The evolution of the concentration of S (from ICP-OES) of aqueous solutions with initial $(SO_4^{2-})/(CO_3^{2-})$ ratios of 0 (A0), 14.3 (A5), 41.8 (A15), and 67.7 (A25), respectively.

4. Discussion

The experimental results described in the previous section (XRD and FTIR analyses) show that the mineral composition of the precipitate recovered in each run varied as a function of two main factors: the high supersaturation of the parental aqueous solution, which controls the phases that are formed at the initial stages of crystallization, and the $(SO_4^{2-})/(CO_3^{2-})$ ratio in the parental solution, which influences the mineral evolution of the precipitates during ageing. After the mixing of the reactants, the aqueous solutions are highly supersaturated with respect to all the crystalline $CaCO_3$ polymorphs (Table 1), and spontaneous precipitation takes place. According with the Ostwald step rule [15], the formation of the most soluble and disorder phase is kinetically favored [47]. However, under the conditions used in these experiments, the precipitation of the amorphous calcium carbonate, the most soluble $CaCO_3$ phase, can be discarded since the aqueous solution is always undersaturated with respect to this phase ($SI_{ACC} \leq -0.1$). Therefore, kinetics factors promote the formation of vaterite as the first phase that precipitates immediately after the mixing of the parental solutions. After vaterite nucleation, the system can further reduce its free energy by the subsequent transformation of vaterite into calcite through a solvent mediated transformation [48]. In addition, a reduction of supersaturation resulting from the growth of vaterite promotes the nucleation of calcite. Therefore, as the system approaches equilibrium, the most stable $CaCO_3$ phase, calcite, should become the prevailing phase at the expense of vaterite. The mineralogical evolution observed in experiments with the lower initial $(SO_4^{2-})/(CO_3^{2-})$ ratios (A0–A5) is in good agreement with this expected evolution. Furthermore, it is in good consonance with the precipitate mineralogical evolution upon ageing previously observed in similar mixing experiments conducted in more highly supersaturated systems (SI_{Cal} approx. 3.7) under higher pH (approx. 10.9) [31]. Our current results are further evidence that the presence of a high amount of sulphate ions in the aqueous media slows down or even inhibits the direct precipitation of calcite and transformation of vaterite into calcite, thereby contributing to the stabilization of vaterite with respect to calcite. The prolonged existence of vaterite as a major constituent of the precipitate is observed in all the experiments. The stabilization of vaterite is more evident the higher the $(SO_4^{2-})/(CO_3^{2-})$ ratio is in the aqueous solutions. Indeed, in experiments A22 and A25, where this ratio is highest, vaterite does not transform into calcite even after 14 days of ageing. These results are again consistent with those previously reported by Fernández-Díaz et al [31], who notice that vaterite can remain as a major constituent phase for long ageing periods when $(SO_4^{2-})/(CO_3^{2-})$ ratios are higher than one. The stabilization of vaterite and the retardation of calcite crystallization in the presence of sulphate ions can be explained by a combination of both thermodynamics and kinetics factors. The computational modelling of the substitution of a small amount of carbonate groups by sulphate groups in the structures of vaterite and calcite [28,31] showed that the vaterite structure is much less disrupted by the isomorphic

incorporation of AO_4^{2-} groups, including sulphate, chromate, and selenate, than the calcite structure. In the case of sulphate, the incorporation of this oxyanion results in an increment of calcite lattice energy, while it has the opposite effect on the lattice energy of vaterite. This different impact of sulphate isomorphic incorporation on the energetics of calcite and vaterite structures is especially relevant for the S content range up to 3% molar fraction, where it translates into an effective reduction of the energy difference between the two calcium carbonate polymorphs. The larger capability of vaterite to accommodate sulphate oxyanions in its structure compared to calcite seems to be in contradiction with the experimental evidence provided by the EDX analyses of calcite and vaterite grains in the precipitates obtained in these experiments. These analyses steadily show a higher S content in calcite crystals than in vaterite aggregates formed in the same experiment. This is regardless of the initial $(SO_4^{2-})/(CO_3^{2-})$ ratio and the ageing time (see Figure 6a). Similar results were reported by Fernández-Díaz et al. [31] for precipitates formed under higher supersaturations and pHs. These authors explain the apparent contradiction between the experimental results and the energy-based expectations considering that the higher S contents measured in calcite most likely were the consequence of this phase forming later than vaterite. In such a scenario, calcite crystals would have grown from a CO_3^{2-}-depleted medium after vaterite nucleation and, consequently, in a solution with a $(SO_4^{2-})/(CO_3^{2-})$ ratio significantly higher than the initial one.

Although the results of computer simulations of sulphate incorporation do not predict stability crossovers between vaterite and calcite, the approximation of the lattice energy of both polymorphs can explain the increasingly larger duration of vaterite as a precipitate component with a growing initial sulphate concentration in the solution.

While the incorporation of impurities from the aqueous solution can change the lattice energy of the bulk crystal, surface-related phenomena like impurity adsorption can modify the surface chemistry of the different polymorphs, thereby changing their surface energies [49]. The impact of this phenomenon is particularly relevant in the case of small particles, where the surface/volume ratio is very high, and the effect of lattice energy in the stability of the different polymorphs is comparatively much less important than that of surface energy. A small increase of the surface energy of calcite nanoclusters and nanoparticles due to sulphate adsorption could dramatically increase the barrier for its nucleation, since such a barrier is proportional to the square of the surface energy. Were this to happen, the main outcome would also be a progressively slower transformation of vaterite into calcite as the $(SO_4^{2-})/(CO_3^{2-})$ ratio in the parent aqueous solutions increases. Kinetics arguments involving the adsorption of impurities have often been invoked to explain the stabilization of vaterite with respect to calcite and the retardation of calcite nucleation and growth. Phenomena observed during the precipitation of $CaCO_3$ from a supersaturated aqueous solution bearing phosphate ions are an example [50]. In this system, the stabilization of vaterite was rather attributed to the blocking of active sites for dissolution on the surface of this phase due to the adsorption of phosphate ions. A similar phosphate adsorption onto surface sites was claimed to explain calcite growth inhibition. Indeed, a similar reasoning can be applied to explain the observed effect of sulphate ions. Another alternative thermodynamic and mechanistic argument has been invoked to explain the inhibition of calcite growth by the effect of sulphate ions. In situ atomic force microscopy AFM experiments of calcite growth performed using a fluid cell and flowing supersatutared sulphate-bearing aqueous solutions showed that a low concentration of sulphate in the aqueous solution (5 mM) is enough to decrease the rate of step spread on the calcite surface [51]. These nanoscale AFM observations supported the interpretation that the trapping of sulphate ions by nanometric growing layers resulted in the generation of interfacial strain energy. A strain relaxation perpendicular to the growing layer introduces local variations in bond lengths, giving rise to local departures from calcite surface ideal nanotopography. The direct consequence of this phenomenon is a decrease of the step advancement rate according to the so-called "template effect" model [20,25,52], which is more marked the larger the amount of sulphate ions trapped within calcite monolayers.

An interesting result observed in experiments A7 to A25, where the initial $(SO_4^{2-})/(CO_3^{2-})$ ratio in the aqueous solution was >19.51, was the formation of aragonite. It took place through the

solvent-mediated transformation of vaterite and could also be explained invoking both the thermodynamic and kinetics arguments. For equivalent compositions of sulphate in the polymorphs, the computer modelling of sulphate isomorphic incorporation predicts a significantly larger increment of aragonite lattice energy compared to that of both calcite and vaterite. This result indicates that the substitution of carbonate groups by sulphate in aragonite structure is very unfavorable [28,31]. As a result, even when this polymorph forms from highly supersaturated solutions with very high $(SO_4^{2-})/(CO_3^{2-})$ ratios, it grows relatively sulphate-free compared to calcite. The direct consequence is a much more marked impact of the presence of sulphate in the growth medium on calcite stability. Indeed, the solubility of a sulphate-bearing calcite can overcome that of sulphate-free aragonite, as pointed out by Busenberg and Plummer [53], who reported this to be the case for calcites with sulphate contents above 3 mole%. Such a solubility crossover could explain the observation that, upon ageing of the vaterite precipitate, aragonite forms simultaneously to or even after the formation of the theoretically stable polymorph calcite when the concentration of sulphate in the aqueous solution is very high. This is the case in experiments A7 to A20. Unfortunately, the small size of the aragonite crystals formed in these experiments has prevented EDX analyses to obtain evidence that could give full support to our interpretation, although the high concentration of sulphate measured in calcite crystals point in this direction (see Figure 6). On the other hand, the fact that sulphate incorporation into aragonite structures is very unfavorable, it can be concluded that the inhibitory effect of sulphate ions during the growth of aragonite will arguably be less effective than in the case of calcite and so will be a hypothetical "template effect" mechanism.

Besides the precipitation of $CaCO_3$ polymorphs, gypsum was unequivocally detected after 7 days of interaction in the experiments with the highest $(SO_4^{2-})/(CO_3^{2-})$ ratios (A20–A25). The precipitation of this phase is not surprising since the initial solutions are supersaturated with respect to this phase (SI_{Gp} approx. 0.17–0.25). However, the early precipitation of $CaCO_3$ phases after the mixing of the parent solutions depletes the solution in Ca^{2+} (and to a much lesser extent in SO_4^{2-}), leading to a very important reduction of aqueous phase SI_{Gp}. Thus, systems initially close to equilibrium with respect to gypsum, as is the case of the solution in experiment A15, will become undersaturated soon after the precipitation of $CaCO_3$ starts, making the formation of gypsum impossible. The systems initially more highly supersaturated with respect to gypsum will either approach equilibrium or become significantly less supersaturated, allowing gypsum precipitation to be prevented over large periods.

The presence of sulphate in the aqueous solutions and ageing not only appears to be a critical factor controlling the mineralogy of the recovered precipitates but also affects the morphology of calcite single crystals. As mentioned in Section 3.2, after a short ageing time, calcite single crystals exhibit the typical rhombohedral idiomorphic shape (see Figures 5a,c,e), which progressively become blockier and elongated along the *c*-axis as ageing progresses. This elongation is clearly more pronounced as the $(SO_4^{2-})/(CO_3^{2-})$ ratio in the aqueous solution increases. Since there is a clear correlation between the concentration of sulphate in the aqueous solution and the amount of this anion that is incorporated into the calcite (and vaterite) structure, directly evidenced by EDX (see Figure 6a) and supported by an ICP analysis (Figure 7a), we can conclude that the modification of the calcite crystal habit is a direct result of the incorporation/sorption of this anion. The effect of several ions on calcite habit has been profusely discussed in the literature. In particular, the elongation of calcite crystals has been interpreted as the result of a significant lowering of the surface energy of certain faces other than {10014} due to a preferential sorption of foreign ions on these faces [54]. It has also been attributed to a modification of calcite surface nanotopography due to step-specific impurity interactions [55]. These interactions contribute to the stabilization of new crystal faces that become prevalent during growth. In the case under consideration here, the habit of calcite crystals grown in the presence of sulphate, we observe the stabilization of the {0221} form. The resulting habits strikingly resembles those of calcite crystals grown in the presence of small cations such as Mg^{2+}, Co^{2+}, or Mn^{2+} [56].

Finally, the progressive decrease of S content in both the calcite and vaterite precipitates with reaction time (Figure 6b), which is in good agreement with a parallel progressive increase of the

sulphate concentration in the aqueous solution (Figure 7b), points to the precipitate undergoing recrystallization processes through a dissolution-precipitation mechanism. The driving force for this recrystallization process could be the reduction of the extra energy associated with an excess of sulphate incorporated in calcite and vaterite structures under the influence of the high supersaturations dominating the early staged of the precipitation process. The progress of this recrystallization process leads to a chemical purification of the precipitates that further contributes to the stabilization of calcite as ageing progresses.

Author Contributions: I.C.M. performed the laboratory experiments and the DRX analysis and prepared the samples for FTIR, SEM images, EDX, and ICP analysis. J.M.A. and L.F.-D. contributed to the conception of the study. All authors analyzed the data and were involved in manuscript preparation. All authors read and approved the manuscript.

Funding: This study was supported by the Ministry of Science, Innovation and Universities (CIENCIA) (Spain) under project CGL2016-77138-C2-1-P. I. Cuesta Mayorga acknowledges an FPI (BES-2014-070279) fellowship from the Spanish CIENCIA.

Acknowledgments: The authors wish to thank the National Centre of Electronic Microscopy (CNME), the X-ray Diffraction Central Service, the Geological Techniques Research Centre of the Complutense University of Madrid (UCM), and the CSIC for kindly providing technical support to their research.

Conflicts of Interest: The authors declare no conflict of interest.

References

1. Anthony, J.W.; Bideaux, R.A.; Bladh, K.W.; Nichols, M.C. Borates, Carbonates, Sulfates. In *Handbook of Mineralogy*; Mineralogical Society of America: Chantilly, VA 20151-1110, USA, 2007; Volume V.
2. Tucker, M.E. *Sedimentary Petrology: An Introduction to the Origin of Sedimentary Rocks*, 3rd ed.; Blackwell Science Ltd.: Oxford, UK, 2001.
3. Lowenstam, H.A.; Weiner, S. *On Biomineralization*; Oxford University Press: New York, NY, USA, 1989; p. 324.
4. Mann, S. *Biomineralization. Principles and Concepts in Bioinorganic Materials Chemistry*; Oxford University Press, Inc.: New York, NY, USA, 2001; p. 198.
5. Lippmann, F. *Sedimentary Carbonate Minerals*; Springer: Berlin/Heidelberg, Germany, 1973; p. 228, doi:10.1007/987-3-642-65474-9.
6. Morse, J.W.; Arvidson, R.S.; Lüttge, A. Calcium carbonate formation and dissolution. *Chem. Rev.* **2007**, *107*, 342–381, doi:10.1021/cr050358j.
7. Morse, J.W.; Mackenzie, F.T. *Geochemistry of Sedimentary Carbonates*; Elsevier: Amsterdam, The Netherlands , 1990.
8. De Yoreo, J.J.; Gilbert, P.U.P.A.; Sommerdijk, N.A.J.M.; Penn, R.L.; Whitelam, S.; Joester, D.; Zhang, H.; Rimer, J.D.; Navrotsky, A.; Banfield, J.F.; et al. Crystallization by particle attachment in synthetic, biogenic, and geologic environments. *Science* **2015**, *349*, 492–502, doi:10.1126/science.aaa6760.
9. Gal, A.; Habraken, W.; Gur, D.; Fratzl, P.; Weiner, S.; Addadi, L. Calcite Crystal Growth by a Solid-State Transformation of Stabilized Amorphous Calcium Carbonate Nanospheres in a Hydrogel. *Angew. Chem.* **2013**, *125*, 4967–4970, doi:10.1002/ange.201210329.
10. Meldrum, F.C.; Cölfen, H. Controlling Mineral Morphologies and Structures in Biological and Synthetic Systems. *Chem. Rev.* **2008**, *108*, 4332–4432, doi:10.1021/cr8002856.
11. Rodriguez-Blanco, J.D.; Shaw, S.; Bots, P.; Roncal-Herrero, T.; Benning, L.G. The role of pH and Mg on the stability and crystallization of amorphous calcium carbonate. *J. Alloys Compd.* **2012**, *536*, S477–S479, doi:10.1016/j.jallcom.2011.11.057.
12. Griesshaber, E.; Kelm, K.; Sehrbrock, A.; Mader, W.; Mutterlose, J.; Brand, U.; Schmahl, W.W. Amorphous calcium carbonate in the shell material of the brachiopod Megerlia truncata. *Eur. J. Mineral.* **2009**, *21*, 715–723, doi:10.1127/0935-1221/2009/0021-1950.
13. Hu, Y.-B.; Wolthers, M.; Wolf-Gladrow, D.A.; Nehrke, G. Effect of pH and Phosphate on Calcium Carbonate Polymorphs Precipitated at near-Freezing Temperature. *Cryst. Growth Des.* **2015**, *15*, 1596–1601, doi:10.1021/cg500829p.

14. Tollefsen, E.; Stockmann, G.; Skelton, A.; Mörth, C.-M.; Dupraz, C.; Sturkell, E. Chemical controls on ikaite formation. *Mineral. Mag.* **2018**, *82*, 1119–1129, doi:10.1180/mgm.2018.110.
15. Söhnel, O.; Garside, J. *Precipitation: Basic Principles and Industrial Applications*; Butterworth-Heinemann: Oxford, UK, 1992.
16. Grasby, S.E. Naturally precipitating vaterite (μ-$CaCO_3$) spheres: Unusual carbonates formed in an extreme environment. *Geochim. Cosmochim. Acta* **2003**, *67*, 1659–1666, doi:10.1016/S0016-7037(00)01304-2.
17. Radha, A.V.; Navrotsky, A. Thermodynamics of Carbonates. *Rev. Mineral. Geochem.* **2013**, *77*, 73–121, doi:10.2138/rmg.2013.77.3.
18. Weiner, S.; Dove, P.M. An overview of biomineralization processes and the problem of the vital effect. *Rev. Mineral. Geochem.* **2003**, *54*, 1–29, doi:10.2113/0540001.
19. Radha, A.V.; Forbes, T.Z.; Killian, C.E.; Gilbert, P.U.P.A.; Navrotsky, A. Transformation and crystallization energetics of synthetic and biogenic amorphous calcium carbonate. *Proc. Natl. Acad. Sci.* **2010**, *107*, 16438–16443, doi:10.1073/pnas.1009959107.
20. Astilleros, J.M.; Fernández-Díaz, L.; Putnis, A. The role of magnesium in the growth of calcite: An AFM study. *Chem. Geol.* **2010**, *271*, 52–58, doi:10.1016/j.chemgeo.2009.12.011.
21. Falini, G.; Gazzano, M.; Ripamonti, A. Crystallization of calcium carbonate in presence of magnesium and polyelectrolytes. *J. Cryst. Growth* **1994**, *137*, 577–584, doi:10.1016/0022-0248(94)91001-4.
22. Fernández-Díaz, L.; Putnis, A.; Prieto, M.; Putnis, C.V. The role of magnesium in the crystallization of calcite and aragonite in a porous medium. *J. Sediment. Res.* **1996**, *66*, 482–491, doi:10.1306/D4268388-2B26-11D7-8648000102C1865D.
23. Reddy, M.M.; Nancollas, G.H. The crystallization of calcium carbonate. IV. The effect of magnesium, strontium and sulfate ions. *J. Cryst. Growth* **1976**, *35*, 33–38, doi:10.1016/0022-0248(76)90240-2.
24. Stanley, S.M.; Hardie, L.A. Secular oscillations in the carbonate mineralogy of reef-building and sediment-producing organisms driven by tectonically forced shifts in seawater chemistry. *Palaeogeogr. Palaeoclimatol. Palaeoecol.* **1998**, *144*, 3–19, doi:10.1016/S0031-0182(98)00109-6.
25. Astilleros, J.M.; Pina, C.M.; Fernández-Díaz, L.; Putnis, A. Nanoscale growth of solids crystallising from multicomponent aqueous solutions. *Surf. Sci.* **2003**, *545*, L767–L773, doi:10.10167j.susc.2003.08.031.
26. González-López, J.; Fernández-González, Á.; Jiménez, A. Precipitation behaviour in the system Ca^{2+}-Co^{2+}-CO_3^{2-}-H_2O at ambient conditions—Amorphous phases and $CaCO_3$ polymorphs. *Chem. Geol.* **2018**, *482*, 91–100, doi:10.1016/j.chemgeo.2018.02.003.
27. Reddy, M.M.; Wang, K. Crystallization of calcium carbonate in the presence of metal ions: I. Inhibition by magnesium ion at pH 8.8 and 25 °C. *J. Cryst. Growth* **1980**, *50*, 470–480, doi:10.1016/0022-0248(80)90095-0.
28. Arroyo-de Dompablo, M.E.; Fernández-González, M.A.; Fernández-Díaz, L. Computational investigation of the influence of tetrahedral oxoanions (sulphate, selenate and chromate) on the stability of calcium carbonate polymorphs. *RSC Adv.* **2015**, *5*, 59845–59852, doi:10.1039/C5RA08574H.
29. Bots, P., Benning, L.G.; Rickaby, R.E.M.; Shaw, S. The role of SO_4 in the switch from calcite to aragonite seas. *Geology* **2011**, *39*, 331–334, doi:10.1130/G31619.1.
30. Cruz, J.A.; Sánchez-Pastor, N.; Gigler, A.M.; Fernández-Díaz, L. Vaterite Stability in the Presence of Chromate. *Spectrosc. Lett.* **2011**, *44*, 495–499, doi:10.1080/00387010.2011.610408.
31. Fernández-Díaz, L.; Fernández-González, Á.; Prieto, M. The role of sulfate groups in controlling $CaCO_3$ polymorphism. *Geochim. Cosmochim. Acta* **2010**, *74*, 6064–6076, doi:10.1016/j.gca.2010.08.010.
32. Fernández-Díaz, L.; Pina, C.M.; Astilleros, J.M.; Sánchez-Pastor, N. The carbonatation of gypsum: Pathways and pseudomorph formation. *Am. Mineral.* **2009**, *94*, 1223–1234, doi:10.2138/am.2009.3194.
33. Fernández-González, Á.; Fernández-Díaz, L. Growth of calcium carbonate in the presence of Se(VI) in silica hydrogel. *Am. Mineral.* **2013**, *98*, 1824–1833, doi:10.2138/am.2013.4397.
34. Hua, B.; Deng, B.; Thornton, E.C.; Yang, J.; Amonette, J.E. Incorporation of Chromate into Calcium Carbonate Structure During Coprecipitation. *Water Air Soil Pollut.* **2007**, *179*, 381–390, doi:10.1007/s11270-006-9242-7.
35. Jroundi, F.; Gonzalez-Muñoz, M.T.; Garcia-Bueno, A.; Rodriguez-Navarro, C. Consolidation of archaeological gypsum plaster by bacterial biomineralization of calcium carbonate. *Acta Biomater.* **2014**, *10*, 3844–3854, doi:10.1016/j.actbio.2014.03.007.
36. Sánchez-Pastor, N.; Gigler, A.M.; Cruz, J.A.; Park, S.-H.; Jordan, G.; Fernández-Díaz, L. Growth of Calcium Carbonate in the Presence of Cr(VI). *Cryst. Growth Des.* **2011**, *11*, 3081–3089, doi:10.1021/cg200357c.

37. Tang, Y.; Zhang, F.; Cao, Z.; Jing, W.; Chen, Y. Crystallization of $CaCO_3$ in the presence of sulfate and additives: Experimental and molecular dynamics simulation studies. *J. Colloid Interface Sci.* **2012**, *377*, 430–437, doi:10.1016/j.jcis.2012.02.068.
38. Wagterveld, R.M.; Yu, M.; Miedema, H.; Witkamp, G.J. Polymorphic change from vaterite to aragonite under influence of sulfate: The "morning star" habit. *J. Cryst. Growth* **2014**, *387*, 29–35, doi:10.1016/j.jcrysgro.2013.10.044.
39. Chavagnac, V.; Ceuleneer, G.; Monnin, C.; Lansac, B.; Hoareau, G.; Boulart, C. Mineralogical assemblages forming at hyperalkaline warm springs hosted on ultramafic rocks: A case study of Oman and Ligurian ophiolites. *Geochem. Geophys. Geosyst.* **2013**, *14*, 2474–2495, doi:10.1002/ggge.20147.
40. Parkhurst, D.L.; Appelo, C.A.J. *User's Guide to PHREEQC (Version 2): A Computer Program for Speciation, Batch-Reaction, One-Dimensional Transport, and Inverse Geochemical Calculations*; Water-Resources Investigations Report 99-4259; USGS: Denver, CO, USA, 1999.
41. Plummer, L.N.; Busenberg, E. The solubilities of calcite, aragonite and vaterite in CO_2-H_2O solutions between 0 and 90 °C, and an evaluation of the aqueous model for the system $CaCO_3$-CO_2-H_2O. *Geochim. Cosmochim. Acta* **1982**, *46*, 1011–1040, doi:10.1016/0016-7037(82)90056-4.
42. Ogino, T.; Suzuki, T.; Sawada, K. The formation and transformation mechanism of calcium carbonate in water. *Geochim. Cosmochim. Acta* **1987**, *51*, 2757–2768, doi:10.1016/0016-7037(87)90155-4.
43. Kile, D.E.; Eberl, D.D.; Hoch, A.R.; Reddy, M.M. An assessment of calcite crystal growth mechanisms based on crystal size distributions. *Geochim. Cosmochim. Acta* **2000**, *64*, 2937–2950, doi:10.1016/S0016-7037(00)00394-X.
44. Kowacz, M.; Putnis, C.V.; Putnis, A. The Control of Solution Composition on Ligand-Promoted Dissolution: DTPA−Barite Interactions. *Cryst. Growth Des.* **2009**, *9*, 5266–5272, doi:10.1021/cg9007894.
45. Söhnel, O.; Mullin, J.W. Influence of mixing on batch precipitation. *Cryst. Res. Technol.* **1987**, *22*, 1235–1240, doi:10.1002/crat.2170221004.
46. KrystalShaper. Available online: http://www.jcrystal.com/ (accessed on 10 February 2019).
47. Sawada, K. The Mechanisms of Crystallization and Transformation of Calcium Carbonates. *Pure Appl. Chem.* **1997**, *69*, 921, doi:10.1351/pac199769050921.
48. Cardew, P.T.; Davey, R.J. The Kinetics of Solvent-Mediated Phase Transformations. *Proc. R. Soc. Lond. A Math.* **1985**, *398*, 415–428, doi:10.1098/rspa.1985.0043.
49. Navrotsky, A. Energetic clues to pathways to biomineralization: Precursors, clusters, and nanoparticles. *Proc. Natl. Acad. Sci. USA* **2004**, *101*, 12096–12101, doi:10.1076/pnas.0404778101.
50. Katsifaras, A.; Spanos, N. Effect of inorganic phosphate ions on the spontaneous precipitation of vaterite and on the transformation of vaterite to calcite. *J. Cryst. Growth* **1999**, *204*, 183–190, doi:10.1016/S0022-0248(99)00174-8.
51. Vavouraki, A.I.; Putnis, C.V.; Putnis, A.; Koutsoukos, P.G. An Atomic Force Microscopy study of the growth of calcite in the presence of sodium sulfate. *Chem. Geol.* **2008**, *253*, 243–251, doi:10.1016/j.chemgeo.2008.05.013.
52. Astilleros, J.M.; Pina, C.M.; Fernández-Díaz, L.; Putnis, A. Molecular-scale surface processes during the growth of calcite in the presence of manganese. *Geochim. Cosmochim. Acta* **2002**, *66*, 3177–3189, doi:10.1016/S0016-7037(02)00892-X.
53. Busenberg, E.; Plummer, N. Kinetic and thermodynamic factors controlling the distribution of SO_3^{2-} and Na^+ in calcites and selected aragonites. *Geochim. Cosmochim. Acta* **1985**, *49*, 713–725, doi:10.1016-0016-7073(85)90166-8.
54. Titiloye, J.O.; Parker, S.C.; Mann, S. Atomistic Simulation of Calcite Surfaces and the Influence of Growth Additives on Their Morphology. *J. Cryst. Growth* **1993**, *131*, 553–545, doi:10.1016/0022-0248(93)90205-B.
55. Davis, K.J.; Wasylenki, L.E.; Dove, P.M.; De Yoreo, J.J. Morphological consequences of differential Mg^{2+} incorporation at structurally distinct steps on calcite. *Am. Mineral.* **2004**, *89*, 714–720, doi:10.2138/am-2004-5-605.
56. Fernández-Díaz, L.; Astilleros, J.M.; Pina, C.M. The morphology of calcite crystals grown in a porous medium doped with divalent cations. *Chem. Geol.* **2006**, *225*, 314–321, doi:10.1016/j.chemgeo.2005.08.024.